UC San Diego

UC San Diego Electronic Theses and Dissertations

Title

Scaffold and stem cell based modeling of brain disease

Permalink

https://escholarship.org/uc/item/79v881g3

Author

Karpiak, Jerome V.

Publication Date

2016

Peer reviewed|Thesis/dissertation

eScholarship.org Powered by the California Digital Library
University of California

UNIVERSITY OF CALIFORNIA, SAN DIEGO

Scaffold and stem cell based modeling of brain disease

A dissertation submitted in partial satisfaction of the requirements for the degree

Doctor of Philosophy

in

Biomedical Sciences

by

Jerome V. Karpiak

Committee in Charge:

Professor Alysson R. Muotri, Chair
Professor Nicola J. Allen
Professor Fred H. Gage
Professor Laurence S. Goldstein
Professor Albert R. La Spada
Professor Karl Willert

2016

Copyright

Jerome V. Karpiak, 2016

All rights reserved.

The Dissertation of Jerome V. Karpiak is approved, and it is acceptable in quality and form for publication on microfilm and electronically:

_____

_____

_____

_____

_____

_____

Chair

DEDICATION

In Memoriam

Justin Michael Gaglione

November 20, 1975 - January 14, 2005



What it be?

What it is.

EPIGRAPH

"*In summary, there are no small problems. Problems that appear small are large problems that are not understood… Nature is a harmonious mechanism where all parts, including those appearing to play a secondary role, cooperate in the functional whole. No one can predict their importance in the future. All natural arrangements, however capricious they may seem, have a function*."

—Santiago Ramón y Cajal, Advice for a young investigator, 1897.

TABLE OF CONTENTS

Signature Page iii
Dedication iv
Epigraph v
Table of Contents vi
List of Abbreviations viii
List of Figures x
List of Tables xii
Acknowledgements xiii
Curriculum Vitae xvi
Abstract of the Dissertation xviii
Chapter 1 - Introduction 1
1.1 The challenge - Building complexity into *in vitro* models to study brain disease 2
1.2 Background and significance 3
1.3 Overview of brain cytoarchitecture and disease 3
1.4 Emerging solutions - Stem cell & 3D scaffold based approaches 13
1.5 Hypothesis and aims of the thesis 18
1.6 Overview of dissertation chapters 20
Chapter 2 - Density gradient multilayer polymerization (DGMP) to create 3D *in vitro* disease models 24
2.1 Abstract 25
2.2 DGMP method for creating complex tissue 28
2.3 Monolayer gradient model of wound healing: Haptotaxis is cell type specific and limited by substrate adhesiveness 44
2.4 Three-dimensional Hyaluronic acid scaffold for *in vitro* neural modeling 76
2.5 Conclusions 83
2.6 Acknowledgements 84
Chapter 3 - Stem cell models of neural development to study human monogenetic brain disorders 86
3.1 Abstract 87
3.2 Monolayer iPSC derived neural cultures reveal neurophysiological phenotypes in Cockayne Syndrome (*ERCC6*) 90
3.3 Monolayer stem cell derived neural co-cultures reveal astroglial non-autonomous neurophysiological phenotypes in Rett Syndrome (*MECP2*) 118
3.4 Conclusions 142
3.5 Acknowledgements 142

Chapter 4 - Three-dimensional scaffolds accelerate *in vitro* neuronal differentiation & laminar co-cultures reveal new neurophysiological RTT phenotypes 144
4.1 Abstract 145
4.2 Brief introduction and rationale 145
4.3 Materials and methods 147
4.4 Results 157
4.5 Summary 189
4.6 Conclusions 192
4.7 Recognitions 193
4.8 Acknowledgements 194
Chapter 5 - Discussion of the thesis 195
5.1 Hypothesis and goals 196
5.2 Summary of principal findings 197
5.3 Scaffold and stem cell based approaches to building functional brain models 200
5.4 Monolayer iPSC derived neural networks reveal altered neuronal connectivity in CS 206
5.5 Monolayer neural co-cultures from isogenic *MECP2* stem cells reveal astroglial non-autonomous phenotypes in RTT 209
5.6 3D neural development models reveal neuronal maturation deficits and altered chemotaxis in RTT 210
5.7 Future perspectives 213
5.8 Conclusions 216
Appendix A - Published US Patent Application # 13/794,546: Single step polymerization of covalently bound multilayer matrices 218
Appendix B - Published online DGMP video protocol: JoVE© summary and URL 251
Appendix C - A pilot MEA study: Monolayer iPSC-derived neural cultures reveal electrophysiological phenotypes in *CDKL5* 262
Appendix D - A pilot API study: MEA platform to screen epilepsy drugs 273
References 278

LIST OF ABBREVIATIONS

1H-NMR-	proton nuclear magnetic resonance
AATC-	American Type Culture Collection
ACM-	astrocyte conditioned medium, or astroglia conditioned medium
AFS-	atomic force spectroscopy
aPEG-	acryloyl polyethylene glycol
BDNF-	brain-derived neurotrophic factor
bFGF22-	fibroblast growth factor-basic
BK-	bradykinin
BSA-	bovine serum albumin
c2c12	murine myoblast cell line
CaCl2-	calcium chloride
CS-	Cockayne syndrome
ctr83-	source of unaffected cells from the father of Rett Syndrome donor Q83X, also abbreviated "WT83"
CytoD-	cytochalasin D
D2O-	deuterium oxide, or "heavy" water
DCDMS-	dichlorodimethylsilane
DGMP-	density gradient multilayer polymerization
DIPEA-	N-Ndiisopropylethylamine
DMF-	dimethylformamide
DMSO-	dimethyl sulfoxide
DS-	degree of substitution
EB-	embryoid body
ECM-	extracellular matrix
EDC/NHS -	1-Ethyl-3-(3-dimethylaminopropyl)-carbodiimide (EDC) crosslinks carboxyl or phosphate groups to primary amines (NHS)
EDTA-	ethylenediaminetetraacetic acid
EGTA-	ethylene glycol tetraacetic acid
ESC-	embryonic stem cell
FACS-	fluorescence-activated cell sorting
FE-SEM-	field emission-scanning electron microscopy
FRET-	Förster resonance energy transfer
GABA-	gamma-Amino Butyric acid
HEK293-	a cell line derived from human embryonic kidney cells
HEPES-	4-(2-hydroxyethyl)-1-piperazineethanesulfonic acid
IKVAV-	pentapeptide isoleucine-lysine-valine-alanine-valine
iPSC-	induced pluripotent stem cell
KCl-	potassium chloride
LPA-	lysophosphatidic acid
MACS-	magnetic-activated cell sorting

MALDI-TOF-	matrix assisted laser desorption/ionization-time of flight
MgCl2-	magnesium chloride
MSC-	mesenchymal stem cell
MTS-	3-(4,5-dimethylthiazol-2-yl)-5-(3-carboxymethoxyphenyl)-2-(4-sulfophenyl)-2H-tetrazolium, used in "one-step" MTT assay
N126I-	nonesense mutation in *MECP2* transforming an asparagine to isoleucine as residue 126
N2-	nitrogen
NaH2PO4-	monosodium phosphate
NaHCO3-	sodium bicarbonate
NEB-	neuralized embryoid body
Noco-	nocodazole
NPC-	neural precursor cell
OVA-	chicken serum ovalbumin
PA-	polyacrylamide, also known as PAM
PAM-	see "PA"
PEG-	polyethylene glycol
PEGda-	polyethylene glycol diacrylate
Pitx-	picrotoxin
PSD95-	postsynaptic density protein 95
Q83X-	nonesense mutation in *MECP2* transforming a glutamine into an early stop codon at the 83rd residue
RGD-	arginylglycylaspartic acid
RGDS-	arginine-glycine-aspartic acid-serine
RTT-	Rett syndrome
SCM-	Succinimidyl Carboxymethyl
TEM-	transmission electron microscopy
TFM-	traction force microscopy
THC-	tetrahydrocannabinol
THF-	tetrahydrofuran
t_S-	settling time
TTX-	tetrodotoxin
UVA-	ultraviolet A: 315-400 nm, wavelength associated with "black light"
WT83-	see "ctr83"
YIGSR-	tyrosine-isoleucine-glycine-serine-arginine

LIST OF FIGURES

Figure 2-1 Schematic representation of two variations of DGMP. 30
Figure 2-2 MALDI-TOF confirms aPEG-SCM and aPEG-RGDS. 32
Figure 2-3 1H-NMR confirms acryloyl-PEG-RGDS. 33
Figure 2-4 Improvised DGMP molds. 34
Figure 2-5 UVA sources for biologics-compatible photopolymerization. 35
Figure 2-6 DGMP results in continuous structures and mechanical stability at interfaces. 38
Figure 2-7 Demonstration of tunable process variables. 39
Figure 2-8 DGMP facilitates spatial control of scaffold bioactivity. 40
Figure 2-9 DGMP can be adapted to produce hydrogels of varying shapes. 40
Figure 2-10 DGMP can separate protein into discrete compartments. 41
Figure 2-11 DGMP facilitates spatial control of scaffold bioactivity gradients. 42
Figure 2-12 DGMP photopolymerization is compatible with live cells. 43
Figure 2-13 Fabrication of polyacrylamide hydrogels with RGD and collagen gradients. 49
Figure 2-14 Characterization of hydrogels with RGD and collagen gradients. 51
Figure 2-15 Cell Spread Area and Attachment on Collagen Gradients. 57
Figure 2-16 Migratory response of MSCs and fibroblasts on ligand gradients. 58
Figure 2-17 Characterization of MSC Migration on Collagen Gradients. 60
Figure 2-18 Characterization of 3T3 Migration on Collagen Gradients. 61
Figure 2-19 Influence of drug treatment on fibroblast morphology and migration. 63
Figure 2-20 Effect of Drug Treatment on 3T3 Migration Paths. 64
Figure 2-21 Influence of drug treatment on fibroblast velocity. 65
Figure 2-22 Fibronectin FRET Intensity Characterization. 66
Figure 2-23 Measuring cell-induced deformations of the underlying substrate. 67
Figure 2-24 Reducing MSC-substrate adhesion by blocking surface integrins with free peptide. 69
Figure 2-25 Increasing fibroblast-substrate adhesion by increasing surface adhesive ligand density. 70
Figure 2-26 Production of hyaluronic acid methacrylate for NPC culture. 77
Figure 2-27 HAMA encapsulation is compatible with NPC neurite extension and neuronal differentiation. 79
Figure 2-28 Determination of NPC migration variables. 80
Figure 2-29 Combinations of variables to allow NPC migration. 81
Figure 3-1 Generation and characterization of CSB iPSCs. 100
Figure 3-2 Generation of CSB-NPCs derived from iPSCs. 101
Figure 3-3 Characterization of CSB neurons. 102
Figure 3-4 FAC sorting for Control-1 C1 and CSB-1 C2. 103
Figure 3-5 Sample correlation via dendrogram and PCA map. 105
Figure 3-6 RNA-seq validation via PCR. 106
Figure 3-7 Transcriptional dysregulation of GH/IGF-1 pathway in CSB neurons. 110
Figure 3-8 CSB neurons have reduced synapse density. 111
Figure 3-9 CSB neuronal cultures have reduced number of spikes and synchrony. 113
Figure 3-10 Establishing neural co-culture using human stem cells. 120
Figure 3-11 Isogenic human ESC model to mimic RTT-like MeCP2 mutation. 124
Figure 3-12 resQ83 Sequence allignment. 125

Figure 3-13 Schematic timeline describing NPC generation. 126
Figure 3-14 Schematic timeline describing astroglia generation from NPC lines. ... 128
Figure 3-15 Schematic timeline for neuronal differentiation and enrichment from NPC lines. 129
Figure 3-16 Neuronal activity is enhanced early by astroglia contact co-culture after two weeks. 133
Figure 3-17 Astroglia and ACM promote cumulative neuronal activity over time..... 134
Figure 3-18 Astroglial co-culture and ACM increase neuronal co-localized synapse density. 135
Figure 3-19 Neural activity is diminished by MeCP2-deficient astroglia. 137
Figure 3-20 Neuronal glutamatergic pre-synaptic puncta density unaffected by feeder cell type. 138
Figure 3-21 Neuronal co-localized synapse density is adversely affected by MeCP2-deficient astroglia. 140
Figure 4-1 Setup of layered hydrogels to study migration of human iPSC-derived NPCs. 159
Figure 4-2 Characterization of NPCs and astrocytes derived from iPSCs..... 160
Figure 4-3 Layered hydrogels to study migration of iPSC-derived NPCs. 162
Figure 4-4 Characterization of NPC-derived neurons. 163
Figure 4-5 Defective migration of Q83X NPCs towards astrocytes or neurons. 166
Figure 4-6 ESC isogenic *MECP2* matched NPCs mimic RTT migration defect..... 168
Figure 4-7 Defective migration of N126I NPCs towards astrocytes or neurons..... 170
Figure 4-8 Rapid structural maturation of human neurons in 3D hydrogels. 172
Figure 4-9 Rapid functional maturation of human neurons in 3D hydrogels. 174
Figure 4-10 Neuronal differentiation in 3D versus in 2D system. 176
Figure 4-11 Representative images of WT83 neurons in 3D hydrogel. 178
Figure 4-12 Neuronal subtypes in 3D versus 2D system. 179
Figure 4-13 Effects of hydrogel mechanical properties on differentiation and neurite outgrowth in 3D. 180
Figure 4-14 2D soft hydrogel NPC attachment and neural induction. 182
Figure 4-15 2D soft hydrogel neural induction and migration assay..... 183
Figure 4-16 Astrocyte conditioned medium disrupts astrocyte-induced chemotaxis. 184
Figure 4-17 Defective maturation of *MECP2*$^{-/y}$ Q83X neurons in 3D hydrogel. 186
Figure 4-18 Isogenic *MECP2* ESC derived neurons verify RTT neural defects in 3D. 187
Figure 4-19 Defective neurite outgrowth and synapse density in *MECP2*$^{-/y}$ N126I neurons in 3D. 189
Figure 5-1 Application of DGMP to model brain disease. 202

LIST OF TABLES

Table 3-1 Description of cells (and their respective donors) used in this study. 92
Table 3-2 PCR primers used in this study. 96
Table 3-3 Significantly altered Ingenuity® pathways. 107
Table 3-4 Top Canonical Pathways significantly altered in CSB neurons. 108
Table 3-5 Top Upstream Regulators significantly altered in CSB neurons. 108
Table 4-1 Number of clones from iPSCs used in each experiment. 152
Table 4-2 Sequence of primers used in qPCR experiments. 155

ACKNOWLEDGEMENTS

I would like to thank my advisor, Dr. Alysson Muotri for providing me space and resources to conclude my PhD, and for pushing me out of his nest when the time came for me to fly. I would also like to thank to Dr. Adah Almutairi for mentoring me and for providing me the freedom to explore numerous areas of research. I learned a tremendous amount in both of your academic laboratories and made life-long friends!

I humbly thank my thesis committee members, Dr. Karl Willert, Dr. Nicola Allen, Dr. Rusty Gage, Dr. Al La Spada, and Dr. Larry Goldstein, for taking the time to help guide my path in the last two years of my PhD.

Special thanks to Dr. Victor Nizet. Your guidance and support throughout encouraged me to endure, overcoming some interesting challenges along the way. I would also like to thank the UCSD BMS department and staff for all their support, especially when things were far beyond my control. Thank you Leanne, Gina, Kathy and Pat & Chairs Tracy Handel & Debbie Spector.

I would like to thank my entire family. Especially my mom, Vivian Karpiak for being my inspiration. My father, James Karpiak for always being supportive and for providing a positive voice whenever I needed it most. My caring brother, Blaise Karpiak for pinging me the day before family member birthdays. Justin Gaglione for being my motivation. Justin Lahdelma for always reminding me who I am, and believing in me.

THANK YOU Hiruy Meharena & Stephanie Weng for always offering me rationale, and rationality (even when I seemed to not listen)! My new family.

And, to ALL my friends that I have neglected for the past five years (Yes, Bryan, you and the entire Ferreira clan), thank you for your understanding. I'm back.

Thanks to my immensely patient wife, Elona Rista. I owe everything to you.

Parts of Chapter 2 sections 2.1, 2.2, 2.4, and 2.5, Figure 5-1 and the contents of Appendix A were adapted for US Patent Application # 13/794,546 and published as "Single step polymerization of covalently bound multilayer matrices." Karpiak JV**,** Ner Y, Morachis J, Almutairi A. US Patent publication # US20130234372A1, March 11, 2013. The dissertation author was the primary investigator and author of this patent.

The contents of Chapter 2 section 2.2 were adapted for the journal Advanced Materials and published as "Density Gradient Multilayer Polymerization for Creating Complex Tissue." Karpiak JV**,** Ner Y, Almutairi A. Advanced Materials, 2012, 24:1466-1470. The dissertation author was the primary investigator and author of this work.

Parts of Chapter 2 sections 2.2 and 2.4, and the contents of Appendix B were adapted for the Journal of Visualized Experiments and published as "DGMP: A novel technique for creating multi-compartment, customizable scaffolds for tissue engineering." Joshi-Barr S, Karpiak JV, Ner Y, Wen JH, Engler AJ, Almutairi A. Journal of Vis Exp, 2013, (72). The dissertation author was the primary investigator and author of this work.

The contents of Chapter 2 section 2.3 were adapted for the journal Cellular and Molecular Bioengineering and published as "Haptotaxis is cell type specific and limited by substrate adhesiveness." Wen JH, Choi O, Taylor-Weiner H, Fuhrmann A, Karpiak JV, Almutairi A, Engler AJ. Cell Mol Bioeng, 2015, 8(4):530-542. The dissertation author was a main contributor and co-author of this work.

Part of Chapter 3 section 3.1 and the contents of section 3.2 were adapted for the journal Human Molecular Genetics and published as “Cockayne Syndrome-derived neurons display reduced synapse density and altered neural network synchrony**.”** Vessoni AV, Herai RH, Karpiak JV, Leal A, Trujillo C, Quinet A, Menck CFM, Muotri AR. Human Molecular Genetics, 2016. Published online Jan 4, doi: 10.1093/hmg/ddw008. The dissertation author was a main contributor and co-author of this work.

The contents of Chapter 4 were adapted for the Proceedings of the National Academy of Sciences and are currently in press as “Layered hydrogels accelerate iPSC-derived neuronal maturation and reveal migration defects caused by MeCP2 dysfunction.” Zhang Z-N, Freitas BC, Qian H, Lux J, Acab AJ, Trujillo C, Herai R, Nguyen Huu VA, Wen JH, Joshi-Barr S, Karpiak JV, Engler AJ, Fu X-D, Muotri AR, Almutairi A. The dissertation author was a main contributor and co-author of this work.

The contents of Appendix C and Appendix D highlight my contributions to an evolving project currently in development through collaboration between the laboratories of Alysson Muotri and Bradley Voytek. Key investigators Priscilla Negraes, PhD and Richard Gao will continue this work towards a peer-reviewed publication as a continuation of our IFCR funded project entitled: “Modeling CDKL5 Syndrome using human Neurons.“ The dissertation author was the primary investigator and author of this work.

CURRICULUM VITAE

EDUCATION

Doctor of Philosophy, Biomedical Sciences, March 2016
University of California, San Diego, CA

Master of Science, Biomedical Engineering, December 2008
University of Florida, Gainesville, FL

Bachelor of Science, December 2005
Wayne State University, Detroit

EXPERIENCE

Graduate Researcher, Biomedical Science 2010-2016
University of California, San Diego, CA

Associate Scientist, Sports Medicine 2008-2010
RTI Surgical, Alachua, FL

Graduate Researcher, Biomedical Engineering 2006-2008
University of Florida, Gainesville, FL

Chemical Engineer, Automotive Polymers 2004-2006
Acuren, Detroit, MI

OUTREACH & TEACHING

Mentor & Volunteer Tutor, College Preparatory 2012-Present
Reality Changers, San Diego, CA

Graduate Teaching Assistant, Intro to Biom Engg, Tissue Engg 2007-2008
University of Florida

PUBLICATIONS (2012 - 2016)

Karpiak JV, Ner Y, Morachis J, Almutairi A. "*Single Step Polymerization of Covalently Bound Multilayer Matrices"* US Patent Application No 13/794,546, published March 11, 2013 as US 20130234372 A1; Allowed, pending issue June 7, (2016).

Zhang Z-N, Freitas BC, Qian H, Lux J, Acab AJ, Trujillo C, Herai R, Nguyen Huu VA, Wen JH, Joshi-Barr S, **Karpiak JV**, Engler AJ, Fu X-D, Muotri AR, Almutairi A. *"Layered hydrogels accelerate iPSC-derived neuronal maturation and reveal migration defects caused by MeCP2 dysfunction"* PNAS, First published online March 4, doi:10.1073/pnas.1521255113 (2016).

Vessoni AV, Herai RH, **Karpiak JV**, Leal A, Trujillo C, Quinet A, Menck CFM, Muotri AR. *"Cockayne syndrome-derived neurons display reduced synapse density and altered neural network synchrony."* Hu Mol Gen, First published online January 10, doi:10.1093/hmg/ddw008 (2016).

Wen JH, Choi O, Taylor-Weiner H, Fuhrmann A, **Karpiak JV**, Almutairi A, Engler AJ. "*Haptotaxis is cell type specific and limited by substrate adhesiveness*" Cell Mol Bioeng, 8(4):530-542, doi:10.1007/s12195-015-0398-3 (2015).

Lewis JS, Dolgova NV, Chancellor TJ, Acharya AP, **Karpiak JV**, Lele TP, Keselowsky BG. "*The effect of cyclic mechanical strain on activation of dendritic cells cultured on adhesive substrates"* Biomat, 34(36):9063-70, doi:10.1016/j.biomaterials.2013.08.021 (2013).

Joshi-Barr S, **Karpiak JV**, Ner Y, Wen JH, Engler AJ, Almutairi A. "*Density Gradient Multilayered Polymerization (DGMP): A Novel Technique for Creating Multi-compartment, Customizable Scaffolds for Tissue Engineering"* J Vis Exp, (72) e50018, doi:10.3791/50018 (2013).

Karpiak JV, Ner Y, Almutairi A. "*Density Gradient Multilayer Polymerization for Creating Complex Tissue"* Adv Mater, 24: 1466-1470, doi:10.1002/adma.201103501 (2012).

FIELDS OF STUDY

Major Field: **Biomedical Sciences** 2010-2016

Studies in Developmental Neurobiology
Professor Alysson Muotri, University of California at San Diego

Studies in Bioresponsive Materials & Nanoscience
Professor Adah Almutairi, University of California at San Diego

Major Field: **Engineering** 2001-2008

Studies in Biomaterials & Immunomodulation
Professor Benjamin Keselowsky, University of Florida

Studies in Chemical Engineering & Materials Science
Professor Guangzhao Mao, Wayne State University

ABSTRACT OF THE DISSERTATION

Scaffold and stem cell based modeling of brain disease

by

Jerome V. Karpiak

Doctor of Philosophy in Biomedical Sciences

University of California, San Diego, 2016

Professor Alysson R. Muotri, Chair

Cellular models of brain disease involve genetic modulation, geometric patterning, neurophysiologic monitoring and analyses of both primary and immortalized cell lines. Additionally, recent neurological disease models often necessitate in vitro directed differentiation and maturation of human stem cell lines. To advance human stem cell based neural disease models within this evolving field, adaptive approaches of progressive complexity are essential. First, I invented an adaptable 3D laminar scaffold fabrication method to facilitate complex in vitro cell and tissue cultures. Next,

we built on the Muotri Laboratory's pioneering iPSC approach, incorporating emergent multi-well microelectrode array technology to establish the first functional in vitro human neural model of Cockayne Syndrome (CS). We revealed previously unreported neural network abnormalities and identified neuronal transcription dysregulation of the GH/IGF-1 signaling pathway. We also enhanced our previously established Rett Syndrome (RTT) model using advanced stem cell methods, including genomic editing technology to create isogenic matched *MECP2* cell lines and establish neural co-cultures. With this system I revealed adverse astroglial non-autonomous effects on neuronal networking in monolayer co-cultures. Finally, we combined my novel multilayer fabrication method with this isogenic *MECP2* approach to pattern neural co-cultures in 3D hyaluronic acid based laminar tissue scaffolds, building further complexity into our original model. We report accelerated in vitro neural development, *MECP2*$^{-}$ NPC chemotaxis defects and additional astroglial non-autonomous effects in this new 3D biomimetic RTT neural model. The methods described herein have allowed us to establish multidimensional individualized human donor-relevant models of a neurodegenerative disorder (CS) and a neurodevelopmental disorder (RTT) in screenable formats.

Chapter 1

Introduction

1.1 The challenge - Building complexity into *in vitro* models to study brain disease

In vitro disease modeling aims to recapitulate pathological processes similar to those of human diseases by taking advantage of naturally occurring or experimentally induced defects. Cell based monogenetic neural disease models include genetic modulation, geometric patterning, scaffolding, physiological monitoring and analyses of both primary and immortalized cell lines; however, typical approaches lack sufficient complexity to match the *in vivo* environment. Animal models often fail to recapitulate human pathology, primary human neural cells are extremely limited in availability and range of cell types, post mortem brain studies are often limited by disease stage and typical stem cell derived neural disease models generally lack dimensionality and complexity. Further, *in vitro* monolayer models often necessitate poorly controlled differentiation into heterogeneous neural cell populations. Building a 3D model brain in a dish with carefully monitored arrangements of neural cell subtypes is necessary to understand how these cells interact, and how normal development progresses. Once this is achieved, we can better study neural development in the context of disease. Therefore, new adaptable approaches of progressive sophistication are critical to advancing human stem cell based neural development and disease modeling.

Unfortunately, few neurological disorders have available effective treatments. Great effort has been directed at new therapeutics; however, potential drugs usually fail in various stages of clinical trials despite initial promise. Enhanced 3D *in vitro* neural disease models more closely mimic the complex *in vivo* environment than typical monolayer cultures and may help identify new therapeutic targets, ultimately leading to better pharmacological candidates before entering clinical trials. The stem cell and

scaffold based approaches described herein have allowed us to establish multidimensional human donor- and mutation-specific models of neural development in screenable formats.

1.2 Background and significance

Neurological diseases affect roughly one in six adults. Most neurodevelopmental and neurodegenerative diseases remain without known cures or treatments and create heavy financial burdens on affected individuals as well as society. For example, more than 3.5 million Americans live with Autism, 40% of which also have intellectual disability. The estimated lifetime cost for such an individual is $2.4 million (Buescher et al., 2014). A 2015 report estimated that over 46 million people worldwide (9.4 million in the U.S. alone) suffer from dementia. Alzheimer's disease is the leading cause of dementia, with an estimated global cost of $818 billion (Prince et al., 2015). Other rarer diseases such as Progeroid syndromes that induce premature aging have a far smaller global financial impact, but are no less significant to the families and communities supporting these individuals. Further, insight gained from studying this phenomenon could have broader impact on how we view and treat a range of neurodegenerative disorders.

1.3 Overview of brain cytoarchitecture and disease

1.3.1 Brain cytoarchitecture

To model brain disease we must first understand the relevant native neurobiology. Underlying all human behavior, the brain comprises a highly complex and hierarchical organization of biomolecules and cellular arrangements. These highly

organized microenvironments modulate functional activity of neural networks regionally, as well as throughout the CNS. The cerebral cortex is the largest and outermost layer of the brain, deeply grooved and consisting mainly of astroglia and neuronal cell bodies. The cortex is arranged into structurally and functionally discrete regions, comprehensively categorized by Korbinian Brodman (Brodmann, 1909), that contain different cell types, collectively known as neural “cytoarchitecture.” Cellular regionalization and the formation of elaborate grooves (sulci) and ridges (gyri) occurs via orchestrated neural stem cell migration (Rakic, 1972) and proliferation (Ronan et al., 2014) mediated by glia cells, gradients of biochemical cues and the extracellular matrix during corticogenesis. The mappable cortical sub-regions control distinct functions such as learning, memory, language, sensory perception, motor facility and sleep. The neocortex, which is the largest part of the cerebral cortex, is further striated, as originally described by Ramón y Cajal, into six distinct layers (Brodmann, 1909). These structural lamellae are delineated by distinct cell type distributions and neuronal connectivity (Mountcastle, 1997). Supported by glia, the neocortex consists of two primary classes of neurons: excitatory pyramidal (glutamatergic) neurons and inhibitory (GABAergic) interneurons. Further, functional identity and circuitry patterns of these cortical neurons exhibit regional and laminar dependence. Normal brain cytoarchitecture is necessary for healthy neuronal function and proper network activity.

The brain can be understood as a global neural network of interconnected components (Meunier, Lambiotte, & Bullmore, 2010). It constantly exhibits electrophysiological activity fluctuations regardless of external stimuli, which is why it is important that we consider the health and organization of functional neural networks. Further supporting this fact, the metabolic cost of intrinsic activity of the brain far

exceeds that of evoked activity (Raichle & Mintun, 2006). Most cortical neurons are neither directly under the influence of sensory input nor directly involved in motor output (Braitenberg, 1998). For example, less than 10% of synapses receive sensory inputs from outside the brain, suggesting they rely on inputs from inside the brain (Peters & Feldman, 1976). Electroencephalography (EEG) studies reveal that the magnitude of task-evoked responses is diminutive compared to the magnitude of spontaneous activity fluctuations. Furthermore, the pattern of spontaneous fluctuations sometimes resembles that of evoked activity (Blankenship & Feller, 2010; Kenet et al., 2003), potentially suggesting predictive programming. This emphasizes the not yet fully understood developmental pressure on healthy cortical neurons to elaborately connect to vastly complex internal neural networks. The mature brain and CNS is composed of three major cell types: neurons, astroglial and oligodendrocytes. Taken together, neuronal network connectivity is necessary for healthy brain function and, importantly, neurons do not work independently!

1.3.1.1 Neural “Stem,” “Progenitor,” and “Precursor” Cells

During embryogenesis, neural development is initiated with the induction of the neuroectoderm giving rise to neuroepithelial cells (NECs) (Kriegstein & Alvarez-Buylla, 2009; Temple, 2001). As cortigogenesis ensues, NECs undergo symmetric division to expand spatially distinct neural stem cell (NSC) populations. In later stages of neural development, NSCs switch to asymmetric division and give rise to lineage-restricted progenitors. Intermediate neuronal and glial progenitor cells are formed, and then separately differentiate to generate neurons, astroglia and oligodendrocytes. Admittedly, I have been confused by the interchangeable application of the terms

“stem,” “progenitor,” and “precursor” used in literature to describe undifferentiated neural cells. For clarity in this dissertation, I will follow criteria outlined in a recent review published by StemCell Technologies (V. M. Lee, Louis, & Reynolds, 2015) and refer to our stem cell-derived mixed population of neural intermediates, consisting of all undifferentiated progeny of NSCs and progenitor cells, as neural precursor cells (NPCs).

1.3.1.2 Neurons

Fundamentally, neurons are highly specialized cells evolved to sense, interpret and propagate electrical events. Through such electrophysiological activity, neurons communicate with each other and with tissues outside the CNS. Therefore, an understanding of basic neurobiology is fundamental to understanding health (and disease) of neurons, neural systems and the brain. While a full discussion on the topic of neuroanatomy and electrophysiology is beyond the scope of this dissertation, basic principles will be discussed here. A neural network is a series of interconnected neurons whose activation response to neurotransmission defines a recognizable linear pathway. Glutamate and GABA are two main excitatory and inhibitory, respectively, amino acid neurotransmitters. Neurons interact within the network through axon terminals connected via synapses to dendrites on other neurons. If the sum of the input signals into one neuron surpasses a certain threshold, a rapid ion flux is induced generating an observable electrical action potential at the axon hillock that propagates the signal along the axon to its terminal and into the next synapse. A neural circuit is a functional sub-unit of interconnected neurons that is able to regulate its own activity using a feedback loop.

1.3.1.3 Astroglia

Astroglia are the most common cell in the CNS. Notably, often referred to as astrocytes (Greek for “star cells”), cells in this category are not necessarily star shaped. For example, radial glia, fibrous glia (in white matter) and protoplasmic glia (in grey matter), each sub-categorized for their respective morphologies, express high levels of signature astroglial proteins such as glutamate transporter (GLAST) and glial fibrillary acidic protein (GFAP). In addition to morphological differences, astroglia are functionally diverse. Immature astrocytes are involved in neuronal synaptogenesis and NPC migration. Radial glia, briefly described in the previous section, are mostly present during development guiding massive neural migration. Fibrous glia exhibit long unbranched cellular processes with vascular feet able to physically connect to capillaries. Lastly, protoplasmic glia are the most prevalent glia in grey matter. The latter astroglia are often distinctively star shaped, provide one third of the tripartite synapse, and play key roles in synaptic plasticity as well as general housekeeping of the neural micro environment (Allen, 2014; Anderson & Nedergaard, 2003; Perea, Navarrete, & Araque, 2009).

1.3.1.4 Corticogenesis

Corticogenesis is the intricate embryonic process of creating the modular cerebral cortex, involving tightly orchestrated differential migration and proliferation of neural cells. Complex spatiotemporal physical and biochemical interactions with the neural extracellular matrix and non-tethered biomolecular messengers promote neural cell migration during embryogenesis. Temporary radial scaffolding made up of glial cells (Noctor et al., 2001; Rakic, 1972) guides regional migration of NSCs. Once these

NSCs relocate, regionally directed proliferation rates of neural progenitors contribute to the patterning of gyri (Ronan et al., 2014). These progenitor cells further give rise to different neuronal subtypes in specified layers of the developing cerebral cortex. This highly regulated neuronal positioning, combined with layer-specific conditions, governs subsequent cell subtype properties including connectivity. In addition to local biomolecular influences, neuronal subtype specification and laminar position are transcriptionally co-regulated (Kwan, Sestan, & Anton, 2012). For example, some neuronal subtype and layer-specific transcription factors critical for designation include *SOX5* for layer 6, *CTIP2* and *FEZF2* for layer 5 subcortical projection neurons, and *SATB2* for upper layer callosal projection neurons.

1.3.1.5 Connectivity and Electrophysiology

Neuronal positioning is only the beginning of functional neural network development in the cortex. As neural progenitors begin to differentiate into glutamatergic and future GABAergic neurons, they are signaled to detach from the radial glia and extend neurites which then begin to form synaptic connections (Hack et al., 2002). Once in their designated position, connections must be properly established both locally and long-range. This requires specification of the projection neuron subtype as well as synaptic connectivity via dendrite development and axon maturation. Projecting growth cones are further directed to their synaptic targets by an interplay of migratory signals including cues from the extracellular matrix (ECM), cell adhesion molecules (CAMs) such as glycoproteins on adjacent cells and soluble chemokine gradients of morphogens produced by astroglia (Marin et al., 2010). Axon and dendrite morphogenesis as well as synapse formation are activity-dependent (R. O. L. Wong &

Ghosh, 2002). Effective neuronal network function and communication is initiated by axonal outgrowth from maturing neurons in the cortex, followed by dendritic arborization, synaptogenesis and a life-long process of activity-dependent glia-mediated pruning and tuning (Schafe, 2014). During development or at any time throughout life, aberrations in any of these events, from NPC migration to synaptic plasticity, will disrupt normal brain function and lead to disease.

1.3.1.6 The extracellular matrix

Brain and CNS health strongly depends on the condition of the unique structural neural microenvironment, generally referred to as the extracellular matrix (ECM). The ECM of healthy brain tissue is composed of four main classes of biomolecules: hyaluronic acid (HA), proteoglycans (lecticans), link proteins and tenascins (Bellail et al., 2004; Bignami, Hosley, & Dahl, 1993; Rauch, 2004; Ruoslahti, 1996; Yamaguchi, 2000). HA is the primary structural component of neural ECM (Anlar & Gunel-Ozcan, 2012; Bignami et al., 1993; Zimmermann & Dours-Zimmermann, 2008). HA is a negatively charged glycosaminoglycan macromer that attracts and binds cations, water and charged soluble proteins which together amplify the hydration capacity of neural tissue (Bignami et al., 1993). Notably, Tenascins contain integrin binding fibrobronectin type III-repeats and a carboxyl-terminal fibrinogen-like globular domain that binds to cell surface ligands in an arginylglycylaspartic acid (RGD)-dependent fashion (Anlar & Gunel-Ozcan, 2012; Bourdon & Ruoslahti, 1989; Zimmermann & Dours-Zimmermann, 2008). Other macromolecular glycoproteins of the CNS include reelin, agrin and thrombospondins which are involved in neural migration and synaptogenesis (Bezakova & Ruegg, 2003; Christopherson et al., 2005; Herz & Chen, 2006).

While adult neural ECM is rich in HA, it lacks high concentrations of rigid structural proteins such as collagen, fibronectin and laminin common throughout other tissues (Bellail et al., 2004). Combined with a lack of structural proteins, the hydrophilic nature of HA causes neural ECM to vastly swell, resulting in the characteristic low stiffness of brain tissue (Bignami et al., 1993). Interestingly, corticogenesis is disrupted in laminin-mediated integrins α3β1 and α6β1 knock-out mice, suggesting laminin ligation is critical during early neural development (Danen & Sonnenberg, 2003; De Arcangelis & Georges-Labouesse, 2000). Laminin is a massive cross-shaped glycoprotein containing integrin binding pentapeptide motifs YIGSR and IKVAV (Mackay et al., 1994; Nomizu et al., 1995; Ranieri et al., 1995).

1.3.2 Disorders of the brain

Brain diseases are caused by genetic defects, infections, structural defects, tumors, autoimmunity, and epigenetics or any combination of such factors. Chronic brain diseases fall into two major categories, degenerative and developmental. Neurodegeneration is the progressive loss of neural function due to structural or cellular degradation in the brain. In healthy adults, neurons are not rapidly repaired or replaced, therefore, regardless of the cause, when neural degradation occurs in the brain, irreversible or progressive dysfunction will result. In neurodegenerative disorders such as amyotrophic lateral sclerosis, Alzheimer's and some progeroid syndromes, cognitive function critically declines and dementia may ensue. When abnormalities occur during cortical development, disorders such as autism, mental retardation, epilepsy, language and behavioral problems, as well as motor dysfunctions are common consequences. Cortical developmental disorders are often associated with problems in NPC migration

or proliferation (Thompson & Toga, 2003). Both glia and neurons are important players in these and other neurological disorders. In this dissertation I will discuss brain disease in the context of two human neurological disorders, one rare neurodegenerative disorder and one more prevalent neurodevelopmental disorder, both with known underlying genetic causes: Cockayne Syndrome and Rett Syndrome, respectively.

1.3.2.1 Cockayne Syndrome

Cockayne syndrome (CS) is an extremely rare Progeroid-type neurodegenerative disorder. Failure to thrive and neurological disorder are criteria for diagnoses. Other common symptoms include the appearance of premature aging, photosensitivity, and vision loss (Natale, 2011). The mechanistic defect underlying CS is the dysregulation of cellular DNA repair via the transcription-coupled repair mechanism (Menck & Munford, 2014). CS cases cover a wide range of neuropathology characterized by hypomyelination and calcification, ultimately resulting in degradation of neurological white matter and progressive neuronal loss in the cortex (Nance & Berry, 1992; Weidenheim, Dickson, & Rapin, 2009). There are three clinically classified severities caused by various mutations in one of two interacting excision repair cross-complementation genes, group 6 (*ERCC6*) or group 8 (*ERCC8*). Classical, or CS Type I, is characterized by apparently normal development with an onset of symptoms in early childhood. In CS-I the CNS progressively degenerates for the first or second decade until premature death as a result of neurological loss. CS Type II is congenital and far more severe with minimal postnatal neurological development and consequent microcephaly. Typically, individuals with CS-II present with severe brain damage including reduced myelination of white matter and more widespread calcifications in

the cortex. CS Type III is characterized by late onset and exhibits the mildest symptoms of the three types (Natale, 2011). Modeling the neurological aspect of CS has proved difficult, since murine models fail to mirror classical human neurological symptoms (Nagtegaal et al., 2015) and human CS cases are rare.

1.3.2.2 Rett Syndrome

Rett Syndrome (RTT) is a clinically diagnosed developmental disorder identified in 1:10,000 primarily female toddlers. A signature aspect of Rett Syndrome is apparent normal postnatal development followed by a period of subtle stagnation and then a subsequent stark regression of acquired language and motor abilities occurring between six and eighteen months of age. Other common symptoms include repeated hand movements, breathing irregularities such as holding breath, and microcephaly. Individuals with Rett syndrome are typically unable to talk and most experience seizures or and other EEG abnormalities from 2 years of age (Jian et al., 2006). RTT is the leading cause of mental retardation in females. While severe on the scale, before an underlying genetic mutation was discovered in 1999 (Amir et al., 1999) RTT was classified on the autism spectrum due to several shared behavioral symptoms. Over 95% of RTT cases are attributed to mutations in methyl CpG binding protein 2 gene (*MECP2)*. Mutations in a gene less frequently associated with the disorder, cyclin-dependent kinase-like 5 (*CDKL5*), cause an atypical form of early-onset seizure RTT. Both of these RTT associated genes are located on the X chromosome. A multitude of reported mutations in these genes present a spectrum of clinical phenotypes in females. In contrast, male fetuses carrying a *MECP2* mutation rarely survive gestation and 46XY karyotyped boys born with the disorder usually die in the first two years of

life from severe neurological dysfunction (Hardwick et al., 2007). The incidence of *MECP2* and *CDKL5* mutations in males is unknown, partly due to a low survival rate and partly due to the advanced disease progression when only one copy of the affected gene is present. Females with RTT, however, presumably have a non-mutated copy of the affected gene that, through X-inactivation, provides enough normal protein to ameliorate the potentially lethal effects. Females with RTT typically thrive through infancy, and often, beyond forty years of age.

1.4 Emerging solutions - Stem cell & 3D scaffold based approaches

Since our lab's seminal iPSC study, new tools have become widely accessible in the areas of human pluripotent stem cell genetics and *in vitro* electrophysiology. New scaffold-based technology has also emerged promoting biomimetic *in vitro* tissue models. Typically, iPSC disease models are compared to unaffected matched controls based on familial relation or other more genetically dissimilar criteria. As stem cell technology develops towards more personalized clinical prognoses, so should the sophistication of traditional biological controls. In this section I will briefly discuss a method for establishing isogenic stem cell models of monogenetic disorders applicable to various human pluriopotent stem cell models. I will then discuss emerging tissue engineering approaches applied to *in vitro* studies of tissue remodeling, development and pathology, touching briefly on recently expanded multi-well MEA technology.

1.4.1 Isogenic stem cell models

Our original iPSC-based female RTT study using paternally-derived biological controls was closely followed up by a corroborating study from Qiang Chang's group

(Ananiev et al., 2011) comparing isogenic pairs of iPSC model cell lines derived from female RTT donors via spontaneous X-inactivation. Additionally, recently optimized genetic editing tools are now widely accessible.

With the advent of CRISPR/Cas9 targeted genome editing, monogenetic disease models have entered a new era. Previous approaches to targeted genome modification fell short. Zinc-finger nucleases (ZFNs) and transcription-activator like effector nucleases (TALENs) are not only time consuming and difficult to optimize, but are also less efficient, consequently limiting common implementation. Alternative shRNA and RNAi techniques are widely used, and are easy to implement, however they provide only temporary, often partial gene inhibition and may cause unpredictable off-target effects. Our lab now routinely generates isogenic matched controls in human ESC and iPSC models using the CRSPR/Cas9 system.

1.4.2 Scaffolds to mimic *in vivo* micro-environments

The discipline of tissue engineering has guided increased sophistication for 3D *in vitro* culture systems in an effort to address rising unmet needs for replacement allografts and transplant tissue. Using typical tissue engineering approaches, 3D tissue models may help bridge the gap between traditional 2D *in vitro* and animal models addressing limitations and facilitating the observation of phenomena otherwise difficult to ascertain. The goal of most current neural tissue models is to establish systems which can be used to study combinations of network connectivity, pathology and pharmacology. Microelectrode array (MEA) substrates, used for many years to measure activity in mouse brain slices, have recently been expanded into multi-well formats for higher throughput stem cell culture applications. These arrays serve as

neural interfaces to connect neurons to analytic electric circuitry. MEAs facilitate *in vitro* assessment of electrical activity with high spatial and temporal resolution. Typically, 2D neural cultures are analyzed via MEA, however Ikuro Suzuki's group recently combined 3D scaffolds and MEA technology to study dissimilarities between local field potentials recorded from patterned 3D neural networks compared to 2D traditional neural cultures. Remarkably, unlike monolayer cultures, in 3D patterned neural networks they demonstrated interlayer propagation rates equivalent to biological tissue (Aoi Odawara, Gotoh, & Suzuki, 2013b). Enhancing stem cell based approaches with rationally designed biomimetic scaffolding can introduce needed complexity into *in vitro* neural systems and begin addressing disease model accuracy, ultimately leading to more efficient therapeutic clinical translation. Critical challenges for *in vitro* scaffolding include selection of biomaterials capable of matching biochemical and biomechanical cues (mediated *in vivo* by the neural ECM), compartmentalization of heterogeneous tissue organization reflective of brain cytoarchitecture, and robust functional assays for *in vitro* neural validation and study of structure-function relationships. For a more detailed discussion, a recent publication from David Kaplan's group comprehensively reviews 3D *in vivo* modeling of the brain and CNS (Hopkins et al., 2015).

1.4.2.1 Biomaterial selection

Hydrogels are the primary class of biomaterials investigated for constructing biomimetic tissue scaffolds due to their high water content and broad dynamic versatility: biochemically, mechanically and structurally. Critical design requirements for modeling various tissues include elastic modulus, tunable durability and biochemistry, and compartmentalization. Additional requirements to support migration

and neural networking are appropriate pore size, porosity and electrical conductance. Another major consideration with respect to *in vitro* disease modeling is that the materials must exhibit properties permissive to evaluation, such as optical clarity for imaging, digestibility for cell and biologics retrieval, and electrical conductance to allow transmittance of activity. Hydrogel polymer candidates include polyacrylamide (PAm), polyethylene glycol (PEG), hyaluronic acid (HA), and Matrigel among many others.

These hydrogels meet basic requirements to support neural cell culture such as low stiffness, efficient nutrient, oxygen and waste diffusion, and inherent, or chemical moieties to covalently incorporate, bioresponsive cell attachment sites [(A. Engler et al., 2004; M. S. Hahn, Miller, & West, 2005). PAm and PEG hydrogels have been investigated for *in vitro* culture as inert biomaterials with tunable stiffness and biochemical profiles. HA is attractive for use in neural tissue engineering due to its prevalence in brain ECM and its availability in a wide range of polymer sizes. Matrigel is a commercially available protein-based thermoreversible hydrogel scaffold commonly employed in modeling *in vitro* neural systems due to high neuron survival, cell attachment, and neurite outgrowth. Biologic hydrogels such as HA and laminin-rich Matrigel contain endogenous cell attachment sites such as the HA monomer itself and integrin ligands. For example, homing cell adhesion molecule (HCAM, also known as CD44) is a HA receptor highly expressed by glia, and to a lesser extent by NPCs. Additionally, neural cells express several laminin-binding β1-subunit integrins (Tate et al., 2004).

1.4.2.2 Tuning biomechanics and biochemical cues

In vitro fabricated biological tissue is a valuable tool to study wound healing and tissue development, or to screen potential drugs. Controlling growth and morphology of the fabricated tissue remains a challenge. Scaffolds should be rationally designed to match the cells and tissues being investigated. Stiffness, structure, topography, chemistry and composition all influence cell behavior (Boland et al., 2006; Lutolf & Hubbell, 2005; Musah et al., 2012; Pelham Jr. & Wang, 1997; Ricoult et al., 2013). Mounting evidence confirms that physical microenvironments and mechanical stresses direct cell fate (A. J. Engler et al., 2006; Wells, 2008), especially in developing or regenerating tissue, as is often mirrored in stem cell models. For example, HA has been shown to guide differentiation of NPCs towards either neurons or glia by the modulation of hydrogel stiffness (Seidlits et al., 2010). Mechanical tuning of polymer systems, including hydrogels, can be accomplished by modulating monomer size and diversity; crosslink density; degrees of substitution for hydrophobic, attractive or repulsive moieties; or by encapsulating immobile constituents. To support diverse cellular models, biomaterials must present binding sites recognized by cell-specific integrins or other expressed adhesion receptors. PAm and PEG are inherently inert synthetic hydrogels that can be functionalized through covalent coupling of bioactive molecules such as peptides or proteins. Similarly, these non-degradable scaffolds can be modified with digestible peptide moieties or cross-linked with hydrolysis-prone chemistry to facilitate cell-mediated remodeling (Chwalek et al., 2011). Hyaluronic acid can be functionalized, for example methacrylated (HAMA), to introduce similar covalent tunability.

1.5 Hypothesis and aims of the thesis

Genetic stem cell models provide the means for understanding cellular contributions in mutation-specific disorders, however, current monolayer cell-based systems fail to recapitulate much of *in vivo* development. And, given the complexity of the brain as a 3D organ, model scaffolds should mimic the neural extracellular matrix to support both neural development and brain-specific processes. Further, it is critical to consider neural cell type and molecular contributions as well as complex networking characteristics when designing and interpreting *in vitro* neural tissue functional assays. **I hypothesize that a 3D laminar co-culture model will better represent the cytoarchitecture of *in vivo* neural environments, and provide a potentially more accurate research tool than animal or 2D models of brain disease.** Therefore, the underlying goal of this thesis is to introduce higher complexity into *in vitro* neural systems for more accurate disease modeling. **I specifically aim to advance stem cell based neural models using genetic tools and higher order electrophysiological analyses, ultimately integrating neural co-cultures into 3D bioengineered scaffolds to better model functional brain development, thereby providing better insight into genetic perturbations of this process.** The broader impact of this research in the context of developmental biology, regenerative medicine and disease modeling is that the fabrication of 3D cell scaffolds herein described is not limited to developing brain and CNS models. DGMP can be easily adapted to emulate *in vivo* conditions for any human tissue and pattern any arrangement of cell types, offering an *in vitro* platform to bridge the gaps between conventional *in vitro* systems, animal models, and human clinical relevance.

Brain disease is a complex and multivariate biomedical problem. The aims of this thesis involve the design and practical application of emerging technologies to overcome challenges in neurological disease modeling. In particular, I am interested in establishing and advancing emergent stem cell and tissue scaffold methods to study rare monogenetic neurological syndromes that, while hopefully revealing features of the specific disorders, will potentially serve as broader models to study other brain diseases with or without shared neurological pathology. In this thesis I will aim to address the following three questions:

1. *Will combining microelectrode array technology with our established iPSC neural development model reveal neural tissue-specific phenotypes of Cockayne Syndrome, a neurodegenerative disorder?*
2. *Will an isogenic human stem cell based neural co-culture reveal non-autonomous effects in Rett Syndrome?*
3. *Will a scaffold based 3D laminar neural co-culture approach reveal new neurophysiologic aspects of Rett Syndrome previously obscured by limitations of monolayer models?*

To address these questions I invented a hydrogel polymerization technique to pattern cells and biologics in 3D tissue culture scaffolds, utilized synthetic and polymer chemistry, atomic force, transmission and field-emission scanning electron microscopy, matrix-assisted laser desorption/ionization mass spectrometry, ^{1}H NMR, Förster resonance energy transfer, iPSC reprogramming of donor somatic cells, microelectrode array technology, FACS and MACS cell separation techniques, and RNA-Seq. We established isogenic stem cell models of monogenetic diseases via CRISPR/Cas9-guided genome editing, directed neural and astroglial differentiation. I

also performed immunocytochemistry and cell morphometry using software-assisted 3D image rendering.

1.6 Overview of dissertation chapters

The work presented in this thesis focuses on two aspects of modeling neural development (ND) in an attempt to advance the complexity, and therefore clinical relevance, of current brain disease models. I describe advances in stem cell and 3D scaffold based approaches, applied in studies of two specific human monogenetic brain disorders, Cockayne Syndrome and Rett Syndrome, and I report important results. The thesis is organized into three parts. PART 1: The development of in vitro tissue scaffolds to create 3D disease models (Chapter 2). PART 2. The enhancement of monolayer stem cell ND models (Chapter 3). PART 3. The establishment of 3D in vitro ND models to study brain disease (Chapter 4).

Chapter 1 provides broad background and motivation of the thesis work. Following the rationale and motivation, I provide a brief review of corticogenesis and disease mechanisms. Finally, I state my hypothesis and aims of the thesis.

Chapter 2 sections 2.2, 2.3, 2.4; Chapter 3 sections 3.2, 3.3; and Chapter 4 are each presented in the style of scientific journal articles including the following sections: Brief introduction and rationale, Materials and methods, Results, and Summary. The Abstract and Conclusions sections are combined in Chapter 2 and Chapter 3, respectively, to reflect the overall content of each chapter.

Chapter 2 - Density gradient multilayer polymerization (DGMP) to create 3D *in vitro* disease models - I describe a novel, patent-pending, laminar tissue scaffold fabrication technique as well as the development, characterization and adaptability of

3D tissue culture scaffolds for disease modeling. This technique was first published in the format of a Letter at Advanced Materials. Then in a published US patent application for this invention, I established a hyaluronic acid based 3D neural tissue scaffold and describe pilot studies to assess feasibility for ND modeling. The procedure was further refined and published as a video protocol at Journal of Video Experiments. In this chapter I also describe our first full study validating the utility of DGMP for *in vitro* disease modeling, assessing haptotaxis in a model of wound healing. I report, from our published Cellular and Molecular Bioengineering manuscript, the dependence of haptotaxis on cell type, limited by substrate stiffness, in the context of mesenchymal stem cell and fibroblast migration at the simulated interface of healthy and fibrotic tissue. This chapter is a consolidation of multiple published sources as described, and I include previously unpublished data to highlight the simplicity and adaptability of my novel tissue scaffold fabrication method.

Chapter 3 - Stem cell models of neural development to study human monogenetic brain disorders - I start the chapter by describing a new application of our previously established *in vitro* ND model to assess functional neuronal defects for a rare monogenic neurodegenerative disorder, Cockayne Syndrome (CS, *ERCC6*). In this study I introduce the microelectrode array (MEA) as a functional assay to assess neural networks *in vitro*. I report, from our published Human Molecular Genetics manuscript, a significant advance in the understanding of functional mechanisms in previously inaccessible affected neural tissue of individuals with dysfunctional *ERCC6* and reveal neuronal-specific transcriptional dysregulation that differs from earlier results from donor fibroblasts. In the latter part of this chapter I refine our ND model to assess astroglial non-autonomous effects on neurophysiology for a monogenetic

neurodevelopmental disorder, Rett Syndrome (RTT, *MECP2*). I describe isogenic *MECP2* stem cell lines, a simple astroglia differentiation protocol and introduce a monolayer neural co-culture model. I report reductions in both network activity and complexity in genetically “normal” neuronal networks co-cultured with MeCP2-defficient astroglia compared to control co-cultures. This chapter combines two studies to demonstrate the evolution of stem cell based approaches to modeling ND and brain disease. The first part of this chapter was published as a full manuscript at Human Molecular Genetics.

Chapter 4 - Three-dimensional scaffolds accelerate neural development & 3D laminar co-cultures reveal new neurophysiological phenotypes in Rett Syndrome (*MECP2*) - In this chapter I advance the bioengineered scaffold presented in Chapter 2, including stem cell approaches described in Chapter 3, and apply it to 3D *in vitro* models of ND to study Rett Syndrome (*MECP2*). I report accelerated neuronal maturation in 3D hydrogels compared to our 2D *in vitro* system described in Chapter 3. I present a 3D laminar co-culture system consisting of iPSC-derived NPCs with human stem cell-derived astroglia or neurons to evaluate cell autonomous and non-autonomous effects of *MECP2*. I describe 3D hydrogel parameters that retain chemotactic gradients generated by astroglia and report chemotaxis deficits in MeCP2-deficient NPCs, exacerbated by the absence of *MECP2* in adjacent astroglia. Importantly, I demonstrate these subtle, yet significant, effects are not obvious in monolayer systems. This work was directly submitted to the Proceedings of the National Academy of Sciences, and is currently in press as a Research Report. I include un-submitted data to underscore the chemotactic nature of 3D directed NPC migration in this study.

Chapter 5 - Discussion of the thesis - I summarize the key findings and propose future experiments to continue the work presented here.

Appendix A - Published US Patent Application No 13/794,546: Single step polymerization of covalently bound multilayer matrices - I describe our invention and claims thereof.

Appendix B - Published online DGMP video protocol: JoVE© summary and URL - I summarize the DGMP protocol and provide the internet Uniform Resource Locator for the Open Source video protocol published at Journal of Visualized Experiments.

Appendix C - A pilot MEA study: Monolayer iPSC-derived neural cultures reveal electrophysiological phenotypes in *CDKL5* - I describe a pilot study using MEAs to investigate advanced aspects of complex *in vitro* neural network electrophysiology as they relate to *CDKL5* disorder and donor-specific EEG data. I initiated this multidisciplinary project and forged an ongoing collaboration at UCSD between Alysson Muotri's pediatric neurodevelopmental biology lab and Bradley Voytek's computational cognitive science lab to continue this important work.

Appendix D - A pilot API study: MEA platform to screen epilepsy drugs - I describe a pilot study using model ESC-derived 2D monolayer neural cultures towards establishing a microelectrode array epilepsy drug screening platform. I report transient and residual neural network activity depression resulting from cannabinoid (THC) treatment. This feasibility data, combined with preliminary *CDKL5* data described in Appendix C, provides rationale to proceed screening our small library of neurotropic active pharmaceutical ingredients (API), including Cannabidiol (CBD). This ongoing work will be continued by the Muotri Lab

.

Chapter 2

Density gradient multilayer polymerization (DGMP) to create 3D *in vitro* disease models

2.1 Abstract

In this chapter I first describe the development and characterization of a novel tissue engineering method, density gradient multilayer polymerization (DGMP), using various density modifiers, biologics and innate polymers, followed by its first practical application to study haptotaxis in a polyacrylamide substrate based monolayer model of wound healing, and finally a successful feasibility study for 3D human neural stem cell encapsulation and differentiation in DGMP fabricated hyaluronan scaffolds. Complex tissue culture matrices, in which types and concentrations of biological stimuli (e.g. growth factors, inhibitors, or small molecules) and matrix structures (e.g. porosity, pore size, or stiffness) vary over space, would support investigations into how these variables affect cell differentiation, migration, and other extracellular matrix (ECM) mediated phenomena. A major challenge in creating modular matrices is maintaining structural integrity at laminar interfaces without loss of constituent discreteness. Density gradient multilayer polymerization (DGMP) is a simple method that facilitates fabrication of complex *in vitro* tissue, forming strong tunable hydrogel scaffolds with structurally continuous laminar interfaces combined with cell patterning. Modular hydrogels are formed by co-dissolving polymer precursers with independently distributed biologics, cosslinkers, and biochemical cues in laminar solvent fractions of tiered densities. Once the prepolymer solutions are discretely layered from high to low solvent density, they can either be allowed to settle for a specified duration (t_S) prior, or be immediately crosslinked in one step to form a continuous polymer matrix with layers of gradient or discreet characteristics, respectively. The resulting stratified biomimetic hydrogels serve as two-dimensional substrates or three-dimensional scaffolds. Early in this chapter we modulate C2C12 and HeLA cell adhesion via patterned adhesion cues

to verify DGMP for 2D cell culture. We then present viable cell encapsulation during and after crosslinking. We successfully demonstrate these approaches to verify DGMP is compatible with cell culture and adaptable for studying a broad range of cell and scaffold mediated phenomena unique to biomimetic 3D environments.

Motile cells navigate through tissue by relying on tactile cues from gradients provided by ECM such as ligand density or stiffness. Mesenchymal stem cells (MSCs) and fibroblasts encounter adhesive or 'haptotactic' gradients at the interface between healthy and fibrotic tissue as they migrate towards an injury site. Mimicking this phenomenon, we developed tunable RGD and collagen gradients in polyacrylamide hydrogels of physiologically relevant stiffness using DGMP to better understand how such ligand gradients regulate migratory behaviors. Independent of ligand composition and fiber deformation, haptotaxis was observed in mouse 3T3 fibroblasts. Human MSCs however, haptotaxed only when cell-substrate adhesion was indirectly reduced via addition of free soluble matrix ligand mimetic peptides. Under basal conditions, MSCs were more contractile than fibroblasts. However, the presence of soluble adhesive peptides reduced MSC-induced substrate deformations; increased contractility may contribute to limited migration, but modulating cytoskeletal assembly was ineffective at promoting MSC haptotaxis. When introduced to gradients of increased absolute ligand concentrations, 3T3s displayed increased contractility and no longer haptotaxed. These data suggest that haptotactic behaviors are limited by adhesion and that although both cell types may home to tissue to aid in repair, fibroblasts may be more responsive to ligand gradients than MSCs.

In the developing brain cells migrate between niche microenvironments to establish complex cytoarchitecture, facilitating synergistic cell and ECM directed neural

differentiation and connectivity. Temporal gradients of chemotactic cues are produced within the developing tissue by astroglia and haptotactic cues are provided by a combination of cellular extensions from radial glia and the surrounding hyaluronan-rich neural ECM. In the latter part of this chapter I describe the synthesis and characterization of crosslinkable hyaluronic acid methacrylate (HAMA) and successfully optimize resulting biomimetic 3D hydrogels to support viable neural precursor cell (NPC) encapsulation, differentiation, and migration in DGMP scaffolds. These initial experiments verified compatibility of DGMP with basic NPC functions, thereby establishing necessary parameters to introduce additional complexity into our previously established iPSC *in vitro* model of neural development and disease.

2.2 DGMP method for creating complex tissue

2.2.1 Brief introduction and rationale

Tissue engineering has recently focused on biomimetic matrices, usually polymer hydrogels, that include multiple layers with distinct structures and chemical components (Khademhosseini & Langer, 2007; K. Y. Lee & Mooney, 2001; P. X. Ma, 2008). Current methods of fabricating such matrices are complex or expensive to implement and often produce mechanical weaknesses between layers (Place, Evans, & Stevens, 2009). Thus, an adaptable, facile, and economical multilayer polymer fabrication technique that produces continuous interfaces between layers is needed. Herein we describe exactly such a method: density gradient multilayer polymerization (DGMP). We demonstrate that DGMP, a straightforward technique that uses inexpensive reagents, yields strong hydrogels with smooth transitions between layers.

Existing strategies allow for construction of multiphase scaffolds with varying degrees of complexity. Multiphase biopolymer-based hydrogel matrices have been previously fabricated by additive photopatterning (V. A. Liu & Bhatia, 2002; Sharma et al., 2007; Weber, Cheung, & Anseth, 2007), laser scanning lithography (M. S. Hahn et al., 2005), printing (Boland et al., 2006), sequential functionalization (Kizilel et al., 2006), and freeze-drying (Harley et al., 2010; Hwang, Zhang, & Varghese, 2010). Additionally, spatial control of chemical or mechanical gradients has been achieved using partial miscibility of biopolymers (Harley et al., 2010; Hwang et al., 2010), gradient makers (Chatterjee et al., 2010), microfluidics (Cosson, Kobel, & Lutolf, 2009; Cuchiara et al., 2010; He et al., 2010), and centrifugation (Roam et al., 2010). Another approach is to attach layers after fabrication (Gleghorn et al., 2008; Straley & Heilshorn, 2009). However, these techniques may not be widely adopted because they require

sophisticated instrumentation and/or technical proficiency. Further, they may yield networks that are susceptible to delamination under mechanical stress due to discontinuity at layer interfaces (Harley et al., 2010; Hwang et al., 2010).

DGMP exploits phase separations between liquids of varying density to create layers of distinct structures and chemical compositions. Briefly, serial concentrations of an inert density modifier, such as sucrose or iodixanol, are co-dissolved with prepolymer (we used bisacrylamide and acrylamide or biocompatible c(PEGda)), crosslinkers, and ligands or proteins (Figure 2-1). Next, these prepolymer solutions are gently layered on top of each other in order of decreasing density. Varying the initial concentrations and types of each of these agents in each layer allows structures and chemical properties to be tailored. Varying the settling time (t_S) before polymerization adjusts the smoothness of gradients between layers. Bulk polymerization yields a multicompartment hydrogel. Finally, the density modifier is removed, resulting in multiphase hydrogels that are structurally uninterrupted at interfaces of chemically and mechanically diverse layers.

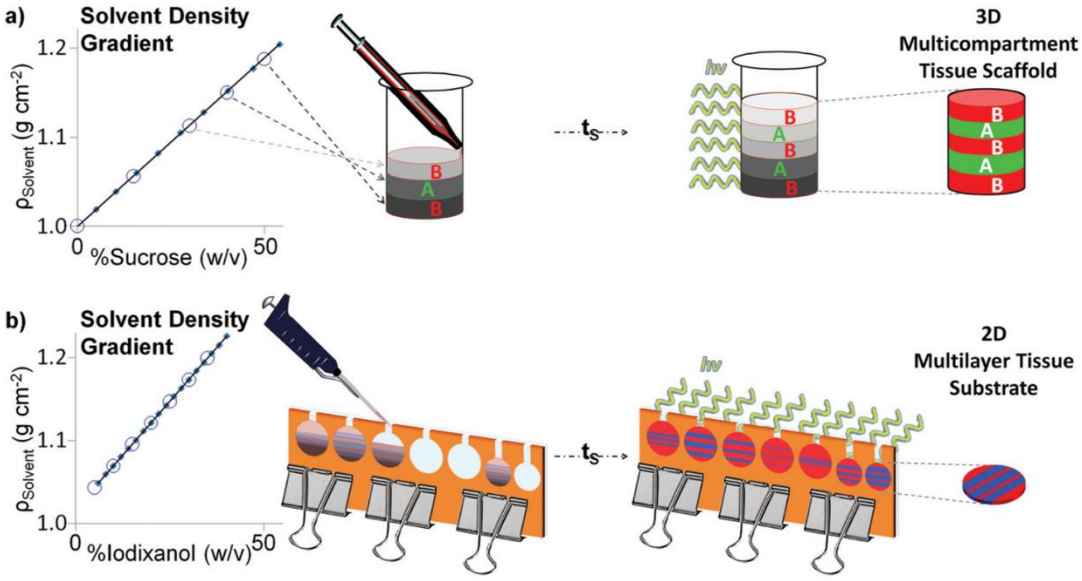


Figure 2-1 Schematic representation of two variations of DGMP.

A) Five serially diluted solutions of sucrose are co-dissolved with prepolymer; and either fluorescently-tagged protein “A” or “B”. B) Seven serially diluted solutions of iodixanol are co-dissolved with prepolymer and either methacrylated rhodamine or RGDS-350. Then, after designated settling time (t_S), stratified hydrogels are bulk polymerized. The density modifier can be washed away, leaving stable microstructures.

We chose reagents for their suitability for this application. Sucrose is a highly soluble density modifier with a linear relationship between concentration and density (Figure 2-1A). Iodixanol, the main ingredient of Optiprep, is a nonionic, iso-osmotic density modifier currently used in viable cell purification (Graziani-Bowering, Graham, & Filion, 1997), also with a linear relationship between concentration and density (Figure 2-1B). Polyethylene glycol (PEG) and polyacrylamide (PAM) based hydrogels are well suited for cell culture applications (Sudhir Khetan & Burdick, 2009) because they are biologically inert and therefore resistant to nonspecific protein adsorption and cell adhesion (Leslie-Barbick et al., 2011; Peng, Yao, & Ding, 2011; J. Tang, Peng, & Ding, 2010), enabling precise engineering of desired biofunctionality through the

covalent addition of ligands such as RGD peptide (Lutolf & Hubbell, 2005; Peppas et al., 1999; Roberts, Bentley, & Harris, 2012; Zhang et al., 2010). With these components, DGMP produces structurally continuous multilayer hydrogels for tissue engineering. Furthermore, the method can be adapted to varying mold shapes, sizes, and materials (Figure 2-9).

2.2.2 Materials and methods

2.2.2.1 Cell maintenance

C2C12 murine myoblasts (AATC) were maintained in Dulbecco's Modified Eagle's Medium supplemented with fetal bovine serum (10% v/v) and penicillin/streptomycin (1% 100x v/v) at 37 °C/5% CO2/95% relative humidity. Cell culture reagents were obtained from Life Technologies.

2.2.2.2 Fluorescently labeled aPEG-RGDS synthesis

aPEG-RGDS-350 was synthesized with slight modifications to a previously described procedure (Hoffmann & West, 2010). Briefly, RGDS peptide (American Peptide, Arginine-Glycine-Aspartic Acid-Glycine) was conjugated to PEG (MW 3400 g mol-1) by reaction with aPEG-SCM (Laysan Bio, SCM: Succinimidyl Carboxymethyl) at 1.2:1 molar ratio in the presence of DIPEA at 1.2:2 molar ratio overnight in DMSO under argon at room temperature. aPEG-RGDS was purified by dialysis, lyophilized and confirmed via matrix-assisted laser desorption/ionization time-of-flight mass spectrometry (MALDI-TOF) in universal matrix (SigmaAldrich, Figure 2-2). Conjugation

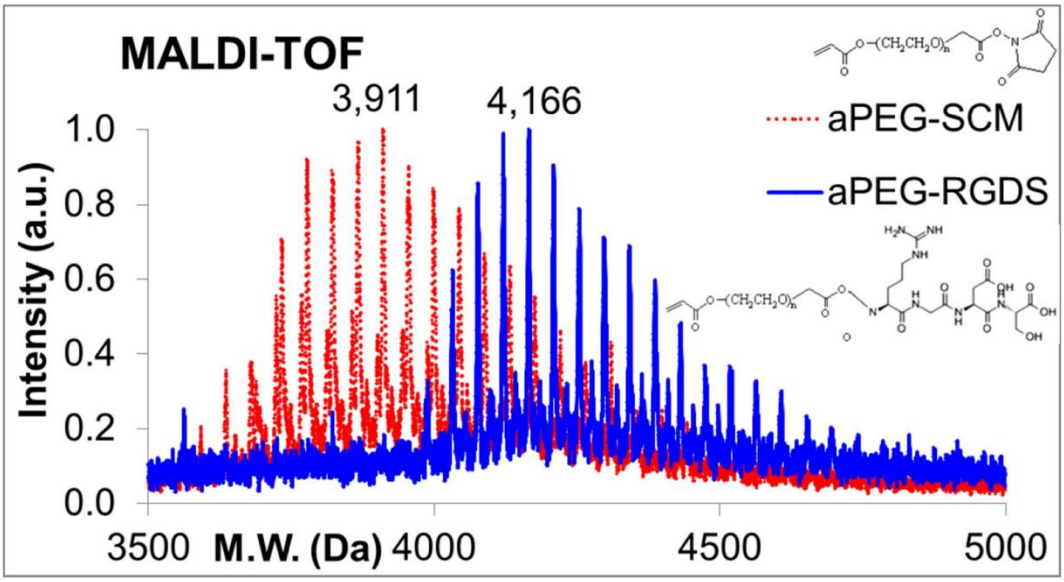


Figure 2-2 MALDI-TOF confirms aPEG-SCM and aPEG-RGDS. Samples dissolved in methanol and drop cast with universal matrix.

was further confirmed by 1H-NMR in D2O (Figure 2-3). An equimolar amount of Alexa Fluor 350 carboxylic acid, succinimidyl ester (Molecular Probes) was then added to aPEG-RGDS dissolved in DMF overnight in DMSO under argon at room temperature and purified by dialysis, lyophilized and stored under argon at -20 °C.

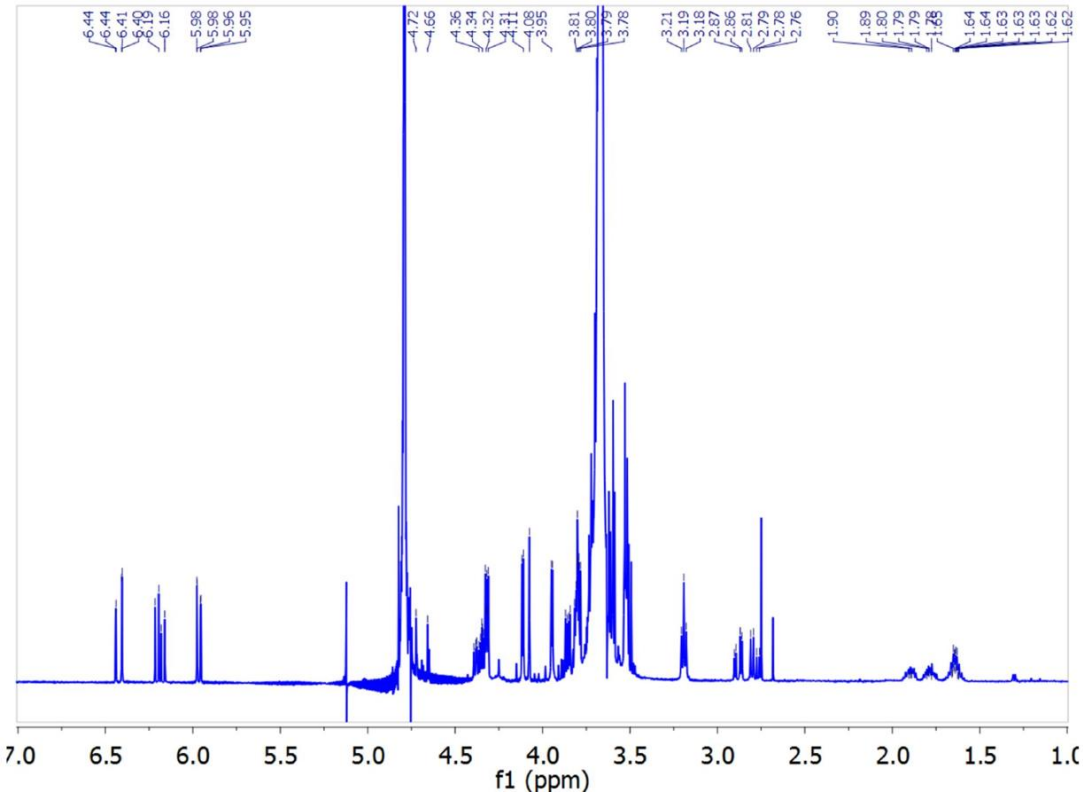


Figure 2-3 1H-NMR confirms acryloyl-PEG-RGDS.

1H NMR (500 MHz, D2O) δ 6.42 (dd, J = 17.4, 1.1 Hz, 1H), 6.19 (dd, J = 17.3, 10.5 Hz, 1H), 5.97 (dd, J = 10.6, 1.1 Hz, 1H), 4.40 - 4.30 (m, 3H), 4.11 (d, J = 3.9 Hz, 1H), 4.08 (s, 1H), 3.95 (d, J = 3.5 Hz, 1H), 3.88 - 3.48 (m, 316H), 3.19 (t, J = 6.9 Hz, 2H), 2.88 (dd, J = 16.9, 5.0 Hz, 1H), 2.79 (dd, J = 16.9, 8.0 Hz, 1H), 1.9 (m, 1H), 1.78 (m, 1H), 1.64 (m, 3H).

2.2.2.3 Multilayer hydrogel fabrication

For 3D sucrose DGMP (Figure 2-1A): aqueous solutions of ethylene glycol diacrylate (Dajac Labs, MW 4000 g mol^{-1}; 7% - 22% w/v; Figure 2-6A & B, Figure 2-7, Figure 2-9B & C, Figure 2-10, and Figure 2-11) or acrylamide (Promega; 10% w/v; Figure 2-6C - G, Figure 2-9A) were separately prepared in water. Precursor densities were individually modified with serial concentrations (0-50% w/v) of sucrose. Each solution was gently layered in transparent cylindrical polypropylene molds made from

modified syringes (Figure 2-4A) or in hydrophobic silanated (Sigmacote, Sigma) glass Pasteur pipettes (Figure 2-4B). For iodixanol DGMP (Figure 2-1B): aqueous precursor

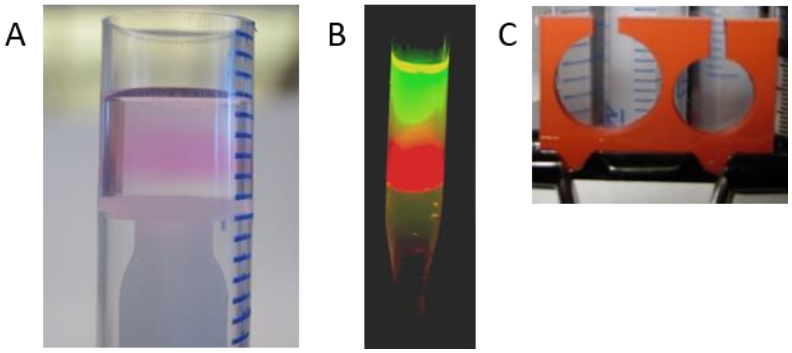


Figure 2-4 Improvised DGMP molds.

A) Polypropylene syringe mold for DGMP polyacrylamide scaffold. B) Glass Pasteur pipette for DGMP polyethylene glycol scaffold. C) 0.8 mm thick silicone spacers fitted between silanated cover glass.

monomer solutions of ethylene glycol diacrylate (15% w/v, Figure 2-8) were separately prepared in Dulbecco's phosphate buffered saline (w/ Ca^{2+} & Mg^{2+}, HyClone). Precursor densities were modified with serial concentrations (5-40% w/v) of iodixanol (Axis-Shield OptiPrep, 60% iodixanol in water). Each solution was gently layered in molds made from 0.8 mm thick silicone spacers (McMaster-Carr) cut with 10 mm and 8 mm biopsy punches (Acuderm) and secured between hydrophobic silanated glass slides (Figure 2-4C). For all precursor solutions, Durocur 2959 photoinitiator (Gibco) was held constant (10 µL of 300 mg mL^{-1} in N-vinyl pyrrolidone per milliliter of solution). Free radical polymerization was photoinitiated under irradiation with 365 nm light for 1 min in a Luzchem Research UV chamber (Figure 2-5A) or between two opposing Bayco UVR-9000 lamps (Figure 2-5A) distance adjusted for ~2500 mW cm^{-2} exposure per side unless otherwise noted. DGMP scaffolds were then washed under agitation in ten

volumes of PBS for minimum of 48 hours with two buffer exchanges per day to remove density modifiers, unreacted prepolymer and photoinitiator.

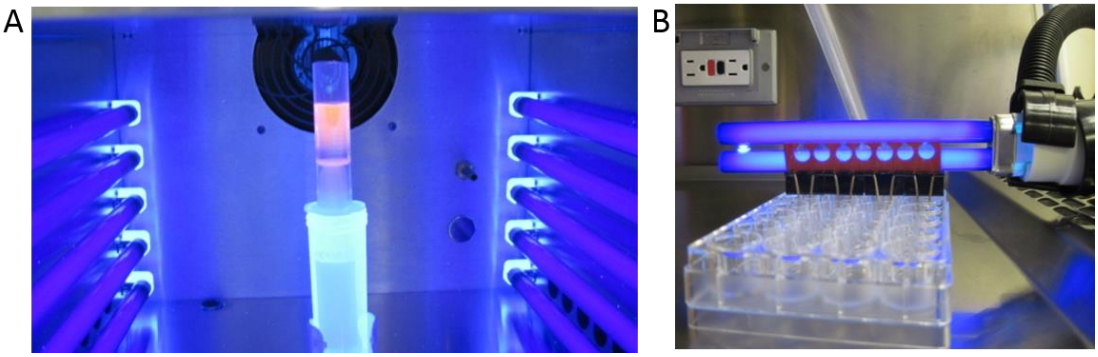


Figure 2-5 UVA sources for biologics-compatible photopolymerization.

A) Luzchem Research UV chamber, constant bilateral exposure measured at center. B) Bayco UVR-9000 13-watt UVA fluorescent cordless work light, unilateral exposure measured at constant distance; image for illustration only - photopolymerization typically carried out with two opposing lamps.

2.2.2.4 Structural stratification

DGMP gradients were compared to sequentially polymerized multi-layer hydrogels, in which precursors identical to those for DGMP were used, both groups were irradiated for 1 min per layer. For microstructural examination, bilayer (10% & 20% w/v, Figure 2-6A & B) or five-layer (7% - 22% w/v, Figure 2-7) PEGda hydrogels were snap frozen in N2, lyophilized overnight, coated with chromium (45 s at 130 mA) and recorded with an FEI XL30 SFEG SEM. For macrostructural examination and mechanical testing, five-layer PAM (10% w/v, 1% w/w crosslink) hydrogels were photographed (Figure 2-6C & D) and compressed with a Satec instrument (Figure 2-6E & F). To examine the effect of graduated transitions on structural properties, PAM mechanical gradients were created in biphasic sucrose DGMP by diffusion of

bisacrylamide from layers of 7% to 1% (w/w) crosslinker for t_S of 0, 15, 30, 60, 120, and 180 min (Figure 2-6G).

2.2.2.5 Chemical stratification

For biochemical patterning within PEGda tissue culture discs (Figure 2-8), co-dissolved iodixanol and prepolymer solutions were combined with either methacryloxyethyl thiocarbamoyl rhodamine B (Polysciences, 20 µM) or aPEG-RGDS-350 (8 mM). Precursor solutions were gently layered stepwise into silicone and glass molds, described above, and photopolymerized. Bioactivity of alternately layered integrin-binding peptide RGDS was evaluated by adhesion of C2C12 myoblasts (20,000 cells cm^{-2}). Resulting cell patterns were observed after 24 hr in culture via overlay of epifluorescence and phase-contrast imaging (Zeiss Axiovert 200; Figure 2-8C). Additional biomolecular patterning was demonstrated using small model molecules in Figure 2-9 or macromolecular proteins in Figure 2-10 and Figure 2-11. Settling time-dependent smooth protein cross-gradients were generated in PEGda (15% w/v) via biphasic sucrose DGMP and counter-diffusion of OVA-488 (Figure 2-11, upper) with BSA-594 (Figure 2-11, lower) for t_S of 0, 30, 90, and 150 min (both proteins initially 4 mg mL^{-1}, Life Technologies).

2.2.2.6 Photography and image processing

Images were obtained in a BioRad VersaDoc-4000MP. Color photographs were taken with a Canon Powershot A11000 IS. Individual field fluorescence and transmitted light microscopy images were color composited with Image Pro Plus software. All multi-field images were manually reconstructed with ImageJ software (NIH) using the

MosaicJ plugin with all corrections disabled. Average and line fluorescence intensity profiles were generated with ImageJ software.

2.2.3 Results

Field emission scanning electron microscopy (FE-SEM) of architecturally varied PEGda layers reveals enhanced continuity at the interface of hydrogels fabricated by DGMP when compared to sequential polymerization (Figure 2-6A *vs.* B). This enhanced continuity can also be observed macroscopically in five-layer PAM hydrogels (Figure 2-6C *vs*. D). Moreover, perpendicular compression testing revealed that PAM hydrogels fabricated via DGMP outperform analogous sequentially polymerized hydrogels (Figure 2-6E *vs*. F).

Biomimetic tissue engineering also requires fabrication of not only discrete multicompartment gels but also gradients of varying degrees. To demonstrate the ability of DGMP to produce a variety of gradients, both smooth and sharp, between layers with different structures, we initially created biphasic matrices with 7% and 1% (w/w) PAM precursor using sucrose solutions of distinct densities and varied the settling times. Immediately polymerized hydrogels exhibited discrete compartments, demonstrated by stark differences in swelling susceptibility (Figure 2-6G, left). However, as t_S is incrementally increased prior to bulk polymerization, the lower layer became less susceptible to swelling (Figure 2-6G, from left to right). This illustrates increasing settling time moderated the transition of structural grade.

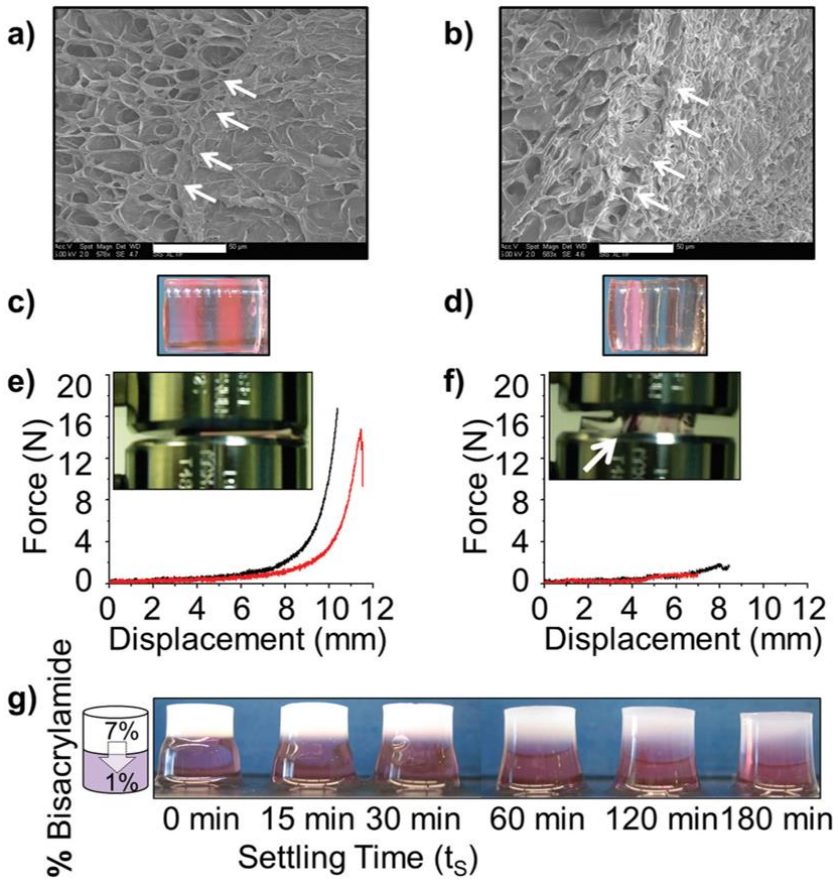


Figure 2-6 DGMP results in continuous structures and mechanical stability at interfaces.

A-B) Multicompartment PEGda hydrogels fabricated via sucrose DGMP (A) are microstructurally more continuous at the interface between 10% (w/v, upper left) and 20% (w/v, lower right) prepolymer than sequentially photopolymerized PEGda (B). White arrows highlight interfaces. Scale bar: 50 μm. C-F) Five-layer PAM (10% w/v, 1% w/w crosslinker) hydrogels approximately 12 mm in diameter prepared by DGMP (left) or sequential photopolymerization (right). DGMP produces hydrogels that are macrostructurally more continuous (C) than sequentially photopolymerized PAM (D). DGMP produces stronger hydrogels (E) than sequential photopolymerization (F) as indicated by perpendicular compression to failure and failure mode. Images inset in force *vs*. displacement curves (n = 2). DGMP hydrogels bulk ruptured at 90% strain while sequentially polymerized hydrogels delaminated at 65% strain. G) Increasing t_S modulates structural gradients in 10% (w/v) PAM bilayer hydrogels. As schematically represented (G, left), bisacrylamide crosslinker diffuses through the density interface to gradual transition between 7% and 1% crosslinker (w/w monomer). Swelling demonstrates the transition from discrete to increasingly smooth mechanical gradients.

Structural gradients can also be generated by stepwise laminar concentrations of crosslinker, or prepolymer in the case of PEGda hydrogels. The FE-SEM composite micrograph in Figure 2-7 demonstrates an increasing porosity gradient resulting from a 4-layer DGMP hydrogel with decreasing PEGda concentration, from left to right.

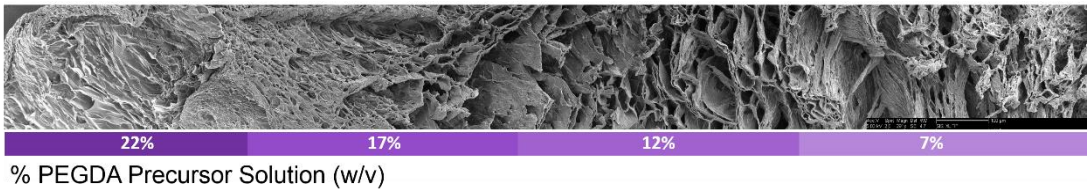


Figure 2-7 Demonstration of tunable process variables.

Adjacent compartment porosity is modulated by sucrose DGMP of varied PEGDA concentration.

To determine if DGMP allows spatial restriction of biological cues, we designed a simple experiment in which the biological cue would promote cell adhesion; the pattern of biomolecules would be demonstrated by the pattern of cell attachment. We fabricated tissue culture compatible two-dimensional (2D) substrates with alternating layers of covalently bound aPEG-RGDS labeled with Alexa Fluor 350 to help visualize patterning (Figure 2-8A). We developed a small scale manufacturing technique using iodixanol concentration gradients to construct laminar disc-shaped PEGda hydrogels specifically for tissue culture with standard well plates (Figure 2-8B). Briefly, molds were cut from 0.8 mm thick silicone sheets sized to fit between glass slides and used to construct seven-layer PEGda substrates via iodixanol DGMP. The tissue culture discs swelled, were sterilized, and then seeded with C2C12 myoblasts. We observed that adhered cells co-localized with covalently grafted RGDS peptide, visualized by alternating substrate fluorescence (Figure 2-8C). To determine whether this method

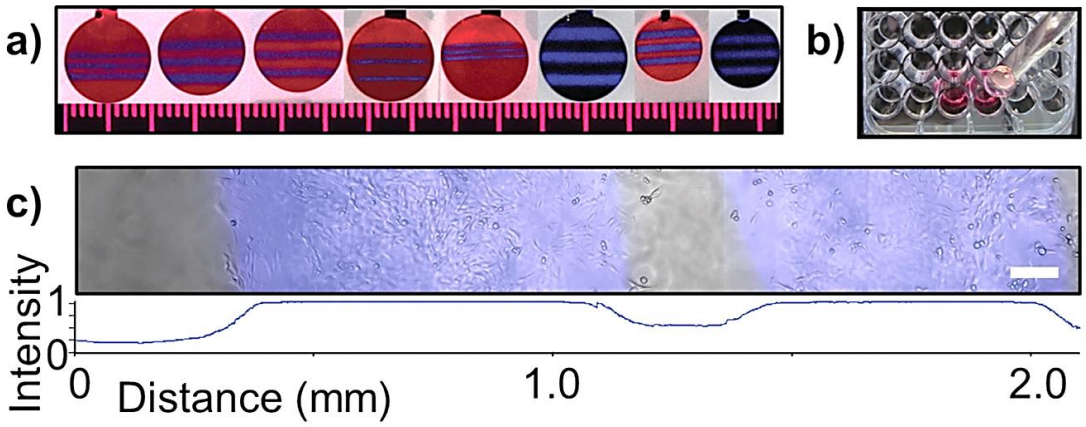


Figure 2-8 DGMP facilitates spatial control of scaffold bioactivity.

A-C) 2D seven-layer PEGda tissue culture substrates prepared as outlined in Figure 1b for 10 mm (A, left six) and 8 mm (A, right two) hydrogel discs with alternating layers of RGDS-AlexaFluor 350 (8 mm) or methacrylated rhodamine B. B) After swelling, discs are added to tissue culture well plates. C) Phase contrast image of C2C12 monolayer, color composited with corresponding epifluorescence image. Note that cell spreading is restricted to two regions of PEG-RGDS, additionally indicated by the normalized average florescence intensity plot below image. Scale bar: 100 μm.

allows spatial control of discretely arranged biomolecules, we created matrices in which small model molecules (fluorescein-o-acrylate or rhodamine B) were bound in alternating layers (Figure 2-9). To determine our ability to restrict macromolecular

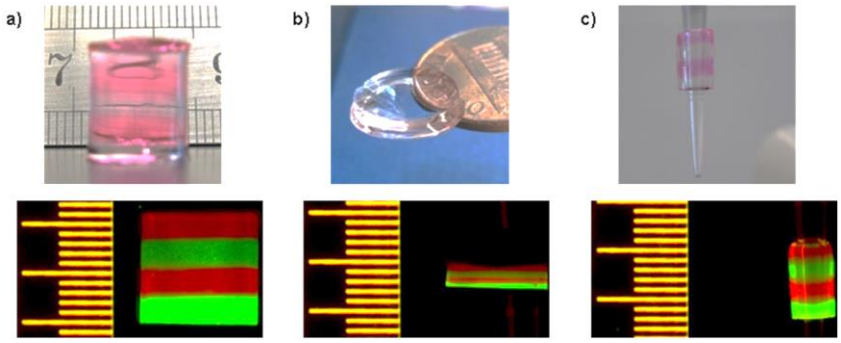


Figure 2-9 DGMP can be adapted to produce hydrogels of varying shapes.

Multicompartment PAM (A) and PEGda (B-C) hydrogels fabricated as outlined in **Figure 2-1**A for several geometries. Discrete layers are indicated by alternating fluorescein-o-acrylate or rhodamine B. Large ticks indicate 5 mm.

protein constituents within DGMP layers, fluorescently labeled bovine serum albumin (BSA) was initially encapsulated in discretely alternating (Figure 2-10A) or stepwise concentrated (Figure 2-10B) layers. To test our ability to fine tune smooth protein cross-

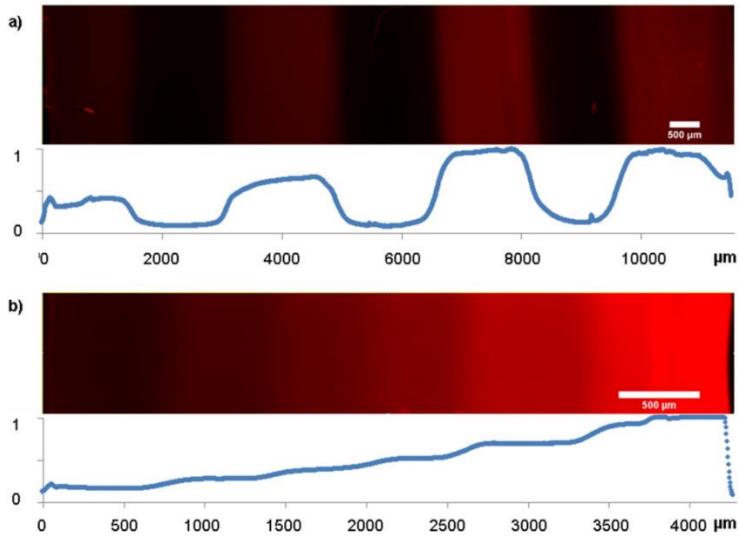


Figure 2-10 DGMP can separate protein into discrete compartments.

PEGda hydrogels were fabricated via DGMP to encapsulate BSA-594 in alternate (A) or adjacent (B) layers. Normalized average intensity plots below images indicate relative BSA-594 concentrations. Bar indicates 500 µm.

gradients across sucrose DGMP layers in PEGda hydrogels, ovalbumin conjugated to Alexa Fluor 488 (OVA-488, 4 mg mL^{-1}; Figure 2-11, upper fraction) and BSA conjugated to Alexa Fluor 594 (4 mg mL^{-1}; Figure 2-11, lower fraction) were encapsulated in adjacent layers and then allowed to diffuse over varied settling times (t_S). Longer t_S resulted in progressively smooth protein concentration profiles.

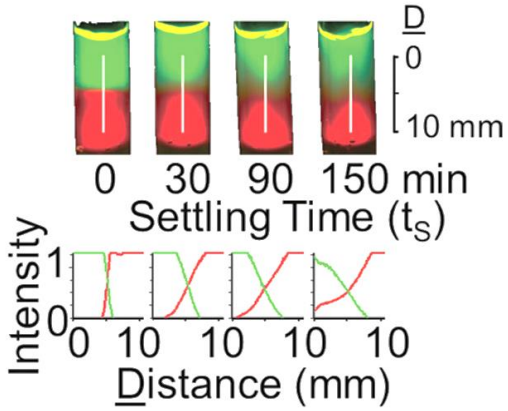


Figure 2-11 DGMP facilitates spatial control of scaffold bioactivity gradients.

Progressive cross-gradients of Ova-488 (upper) and BSA-594 (lower) encapsulated via DGMP at different t_S, as outlined in **Figure 2-1**A, with intensity plots. Scale bar: 10 mm.

Additionally, we successfully encapsulated C2C12 myoblasts by photopolymerization of the solutions, containing these cells, to form gels in the presence of 35% (w/v) iodixanol. Briefly, 500,000 cells cm^{-3} were photoencapsulated in single compartment PEGda hydrogels with 8 mM RGDS and expanding cell colonies were confirmed viable by calcein-AM live stain after two weeks in culture (Figure 2-12). These results show that the iodixanol DGMP method allows fast, simple fabrication of hydrogel scaffolds with spatially defined active biological cues and that DGMP is compatible with live cell encapsulation.

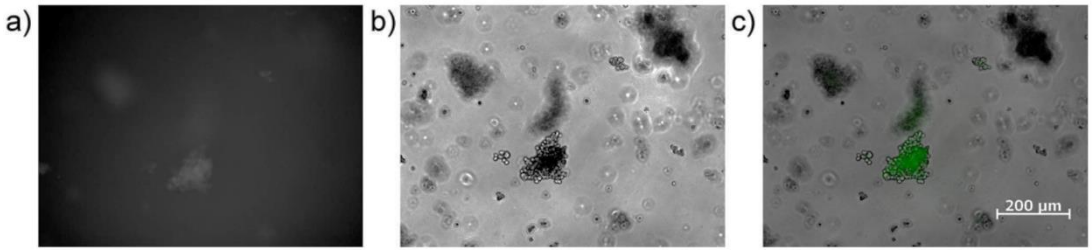


Figure 2-12 DGMP photopolymerization is compatible with live cells.

Day 17 calcein-AM live stain of C2C12 myoblasts encapsulated in PEGda (10% w/v) with bound RGDS (8 mM), photopolymerized in the presence of iodixanol (35% w/v). Left: epifluorescence with FITC filter set; middle: bright field phase contrast; right: composite.

2.2.4 Summary

In summary, we introduce a novel hydrogel fabrication method to generate modular in vitro tissue scaffolds. Importantly, the range of geometries and feature sizes presented throughout this communication were fabricated with common laboratory equipment and reagents. This powerful and adaptable technique is compatible with a range of polymer types (including those suitable for *in vivo* applications, such as hyaluronic acid) and solvents, as iodixanol is also compatible with organic solvents.

2.2.5 Recognitions

The authors gratefully acknowledge support from the NIH Directors New Innovator Award (1 DP2 OD006499-01), and King Abdulaziz City for Science and Technology. The authors thank Prof. Marc A. Meyers for assistance with mechanical measurements, Dr. Nadia Fomina for assistance with H-NMR analysis, and Ryan Anderson of Calit Nano3 for FESEM technical support.

2.3 Monolayer gradient model of wound healing: Haptotaxis is cell type specific and limited by substrate adhesiveness

2.3.1 Brief introduction and rationale

Anchorage dependent cells sense and respond to properties of the extracellular matrix (ECM), e.g., stiffness (Lo et al., 2000; Vincent et al., 2013; Zaari et al., 2004) and ligand density (A. Engler et al., 2004; Gaudet et al., 2003; Reinhart-King, Dembo, & Hammer, 2005). Gradients of these cues are often found together *in vivo* via normal tissue variation or pathological conditions, e.g., the post-infarct myocardial scar that is stiffer than, and compositionally different from, healthy cardiac muscle (Berry et al., 2006; Singelyn et al., 2009; Sullivan et al., 2014). These gradients are thought to aid in directional migration through tissue; for example, mesenchymal stem cells (MSCs) whose fate can be regulated by ECM stiffness (A. J. Engler et al., 2006; Tse & Engler, 2011; Wen et al., 2014) also durotax or migrate in the direction of an increasing stiffness gradient (Vincent et al., 2013). Dermal fibroblast migration into cutaneous wound spaces is also well known and critical for assembly of new ECM (Lauffenburger & Linderman, 1996; W. Li et al., 2004). However, spatial variation in tissue stiffness *in vivo* is often accompanied by variation in adhesive ligand density. During fibrosis, ECM accumulates and may present several ligand gradients at the interface of healthy and pathological tissue (Penelope C Georges et al., 2007). Because *in vivo* spatial distributions of ECM proteins (Penelope C Georges et al., 2007) and stiffness (Berry et al., 2006) have been shown to change with fibrosis and animal models have documented directed migration (Lauffenburger & Linderman, 1996; W. Li et al., 2004), it is of interest to develop systems to investigate cell migratory behaviors in response to spatial gradients *in vitro*. Although we and others have developed simplified systems

to probe durotaxis (Lo et al., 2000; Marklein & Burdick, 2010; Vincent et al., 2013; Zaari et al., 2004), few systems with the ability to separately modulate directed migration due to adhesive ligand gradients (Burdick, Khademhosseini, & Langer, 2004), i.e., haptotaxis, and migration due to substrate stiffness have been developed.

Adhesive ligand gradients have been shown to induce directed cell migration in human dermal fibroblasts *in vitro* (DeLong, Gobin, & West, 2005). However, cell type-specific differences in the degree of haptotaxis could be simultaneously influenced by physiologically-relevant substrate stiffness, which is a major regulator of stem cell fate (A. J. Engler et al., 2006; Wen et al., 2014). Moreover, haptotactic mechanisms remain unclear; this is in part due to the fact that systems commonly used to study haptotaxis are often limited in gradient resolution, and typically utilize substrates of non-physiologically relevant stiffness. Furthermore, haptotaxis studies often lack direct comparisons between cell and adhesive ligand types. For example, human melanoma cells undergo haptotaxis when exposed to gradients of collagen type IV, fibronectin, and laminin using Boyden chambers; these chambers however, can create only step gradients (Aznavoorian et al., 1990). Myoblast haptotaxis has been observed with more gradual nanodot adhesive gradients; however, these gradients were printed on rigid glass (Ricoult et al., 2013). Literature suggests that cell forces exerted on adhesive matrix proteins contribute to cellular mechanical signaling (Trappmann et al., 2012; Wen et al., 2014) and that *in vivo* gradients are gradual (Berry et al., 2006; Tse & Engler, 2011). Reductionist systems employing compliant hydrogels deformable by cells, e.g., polyacrylamide (Grevesse, Versaevel, & Gabriele, 2014; Joshi-Barr et al., 2013), and polyethylene glycol (DeLong et al., 2005), with gradual haptotactic gradients are thus needed to determine which signaling networks within a variety of cell types

regulate haptotaxis. Although not yet studied in detail, mechanisms regulating haptotaxis likely involve adhesive and/or cytoskeletal proteins given their roles in other migratory control mechanisms in processes such as chemotaxis (Affolter & Weijer, 2005), and the establishment of cell polarity and shape (Hoffman, Grashoff, & Schwartz, 2011; Vogel & Sheetz, 2006).

Gradients of protein attachment to compliant hydrogels have been achieved via microcontact protein printing, self-assembled monolayers, and microfluidic mixing devices (DeLong et al., 2005; H.-D. Kim & Peyton, 2012; Pulsipher & Yousaf, 2010). Despite the use of compliant hydrogels, these methods are often difficult to scale down, tune, and require significant quantities of protein or peptide, much of which does not bind. Here, we used density gradient multilayer polymerization (DGMP), to construct compliant culture substrates with spatial gradients of composition(Joshi-Barr et al., 2013; Karpiak, Ner, & Almutairi, 2012). DGMP, a simple method that does not require specialized equipment, ingredients, or expertise, relies on density- mediated phase separation to construct layers of distinct composition. By using this method to fabricate gradients of adhesive peptide RGD or collagen type I on a polyacrylamide (PA) hydrogel platform, we demonstrate that while fibroblasts undergo haptotaxis in response to both gradient types under basal conditions, MSC haptotaxis appears to be limited by cell- substrate adhesiveness, and is observed only when cell affinity for the substrate is reduced.

2.3.2 Materials and methods

2.3.2.1 Functionalized coverslips

To covalently attach hydrogel substrates to glass, 25 mm square glass coverslips were cleaned and oxidized by exposing both sides to UV/ozone (BioForce Nanoscience) for 3 min. Samples were subsequently functionalized with 20 mM 3-(trimethoxysilyl)propyl methacrylate in 10% acetic acid (AA) in ethanol for 3 min, washed with ethanol, and dried. All chemicals were obtained from Sigma-Aldrich and other products from ThermoFisher unless otherwise indicated.

2.3.2.2 DGMP hydrogel fabrication

DGMP involves layering pre-polymer hydrogel solutions into rubber molds cut to fit between two glass slides, followed by UV polymerization. 5 x 5 mm molds cut from super-soft 35A silicone rubber sheets (McMaster-Carr) were clamped between a glass slide, a functionalized glass coverslip to facilitate gel attachment, and a dimethylchlorosilane (DCDMS)-treated glass slide to inhibit gel attachment. Pre-polymer solutions composed of acrylamide, bis-acrylamide, acrylated poly(ethylene) glycol conjugated to RGD (aPEG-RGD) or acrylic acid, 2,2,-Azobis(2-methyl-propion0amidine) dihydrochloride photoinitiator (Sigma), and serial dilutions of iodixanol (Sigma), an inert density modifier, were layered into the silicone molds in order of decreasing density. Hydrogels with gradients of adhesive ligands were fabricated by allowing two 12 µL layers of pre-polymer solution of distinct composition (Figure 2-13A) to diffuse and settle for 10 s creating a gradient at the mixing interface (Figure 2-13B). Layered hydrogels were subsequently polymerized via exposure to 350 nm UVA light for 4.5 min.

10/0.15% acrylamide/bis-acrylamide solutions composed of 0.1 or 10 mM aPEG-RGD with 1 or 4% iodixanol respectively, were used to obtain PA-PEG- RGD hydrogels with adhesive RGDS ligand gradients of approximately 10 mM/mm that span an 800 μm region across the center of the hydrogel (Figure 2-13C). A hydroxycoumarin dye (excitation 350 nm) preconjuated to aPEG-RGD allowed us to visualize serial dilutions of adhesive peptide; differences in cell spreading and fluorescent intensity confirm that substrate adhesiveness scales with aPEG-RGD concentration (Figure 2-13D). aPEG-RGD, or acryl-PEG3400-GRGD- amide and acryl-PEG3400-[K-7-hydroxycoumarin-3-OH]GGGRGD-amide were custom ordered (21st Century Biochemicals).

To investigate the migration behavior of cells in response to solely a ligand gradient on a substrate of physiologically relevant stiffness, AFM was used to characterize the hydrogel stiffness in order to ensure that no simultaneous stiffness gradients were created as a consequence of the haptotactic gradient fabrication process (Figure 2-13E). Iodixanol and aPEG-RGD did not significantly alter hydrogel stiffness at the concentrations used in this study, as stiffness was maintained at 10 kPa across the substrate.

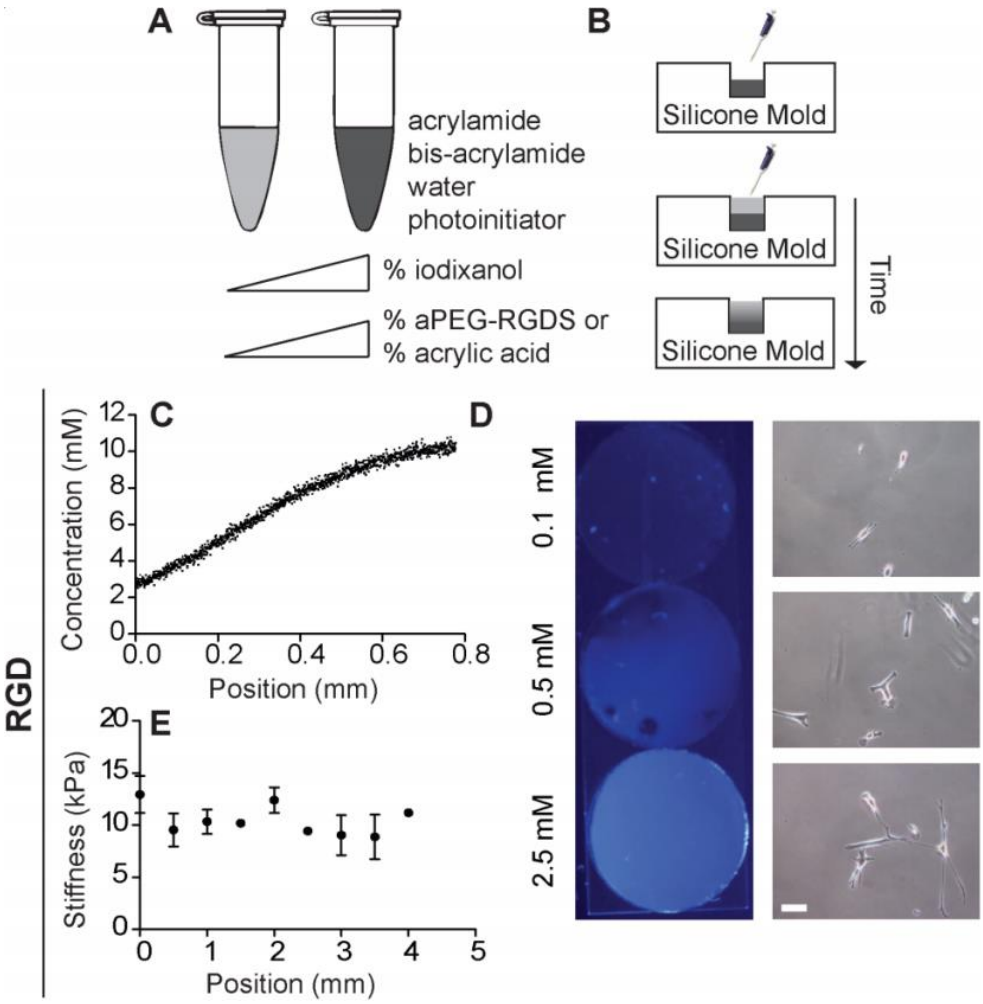


Figure 2-13 Fabrication of polyacrylamide hydrogels with RGD and collagen gradients.

A) Pre-polymer solutions of acrylamide, bis-acrylamide, water, photoinitiator, acrylic acid or acrylated-PEG-RGD, are dissolved with serial dilutions of iodixanol. B) Two pre-polymer solutions are layered in order of decreasing density into a silicone rubber mold that is clamped with a methacrylated glass coverslip in between an untreated glass slide, and a DCDMS-treated glass slide. After a settling time of 10 s, layered hydrogels are polymerized with UVA light for 4.5 min. The iodixanol is rinsed away subsequent to polymerization. C) A hydroxycoumarin dye (excitation 350 nm) pre-conjugated to aPEG-RGD allows for gradient characterization; incorporating 0.1 and 10 mM aPEG-RGD into two layers yield a gradient of approximately 10 mM/mm. D) Images of static polyacrylamide gels with 0.1, 0.5, and 2.5 mM aPEG-RGD-dye under UVA light (left); brightfield images indicate that MSC spreading correlates with RGD concentration. Scale bar: 100 µm). E) Elastic modulus measured every 500 µm via AFM across the RGD gradient hydrogel substrate (n > 3; mean 6 SD).

To obtain collagen gradients, 10/0.1% acrylamide/ bis-acrylamide, acrylic acid, and serial dilutions of iodixanol were used. Solutions of 0.005 and 0.1% acrylic acid, with 1 and 4% iodixanol respectively, were used to fabricate PA-AA hydrogels with gradients of acrylic acid that span a similar 800 µm region across the hydrogel at the mixing interface. Hydrogels were then subsequently functionalized with type I collagen using EDC/NHS crosslinking to create a gradient of collagen on the substrate surface. Hydrogels were incubated in 5 mg/mL EDC (Alfa Aesar) and 9 mg/mL NHS (Alfa Aesar) dissolved in water for 10 min at room temperature, rinsed in water, then incubated in 100 µg/mL rat tail collagen type I (BD Biosciences) in DI water for 30 min.

AFM indentation indicates that hydrogel stiffness of 5 kPa remained constant across the substrate (Figure 2-14A). Force spectrograms from microindentations on both low and high collagen density sides of the substrate were obtained via atomic force spectroscopy (AFS) using a probe functionalized with an anti-collagen type I antibody as described below. When the tip makes contact with the substrate, protein-antibody bonds form. As the tip is retracted from the surface, segments of collagen fibers unfold and stretch until antibody- collagen bonds rupture. These rupture events can be visualized within each spectrogram. A greater number of events (Figure 2-14B, left) detected on the high collagen density side of the substrate indicate that collagen density scales with acrylic acid concentration, and shorter rupture lengths on this side of the substrate indicate a greater degree of collagen fiber-EDC/NHS tethering to the surface (Figure 2-14B, right). All hydrogels were soaked in sterile PBS, stored at 4 °C, and UV sterilized for 10 min prior to use in cell culture.

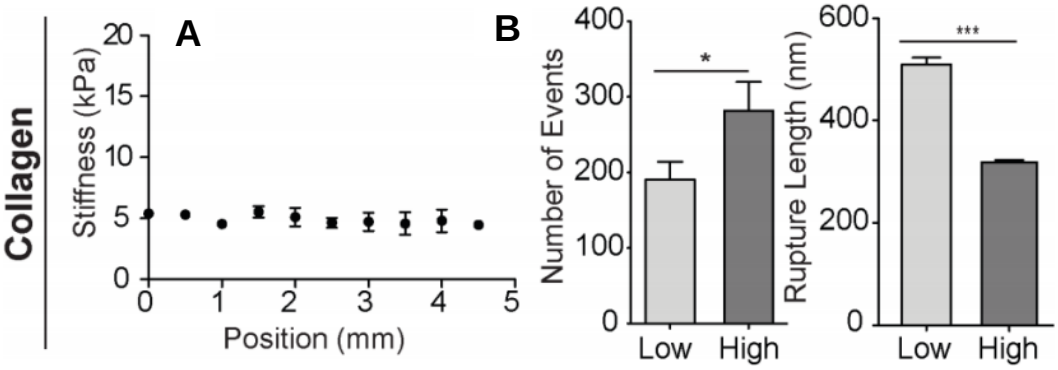


Figure 2-14 Characterization of hydrogels with RGD and collagen gradients.

A) Elastic modulus measured every 500 µm via AFM across the acrylic acid/collagen gradient hydrogel substrate (n > 3; mean 6 SD). B) Antibody-protein rupture events detected via AFS (left) and corresponding measured rupture lengths (right) on low (0.005%) and high (0.1%) acrylic acid hydrogels activated with collagen I. (n > 500; mean 6 SEM; *p < 0.05, ***p < 0.005).

2.3.2.3 Atomic force microscopy

Substrate stiffness was measured via indentation using an MFP-3D-Bio (Asylum Research) atomic force microscope (AFM). Chromium/gold-coated, silicon nitride (SiN) cantilevers with pyramid tips (PNP-TR; NanoWorld) with ~30 pN/nm spring constants as determined from the MFP-3Ds built-in calibration function were used. Samples were mounted on glass slides using vacuum grease and immersed in PBS. The probe was indented into the sample with approach and retraction velocities of 2 and 20 µm/s and a force trigger of 2 nN. AFM data was analyzed using custom code in Igor Pro (Wavemetrics); the substrate spring constant, i.e., Young's Moduli, was determined using a linearized Sneddon model (Kaushik et al., 2011).

To detect fibrous protein on the substrate surfaces, cantilevers were functionalized with the C2456, a mouse monoclonal anti-collagen type I antibody (Sigma) using a previously established method (Bonanni et al., 2005; Chirasatitsin &

Engler, 2010). Briefly, cantilevers were cleaned with chloroform for 30 s and immersed in 5 M ethanolamine-HCl in dimethylsulfoxide (DMSO) at room temperature for 3 h, resulting in the functionalization of an amine group to the surface of the probe. Tips were rinsed in PBS, incubated in 25 mM bis[sulfosuccinimidyl] suberate crosslinker (BS3; Pierce) for 30 min, rinsed again in PBS, then immersed in 200 µg/mL C2456 for 30 min to crosslink the antibody to the tip. Functionalized cantilevers were rinsed, dried, and stored at 4 °C until use. Force spectrograms were taken in 10 x 10 arrays, with indentations spaced 10 µm apart. The functionalized tips were indented and retracted at 2 µm/s. Force curves were converted to force vs. tip Z-position and analyzed for rupture events using a previously described algorithm (Fuhrmann et al., 2008). Rupture event count along with corresponding event lengths and forces were recorded.

2.3.2.4 Cell culture

Human MSCs (Lonza) were cultured between passages 4 to 7 in low glucose Dulbecco's modified eagle medium (DMEM) (Gibco) supplemented with 5% fetal bovine serum (Gemini Bio-Products) and 1% antibiotic/antimycotic (Corning). NIH-3T3s were cultured in DMEM supplemented with 5% fetal bovine serum (Gemini Bio-Products), 4 mM L-glutamine, 1 mM sodium pyruvate, and 1% penicillin-streptomycin (Corning). For migration experiments, MSCs and 3T3s were seeded on hydrogels at densities of 1,000 cells/cm^2 and 5,000 cells/cm^2, respectively. Cells were allowed to attach and spread for 3 hr prior to migration tracking.

2.3.2.5 Migration studies

Migration experiments were conducted using brightfield time-lapse microscopy over a period of 48 hr. Cells were placed in a temperature, CO2, and humidity controlled LiveCell chamber (Pathology Devices). Images were taken every 15 min, and cell positions were tracked in FIJI. Absolute migration velocities, velocities in the gradient direction, tactic indices, and angle histograms were calculated from raw position values using custom MATLAB scripts. To minimize error in tracking, a running average was taken of every four velocities. Tactic index, or persistence, is calculated by taking the ratio of displacement (from initial to final position) to total distance traveled. Where indicated, cells were chosen from three regions of the gradient substrates: the low adhesive ligand density region, the gradient region, and the high adhesive ligand density region.

2.3.2.6 Inhibitors, drugs and RGD blocking

Lysophosphatidic acid (Enzo Life Sciences #BML-LP100), bradykinin (Sigma #B3259), nocodazole (Sigma #M1404), cytochalasin D (Sigma #C2618), and Rac inhibitor (Millipore #553502) were included in culture media at concentrations of 20 µM, 10 nM, 0.5 µM, 0.5 µM, and 50 µM respectively. Drugs were stored at 100x in DMSO at -20°C until use. To reduce MSC adhesion to the hydrogel substrate surface by blocking RGD peptide-binding integrins, 0.02, 0.05, 0.1 and 0.2 mM free RGD peptide was included in the culture media throughout the duration of the time-lapse.

2.3.2.7 Immunofluorescence

Cells were fixed in 3.7% formaldehyde for 15 min at room temperature, rinsed in PBS, and permeabilized with 1% triton-X in PBS for 15 min at room temperature. Cells were incubated in 1:400 rhodamine phalloidin (Life Technologies) in 2% bovine serum albumin (BSA) in PBS supplemented with MgCl2 for 30 minutes, then incubated in 1:2000 Hoescht in DI water for 10 min. Samples were washed with DI water and mounted with fluoromount-G (SouthernBiotech). Imaging was performed using a Nikon Eclipse TI microscope equipped with a CARV II confocal system (BD Biosciences), motorized stage and MS-2000 controller (Applied Scientific Instrumentation), and a Cool-Snap HQ camera (Photometrics) and controlled by Metamorph (Molecular Devices).

2.3.2.8 Förster resonance energy transfer (FRET)

Fibronectin was isolated from human plasma using gelatin-Sepharose binding and eluted with 6 M urea. Isolated fibronectin was concentrated to approximately 3 mg/mL using an Amicon Ultra Centrifugal Filter (10 kDa NMWL) (Millipore) and denatured for 15 min in 4 M guanidine hydrochloride (GdnHCl). Denatured fibronectin was dual-labeled with Alexa Fluor 488 (donor) and Alexa Fluor 546 (acceptor) fluorophores, as previous described (Baneyx, Baugh, & Vogel, 2002; Taylor-Weiner, Ravi, & Engler, 2015). Briefly, denatured fibronectin was incubated with a 30-fold molar excess of Alexa Fluor 546 C5 Maleimide (Life Technologies) for 2 hr to label cysteine residues within the III7 and III15 domains of fibronectin. The single-labeled fibronectin was buffer exchanged into 0.1 M sodium bicarbonate pH 8.3 and separated from unreacted acceptor fluorophores using a spin desalting column (Thermo Scientific).

The single-labeled fibronectin was then incubated with a 40-fold molar excess of Alexa Fluor 488 succinimidyl ester (Life Technologies) for 1 hr to label amine residues throughout fibronectin. Unreacted donor fluorophores were removed using a spin desalting column and dual-labeled fibronectin was stored with 10% glycerol at -20 °C. The average number of acceptor and donor fluorophores per fibronectin dimer was 3.6 and 8.8, respectively, and was determined using published extinction coefficients and absorbance values for the dual-labeled fibronectin at 280, 498, and 556 nm.

Images of the dual-labeled fibronectin were acquired on a Zeiss LSM 780 Confocal Microscope and analyzed using a custom MATLAB script, as previously described (Smith et al., 2007). Briefly, images were averaged with a 3 x 3 pixel-sliding block and perinuclear regions of DAPI stained cells were manually selected for analysis. The FRET ratio for each pixel within a selected region was calculated by dividing the pixel intensity in the acceptor image by the corresponding pixel intensity in the donor image. FRET ratios less than 0.05 and greater than 1.0 were excluded from analysis. The mean FRET ratio within the selected regions was calculated for each cell and then averaged over all the cells in each condition.

2.3.2.9 Traction force microscopy

Traction force microscopy (TFM) was performed as previously described (Del Álamo et al., 2013). Briefly, fluorescent 0.2 µm microspheres (Invitrogen) were added to the pre-polymer solution to a concentration of 1% v/v. 0.1% v/v TWEEN was added to the solution to prevent microspheres from forming aggregates. Hydrogel substrates used in TFM experiments were cast in 35 mm glass bottom dishes (MatTek) and layered with an 18 mm DCDMS-treated circular coverslip, then UV polymerized for 4.5

min at 350 nm as described above. The microspheres directly underneath selected live cells were imaged with a 60x confocal objective (Zeiss) using the Nikon Eclipse TI microscope. Cells were released with 2.5% trypsin and the same microspheres were imaged again. Embedded microsphere displacement from prior to subsequent to trypsin treatment was determined using a particle image velocimetry script in MATLAB (MathWorks). Mean displacements were calculated for each cell, and averaged over all cells within one condition.

2.3.2.10 Statistical analyses

All data are expressed as mean ± standard error of the mean. Student's t-tests were used to determine statistical significance in Figure 2-14B, Figure 2-16, Figure 2-18B, Figure 2-19, Figure 2-22B, Figure 2-24C and Figure 2-25C. 1- or 2-way ANOVAs were used in Figure 2-19, Figure 2-23, Figure 2-24B, and Figure 2-25B as indicated. Significant differences were considered for $p < 0.05$ as indicated; n.s. denotes not significant. Multiple comparisons Tukey's post hoc tests were performed where appropriate.

2.3.3 Results

2.3.3.1 Fibroblasts exhibit haptotaxis

Murine 3T3 fibroblasts and human MSCs attached to and spread on RGD and collagen ligand gradients within 4 hr of seeding. Quantifying cell density and spread area and across collagen gradient substrates (Figure 2-15) 15 hr post-seeding demonstrated that density and spread area both scale with surface collagen density, and further confirmed the presence of a surface adhesive gradient. Migration velocity

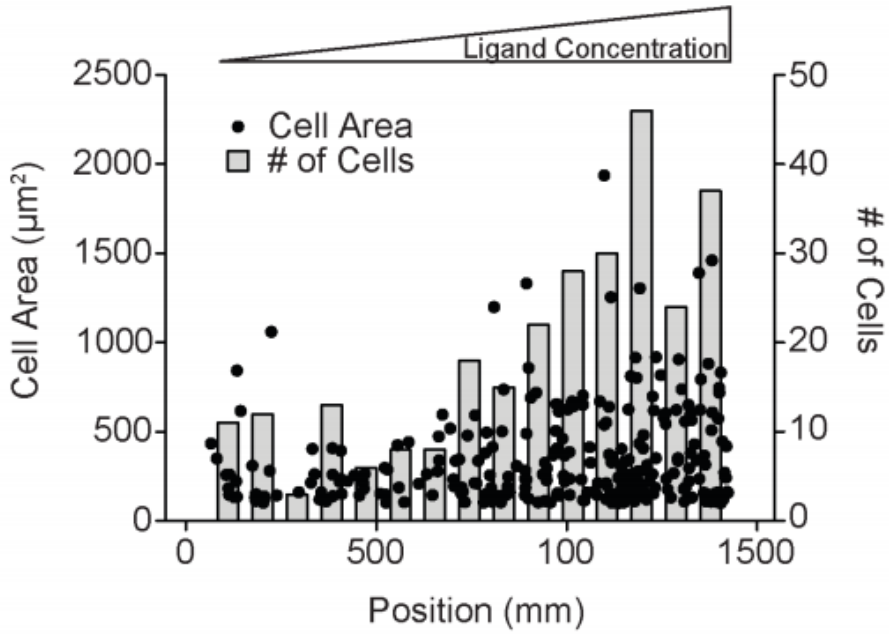


Figure 2-15 Cell Spread Area and Attachment on Collagen Gradients.

Dots indicate the distribution of cell spread areas, and grey bars indicate the number of cells found across the gradient region of a surface collagen density gradient substrate 15 hr post-seeding.

and haptotactic velocity, i.e., migration in the gradient direction, were measured. MSCs did not display any preferential migration within 48 hr of spreading on gradients of RGD peptide. Absolute MSC migration velocity was also insensitive to ligand density (Figure 2-16A, left). However fibroblasts exhibited haptotactic migration in the direction of higher RGD concentration. Moreover, absolute fibroblast migration velocity inversely scaled with RGD concentration, i.e., cells moved faster at low RGD concentration (Figure 2-16A, right). To determine whether migration was affected by the presence of

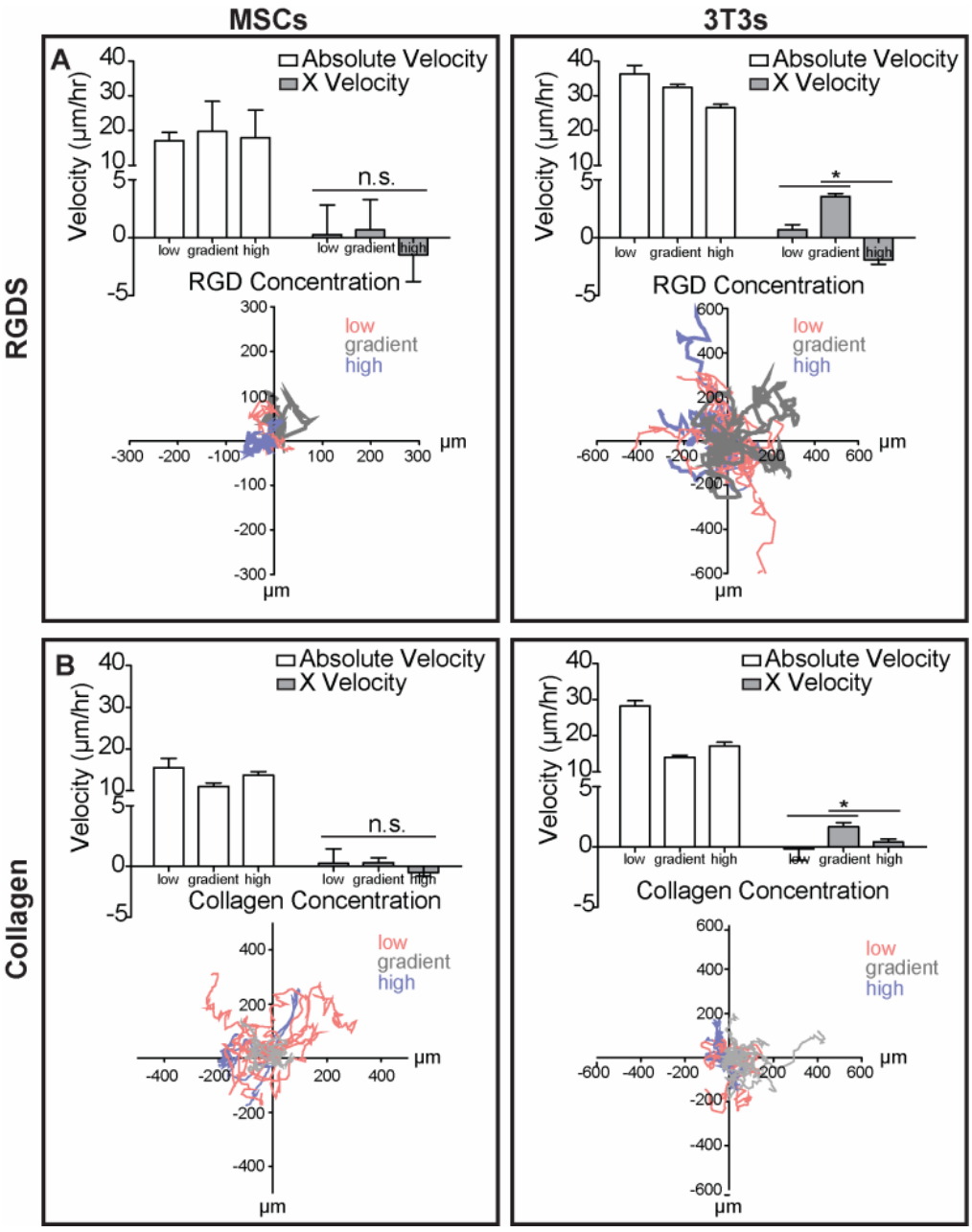


Figure 2-16 Migratory response of MSCs and fibroblasts on ligand gradients.

Absolute and X velocities of MSCs (left) and 3T3s (right) on indicated regions of RGD concentration gradients A) and surface collagen density gradients B). Low and high indicates cells found on the low and high static concentration regions of the substrate; gradient indicates cells found at the mixing interface of the substrate. Positive X velocity indicates migration towards regions of increasing ligand density. Representative rose plots show migratory paths of cells normalized to origin. (n > 20; mean 6 SEM; *p < 0.05; n.s.: not significant)

a full-length, fibrous protein compared to the short adhesive RGD peptide, MSC and fibroblast migration was assessed on collagen density gradients. Consistent with RGD, MSCs on collagen substrates displayed random migration that lacked preference for either low or high ligand density (Figure 2-16B, left) and was not processive (Figure 2-17) as measured by a tactic ratio of displacement to total distance travelled over a period of 48 hr. Fibroblasts, on the other hand, displayed biased net migration towards

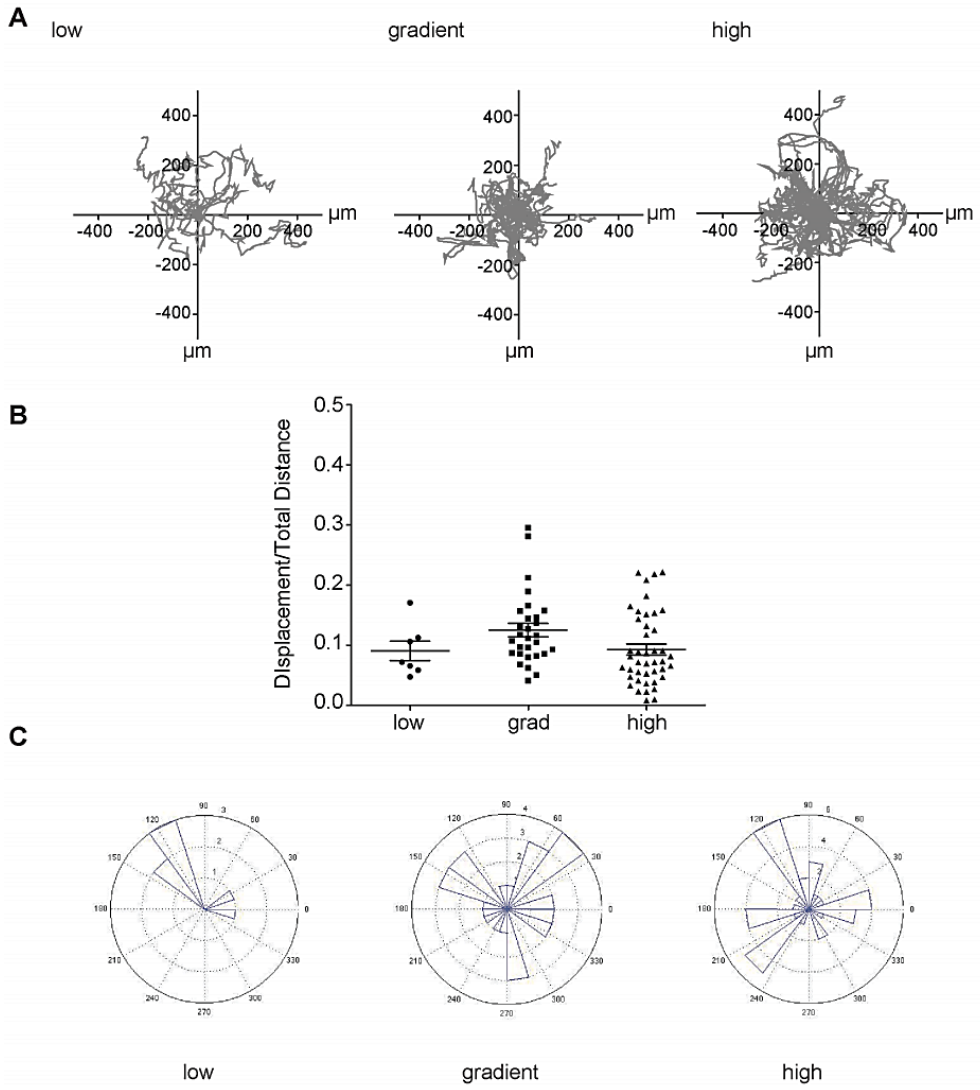


Figure 2-17 Characterization of MSC Migration on Collagen Gradients.

A) Rose plots of MSC migratory paths beginning at the origin on low, gradient, and high collagen density regions of PA-AA hydrogels. B) Tactic index, or the ratio of displacement to total distance traveled by cells on low, gradient, and high collagen density regions of PA-AA hydrogels. Each data point indicates one cell (mean ± S.E.M.). C) Histograms depicting initial to final position displacement vector angles of MSCs on low, gradient, and high collagen density regions of PA-AA hydrogels. 0 angle indicates migration directly up the ligand gradient.

higher collagen density (Figure 2-16B, right) that was more processive compared to cells found on static regions of the substrate (Figure 2-18). Taken together, these data

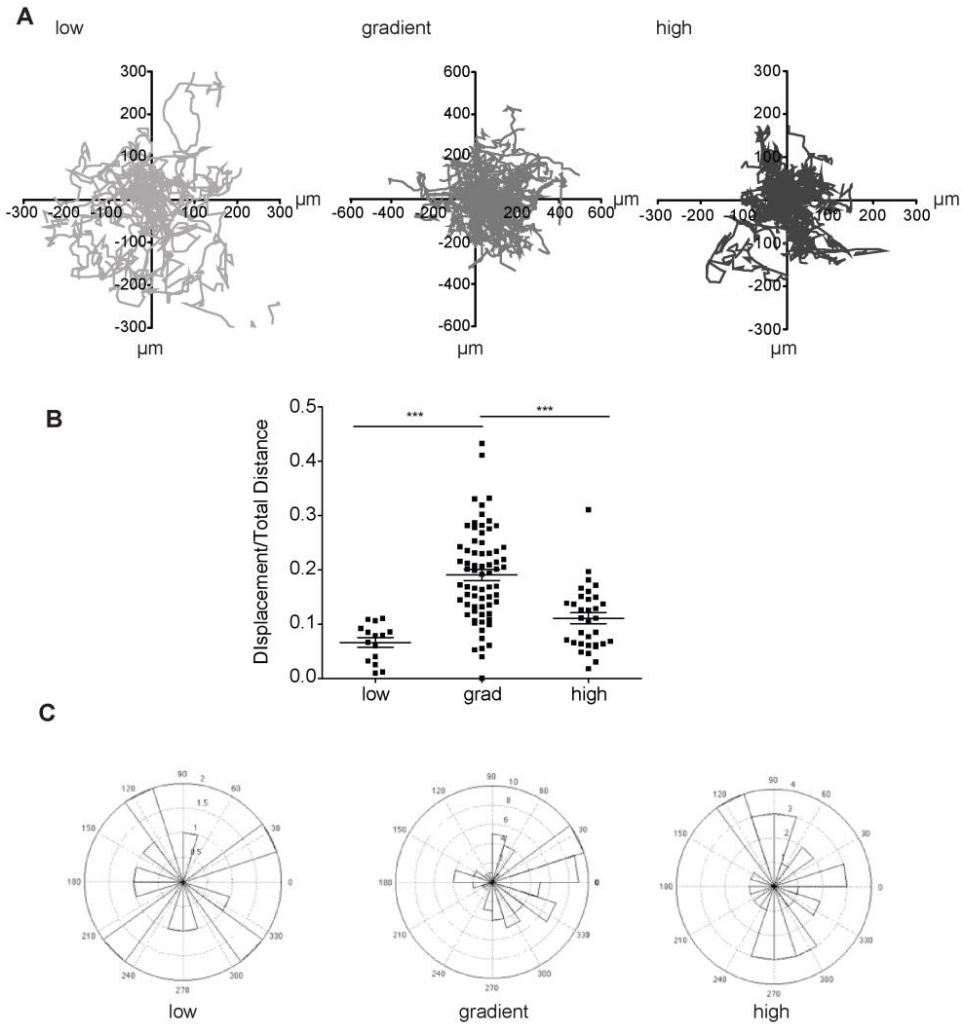


Figure 2-18 Characterization of 3T3 Migration on Collagen Gradients.

A) Rose plots of 3T3 migratory paths beginning at the origin on low, gradient, and high collagen density regions of PA-AA hydrogels. B) Tactic index, or the ratio of displacement to total distance traveled by cells on low, gradient, and high collagen density regions of PA-AA hydrogels. Each data point indicates one cell (mean ± S.E.M.; ***$p < 0.005$). C) Histograms depicting initial to final position displacement vector angles of 3T3s on low, gradient, and high collagen density regions of PA-AA hydrogels. 0 angle indicates migration directly up the ligand gradient.

indicate that fibroblasts undergo haptotaxis on both ligand gradients of RGD and collagen under the basal conditions described in this study, while MSCs do not.

2.3.3.2 Fibroblast haptotaxis is regulated by a cytoskeletal-mediated mechanism

To provide insight into how the cytoskeleton potentially regulates migration and haptotaxis, we treated fibroblasts with contractile agonists lysophosphatidic acid (LPA) and bradykinin (BK) as well as with cytoskeleton-perturbing drugs cytochalasin D (CytoD) to prevent actin polymerization and nocodazole (Noco) to prevent microtubule polymerization. Cells treated with nocodazole and cytochalasin D exhibited less-spread and rounded morphology compared to untreated cells (Figure 2-19A), while cells treated with LPA and bradykinin were more spread compared to untreated cells, especially at low RGDS concentration (Figure 2-19B). While LPA and bradykinin *vs*.

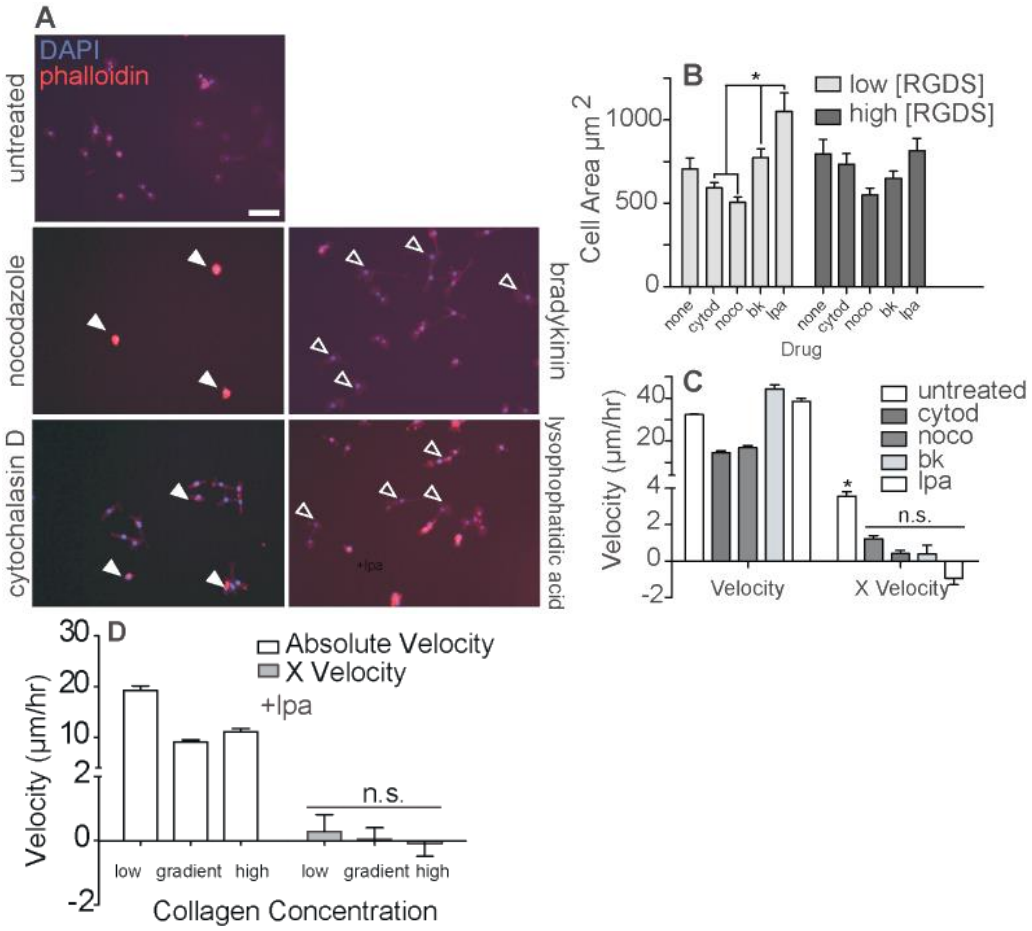


Figure 2-19 Influence of drug treatment on fibroblast morphology and migration.

A) 3T3 fibroblasts spread on PA-PEG-RGD hydrogels 24 h after seeding and treating by the indicated drugs (actin, red; nuclei staining, blue). Filled white arrows indicate cells that are smaller and less spread than untreated control cells. Open white arrows indicate cells that are larger and more spread than untreated control cells. (Scale bar: 100 µm). (B) Spread area and (C) absolute migratory velocities and X velocities of cells treated with the indicated drugs on low, gradient, and high regions of RGD gradient hydrogel substrates. (n > 20; mean 6 SEM; *p < 0.05; n.s.: not significant). D) Absolute velocities and X velocities of 3T3s treated with LPA on indicated regions of acrylic acid hydrogels activated with surface gradients of collagen type I. (n > 20; mean 6 SEM; n.s.: not significant).

nocodazole and cytochalasin D treatment increased and decreased absolute migration velocity respectively, all drug treatments inhibited haptotaxis (Figure 2-19C and Figure

2-20A). LPA was similarly effective at reducing haptotaxis on collagen gradients (Figure 2-19D and Figure 2-20B). These data suggest that while depolymerizing the

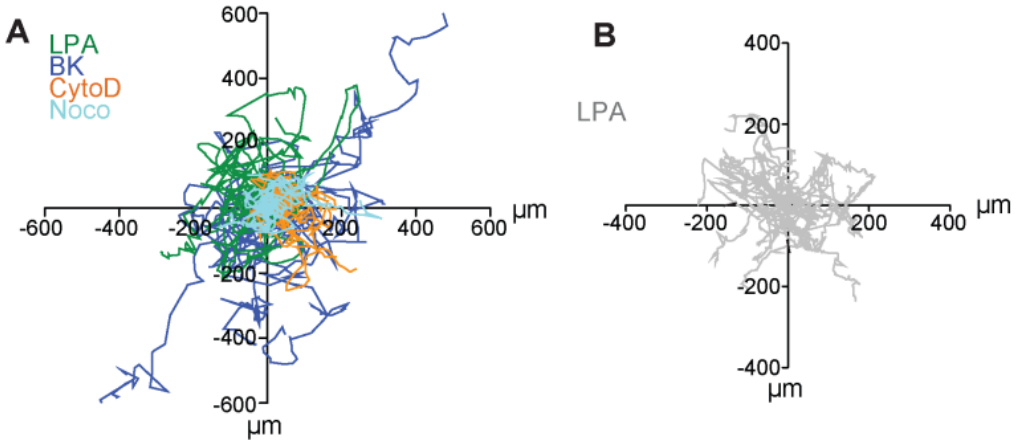


Figure 2-20 Effect of Drug Treatment on 3T3 Migration Paths.

A) Rose plots of migratory paths beginning at the origin on the gradient region of PA-PEG-RGD hydrogels with RGD gradients of 3T3s treated with lysophosphatidic acid, bradykinin, nocodazole, and cytochalasin-D. B) Rose plots of migratory paths beginning at the origin on the gradient region of PA-AA collagen gradient hydrogels of 3T3s treated with lysophosphatidic acid.

cytoskeleton prohibits both spreading and migration, promoting its assembly and contraction produces overly spread, faster moving cells that lose their sensing capabilities. Rac1, a GTP-binding protein that regulates membrane ruffling in migrating cells (Giannone et al., 2004) and facilitates labile adhesion (Ehrlich, Hansen, & Nelson, 2002), may be involved in the sensing capabilities that cause biased migration that which LPA and bradykinin treatment reduced. While Rac-inhibited fibroblasts still adhered to and spread on collagen gradient hydrogels, cells were no longer capable of haptotaxis (Figure 2-21). These data overall suggest that appropriate protrusive capabilities, i.e., membrane ruffling, followed by modest cytoskeletal assembly and contractions appear to be crucial for haptotaxis.

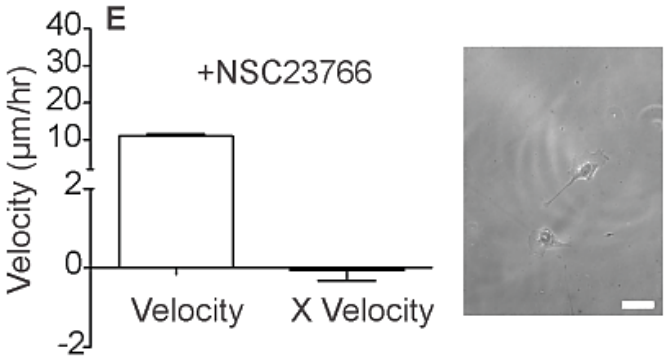


Figure 2-21 Influence of drug treatment on fibroblast velocity.

Absolute and X velocities of 3T3s treated with NSC23766 Rac inhibitor on gradient regions of acrylic acid hydrogels activated with surface gradients of collagen type I. Positive X velocity indicates migration towards regions of increasing adhesive ligand density. (n > 20; mean 6 SEM; Scale bar: 100 μm).

Biased migration resulting from cell protrusions produces substrate deformations that are small and transient (Vincent et al., 2013) and may be reflected in deformation of matrix proteins and/or the substrate (Vincent et al., 2013; Wen et al., 2014). Förster resonance energy transfer (FRET) and TFM were utilized to investigate the effect of adhesive ligand density on cell-induced deformations of the ligand coating and substrate. The FRET ratio decreased underneath both stem cells and fibroblasts, suggesting that the cells exerted traction forces on the ligand coating thus deforming protein fibers, effectively decreasing the FRET ratio. Consequentially, the protein underneath blebbistatin-treated cells that lack the ability to exert forces due to perturbed myosin contractility exhibited increased FRET ratios (Figure 2-22).

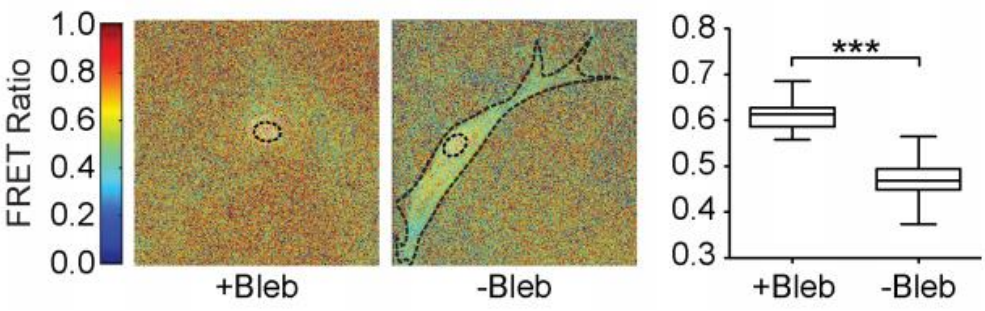


Figure 2-22 Fibronectin FRET Intensity Characterization.

FRET intensity ratio map of a blebbistatin treated cell (left) and an untreated cell (center), and measured FRET intensity ratio of undeformed protein underneath a blebbistatin treated cell and an untreated cell (right) seeded on a polyacryalmide hydrogels (right). (n = 8; ***p<0.005).

Although fibronectin FRET ratios underneath both cell types scaled with fibronectin surface density, absolute FRET ratio values were similar between the two cell types on both low and high ligand density substrates (Figure 2-23A & B). These observations suggest that although a greater degree of attachment effectively ‘‘ties’’ down fibronectin to the substrate more tightly and hinders fiber unfolding to a greater extent at higher ligand concentrations, protein tethering is perhaps unrelated to haptotaxis due to differences in migratory behaviors between MSCs and fibroblasts. Conversely, although both fibroblasts and MSCs exhibited adhesive ligand density-dependent differences in mean substrate displacements observed by TFM (Figure 2-23C), MSCs displaced the substrate fivefold more than fibroblasts, regardless of ligand density and degree of tethering (Figure 2-23D). Together these data along with the observation that fibroblasts but not MSCs haptotaxed suggest that although the ability of a cell to exert traction forces may be necessary for motility and migration, MSCs tend to surpass traction or adhesiveness thresholds which results in extremely large cell-induced deformations of the substrate. This perhaps occurs to an extent

where cells no longer can sense a directional cue such as increasing adhesive ligand density.

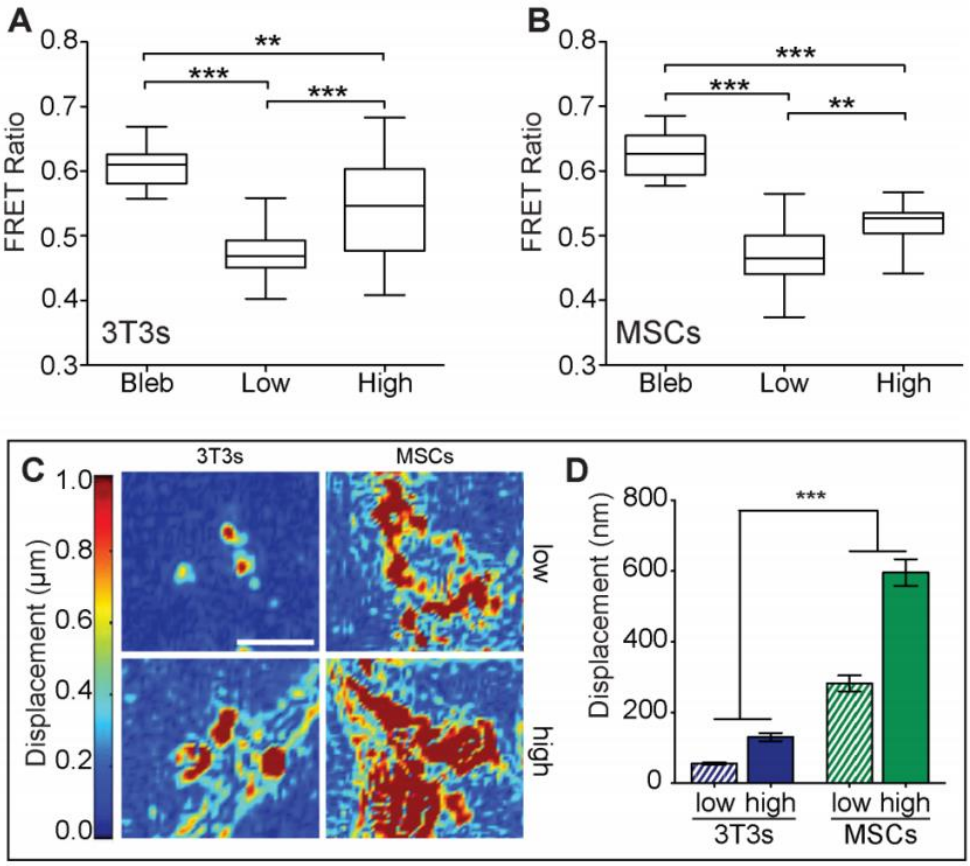


Figure 2-23 Measuring cell-induced deformations of the underlying substrate.

Mean FRET intensity ratio and ratio maps of fibronectin. Spread 3T3s (A) and MSCs (B) on low and high acrylic acid PA hydrogels activated with EDC/NHS and coated with dual-labeled fibronectin. ($n > 16$; mean 6 SEM; $^{**}p < 0.01$; $^{***}p < 0.005$). Displacement maps of embedded fluorescent particles (C) and mean particle displacement (D) resulting from 3T3 and MSC tractions exerted on low and high acrylic acid PA hydrogels activated with EDC/NHS and coated with collagen type I. ($n = 25$; mean 6 SEM; $^{***}p < 0.005$).

2.3.3.3 Modulating cell-substrate adhesion affects haptotactic behavior in both stem cells and fibroblasts

To determine whether or not exceeding a traction or adhesiveness threshold can explain the absence of haptotaxis in MSCs, we reduced MSCs tractions by adding free RGD peptide to the culture media to block RGD binding sites on integrins to effectively reduce cell-substrate adhesiveness. MSCs had slightly smaller but still spread morphology (Figure 2-24A). Including RGD in the culture media increased absolute migration velocities (Figure 2-24B), consistent with the observation of higher migration velocities on substrates with low ligand densities (Figure 2-16). Additionally, MSCs displayed haptotaxis in an RGD dose-dependent manner, where 20 μm RGD peptide resulted in the most significant haptotactic response. The presence of free peptide also decreased mean substrate displacement compared to untreated MSCs cultured on high concentration RGD substrates (Figure 2-24C). This sevenfold reduction yields deformations within range of fibroblast-induced hydrogel deformations at surface ligand densities where directed migration is observed (Figure 2-16). These data also imply that while haptotactic migratory behaviors may be achieved by reducing cell-substrate binding by blocking a subset of relevant integrins, if too many integrins are blocked, cells potentially lose their ability to sufficiently sense ligand density gradients. This further suggests a biphasic phenomenon where cells lose the ability to haptotax if they are too strongly or too weakly adhered to the surface, and the existence of a mid-range of adhesive ligand density where haptotaxis is most profound.

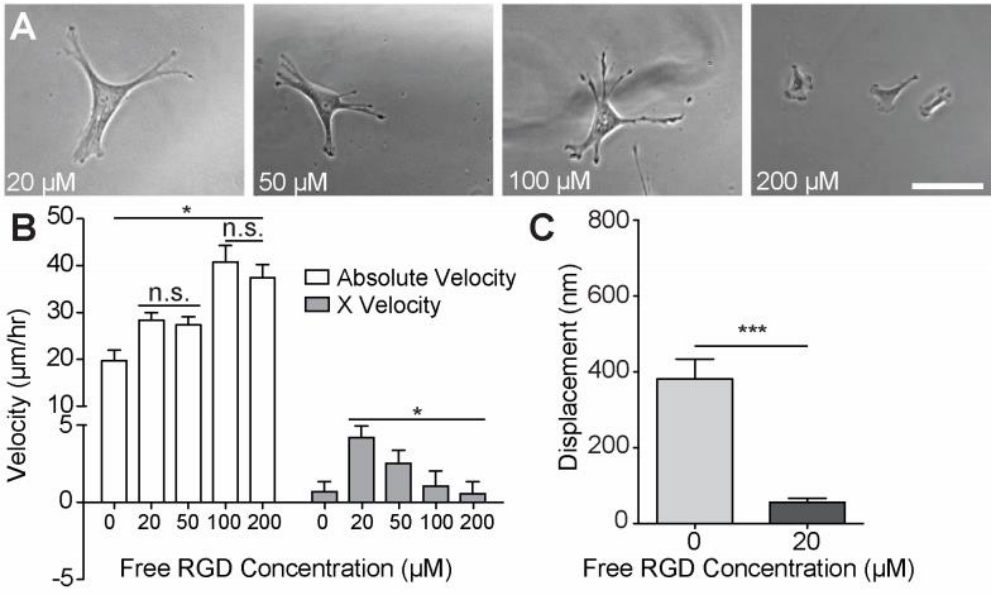


Figure 2-24 Reducing MSC-substrate adhesion by blocking surface integrins with free peptide.

A) MSCs spread on 10 mM PA-PEG-RGD hydrogels with indicated concentrations of free RGD peptide in the culture media. (Scale bar: 100 μm). B) Absolute and X velocities of MSCs on the gradient region of RGD gradient PA hydrogels with indicated concentrations of free RGD peptide in the culture media. ($n > 40$; mean 6 SEM; $*p < 0.05$). C) Mean displacement of particles embedded in PA hydrogels with 10 mM aPEG-RGD resulting from tractions of MSCs in normal media, and media supplemented with 0.02 mM free RGD peptide. ($n > 10$; mean 6 SEM; $***p < 0.005$).

To further support this theory, 3T3 migration was assessed on RGD gradients of similar steepness, but of higher absolute peptide concentrations. Low and high RGD concentrations were increased from 0.1 and 10 mM, to 5.6 and 15.8 mM respectively (Figure 2-25A). Total migration velocity and haptotactic velocity were measured. In this system, 3T3s did not display preferential migration towards either end of the gradient substrate (Figure 2-25B). Furthermore, absolute fibroblast migration velocity no longer scaled with RGD concentration; cells moved at similar speeds regardless of their position relative to the gradient (Figure 2-25B). Mean substrate displacements induced by fibroblasts seeded on these more-adhesive substrates increased by several fold

compared to fibroblasts that haptotaxed on gradients of lower absolute ligand concentrations; these displacements are on par with non-haptotaxing MSCs (Figure 2-23D). These data provide additional evidence suggesting that haptotactic behavior is limited by cell-substrate adhesion, and that these adhesion limits are cell-type specific.

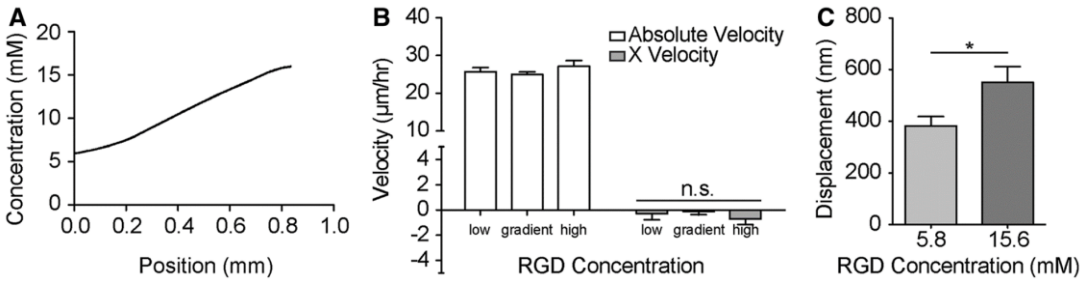


Figure 2-25 Increasing fibroblast-substrate adhesion by increasing surface adhesive ligand density.

A) A hydroxycoumarin dye (excitation 350 nm) pre-conjugated to aPEG-RGD allows for gradient characterization; incorporating 5.8 and 15.6 mM aPEG-RGD into two layers yield a gradient of approximately 10 mM/mm. B) Absolute velocities and X velocities of 3T3s on indicated regions of hydrogels with RGD concentration gradients spanning a 5.8-15.6 mM range. Low and high indicates cells found on the low and high static concentration regions of the substrate; gradient indicates cells found at the mixing interface of the substrate. Positive X velocity indicates migration towards regions of increasing adhesive ligand density ($n > 50$; mean 6 SEM; n.s. not significant). C) Mean displacement of particles embedded in PA with 5.8 and 15.6 mM aPEG-RGD resulting from tractions of 3T3s in normal media. ($n > 10$; mean 6 SEM; $^*p < 0.05$).

2.3.4 Summary

By directly comparing migratory behaviors of MSCs and fibroblasts in two systems using DGMP, these data demonstrate that when introduced to an adhesive ECM ligand gradient-irrespective of whether the ligand is a short adhesive peptide or full length fibrous protein-fibroblasts underwent haptotaxis, while under the same basal culture conditions, MSCs did not. We note two observations contrasting the motility of

the two cell types under the same culture conditions and seeded on the same gradient substrates: (1) fibroblasts migrate at faster absolute velocities compared to MSCs, and perhaps more importantly, (2) fibroblasts display a significant inverse relationship between surface ligand density and absolute velocity, similar to classic experiments on uniformly adhesive substrates (Lauffenburger & Linderman, 1996), while MSCs do not. First, the ability of fibroblasts to move faster overall may suggest that they ‘‘feel’’ their surroundings at a faster rate; this perhaps heightens their sensitivity to small changes in adhesive ligand density in their microenvironment, allowing them to respond more quickly relative to slower moving, well-spread MSCs. Second, the inverse scaling of absolute velocities and both RGD and collagen density for fibroblasts confirms that although the exact mechanism is unknown, fibroblasts sense and respond to differences in absolute adhesive ligand density more acutely. Similar MSC motility on all regions of both RGD and collagen coated substrates suggests that MSCs may not be as sensitive as the fibroblasts to these density differences at the ligand concentrations and culture conditions used here. While haptotaxis may play a significant role in directing fibroblasts towards a site of injury, these data suggest that MSCs *in vivo* may be less sensitive to adhesive ligand gradients. Given that they have been reported to home to sites of injury (Katayama et al., 2006), these data would imply that the MSC migratory process could be regulated by varying concentrations of free ligands in areas of active matrix remodeling, or may perhaps be instead guided by durotactic or other gradient cues.

2.3.4.1 Intact cytoskeleton is necessary for migration, but cell-induced deformations dictate haptotaxis

To provide insight into intracellular mechanisms of haptotaxis, fibroblasts were treated with various cytoskeleton inhibitors and activators. Drugs that prevented polymerization of actin and the formation of stable microtubules eliminated haptotaxis and decreased overall motility, as expected. Fibroblasts remained mainly stationary on PA-PEG-RGD hydrogel substrates after treatment with nocodazole and cytochalasin D, reinforcing the well-established principle that a stable and intact cytoskeleton is necessary for cell motility (Fletcher & Mullins, 2010; Hoffman et al., 2011; Vogel & Sheetz, 2006); similar effects have been shown with MSCs treated with the same inhibitors on durotactic gradients (Vincent et al., 2013). One might expect contractile agonists such as LPA and bradykinin however, to enhance haptotactic migratory behaviors by heightening contractility and thus amplifying the sensitivity or aggregating signal from sensing mechanisms. In fact in fibrotic lungs, LPA treatment induces MSC differentiation into more contractile phenotypes such as myofibroblasts (N. Tang et al., 2014); LPA is also known to increase cell motility, and enhance chemotaxis (Cencetti et al., 2014). Although cells treated with both bradykinin and LPA in this model of fibrosis displayed increased cell motility and spread area, they no longer underwent directed migration on RGD gradient substrates despite their enhanced ability to ‘‘feel’’ their surroundings, supporting our observations. Lack of tactic enhancement subsequent to LPA treatment is also consistent with previous observations where LPA treatment decreased durotaxis of MSCs on stiffness gradients (Vincent et al., 2013). While chemo- and haptotaxis have been reported to have different signaling

mechanisms (Aznavoorian et al., 1990), they would appear to be more complex than simply tuning contractility.

One observation that perhaps relates these results to migrating MSCs is spread area. MSCs are much larger than fibroblasts, regardless of what adhesive ligand was used. Here we found that when fibroblasts are treated with LPA, cells are 1.5-fold larger in spread area, but lose their ability to undergo haptotaxis, i.e., their migratory behavior becomes more similar to MSCs subsequent to LPA treatment. These observations, perhaps reflective of decade-old observations in correlations between cell spread area and both substrate stiffness and adhesive ligand density (A. Engler et al., 2004; Lauffenburger & Linderman, 1996; Peyton & Putnam, 2005), suggest that extracellular biophysical cues that dictate cell spread area may play a role in limiting taxis. However, closer inspection of the deformations imparted by cells was more suggestive of a mechanism. Deformations within the adhesive ligand coating and in underlying hydrogel substrate revealed that both stem cells and fibroblasts could sense differences in low and high surface densities of fibronectin, but absolute protein deformations were similar between cell types. These results are consistent with previous findings that although cells may potentially feel differences in fiber tethering, the degree of tethering does not seem to dictate cell behaviors such as differentiation (Wen et al., 2014) and in this case, migration. However, significant differences in hydrogel deformations between MSCs and fibroblasts suggests that greater MSC tractions may impair their ability to sense differences in adhesive ligand density and thus hinder their ability to undergo preferential migration.

2.3.4.2 Optimal cell-substrate affinity maximizes haptotaxis

By including free RGD peptide in the culture media, we were able to effectively diminish MSC-substrate adhesiveness, reduce MSC tractions thus decreasing substrate deformations, and induce haptotactic migratory behaviors in MSCs. By blocking integrin-substrate binding sites, we observed haptotactic velocities in MSCs that were on par with fibroblasts undergoing haptotaxis. However, once the free RGD peptide exceeds an optimal threshold, haptotactic migration is weakened, as MSCs are no longer sufficiently adhered and spread to the substrate. The inhibition of haptotaxis via blocking integrin receptors using free RGD peptide has previously been shown for melanoma cells on fibronectin gradients (Aznavoorian et al., 1990); our results extend these conclusions to MSCs for free RGD peptide beyond a concentration threshold to suggest that MSC haptotactic capabilities are biphasic with respect to adhesiveness.

Furthermore, by increasing the absolute values of RGD surface concentration, we were able to effectively increase fibroblast-substrate adhesiveness and increase fibroblast tractions, thus increasing substrate deformations; this consequently eliminated haptotactic behaviors in fibroblasts. These increased substrate deformations are similar to deformations induced by non-haptotaxing MSCs, suggesting that the ability of a cell to significantly deform the underlying substrate may block haptotactic migratory behaviors. Our results indicate that the ligand concentration range at which haptotaxis is observed differs by cell type, and further emphasize that haptotactic capabilities are dependent on cell-substrate affinity and adhesiveness.

Thresholds for adhesive ligand density that induce haptotaxis are likely adhesive ligand type dependent, as different ligands yield different degrees of cell-substrate affinity (DiMilla et al., 1993). Maximal migration of smooth muscle cells has

been shown to occur on substrates coated with different densities of collagen and fibronectin that yield similar cell-substrate attachment strength (DiMilla et al., 1993). If cyclic RGD or full-length fibronectin bound to the substrate in place of linear RGD, maximal haptotactic migratory behaviors might be displayed at higher concentrations of free peptide or protein in the culture media, as these ligand types have been shown to better facilitate cell-substrate adhesion compared to linear RGD. However as RGD-binding integrins have not been implicated in haptotactic responses to collagen gradients (Aznavoorian et al., 1990), free RGD peptide is unlikely to affect haptotaxis on collagen gradients. Conversely, alternate integrin binding peptides, e.g., laminin-binding YIGSR, would likely not affect MSC migratory behaviors on substrates with bound RGD.

2.3.5 Recognitions

This work was supported by grants from the National Institutes of Health (DP2OD006460 to A.J.E.), National Science Foundation (1463689 to A.J.E.), and the National Science Foundation Graduate Research Fellowship Program (to J.H.W. and H.T.-W.). The authors declare no commercial affiliations or conflicts of interest.

2.4 Three-dimensional Hyaluronic acid scaffold for *in vitro* neural modeling

2.4.1 Brief introduction and rationale

Until recently, technologies for organizing cells, matrix components and biochemical cues in 3D were complicated and required expensive equipment. Thus, their use had been limited to only a few labs. This narrow application meant that other labs were either limited in their research questions to those addressable in 2D cell culture or in animals. To study genetic brain disorders, the most appropriate animal models are mice or rats, which can be expensive and, more importantly, often yield results that do not correlate with human phenotypes. DGMP in combination with human stem cell-derived neural cells will help bridge the gap between human pathology and studies in animal models. In this section I describe the synthesis of a crosslinkable hyaluronic acid polymer, the main structural component in the brain. I then present results from initial optimization studies demonstrating the ability to not only maintain encapsulated neural stem cells (NSC) under DGMP conditions, but also to facilitate differentiation and outgrowth in 3D.

2.4.2 Materials and methods

2.4.2.1 Cell maintenance

NPCs generated from human iPSCs following informed consent (under protocols approved by the UCSD Institutional Review Board and the Embryonic Stem Cell Research Oversight Committee), generated by transduction of Sox2, Oct4, c-Myc and Klf4. NPCs are produced by dissociating neural rosettes and confirmed by immunocytochemistry against early neural progenitor markers, such as nestin (Figure

2-27C, (Marchetto et al., 2010). NPCs are labeled by infection with a lentivirus carrying the CAG promoter driven EGFP reporter (CAG::eGFP).

2.4.2.2 HAMA synthesis, functionalization and hydrogel fabrication

Hyaluronic acid methacrylate (HAMA) was synthesized (Figure 2-26A) using the method described by Schmidt and colleagues (Seidlits et al., 2010) based on the seminal innovation described in Smeds, *et. al.* (Smeds et al., 1999).

To determine effects of iodixanol on matrix elastic modulus, atomic force microscopy (AFM) was performed. Initial results suggest that its effect is not concentration independent in the range under investigation (Figure 2-26B). It was also observed that iodixanol minimally affects viability; groups were compared by the ratio of constitutively expressed eGFP to ethidium homodimer-1 necrotic nuclear counter staining.

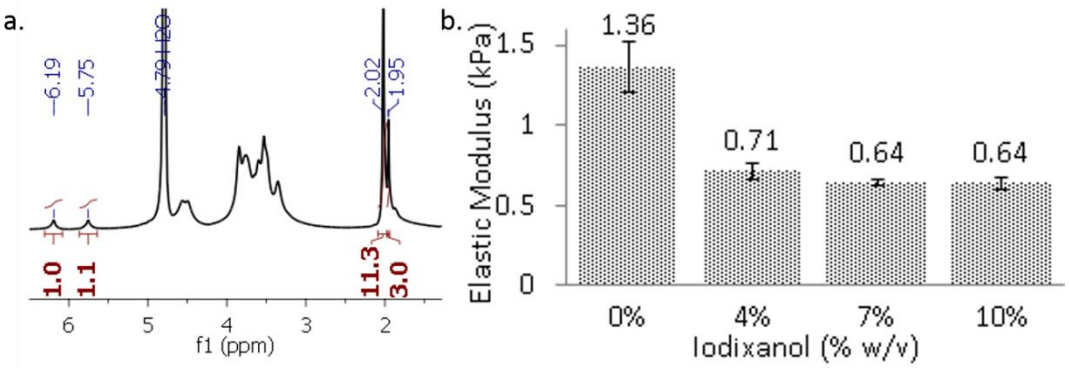


Figure 2-26 Production of hyaluronic acid methacrylate for NPC culture.

A) NMR characterizations of modified hyaluronic acid with 0.27 methacrylates per disaccharide repeat (HAMA-DS 0.27). B) Elastic moduli of HAMA-DS 0.27 (1% w/v) matrices with varied concentrations of iodixanol density modifier characterized by AFM.

Combinations of tethered adhesion peptides and varied encapsulated cell densities were investigated to improve viability and promote neurite extension. A combination of YIGSR, a peptide sequence of laminin responsible for integrin binding, and RGDS, a peptide that binds many integrins, yielded the highest 24 hr viability (~80%, Figure 2-27A). This combination also promoted extensive neurite outgrowth by NPCs (Figure 2-27B). Not only did HAMA matrices maintain NPCs (nestin expression, Figure 2-27C), they also supported differentiation when soluble BDNF was provided in the medium (MAP2 expression, Figure 2-27D).

Cell, adhesion peptide, and photoinitiator concentration, as well as HAMA degree of substitution (DS), were adjusted to establish consistent NPC viability. To maintain NPC multipotency, cells were cultured in an NPC medium with bFGF22, which bars differentiation and limits neurite outgrowth. Percent eGFP positive cells was assessed via FACS analysis. HAMA with varied DS, which affects elastic modulus, was synthesized by adjusting molar ratios of reactants, methacrylic acid and hyaluronan (Smeds et al., 1999).

Since scaffold elastic modulus affects differentiation (Seidlits et al., 2010) and pore size sterically affects locomotion, hydrogel elastic modulus and pore size were measured for each condition tested. Viability was assessed as in preliminary experiments (Figure 2-27A).

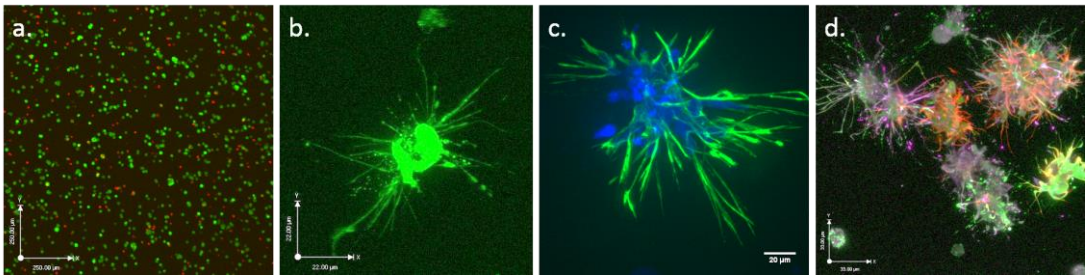


Figure 2-27 HAMA encapsulation is compatible with NPC neurite extension and neuronal differentiation.

A) Viability assay of encapsulated iPSC-derived NPCs (cmv::eGFP) in 3D HAMA matrices, Day 1. “Live” eGFP expression (green) and “dead” nuclear staining (red for 1.4 million cells/mL in HAMA photopolymerized with a combination of acrylated YIGSR-NH2 (250 µM) and RGDS (250 µM). Scale bar: 250 µm. B) Combination of YIGSR-NH2 (250 µM) and RGDS (250 µM) permitted neurite outgrowth from an aggregate of NPCs. Scale bar: 22 µm. C) NPC maintenance evidenced by expression of nestin (green) when cultured with bFGF22 at Day 12 post encapsulation, counterstained with DAPI. Scale bar: 20 µm. D) Neurogenesis evidenced by expression of MAP2 (magenta) at Day 10 pose encapsulation, in the presence of BDNF for 1 week, counterstain of F-actin (red) and eGFP (green). Scale bar: 33 µm.

2.4.2.3 Viability assay

A set of permissive (later referred to as “baseline”) conditions that reliably promote cell viability (at least 90% of total encapsulated cells) with little effect on cell spreading, migration, and neurite outgrowth were identified. It was then determined which adhesion cues are required to prevent anoikis and, through fine tuning, what range of crosslinking density allowed nutrient transport, cell locomotion and neurite outgrowth.

2.4.2.4 Optimizing variables to modulate NPC outgrowth and migration

Many variables influence NPC migration, so focus was applied to those inherent to the matrix itself. The gradients of crosslink densities or concentrations of extracellular

matrix derived integrin-binding peptides YIGSR, IKVAV, and RGD, both individually and in combination, were examined. Non-gradient hydrogel matrices served as controls. And, while many cues that promote directional migration of cell bodies may also promote neurite extension in the same direction, cultures were maintained in NPC medium (with bFGF22) to limit outgrowth. In each of these experiments, cells were encapsulated in the middle layer of a HAMA matrix in which adjacent layers contain semi-continuous gradients (Figure 2-28). The cell-loaded layers were fluorescently marked with methacrylated rhodamine-B and matched the conditions determined to maintain NPC viability.

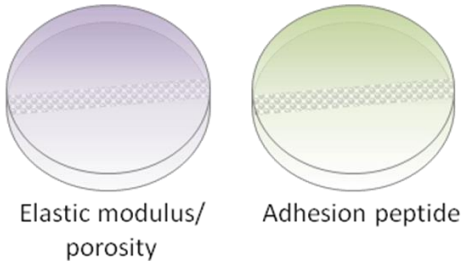


Figure 2-28 Determination of NPC migration variables.
(A) Elastic modulus/porosity. (B) Adhesion peptide.

Migration was quantified using confocal microscopy at static time points. NPCs were monitored daily to determine preferential migration up or down gradients of each variable or combination of variables. The total number of cells crossing into adjacent layers and total distance traveled away from the initial center layer were measured. The combinations of gradients or opposing gradients were further measured to enhance migration (Figure 2-29).

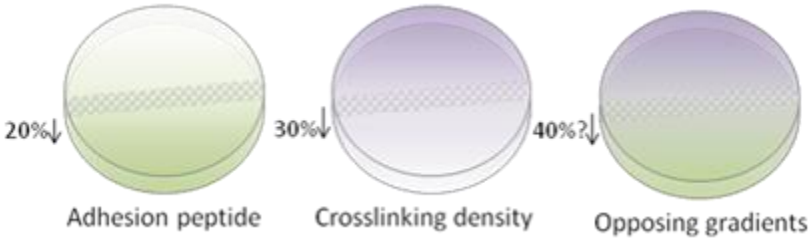


Figure 2-29 Combinations of variables to allow NPC migration.

This combination may allow grated migration than that in either gradient alone. A) Adhesion Peptide. B) Crosslinking Density. C) Opposing Gradients.

2.4.3 Results

Gradient conditions that reliably facilitate cell migration were identified. Contrary to many somatic cell types, NPCs were expected to migrate towards decreasing crosslinking density (HAMA DS or HAMA concentration), as migration in HAMA has been demonstrated to coincide with hydrogel degradation (Seidlits et al., 2010). We expected NPCs to migrate towards greater concentrations of adhesion peptide (Luo & Shoichet, 2004; Tate et al., 2004). In many conditions spontaneous mobility was inhibited and we determined a HAMA hydrogel stiffness above approximately 100 Pa restricted movement even when the scaffolds were co-cultured with underlying monolayer cultures of astrocytes, which have been shown to promote neural migration (Mason, Ito, & Corfas, 2001). Further studies suggest a maximal DS of 17% and final stiffness of 50-100 Pa permitted migration, however laminar control of varied stiffness was very difficult at this range to investigate durotaxis. Additional experimentation is necessary to fully characterize scaffold-mediated durotaxis and haptotaxis.

2.4.4 Summary

The short term goal of this study was to develop a scaffold that would facilitate complex migration, neurite outgrowth and synaptogenesis assays for the functional comparison of iPSC-derived NPCs, neurons and astroglia generated from Rett syndrome (RTT) donors to those from controls, which we accomplished. Owing to the adaptability of DGMP, these assays may be modified to suit a variety of neuroscience questions, from the study of responses to specific migratory cues by a particular cell to screening drug candidates for their ability to rescue disease-associated defects in neural organization.

2.4.5 Recognitions

The authors are grateful for support from NIH Director's New Innovator Awards (1DP2 OD006499-01 to A.A. and 1DP2 OD006460-01 to A.J.E.), and King Abdulaziz City for Science and Technology (UC San Diego Center of Excellence in Nanomedicine). We would like to thank Ms. Jessica Moore for her critical comments and Dr. Allan Acab for technical support on the manuscript.

2.5 Conclusions

In conclusion, we introduce a novel cell culture compatible multilayer single step polymerization technique that separates phases by solvent density. This method is accessible, versatile, and facilitates control of discrete, as well as continuously graduated, mechanical and chemical interfaces within structurally uninterrupted hydrogel networks. Although we demonstrate this technique in photopolymerized model hydrogel scaffolds, this simple method can be applied to any polymer system. We apply a sucrose DGMP method to spatially control mechanics, encapsulated proteins, and covalently bound small molecules within hydrogel matrices. We use iodixanol DGMP to pattern bioactive peptides and cells on 2D tissue culture substrates. DGMP could be combined with a multitude of current fabrication paradigms to increase the complexity of matrices for tissue engineering, controlled drug delivery, or biological investigation.

Using DGMP, we presented a gradient fabrication system that is tunable for adhesive ligand type, gradient range, gradient steepness, as well as substrate stiffness. Applying DGMP to a substrate-mediated model of wound healing, we demonstrate significant differences in the ability of disease relevant fibroblasts and mesenchymal stem cells to undergo haptotaxis. Our results indicate that haptotaxis mechanisms are dependent on cell-induced tractions, which are largely regulated by substrate adhesiveness, and are cell-type specific. We report that fibroblasts haptotax at faster absolute migration velocities compared to MSCs, and that fibroblasts display a significant inverse relationship between surface ligand density and absolute velocity, similar to classic experiments using non-gradient substrates (Lauffenburger & Linderman, 1996), while MSCs do not.

Accurately modeling diseases using human cells requires 3D *in vitro* culture systems that mimic the degree and nature of variation found *in vivo*: both structural and biochemical, allowing cells to integrate multiple signals from various directions. Not only could such systems be used to generate functional models of laminar tissues, but they could also facilitate otherwise problematic investigations of migration, polarization, differentiation, and intercellular communication, among other phenomena, in a more *in vivo*-like setting. Unfortunately, such variation in 3D hydrogel matrices has, until now, been difficult to generate; previous methods to create multilayer or gradient hydrogels involved complex instrumentation that required technical skill and interpretation. Our long term goal within the field of brain disease modeling is to study several rare genetic neural disorders for which animal models fail to recapitulate human pathology. The broader impact of this work potentially spans other areas of developmental biology, regenerative medicine and disease modeling for many types of *in vitro* human tissues.

2.6 Acknowledgements

Parts of Chapter 2 sections 1, 2, 4, and 5, were adapted for a US Patent Application and published as “Single step polymerization of covalently bound multilayer matrices.” Karpiak JV**,** Ner Y, Morachis J, Almutairi A. US Patent Application US 20130234372 A1, published 2013. The dissertation author was the primary investigator and author of this patent.

The contents of Chapter 2.2 were adapted for the journal Advanced Materials and published as “Density Gradient Multilayer Polymerization for Creating Complex Tissue.” Karpiak JV**,** Ner Y, Almutairi A. Advanced Materials, 2012, 24:1466-1470. The dissertation author was the primary investigator and author of this work.

Parts of Chapter 2 sections 2 and 4 were adapted for Journal of Visualized Experiments and published as “DGMP: A novel technique for creating multi-compartment, customizable scaffolds for tissue engineering.” Joshi-Barr S, Karpiak JV, Ner Y, Wen JH, Engler AJ, Almutairi A. Journal of Vis Exp, 2013, (72). The dissertation author was the primary investigator and author of this work.

The contents of Chapter 2.3 were adapted for the journal Cellular and Molecular Bioengineering and published as “Haptotaxis is cell type specific and limited by substrate adhesiveness.” Wen JH, Choi O, Taylor-Weiner H, Fuhrmann A, Karpiak JV, Almutairi A, Engler AJ. Cell Mol Bioeng, 2015, 8(4):530-542. The dissertation author was a main contributor and co-author of this work.

Chapter 3

Stem cell models of neural development to study human monogenetic brain disorders

3.1 Abstract

Advances in stem cell technology will help identify molecular and cellular characteristics of brain disease. In addition to the interesting scientific results, this chapter is intended to serve as a reference for stem cell based approaches to building neural complexity into *in vitro* brain development and disease models. Several tools are described and established with broad applicability in a range of investigations. I present methods to specifically study genetic and cellular contributions to neural development in the context of Cockayne Syndrome (CS) and Rett Syndrome (RTT), two devastating monogenetic brain disorders.

In the first study I highlight our routine neural development model combined with emergent microelectrode array (MEA) technology to investigate neural network behavior in CS. CS is a rare monogenetic disorder in which 80% of cases are caused by mutations in the Excision Repair Cross-Complementation group 6 gene (*ERCC6*). The encoded ERCC6 protein is more commonly referred to as Cockayne Syndrome B protein (CSB). Classical symptoms of CS patients include failure to thrive and a severe neuropathology characterized by microcephaly, hypomyelination, calcification and neuronal loss. Modeling the neurological aspect of this disease has proven difficult since murine models fail to mirror classical neurological symptoms (Brace et al., 2013; Van der Horst et al., 1997). Therefore, a robust human *in vitro* cellular model would advance our fundamental understanding of the disease and reveal potential therapeutic targets. Herein, we successfully derived functional CS neural networks from human CS induced pluripotent stem cells (iPSCs) providing a new tool to facilitate studying this devastating disease. We identified dysregulation of the Growth Hormone/Insulin-like Growth Factor-1 (GH/IGF-1) pathway as well as pathways related to synapse

formation, maintenance and neuronal differentiation in CSB neurons using unbiased RNA-seq gene expression analyses. Moreover, when compared to unaffected controls, CSB-deficient neural networks displayed altered electrophysiological activity, including decreased synchrony, and reduced synapse density. Collectively, our work reveals that CSB is required for normal neuronal function and we have established an alternative to previously available models to further study neural-specific aspects of CS.

The aim of the second study was to introduce additional complexity into our previously described neural development model of RTT to specifically examine the effects of MeCP2-deficient astroglia on neuronal networking. RTT is a primarily monogenetic neurological disorder caused by mutations in the X-linked methyl-CpG-binding protein-2 (MeCP2) gene (Amir et al., 1999) with a spectrum of human pathology. Previously, our group reported differences in RTT cellular phenotype compared to unaffected paternal controls, including reduced soma size, decreased number of excitatory spines, and decreased frequency of spontaneous of post-synaptic currents further supported by altered activity-dependent calcium transiens *in vitro* for an induced pluripotent stem cell (iPSC) model of neural development derived from female donors (Marchetto et al., 2010). Several of the reported phenotypes were observed in subsequent independent studies (Ananiev et al., 2011; Cheung et al., 2011; K. Y. Kim, Hysolli, & Park, 2011), including the potential for functional recovery with IGF1 treatment in a murine RTT model (Castro et al., 2014) which has lead to an ongoing clinical trials (Khwaja et al., 2014; Pini et al., 2012). For this study, isogenic *MECP2* stem cell lines were developed using CRISPR/Cas9 genetic editing tools, first introducing a mutation in a human embryonic stem cell line and next reversing a mutation in a RTT donor iPSC line. Next, I present a simple method for generating

astroglial cells from our NPC lines. A neuronal enrichment step was added to our routine neural differentiation protocol using magnetic activated cell sorting (MACS). I describe neuron and astroglial monolayer co-cultures on MEA substrates established to probe the role of astroglia in the development, maturation and maintenance of functional *in vitro* neuronal networks. I then describe synapse density analysis using an immunocytochemistry assay developed to geometrically determine co-localized signature pre- and post-synaptic proteins using Imaris, a sophisticated 3D rendering software. Finally, I present a monolayer neural co-culture model using induced *MECP2* isogenic cell lines, carried out in preparation of more complex 3D studies described in Chapter 4 of this dissertation. I report non-autonomous neuronal network deficits caused by MeCP2-defficient astroglia. Specifically, we observed reduced synapse density, diminished neuronal activity and an absence of synchronized network activity in genetically normal neurons co-cultured with MeCP2-deficient astroglia compaired to synchronously active control co-cultures.

3.2 Monolayer iPSC derived neural cultures reveal neurophysiological phenotypes in Cockayne Syndrome (*ERCC6*)

3.2.1 Brief introduction and rationale

Cockayne Syndrome (CS) was initially characterized by sunken eyes and a bird-like face, impaired hearing, retinal atrophy, erythematous dermatitis in sun-exposed skin, growth failure and mental retardation (Cockayne, 1936). Subsequent reports evinced a severe and multifaceted neuropathology involving not only developmental deficiencies of the central nervous system (CNS), but also neuronal loss, calcification, spasticity, tremors, vasculopathy and hypomyelination (Brooks, 2013; Koob et al., 2010; Weidenheim et al., 2009). Clinical indicators appear during the first years of life in classic manifestations of CS (Natale, 2011). Approximately 80% of CS cases are caused by mutations in the Excision Repair Cross-Complementation group 6 gene (*ERCC6*) which encodes the Cockayne Syndrome B protein (CSB). CSB is a key component of the transcription-coupled nucleotide excision repair pathway (Hanawalt & Spivak, 2008; Venema et al., 1990), acts as a component of RNA polymerase I (Bradsher et al., 2002), enhances elongation of RNA polymerase II (Selby & Sancar, 1997), prevents accumulation of oxidative damage in both mitochondrial (Kamenisch et al., 2010) and nuclear DNA (Pascucci et al., 2012), and promotes autophagy-mediated quality control of mitochondria (Scheibye-Knudsen et al., 2012). More recently, a CSB defect was associated with an imbalance in POLG1/POLG2 subunits of mitochondrial polymerase gamma (Chatre et al., 2015).

In this work, we sought to generate a new *in vitro* model to study live human neurons derived from individuals with classical neurological manifestations of CS. We reprogrammed fibroblasts from two individuals with CS to generate induced pluripotent

stem cell (iPSC) lines. We differentiated these cell lines into expandable neural precursor cells (NPCs) and further into neurons. We employed unbiased next generation sequencing to analyze RNA transcription in neurons derived from CS and unaffected control iPSC lines. Comparative gene expression analysis revealed dysregulation of several cellular pathways related to synapse formation and maintenance including the Growth Hormone/Insulin-like Growth Factor-1 (GH/IGF-1) signaling pathway, previously implicated in synaptogenesis (Marchetto et al., 2010; Shcheglovitov et al., 2013). Accordingly, we report that CSB neurons displayed reduced neuronal activity, altered network synchrony and reduced synapse density when compared to neurons derived from unaffected individuals. Our data suggest that CSB plays a previously unappreciated role in the homeostasis and function of human neurons.

3.2.2 Materials and methods

3.2.2.1 Cell culture

Skin-derived human fibroblasts GM00969, GM00739 and GM10903 were purchased from CORIELL Cell Repositories. The fibroblasts 5461 and W83 belong to Dr. Alysson Muotri's laboratory cell repository and were obtained from skin biopsies of a teenage female and a 38-year-old male, respectively, both of whom are Caucasian non-affected donors. Clinical features of the donors and genetic mutations are shown in Table 3-1. Fibroblasts were routinely grown in DMEM (Cell Gro, Corning, NY, USA) supplemented with 10% fetal bovine serum (FBS, Gibco, Life Technologies, Carlsbad, CA, USA). iPSCs were grown on Matrigel-coated plates (BD Biosciences, San Jose, CA, USA) in mTeSR1 (Stemcell Technologies, Vancouver, BC, Canada). NPCs were

grown on poly-l-ornithine (PO, 10 µg/ml) and laminin (2.5 µg/ml)-coated plates, in the presence of DMEM/F12 1:1 with L-glutamine (Cell Gro) supplemented with 0.5 X N2 Neuroplex (Gemini, West Sacramento, CA, USA), 0.5 X Gem21 Neuroplex (Gemini), 1% penicillin/streptomycin (Life Technologies) and 20 ng/ml of bFGF2 (Life Technologies). Neurons were differentiated and maintained under the same conditions as NPCs, except in the absence of bFGF2. All cells were maintained at 37^{o}C in a humidified atmosphere of 5% CO_2. iPSCs were passaged every 8-10 days under an EVOS microscope (AMG, Life Technologies) by mechanically detaching fragments of colonies with the aid of a P1000 tip. NPCs were enzymatically dissociated with Accutase (Sigma-Aldrich, St. Louis, MO, USA), and resulting single cell suspensions were sub-cultured. This work was approved by the UCSD human research protection program committee meeting under the IRB/ESCRO protocol #141223ZF.

Table 3-1 Description of cells (and their respective donors) used in this study.

Fibroblast	**GM00969**	**5461**	**W83**	**GM00739**	**GM10903**
Cell Code in this manuscript	Control-1	Control-2	Control-3	CSB-1	CSB-2
Gender	Female	Female	Male	Female	Female
Age (years)	2	Teenage	38	3	9
Race	Caucasian	Caucasian	Caucasian	Caucasian	Hispanic/Latin
***ERCC6* mutation(s)**	-	-	-	One allele has a A>T transversion at nucleotide 1088; Second allele has a C>T transition at nucleotide 2648	Homozygous for a C>T transition at nucleotide 2282
Clinical features				Typical appearance of CS at 2 years of age; Punctate cataracts; Diffuse retinitis pigmentosa; Contracture of joints; Growth failure; Generalized progressive wasting. (Schmickel et al, 1977)	Development ceased at 3 years of age; Lost ability to walk and most of speech; Increased muscle tone; Leukodistrophy; Ataxic and scissoring gait (when supported) Olivopontocerebellar atrophy. (Greenhaw et al, 1991)
Source	CORIELL	Muotri	Muotri	CORIELL	CORIELL

3.2.2.2 Cell reprogramming

Fibroblasts were reprogrammed by Sendai virus vector-mediated expression of Oct4, Sox2, Klf-4 and c-myc (CytoTune®-iPS Kit, Life Technologies) according to manufacturer's protocol, with minor modifications. Briefly, 2 x 10^5 cells were seeded on 35 mm tissue culture plates (Corning). The next day, medium was replaced by DMEM supplemented with 5% FBS containing 1/5 of the stock mix viral vectors mix. The next day vectors were removed and replaced with fresh medium. The next day, cells were moved to a feeder layer (MEFs, Globalstem, Miami Lakes, FL, USA). Medium was changed daily (DMEM/F12 1:1 with L-glutamine (Cell Gro) supplemented with 20% knockout serum replacement, 1% non-essential amino acids, 0.2% β-mercaptoethanol and 30 ng/ml bFGF2 (Life Technologies). During the first 5 days, medium was further supplemented with 100 µM of valproic acid (Sigma-Aldrich). Two clonally derived iPSC colonies for each cell type were isolated and re-plated on Matrigel-coated plates (feeder-free) approximately four weeks after initial viral transduction.

3.2.2.3 Neuronal differentiation

Neuronal differentiation was performed in two stages: NPC generation and neural differentiation. Briefly, iPSC colonies were cultured for two days in the presence of DMEM/F12 1:1 containing 1 X N2 (Life Technologies), 1 µM dorsomorphin (Tocris Biosciences, Bristol, UK) and 10 µM SB431542. Then, colonies were detached with the aid of a cell lifter and in the presence of 5 µM Y-27632 (ROCK inhibitor, R&D Systems, Minneapolis, MN, USA), and maintained in suspension at 90 RPM for five days in an incubator (medium was exchanged every other day) in order to form embryoid bodies (EBs). EBs were gently mechanically disrupted, plated on Matrigel-coated plates and

cultured in NPC medium for five days. Then rosettes were manually collected under an EVOs microscope inside a biological laminar flow cabinet, dissociated with Accutase, and resulting NPCs were re-plated on poly-L-ornithine/laminin-coated plates. At this stage, NPCs could be expanded and cryopreserved in NPC medium with 10% DMSO. For neural differentiation, NPCs were grown to approximately 80% confluence before bFGF2 withdrawal. ROCK inhibitor was added at 5 µM for the first two days. After that, cells were allowed to differentiate for five weeks, and the medium exchanged twice per week.

3.2.2.4 RNA isolation, microarray, RNA-seq and PCR analysis

For microarray analysis, 1 µg of total RNA (Trizol, Life Technologies) was biotinylated (Affymetrix, Santa Clara, CA), fragmented and hybridized to the GeneChip Human 1.0 ST microarray at University of California DNA Core Facility (Biogen). Arrays were analyzed by the R-based bioconductor software package Affy (Affymetrix pre-processing (Gautier et al., 2004)). After data normalization by the robust multichip averaging method, samples were clustered based on Euclidean distance between the transcripts over a pair of samples representing a variation between two samples. The dendrogram and heatmap were created using sample expression similarities.

For RNA sequencing sample preparation, NPCs were transduced with a lentivirus expressing eGFP under the control of the Synapsin I gene promoter (Marchetto et al., 2010). After five weeks of neuronal differentiation, total RNA of neurons (BD Influx FAC sorted eGFP-positive cells, BD Biosciences) was obtained using Trizol. cDNA was then synthesized and subjected to multiplexed RNA-seq on an Illumina HiSeq 2000 at UCSD/Biogen sequencing facility and stored at NCBI BioProject

(# PRJNA297108). Poly-A transcript sequencing produced more than forty million 150 bp paired-end reads per sample. Filtered high-quality reads (NGS QC Toolkit (Patel & Jain, 2012)) were mapped to human reference genome Hg19 (Star software (Dobin et al., 2013)). In-house scripts were used to obtain the absolute number of aligned reads per transcript (Ensembl Hg19 transcriptome annotation as reference). Count data was normalized using a model based on negative binomial distribution for differential expression (DE) analysis (DESeq (Benjamini & Hochberg, 1995)) (DE transcripts defined as p-value<0.05). Count data were also used to calculate Euclidian distance between each pair of samples, including biological replicates, which were clustered based on shorter distances. Additionally, count data was used to create a heatmap and a two component based Principal Component Analysis (PCA) to show relative relationships between each sample in a 2D coordinate space.

For PCR reactions, cDNA (SuperScript III) was amplified using Accuprime Taq DNA polymerase (Life Technologies). SYBR Green was used to perform quantitative PCR (qPCR) in a 7500 Real Time PCR (Life Technologies), and relative expression levels were calculated according to the $2^{-\Delta\Delta Ct}$ method (Schmittgen & Livak, 2008). Primers used are listed in Table 3-2.

Table 3-2 PCR primers used in this study.

Primer Name	5' - 3' Sequence
Oct4 For	GGGAGGGGAGGAGCTAGG
Oct4 Rev	TCCAACCAGTTGCCCCAAAC
NANOG For	CCTATGCCTGTGATTTGTGG
NANOG Rev	CTGGGACCTTGTCTTCCTTT
AFP For	AAAAGCCCACTCCAGCATC
AFP Rev	CAGACAATCCAGCACATCTC
MSX1 For	AGGACCCCGTGGATGCAGAG
MSX1 Rev	GGCCATCTTCAGCTTCTCCAG
PAX6 For	CCCATTATCCAGATGTGTTTGC
PAX6 Rev	TGGTGAAGCTGGGCATAGGC
IGF1 For	CTAAGGAGGCTGGAGATGTATTG
IGF1 Rev	GGCTGATACTTCTGGGTCTTG
STAT5A For	GACCTTCTTGTTGCGCTTTAG
STAT5A Rev	GTGGTGAATGGTTTCAGGTTC
GAPDH For	ACCCACTCCTCCACCTTTGA
GAPDH Rev	CTGTTGCTGTAGCCAAATTCGT
MAP2 For	GAGAATGGGATCAACGGAGAG
MAP2 Rev	TTCACCTTTCAGGACTGCTAC
NeuN For	GGCAAATGTTCGGGCAATTC
NeuN Rev	GATCGTCCCATTCAGCTTCTC
ZIC4 For	ACAAGACATCCTTGGTGATGAG
ZIC4 Rev	CAGAGCTGCTACTTGACTCTTT
CBLN3 For	GTGTCTACAGCTTCCGGTTC
CBLN3 Rev	GGTCACGTCAGGATCATTGG
TGFBR2 For	GCTGTAATGCAGTGGGAGAA
TGFBR2 Rev	CTCTCAACACGTTGTCCTTCA
SYNJ1 For	ATACAGTACAGCCAGACCGA
SYNJ1 Rev	CTTTGGCTTTCAGGAGTCAGT
PCLO For	CCTCAGCATGGCAGCTTAATG
PCLO Rev	GAGAACAGGGTGAGCAGAGG

3.2.2.5 Immunofluorescence and synapse density analysis

Cells plated on glass coverslips pre-coated with Matrigel (iPSCs) or 100 µg/ml of pOrn and 10 µg/ml of laminin (NPCs/neurons) were fixed with 4% paraformaldehyde for 10 min at room temperature. After permeabilization (0.1% TritonX in PBS) and blocking (2% BSA on PBS), cells were incubated with primary antibodies (see list below), followed by Alexa Fluor-conjugated secondary antibodies (Life Technologies). Cell nuclei were treated with DAPI, and imaging was performed on a Zeiss Apotome

epifluorescent microscope (Carl Zeiss, Oberkochen, Germany). Primary antibodies used were: Oct4 (ab19857), Lin28 (ab46020), Musashi (EP1302), Map2 (ab5392, Abcam); Sox2 (2748S, Cell Signalling): GFAP (Z0344, DAKO); SSEA4 (MAB4304), NeuN (MAB377), Synapsin I (AB1543p, Millipore); PSD-95 (75-028, Neuromab); Nestin (MA1-46100, Thermo Scientific); Tuj-1 (01409, StemCell). For synapse density analysis, 1.25 x 10^5 NPCs were plated on 12 mm cover glass, and after two days neuronal differentiation was started. After five weeks of differentiation, cells were fixed, stained for Synapsin I, PSD-95, and MAP2 and imaged on the Zeiss Apotome with a 100 X oil-immersion objective in the Apotome Z-stack mode (nine slices with 0.56 µm interval). The number of synapses (Synapsin I co-localizing to PSD-95) over 50 µm of neuron filament (MAP2) was evaluated. Synapses were scored when they were within 5 µm from the MAP2 filament center, in agreement with previous work (Benavides-Piccione et al., 2002).

3.2.2.6 Microelectrode array (MEA) analysis

Neuronal activity was recorded using a multi-well MEA system (Maestro, Axion BioSystems, Atlanta, GA, USA). Briefly, 5 x 10^4 NPCs (re-suspended in a 5 µl droplet of NPC medium) were plated on top of 16-electrode array substrates inside 48-well pre-coated plates. The day after, neuronal differentiation was initiated. In the second week of differentiation, neuronal medium was switched to Neurobasal medium supplemented with 1 X B-27 and 2 mM Glutamax (Life Technologies). Neuronal activity was continuously recorded for three minutes, 24 h after medium exchange during the fifth week of differentiation, and action potentials (measured as field potential changes) were recorded and analyzed using Axis 2.0 software (Axion Biosystems). The

parameters used for data acquisition and processing were: Neuronal Broad Band filter frequency = 10-5000 Hz; referencing method = Fpga Median. Spike detection was performed by adaptive threshold crossing at 5.5 X Std Dev above or below noise, and Poisson surprise algorithm (surprise factor = 3) was used to detect bursts. Temporal raster plots were generated in the MATLAB based Neural Metric Tool software (Axion BioSystems).

3.2.3 Results

3.2.3.1 CSB iPSC characterization

We previously reported successful reprograming of CSB-mutated GM10903 fibroblasts (NIGMS Human Genetic Cell Repository) into iPSCs using retrovirus vectors (Andrade et al., 2012). Here, by using non-integrative Sendai virus vectors (Life Technologies), we reprogrammed fibroblasts derived from the individuals GM00969 (Control-1), 5461 (Control-2), GM00739 (CSB-1) and GM10903 (CSB-2) into iPSCs. Immunofluorescence analysis showed that all iPSC clones described in this manuscript express Oct4, SSEA4 and Lin28 markers (representative images of Control-1 iPSCs are shown in Figure 3-1A). Expression of OCT4 and SOX2 genes was also detected by PCR in control and CSB iPSCs, (Figure 3-1B, human embryonic stem cell line (ESC) H1 (WiCell) and GM00739 primary human fibroblasts were used as a positive and negative control, respectively). Upon differentiation of iPSCs into embryoid bodies (EBs) in suspension culture with 10% FBS, we detected expression of the endo-, meso- and ectodermal markers AFP, MSX1 and PAX6, respectively, confirming the pluripotent potential of these cells (Figure 3-1C). Cell karyotyping was performed in all iPSC clones, and no detectable gross chromosomal abnormalities were observed

(Figure 3-1D). Transcriptional profiles of the new iPSC lines were evaluated through microarray, and compared to controls. All iPSC clones showed a gene expression pattern similar to ESCs and distinct from skin fibroblasts (Figure 3-1E, ESC lines H1 and Hues6 (Harvard HUES Cell Facility) and primary human fibroblasts were used as positive and negative controls, respectively). The analyses of pluripotency-related genes showed a strong association between the iPSCs and ESCs, in comparison to fibroblasts (Figure 3-1F), confirming successful reprogramming.

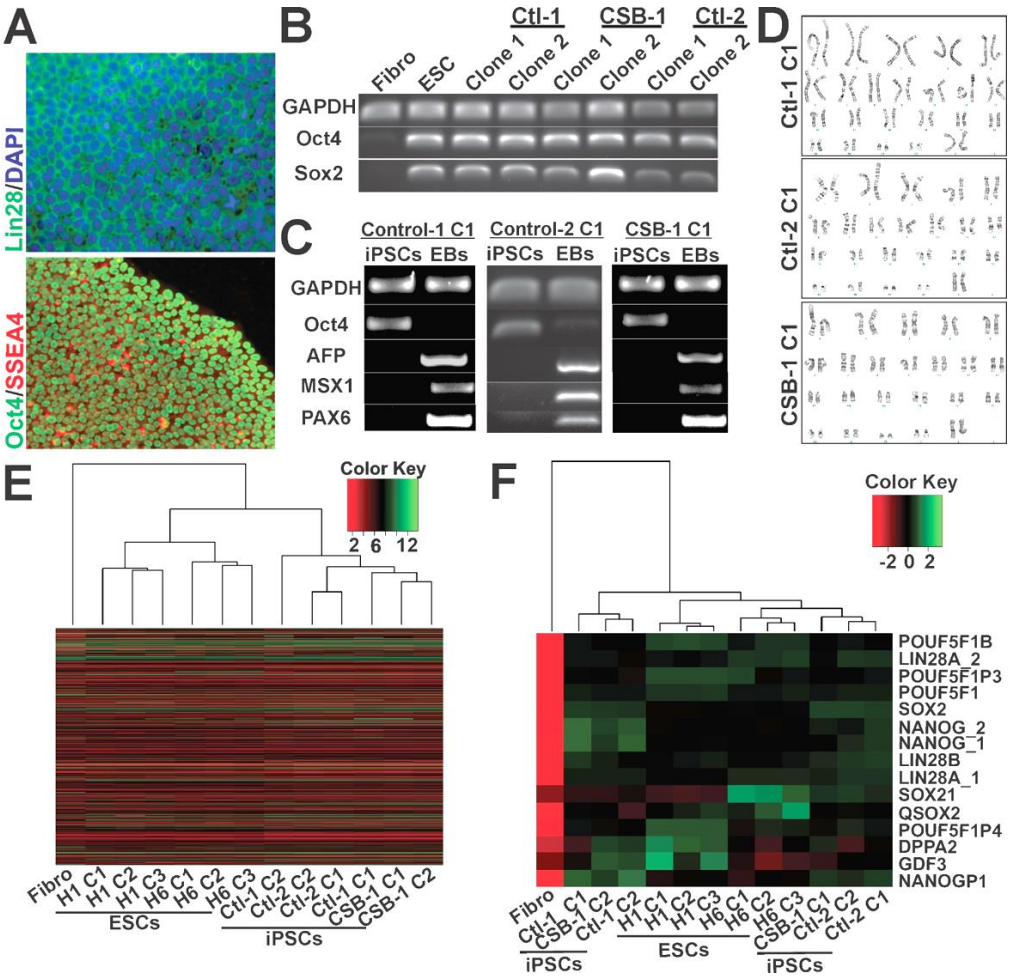


Figure 3-1 Generation and characterization of CSB iPSCs.

A) Immunofluorescence analysis of Oct4, SSEA4 and Lin28 expression in iPSCs (representative images of clone 1 of Control-1 derived cells). B) Expression of *OCT4*, *SOX2* and *GAPDH* in fibroblasts (Fibro), H1 embryonic stem cells (ESCs) and two clones of Control-1, Control-2 and CSB-1 derived iPSCs, as measured by RT-PCR. (Ctl: Control). C) Expression of *OCT4*, *AFP*, *MSX1*, *PAX6* and *GAPDH* in iPSCs and in the iPSC derived EBs of control and CSB cells. D) Karyotype of clone 1 of each indicated iPSC line. Correlation distances (microarray) between fibroblasts, ES cells and iPSC samples, based on global gene expression profile (E) or on pluripotency-associated genes (F).

3.2.3.2 Transcriptional dysregulation of GH/IGF-1 pathway in CSB neurons

Next, we aimed to differentiate CSB and control iPSCs into neural cultures as previously described (Griesi-Oliveira et al., 2015; Marchetto et al., 2010). Briefly, we

initially differentiated iPSCs into EBs in suspension cultures followed by dual SMAD inhibition (Chambers et al., 2009). Next, adhered EBs gave rise to neural rosettes which were then dissociated to generate NPCs (Figure 3-2A and methods section below). All iPSC clones used in this study generated NPCs expressing Sox2, Musashi and Nestin (representative images of Control-1 NPCs are shown in Figure 3-2B & C). NPCs were further differentiated into neural cells by ongoing culture in the absence of bFGF2 for five weeks. Control and CSB neural cultures gave rise to neurons and astrocytes as

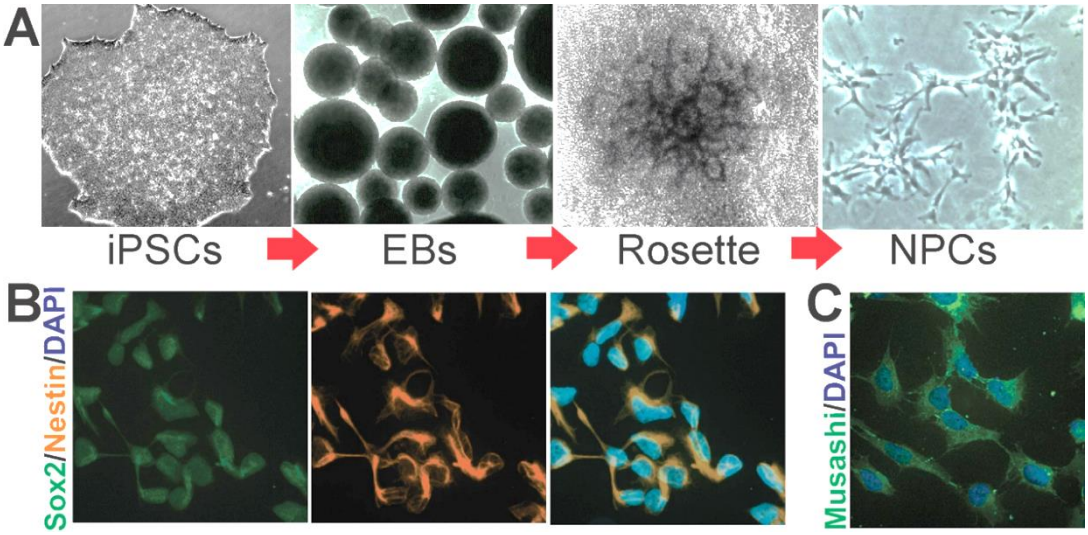


Figure 3-2 Generation of CSB-NPCs derived from iPSCs.

A) Differentiation steps of iPSCs into NPCs, as visualized under a light microscope. B & C) Representative images of Sox2, Nestin and Musashi expression in NPCs, as visualized under a fluorescence microscope.

evidenced by MAP2/TUJ1 and GFAP staining, respectively (representative images for Control-1 and CSB-1 neural cultures are shown in Figure 3-3A). PCR analysis confirmed expression of *MAP2* and *NEUN* (a marker for late stage neuronal maturation (Sarnat, Nochlin, & Born, 1998)) for control and CSB neural cultures, in contrast to fibroblasts (Figure 3-3B). By immunofluorescence, we report the percentage of NeuN-

positive nuclei (co-localized with DAPI) was similar between control and CSB neural populations, except for CSB-2 C1, for which the values were lower (Figure 3-3C).

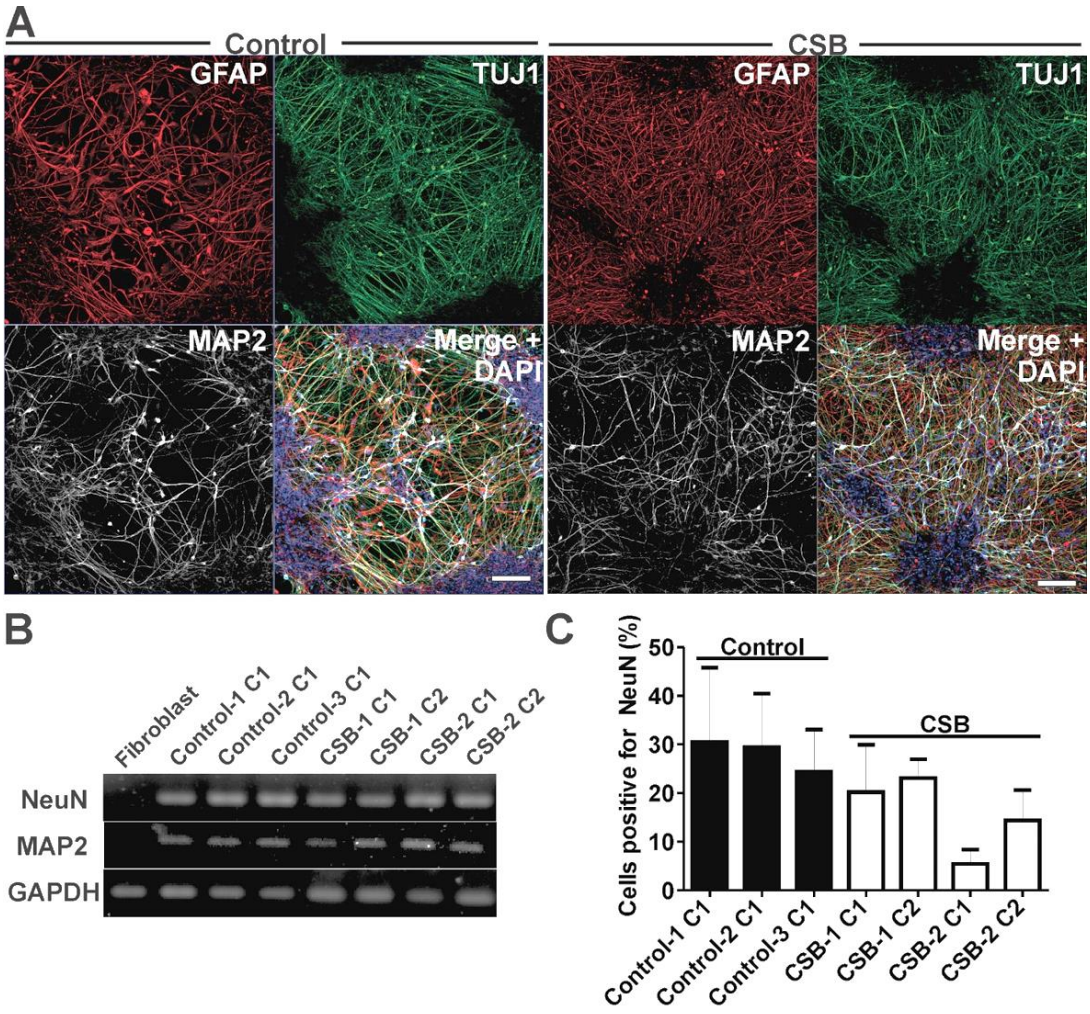


Figure 3-3 Characterization of CSB neurons.

A) Representative images of clone 1 of both Control-1 and CSB-1 derived neurons, respectively, showing expression of TUJ1, Map2 and GFAP. Bars: 100 µM. B) Expression of *MAP2, NEUN* and *GAPDH* in fibroblasts, clone 1 of Control-1, Control-2 & Control-3, and clones 1 and 2 of CSB-1 and CSB-2 neural cell cultures. C) Percentage of NeuN positive nuclei (DAPI) as shown by immunofluorescence in 5-week old neural cultures (at least 1000 nuclei were analyzed in two independent experiments for each clone).

Since CSB plays an important role in mRNA and rRNA synthesis (Bradsher et al., 2002; Selby & Sancar, 1997; Venema et al., 1990), we investigated unbiased gene

expression in neurons derived from the CSB-1 donor iPSC line using RNA-seq. RNA was obtained from FACS separated cells expressing eGFP (Figure 3-4; Figure 3-7A & B) under the control of the neuron-specific *SYN1* promoter (Marchetto et al., 2010). We

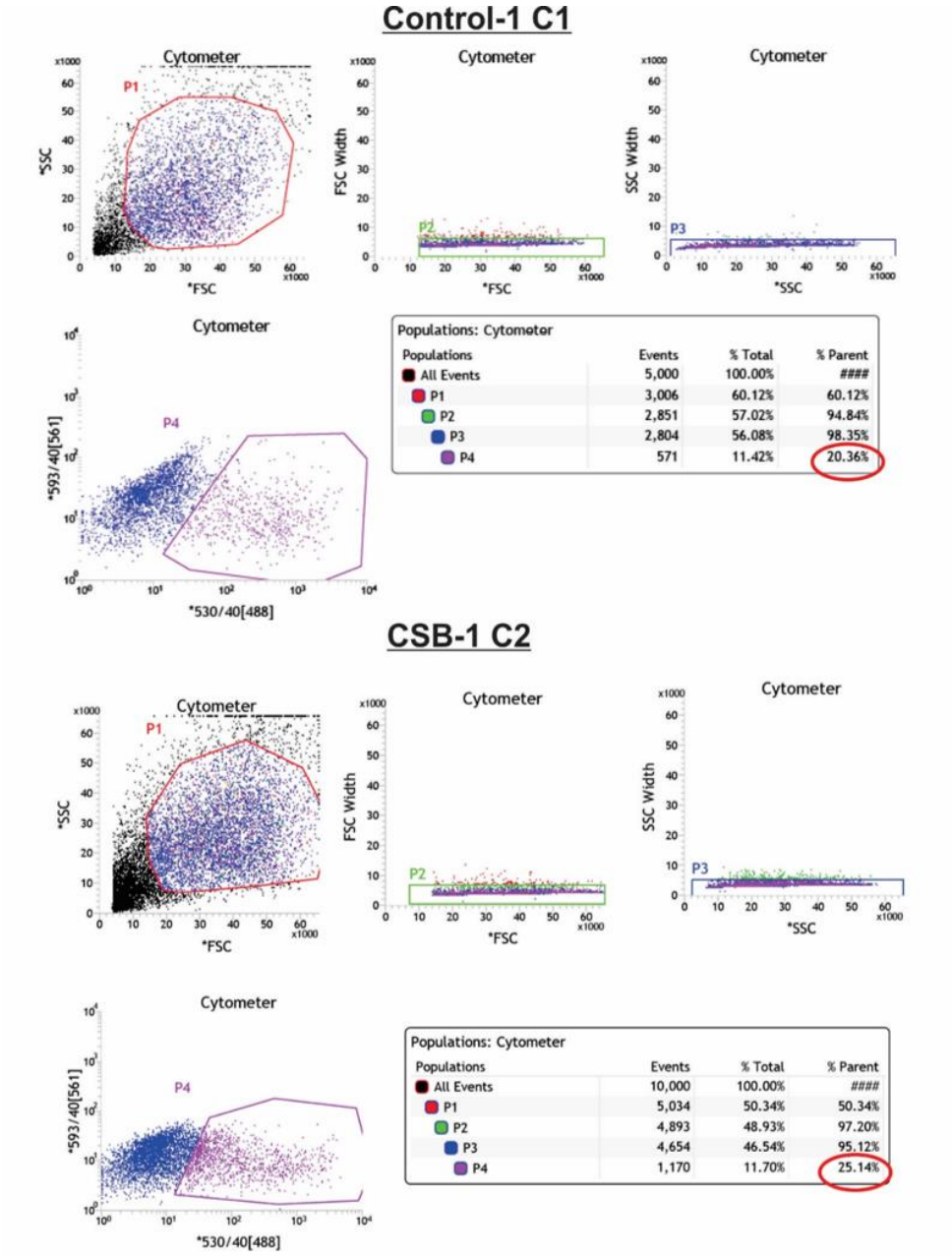


Figure 3-4 FAC sorting for Control-1 C1 and CSB-1 C2.

Percentage of *SYN1*::eGFP positive cells (red circle) in the population.

compared gene expression of the CSB-1 neurons with Control-1 and Control-2 neurons (two clones for each cell line) and identified 4,930 differentially expressed transcripts in the CSB neurons, in which 1,924 were upregulated, and 3,006 were downregulated (p-value<0.05, table of differentially expressed transcripts is published at: http://hmg.oxfordjournals.org/content/early/2016/01/26/hmg.ddw008/suppl/DC1). Protein coding transcripts represent 1,123 and 1,914, respectively. This observation is striking considering that the level of gene dysregulation in CSB neural cultures is greater than three times higher than previous observed for CSB skin fibroblasts (Newman, Bailey, & Weiner, 2006; Y. Wang et al., 2014). It is likely that the use of relevant neural cell types, from a characteristically severely affected tissue in CS, contributed to these differences. Correlation dendrograms and a PCA map are presented in Figure 3-5.

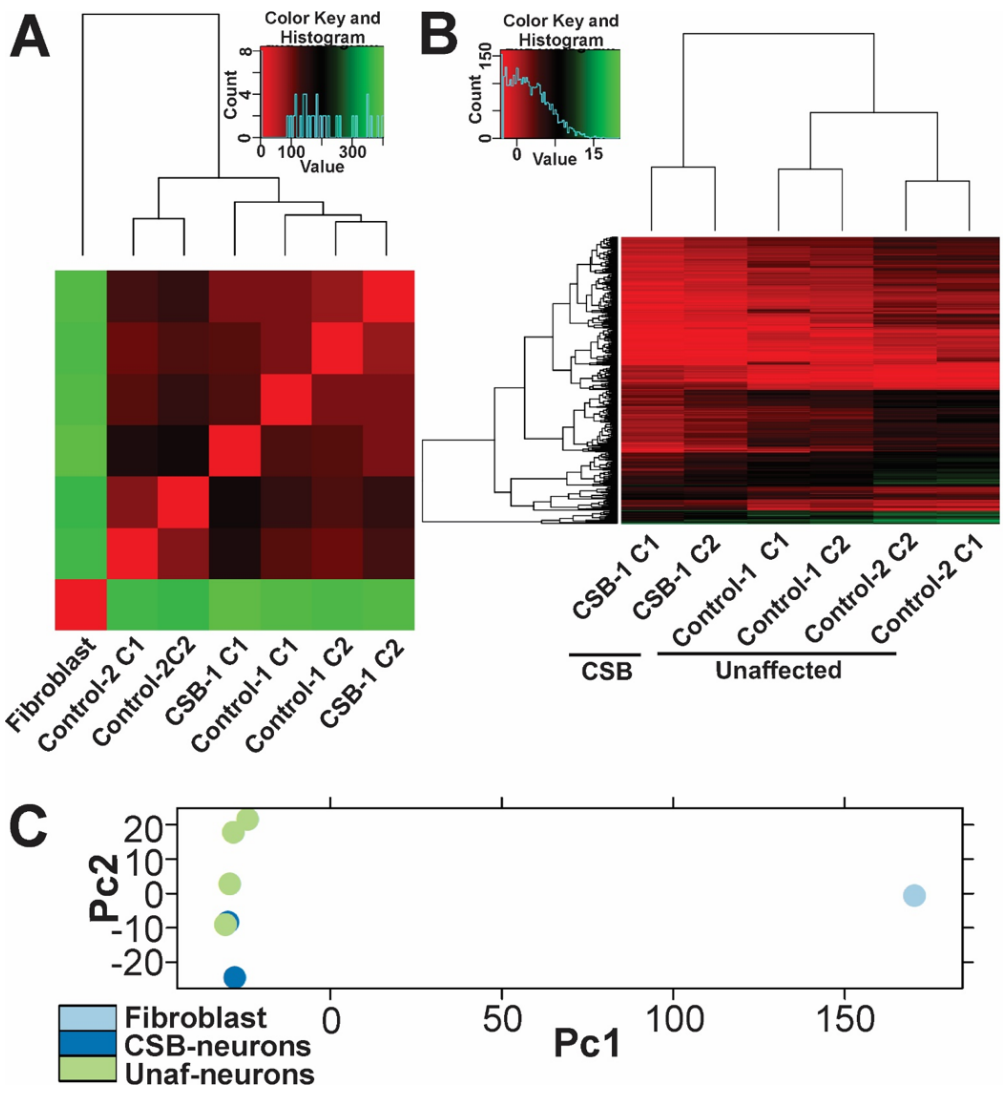


Figure 3-5 Sample correlation via dendrogram and PCA map.

A) Hierarchical clustering (dendrogram) and heatmap to show sample-level correlation between fibroblasts and iPSC-derived neurons based on normalized gene expression of sequenced RNA-seq samples. B) Hierarchical clustering and heatmap showing sample and gene expression correlation between iPSC-derived neurons of unaffected and CSB samples. C) PCA (Principal Component Analysis) showing relative gene expression relationship between iPSC-derived neurons and a fibroblast sample in a 2D coordinate space (components Pc1 and Pc2).

RNA-seq validation by quantitative RT-PCR of selected genes is shown in Figure 3-6. Next, using the Ingenuity Pathway Analysis software, we report that

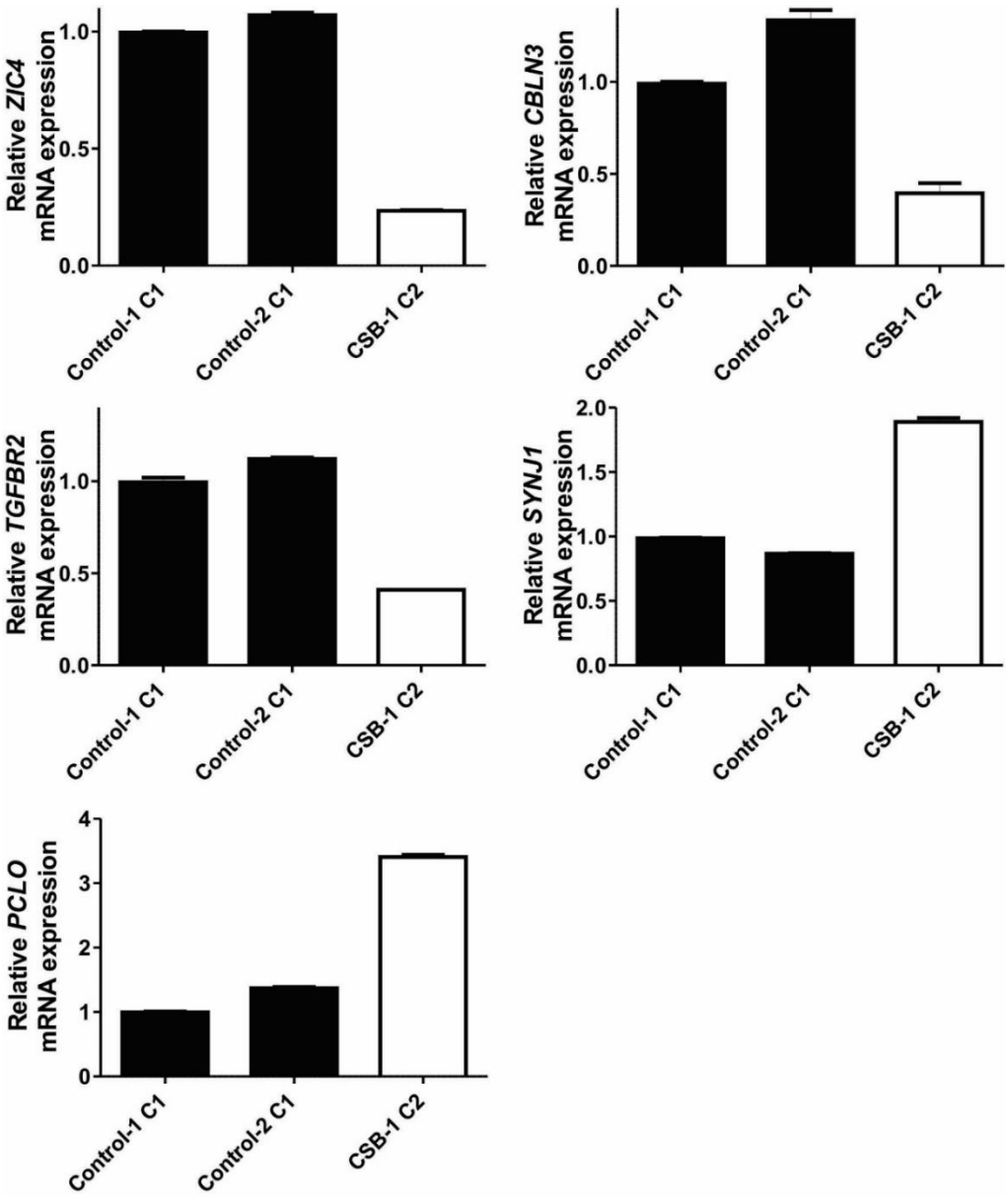


Figure 3-6 RNA-seq validation via PCR.

Relative gene expression of *ZIC4*, *CBLN3*, *TGFBR2*, *SYNJ1* and *PCLO* via qPCR in Control-1 C1, Control-2 C1 and CSB-1 C2 iPSC derived neurons.

"*Nervous System Development and Function*" is the most representative category within "*Physiological System Development and Function*" (Figure 3-7C). Within this category, we found several dysregulated pathways related to neuronal function, such

as morphology of the nervous system (p-Value = $4.85x10^{-36}$), axonogenesis (p-Value = $5.73x10^{-15}$), action potential of neurons (p-Value = $1.97x10^{-7}$), long term potentiation (p-Value = $3.7x10^{-15}$) and neurotransmission (p-Value = $1.75x10^{-17}$), (Table 3-3 lists thirty of these altered pathways). From the top-altered canonical pathways, the "Axonal

Table 3-3 Significantly altered Ingenuity® pathways.

Diseases or Functions Annotation	p-Value	Activation z-score (WT/CS)	# Molecules
morphology of nervous system	4.85E-36	-1.442	394
neuritogenesis	6.52E-29	1.457	252
morphology of neurons	1.11E-27	-0.896	225
abnormal morphology of central nervous system	3.27E-22	-0.973	232
abnormal morphology of brain	1.06E-19	-0.973	212
neurotransmission	1.75E-17	-2.267	197
morphogenesis of neurons	2.87E-17	1.091	172
proliferation of neuronal cells	6.16E-17	0.757	261
long-term potentiation	3.70E-15	-2.423	125
axonogenesis	5.73E-15	2.232	97
synaptic transmission	5.83E-15	-2.540	160
coordination	1.94E-14	-2.834	105
development of central nervous system	3.29E-14	-0.495	249
morphology of cerebral cortex	9.68E-14	-1.070	96
branching of neurons	1.31E-13	0.912	128
abnormal morphology of cerebral cortex	2.94E-13	-1.070	89
synaptogenesis	3.47E-13	-0.891	86
potentiation of synapse	1.60E-12	-1.955	76
branching of neurites	1.70E-12	1.069	121
long-term potentiation of synapse	3.62E-12	-2.221	74
excitatory postsynaptic potential	9.79E-12	1.923	61
quantity of synaptic vesicles	6.33E-10	-2.540	28
formation of dendrites	3.84E-09	1.726	56
synaptic transmission of nervous tissue	1.94E-08	-2.430	52
synaptic transmission of cells	6.69E-08	-2.443	106
density of synapse	1.63E-07	-2.879	21
action potential of neurons	1.97E-07	2.327	55
excitatory postsynaptic potential of neurons	4.91E-07	1.862	32

Guidance Signaling" pathway was the second most altered, with a p-value of $4.33x10^{-13}$, showing 36% of its molecules dysregulated (Table 3-4).

Table 3-4 Top Canonical Pathways significantly altered in CSB neurons.

Top Canonical Pathways	p-value	Overlap
ELF2 Signalling	8.89E-23	101/188 (53.7%)
Axonal Guidance Signalling	4.33E-13	158/439 (36%)
mTOR Signalling	2.49E-11	82/194 (42.3%)
Molecular Mechanisms of Cancer	1.17E-09	129/373 (34.6%)
Cell Cycle: G2/M DNA Damage Checkpoint Regulation	1.40E-09	30/49 (61.2%)

Table 3-5 describes a list of molecules corresponding to upstream transcriptional regulators that may relate to the expression alterations found by RNA-seq analysis. These transcriptional regulators include miRNA and the TGFB1 gene (downregulated in CSB neurons), which is involved in differentiation and maintenance of neurons, conversion of NPCs into active neurons and synaptogenesis (Kraus et al., 2013; Misumi et al., 2008; Walshe, Leach, & D'Amore, 2011). Although the implication of miRNA dysregulation in CS needs to be clarified, this is the first time, to our knowledge, that a robust bioinformatics analysis suggests miRNA as potential candidate contributing to transcriptional dysregulation in CS cells.

Table 3-5 Top Upstream Regulators significantly altered in CSB neurons.

Top Upstream Regulators	p-value of overlap	Predicted Activation (WT/CSB)
miR-124-3p (and other miRNAs w/ seed AAGGCAC)	2.86E-57	Inhibited
miR-149-3p (and other miRNAs w/ seed AGGGAGGG)	4.89E-45	-
TGFB1	1.27E-43	Activated
miR-96-5p (and other miRNAs w/ seed UUGGCAC)	1.30E-41	-
miR-137-3p (and other miRNAs w/ seed UAUUGCU)	4.30E-40	-

We show that the GH/IGF-1 signaling pathway was dysregulated in CSB neurons (p-value of 1.35×10^{-2}, Z-score of 1.964, Figure 3-7D & E). Specifically, we

reveal key components of this pathway (*IGF1*, *IGF2*, *IGFBP3* and *STAT5A*) showed an expression greater than thirteen times higher in the control cells than in the CSB neurons (Figure 3-7D). These genes regulate brain size and neuronal differentiation and survival (Beck et al., 1995; Croci et al., 2011; Markham, Schuurmans, & Weiss, 2007; Shcheglovitov et al., 2013; Tao et al., 2015), suggesting a correlation with CS clinical characteristics. By qPCR, we confirm that expression of *IGF1* and *STAT5A* was downregulated in CSB neurons derived from both CS donor iPSC lines (Figure 3-7F & G).

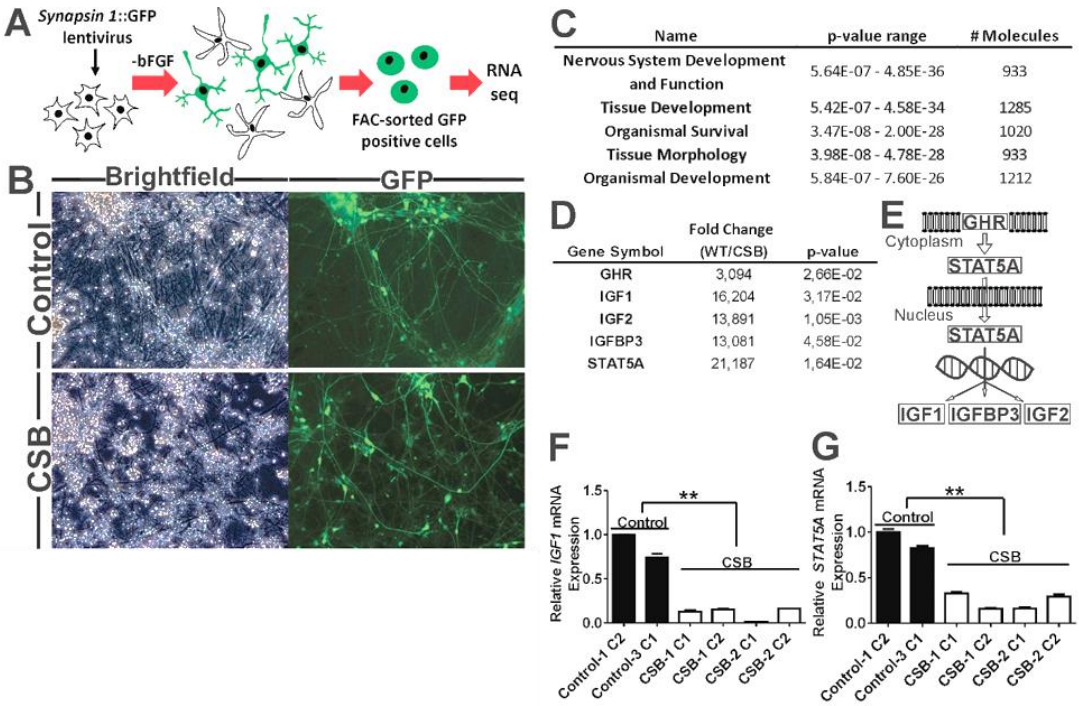


Figure 3-7 Transcriptional dysregulation of GH/IGF-1 pathway in CSB neurons.

A) Scheme of the methodology employed to isolate neurons and extract RNA for sequencing. B) Brightfield and eGFP-channel images of clone 1 of both Control-1 and CSB-1-derived neurons expressing eGFP under the control of the neuron-specific synapsin I promoter. C) Top significant "Physiological System Development and Function" categories revealed by the Ingenuity Pathway Analysis software. D) Expression of GH/IGF-1 pathway-related genes. Results are expressed as fold change of controls (WT) to affected (CSB). Key components of this pathway are shown in (E). Relative expression of *IGF1* and *STAT5A*, as measured by qPCR (F & G). Statistical analysis (unpaired t-test) express mean ± s.e.m. of clones 1 of both Control-1 and Control-2 versus two clones of CSB-1 and CSB-2 neurons (** $p<0.01$).

3.2.3.3 CSB-deficient neurons have reduced synapse density

Unbiased gene expression analyses revealed several downregulated pathways in CSB neurons implicated in synaptic activity such as synaptic transmission (p-Value = $5,83x10^{-15}$), synaptogenesis (p-Value = $3.47x10^{-13}$) and density of synapses (p-Value = $1.63x10^{-7}$, Table 3-3). Thus, we next quantified synapse density via

immunofluorescence by co-immunostaining Synapsin I (pre-synaptic marker) and PSD-95 (post-synaptic marker) on Map2 positive processes (neuron filament marker, Figure 3-8A & B). Our data showed that CSB neurons have significantly reduced synapse density when compared to controls (Figure 3-8C), suggesting that CSB is important for synapse formation, maintenance or a combination in human neurons.

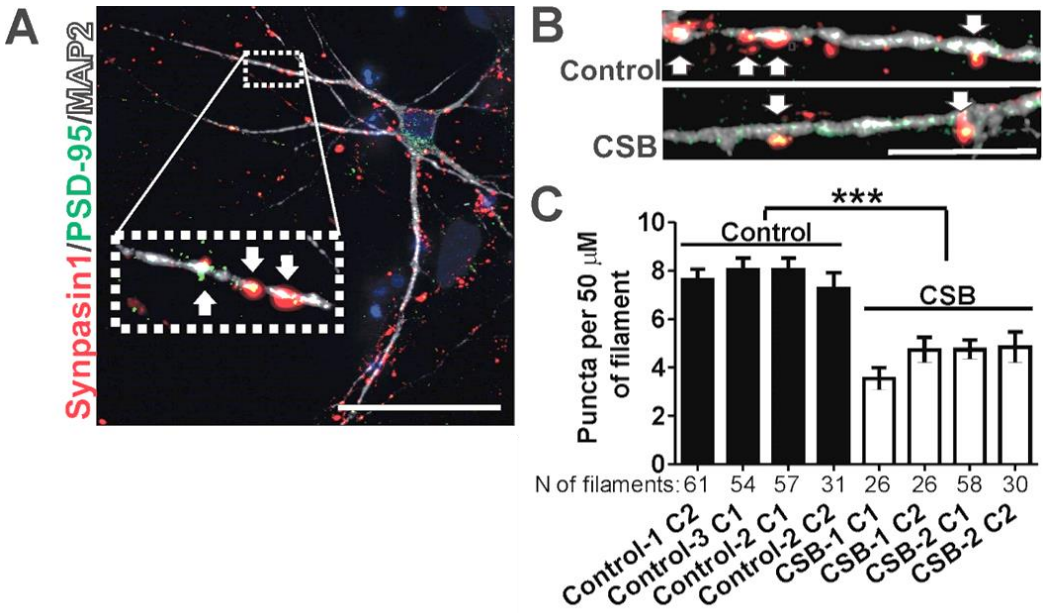


Figure 3-8 CSB neurons have reduced synapse density.

A) Illustrative picture of co-localization of synapsin I to PSD-95 on neuronal filaments (Map2), as evidenced by fluorescence microscopy. Bar: 50 µM. B) Illustrative images of synaptic puncta in clones 1 of Control-1 and CSB-1 neurons. Bar: 10 µM. C) Synapse density each clone analyzed (two independent experiments, and total number (N) filaments analyzed are indicated). Statistical analysis (unpaired t-test) express mean ± s.e.m. of the 4 clones of unaffected (clones 1 and 2 of Control-1, clones 1 of Control-2 and Contol-3 neurons) versus the 4 clones of the CSB derived neurons (clones 1 and 2 of CSB-1 and CSB-2) (*** $p<0.001$).

3.2.3.4 CBS neurons are functional, but display reduced network synchrony

The reduced synapse density observed in CSB neurons prompted us to investigate electrophysiological network connectivity. Thus, we analyzed neuronal

activity of CSB neural networks on microelectrode arrays (MEAs), which allow mapping of action potentials (spikes) through detection of field potential changes (an illustrative scheme is presented in Figure 3-9A). We differentiated the following NPCs directly on MEA substrates for five weeks: two clones for Control-1, one clone each for Control-2 and Control-3, and two clones each for CSB-1 and CSB-2 lines. Representative temporal raster plots illustrating timestamps of spikes over three minutes of continuous recording and overlaid representative wave forms are shown in Figure 3-9B & C, respectively, for both control and CSB neurons. Results show that iPSC derived neurons spontaneously generated action potentials, confirming successful differentiation of both CSB and control NPCs into functional neurons. However, comparing CSB to controls revealed overall spike number was significantly lower ($p<0.05$) in CSB neurons (Figure 3-9D). Aligned raster plots of independent electrodes show that both CSB and control neural cultures displayed varying degrees of synchronized neural network activity, measured by overlapping spike burst from different channels (vertical rectangles in Figure 3-9B). Synchronized activity spreading through multiple electrodes indicates information flow in the neuronal network via synaptic signaling. Interestingly, overlapping the spike activity histogram from different channels reveals a distinct frequency of synchronized activity for CSB neuronal networks, with significantly less synchronized events compared to controls ($p<0.05$, Figure 3-9E). These results suggest that although CSB iPSCs generate functional neurons, their coordinated activity at the network level is diminished when compared to control cells.

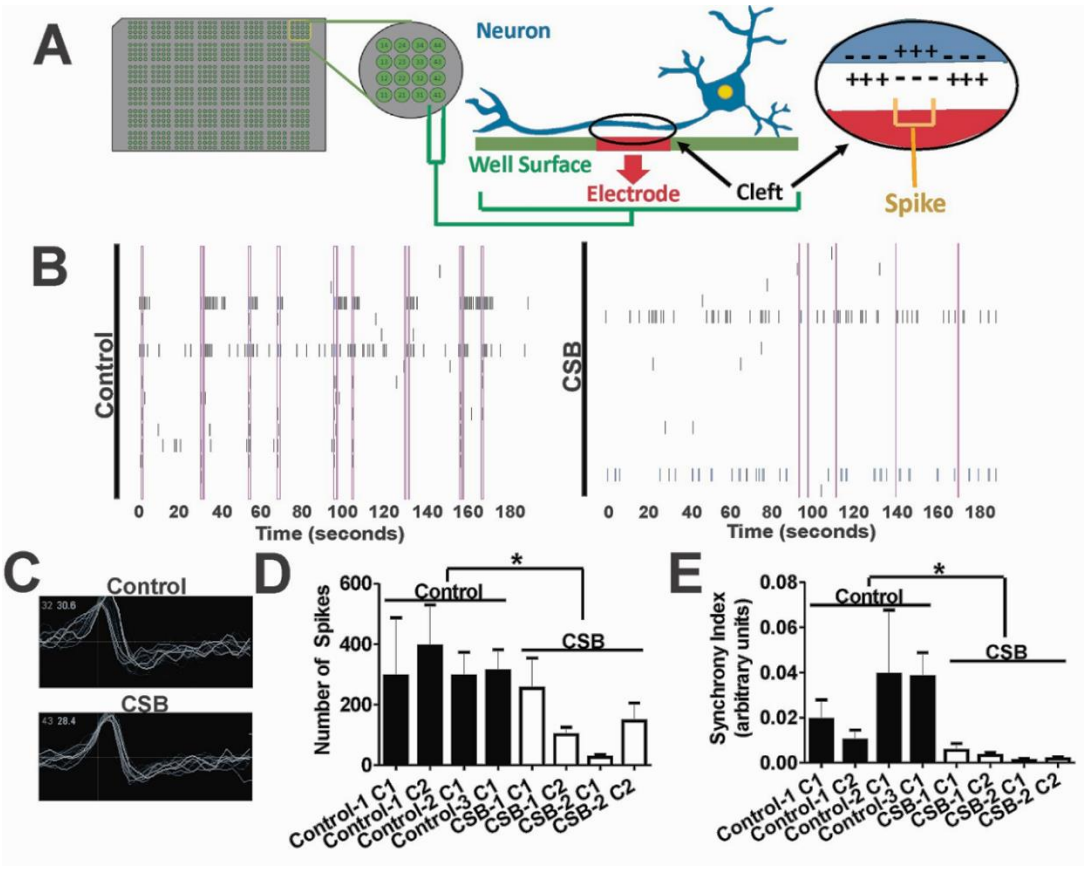


Figure 3-9 CSB neuronal cultures have reduced number of spikes and synchrony.

A) Illustrative representation of a neuron plated on top of an electrode and the generation of field potentials changes (spikes). B) Illustrative raster plot images of unaffected (W83 clone 1) or CSB (GM00739 clone 1) neurons over a 3-minute recording in the MEA. Vertical pink rectangles indicate synchronization of network activity. C) Representative wave forms of spikes detected in one electrode of each unaffected (W83) or CSB (GM00739) neural cultures. Total number of spikes (D) and synchrony index (E). At least three independent experiments in quadruplicate were carried out for all clones. Statistical analysis (unpaired t-test) express mean ± s.e.m. of the four clones of unaffected versus the four clones of CSB-deficient neurons (* $p<0.05$).

3.2.4 Summary

Cockayne Syndrome (CS) is a monogenetic disease in which human subjects display neurodevelopmental dysfunction and degeneration. A majority of CS patients are affected by mutations in *ERCC6* that encodes CSB protein which functions in

transcription-coupled repair of damaged DNA (Lehmann, 2003; Menck & Munford, 2014), RNA synthesis (Brooks, 2013; Vélez-Cruz & Egly, 2013) and mitochondrial metabolism (Cleaver et al., 2013; Scheibye-knudsen, Croteau, & Bohr, 2013). However, understanding the impact of CSB deficiency on neurons has historically been hampered by limitations of available disease models.

As previously reported (Andrade et al., 2012), we successfully generated iPSCs from CSB fibroblasts, implicating that the gene is not essential for reprogramming. Here, we were further able to differentiate CS iPSCs into NPCs and functional neurons. These cells expressed classical neuronal markers (MAP2, Tuj1 and NeuN), formed synapses (co-localization of Synapsin I with PSD-95 on neuronal filaments) and generated action potentials (as measured by field potential changes on MEA substrates). However, we observed reduced connectivity in CSB neural networks, confirmed by reduced synapse density and reinforced by decreased synchronized firing, when compared to neural networks derived from unaffected donor cells. These results are in agreement with the reduction of dendritic spines (which are critical structures for synaptic activities) observed in CSB-KO mice (J. Wong et al., 2013), suggesting that CSB is critical for synapse maintenance and neural networking.

A reduction in synapse density can be a result of diminished synaptogenesis, increased synaptic degeneration, or a combination (Buttini et al., 2005; Conforti, Adalbert, & Coleman, 2007; Marchetto et al., 2010; Shcheglovitov et al., 2013). With regards to observed developmental deficiency and neurodegeneration in CS, a leading cause for reduced synapse density is still unknown. However, NeuN-positive cell numbers in the CSB-1 neural cultures were similar to control cells, suggesting that factors other than neuronal density may play a critical role. Transcriptome sequencing

of CSB neurons revealed that several pathways related to neuronal function and communication were dysregulated in CSB neurons, suggesting cell-autonomous transcriptional dysregulation as a key contributor to reduced synapse density, in accordance with CSB playing a critical role in RNA synthesis (Bradsher et al., 2002; Dianov et al., 1997). In agreement, Wang and collaborators found that neuron-associated genes were among the most altered classes of molecules through microarray-based analysis of RNA obtained from CSB-deficient fibroblasts (Y. Wang et al., 2014).

Notably, we discovered impaired transcription of the GH/IGF-1 signaling pathway in CSB neurons, further confirmed by qPCR for *IGF1* and *STAT5* genes in neurons of two unrelated CS donors (Figure 3-7). *IGF1* disruption results in reduction of brain size, hypomyelination and loss of granule cells (Beck et al., 1995). Reduced *IGF1* expression also compromises survival of Purkinje cells in neonatal cerebella (Croci et al., 2011). All of these features are commonly observed in classical CS cases (Weidenheim et al., 2009). *STAT5* was also shown to regulate *IGF1* expression (Baik, Yu, & Hennighausen, 2011). Finally, reduced IGF-1 serum levels were reported in one CS patient (Park et al., 1994). It is noteworthy that although $CSB^{m/m}$ mice fail to display several human neurological phenotypes (Scheibye-Knudsen et al., 2012), a double-deficient ($XPA^{-/-}$, $CSB^{m/m}$) murine model that recapitulates growth retardation, progressive cachexia and neurodegeneration also displays reduced GH/IGF-1 axis transcription (Van Der Pluijm et al., 2007). The *Ercc1* KO murine model (deficient in nucleotide excision repair) also shows a decline in the GH/IGF-1 axis, in parallel with signs of neurodegeneration and premature aging (Niedernhofer et al., 2006). Therefore, the identification, for the first time, of transcriptional downregulation of key

components of the GH/IGF-1 pathways in CS donor-derived neurons constitutes evidence that it may play a key role in the neuropathology of CS. Remarkably, IGF-1 administration to iPSC-derived neuronal models of Rett Syndrome (Marchetto et al., 2010) and of Phelan-McDermid syndrome (Shcheglovitov et al., 2013) rescued synapse density, and is currently in clinical trials for Rett Syndrome (ClinicalTrials.gov identifiers: NCT01253317 and NCT01777542). Now that we have established a human CSB neuronal model and revealed dysregulation in the GH/IGF-1 pathway, investigating the potential effects of IGF-1 treatment on iPSC-derived CSB neurons may be of compelling clinical interest.

Recently, Ciaffardini and coworkers reported that *ERCC6* knockdown severely compromised differentiation of v-Myc immortalized NPCs (ReNcell VM) into neurons (Ciaffardini et al., 2014). Wang and collaborators reported that SV40-transformed CSB-null fibroblasts failed to transdifferentiate into neurons (Y. Wang et al., 2014), providing additional rationale for our successful iPSC platform. Since classical CS patients are born with apparently normal brains (Rapin et al., 2006; Weidenheim et al., 2009), we expected a cell model that relies on differentiation from pluripotent cells (therefore mimicking embryonic development) would facilitate neural development. The iPSC-derived neurons recapitulate not only the pathogenic mutation, but also the genetic background of the CS donor in karyotypically stable cells (contrary to SV40-transformed cells). It is worth noting that CS patients with identical mutations, yet contrasting phenotypes, have been described (Colella et al., 2000). Therefore, the ability of our iPSC model to recapitulate the genetic background of each individual donor (in contrast to knockdown models) makes it an attractive new alternative for CS studies.

3.2.5 Recognitions

Authors want to thank Cassiano Carromeu and Brian Lee for helping with cell reprogramming and neuronal differentiation. This work was supported by a grant from the California Institute for Regenerative Medicine (CIRM) TR4-06747, the National Institutes of Health through the NIH Director's New Innovator Award Program (DP2-OD006495-01), R01MH094753, R01MH103134, U19MH107367, a NARSAD Independent Investigator Grant to A.R.M., and from Fundação de Amparo à Pesquisa do Estado de São Paulo (FAPESP, São Paulo, Brazil) and Coordenação de Aperfeiçoamento de Pessoal de Nível Superior (CAPES, Brasilia, Brazil).

3.3 Monolayer stem cell derived neural co-cultures reveal astroglial non-autonomous neurophysiological phenotypes in Rett Syndrome (*MECP2*)

3.3.1 Brief introduction and rationale

The technology to derive and maintain human embryonic stem cells (ESCs) in artificial culture systems is now nearly two decades old (Thomson et al., 1998). Building on this revolutionary technology, many cellular tools have since been developed with ever growing potential for disease modeling. An early feature, and requirement, of stem cell technology was to co-culture human ESCs with murine embryonic fibroblasts (MEFs) as a supportive non-cell autonomous “feeder” layer, providing soluble factors to promote pluripotency. Since, progressive discoveries have led to our current ability to reprogram human somatic cells into an induced pluripotent stem (iPS) state (Takahashi et al., 2007) and maintain their pluripotency, or direct specified differentiation under chemically defined conditions. While iPSCs are similar to ESCs regarding pluripotency, they carry the unique genetic identities of their donors including disease-causing mutations. Additionally, recent advances in mammalian cell genetic editing, such as the CRISPR/Cas9 system, facilitate not only the creation of isogenic matched iPSC controls in established iPSC models of disease, but also allow the introduction of targeted mutations in unaffected stem cell genomes to generate new isogenic disease models. Using these techniques to study monogenetic diseases is essential and allows the controlled *in vitro* observation of disease-relevant yet poorly accessible human tissue - such as the brain. Given the complex cytoarchitecture of the brain, to identify genetic and cellular features of neural phenotypes it is necessary to scrutinize specific cell type-specific contributions within functional neural networks. The brain consists of various subtypes of neurons and glia. While neurons generate action

potentials and historically have been the most studied neural cell type, astroglia are the most abundant cells in the brain.

It is well supported that astrocytes actively contribute to the information processing of neural networks in a non-autonomous manner (Allen, 2014; Allen et al., 2012; Christopherson et al., 2005; Lobsiger & Cleveland, 2007; Perea et al., 2009). Astroglia build a neural sub-network that actively participates in CNS maintenance and healthy neuronal networking. Aberrant astroglial behavior is implicated in numerous human diseases including ALS and RTT (Lobsiger & Cleveland, 2007; Williams et al., 2014). Until recently, it has been a challenge to isolate or generate human astrocytes for *in vitro* studies. There are now several published protocols available to generate human astroglia from human stem and progenitor cell sources, specifically from genetic iPS cellular models (C. Chen et al., 2014; Haidet-Phillips et al., 2013). I sought to establish *in vitro* human neural cultures with the express ability to probe the effects of genetically variable astrocytes on functional neural networks. The initial aim for the latter experimental part of this chapter was to establish neuronal culture or co-cultures to measure general effects of astroglia on physical and elecrophysiological aspects of neuronal networks. The preliminary experiments designed to determine parameters sufficient to probe astroglial contributions in functional neural networks were not exhaustive. However, based on the robustness of initial results I decided to use physical contact co-cultures as depicted in the schematic in Figure 3-10 to design a short study investigating the role of astroglial MeCP2 on neural networking.

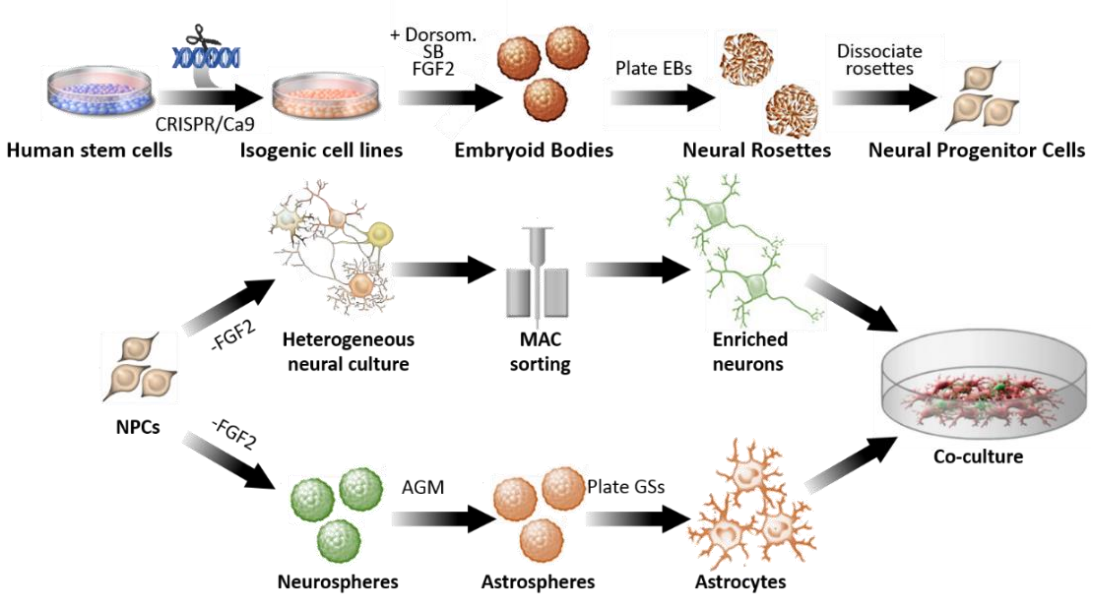


Figure 3-10 Establishing neural co-culture using human stem cells.
Schematic overview of the three-part neural co-culture protocol.

Rett syndrome (RTT) is a debilitating disease that affects approximately 1 in 10,000 female births in the U.S. About 95% of cases are caused by mutations in methyl CpG binding protein 2 gene (*MECP2*) on the X chromosome. Typically, girls diagnosed with RTT have undergone seemingly normal development until six to eighteen months of age, followed by an onset of impaired motor function, stagnation and then regression of developmental skills, hypotonia, seizures and a spectrum of autistic behaviors (Amir et al., 1999). RTT is considered a primarily female disease because male fetuses carrying a *MECP2* mutation on their single affected allele rarely survive gestation. Rare males born with a RTT mutation typically present a more severe and accelerated disease progression, further obscuring clinical diagnoses. RTT was considered severe on the autism disorder spectrum (ASD) prior to causal genetic linkage to *MECP2*, after which ASD is clinically considered one characteristic symptom of RTT.

In this work, we sought to refine our seminal model of *in vitro* neural development to study the effects of astroglial MeCP2 on neuronal networking. We generated isogenic matched *MECP2* stem cell lines by genetically inducing non-sense mutations targeted to the MeCP2 gene in a broadly accessible human embryonic stem cell line: WA09 or "H9." We clonally expanded new H9 derivative stem cell lines, both with and without mutated *MECP2*. We differentiated these cell lines into expandable neural precursor cell (NPC) lines for subsequent astroglial differentiation. We used a control iPSC-derived NPC line, previously generated and widely used in our lab as a neural benchmark, to robustly differentiate unaffected neural cultures for further neuronal enrichment. We then established heterogenic co-cultures to examine effects on electrophysiology and connectivity.

Emerging multi-well MEA technology was used to analyze network activity in neuronal co-cultures on feeder astroglia derived from isogenic MeCP2-deficient or unaffected ESC sublines. In addition we performed immunocytochemistry and 3D image analysis to compare synapse densities. We noticed that neuronal networks co-cultured on MeCP2-deficient astroglia exhibited greatly reduced neuronal activity, altered network synchrony and reduced synapse density when compared to neuronal networks co-cultured on unaffected astrocytes. Interestingly, while reduced for neuronal co-cultures on affected astroglia, synapse density was maintained for neuronal co-cultures on control human primary fibroblasts derived from the same iPSC donor, despite a stark reduction in analyzed electrophysiological metrics. Our data compliment previous observations that astroglial MeCP2 plays a role in single neuron electrophysiology (via patch clamp recordings) and neural connectivity, and further

supplements the rapidly growing body of work elucidating extensive roles for astroglia in RTT and other diseases affecting the brain.

3.3.2 Materials and methods

3.3.2.1 Cell culture media

mTeSR1 medium was prepared as directed by Stemcell. FB medium contained DMEM (Cell Gro, Corning) supplemented with 10% FBS and (concentration) P/S (both from Thermo Fisher). N2 medium contained DMEM:F12 with HEPES and glutamate (1:1, Lonza) supplemented with 1% N-2 (100X, Thermo Fisher). NG medium contained DMEM:F12 (1:1, Lonza) supplemented with 1% Gem21 NeuroPlex (50X, Gemini), XX µM HEPES, 0.5% N-2, and 8 mM Glutamax (all from Thermo Fisher). NBA medium contained Neurobasal A with 2% B-27 (50X) and 2 mM Glutamax (all from Thermo Fisher). AGM with 3% FBS was prepared as directed by Thermo Fisher (AGM SingleQuot Kit), excluding the provided read-through antibiotic Gentamycin to avoid potential experimental interference.

3.3.2.2 Cell culture

The Rett Syndrome donor-derived iPSC line Q83X was retrieved from the Muotri Laboratory cell repository (originally derived from a RTT-affected male, age 5). The Q83X paternal control fibroblasts and iPSC NPC line ctr83 were retrieved from the Muotri Laboratory cell repository (originally derived from a non-affected male, age 38). The NIH-approved ESC line WA09 (H9) was acquired from WiCell. Fibroblasts were maintained on typical tissue-culture-treated (TC) polystyrene dishes in FB medium, refreshed 2x per week and passaged as needed via TrypLE (Thermo Fisher) enzymatic

dissociation. NPCs were generated as described below and maintained on TC dishes pre-coated with 10 µg/ml poly-L-ornithine (pO, Sigma Aldrich) and 2.5 µg/ml laminin (Ln, Thermo Fisher) in NG supplemented with 20 ng/mL bFGF2 (Thermo Fisher), refreshed 3x per week and passaged every 3 days via Accutase (Stemcell) enzymatic dissociation. Human ES cells were routinely maintained as previously described (Griesi-Oliveira et al., 2015; Vessoni et al., 2016) on Matrigel (Corning) in mTeSR1 medium, refreshed daily and passaged weekly via microscopic manual mechanical fragmentation. Neural cultures were generated as described below and maintained on pOrn/Ln-coated TC dishes in NG medium, refreshed up to 2x per week and enzymatically dissociated for enrichment as needed via Accutase:Accumax (1:1, Stemcell). Astroglia were generated as described below and maintained on pOrn/Ln-coated TC dishes in AGM medium, refreshed 2x per week and passaged with either TrypLE or papain supplemented with DNAse (Worthington) weekly. All cells were maintained at 37C in an aseptic humidified atmosphere of 5% CO2.

3.3.2.3 Establishing isogenic *MECP2* lines from engineered ESC lines

The H9 ES cell line was modified via CRISPR/Cas9 genome editing (described in a separate manuscript currently in preparation) to genetically disrupt *MECP2* by introducing a single nucleotide deletion at the lysine 82nd residue of exon 3, resulting in a nonsense frame shift with multiple early stop codons (K82*fs*, Figure 3-11A). For isogenic experimental controls (ctr905 and ctr916) we clonally expanded cell lines derived from the CRISPR-treated H9 population that expressed MeCP2 after expansion. Karyotyping revealed no gross abnormalities in the clones picked for further analysis (Figure 3-11B). Two MECP2-affected ES lines derived from the H9 line, K82*fs*-

1 and K82*fs*-2, exhibit reduced MeCP2 expression comparable to that observed for RTT donor iPSCs (Figure 3-11A) as well as loss of MeCP2 protein (Figure 3-11C). We have successfully generated NPCs, neurons, and astrocytes from the new K82*fs* and ctr82 cell lines. Unspecific cleavage by RGENs at potential off-target sites was analyzed by targeted deep sequencing and exon sequencing of DNA from H9-derived CRISPR/Cas9-treated ES lines.

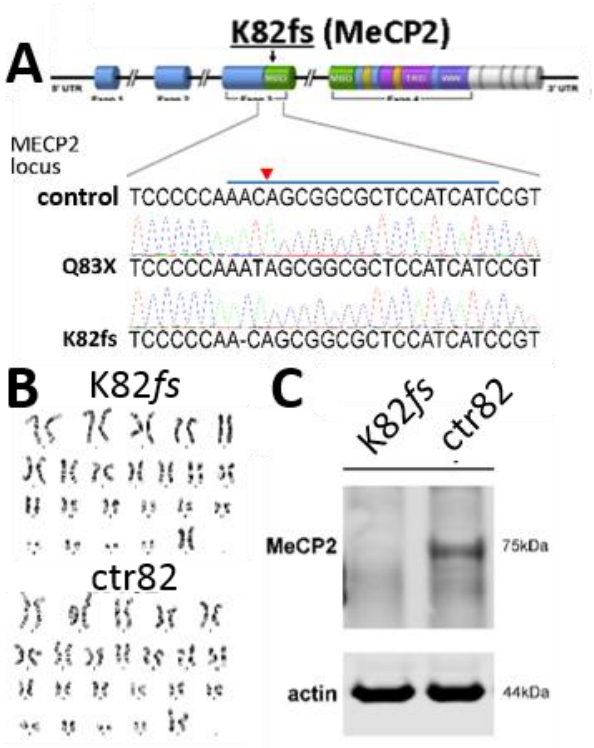


Figure 3-11 Isogenic human ESC model to mimic RTT-like MeCP2 mutation.

A) Sequencing to verify CRISPR/Cas9-induced genetic editing of MeCP2 resulting in a nonsense mutation. B) No karyotypic abnormalities were observed in ESC subclones. C) Western Blot exhibiting loss of MeCP2 protein in stably edited clones.

3.3.2.4 Establishing isogenic *MECP2* lines from engineered RTT iPSC lines

A RTT iPSC line derived from a rare male (46XY) donor with a Q83X *MECP2* mutation was modified via CRISPR/Cas9 genome editing by Applied StemCell to genetically revert the mutation by introducing a single nucleotide (T to C) substitution in an early TAA stop codon to correct the glutamine 83nd residue of exon 3. MeCP2-specific gRNA was generated based on the published sequence at the targeted site and cloned into the Cas9-Puro vector. Single-stranded donor DNA was synthesized to deliver the “wild-type” (WT) nucleotide. gRNA-Cas9-Puro plasmid and donor DNA was delivered into the Q83X IPSC line via electroporation. The Puro-resistant gene in the gRNA-Cas9-Puro plasmid allows a transient 48hr Puromycin selection that enriches the transfected cells. After clonal growth, colonies were handpicked and expanded for genotyping by sequencing. Clone B11 used in this study was confirmed to have the WT *MECP2* allele confirmed by Sanger sequencing (Figure 3-12) and normal karyotype.

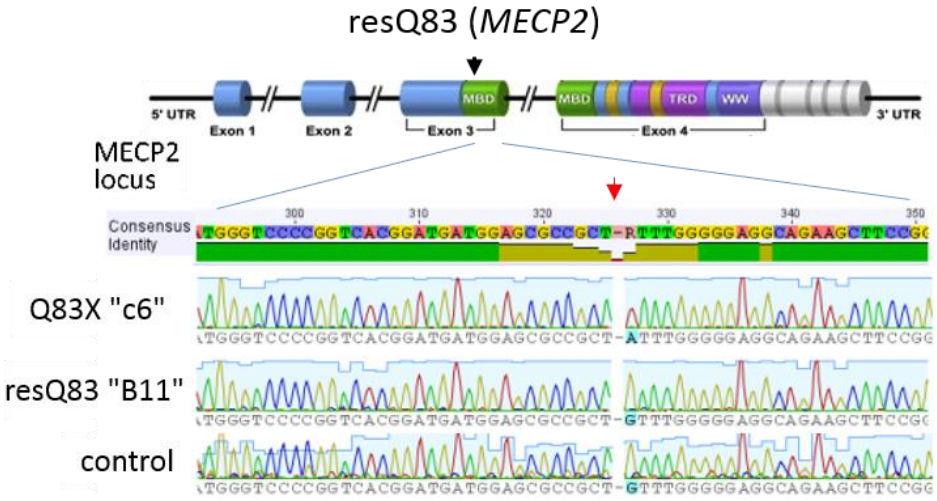


Figure 3-12 resQ83 Sequence alignment.

Sequencing results show that *MECP2* sequence of clone B11 was successfully corrected. Clone C6 had the same unmodified sequence as original.

3.3.2.5 Generation of NPC lines

Our lab routinely generates neural precursor cell (NPC) lines derived from human embryonic stem (ES) and induced pluripotent stem (iPS) cells as depicted in Figure 3-13 (Griesi-Oliveira et al., 2015; Vessoni et al., 2016). To establish NPC lines for this study, ES or iPS colonies were neuralized by dual inhibition of SMAD signaling for two days in N2 medium supplemented with 1 µM dorsomorphin (Tocris) and 10 µM SB431542 (Stemgent). Then, colonies were mechanically scored, separated and maintained in suspension culture for five days in NG medium supplemented with 20 ng/mL bFGF2 (NGf) to further develop into neuralized embryoid bodies (NEBs, NGf medium was exchanged every two days). NEBs were gently disrupted by fluid shear during pipetting and cultured on Matrigel surfaces for an additional five days in NGf medium. Neural rosettes were manually selected and re-plated for up to five days on tissue culture plates pre-coated with poly-L-ornithine (Sigma-Aldrich) and laminin (Thermo Fisher). After a secondary picking, rosettes selected for abundant radial glia-like extensions were dissociated with Accutase (StemPro) and initially re-plated at high density for further expansion. A highly homogenous NPC line results after four to five passages (1:3). Stability of these lines is highly dependent on initial quality of manually picked rosettes, therefore additional iterations of selection are recommended as necessary.

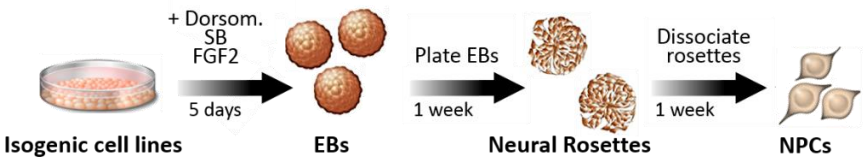


Figure 3-13 Schematic timeline describing NPC generation.

For routine characterization reference Figure 3-2, Figure 4-2 and Figure C-1G.

3.3.2.6 Generation of astroglia from NPC lines

Our lab routinely generates functional astroglia from NPC lines. Taking advantage of the robust phenomenon of spontaneous *in vitro* radial outgrowth from adhered neurospheres, which mimics radial glial scaffolding and outward migration during early human development, we adapted our neurosphere protocol. First, NPCs are lifted in PBS stripped of cations required for integrin binding, and then lifted sans enzymatic assistance. bFGF2 is removed and suspension rotary cultures are treated with Y-27632 for two days. After five additional days NG medium is replaced with AGM and cultured in suspension for an additional two weeks. Next “glial spheres” are adhered to pOrn/Ln-pre-coated surfaces. After one day, spheres with excessive non-glial outgrowth are manually removed. After one week, adhered cultures are enzymatically passaged regardless of outgrown cell density. Passaging is repeated every one to two weeks at 1:1 or 1:2 ratio. This protocol generates a relatively pure population of $GFAP^+$ astrocytes from NPCs in approximately six weeks (Figure 3-14). Efficiency of this protocol is demonstrated by robust immunostaining for GFAP. Resulting cultures include mature astroglia Figure 3-14G with varied sub-types Figure 3-14H for example, cells differentially express GFAP and vimentin. Radial glia and some neurons typically extend out from the glial spheres but neurons rarely migrate beyond the radial glia in the presence of astrocyte growth medium (AGM). This is possibly due to an absence of detachment signaling in the *in vitro* environment. After two gentle enzymatic passages of migrating astrocytes in AGM leaving the glial spheres intact, the spheres are manually removed. The result, as shown in Figure 3-14E, is an initially rapidly expanding population of homogeneous astrocytes that stain

positive for GFAP, S100β and vimentin. Additionally, using GFAP::dTomato we verified efficiency via FACS analysis (Figure 3-14F).

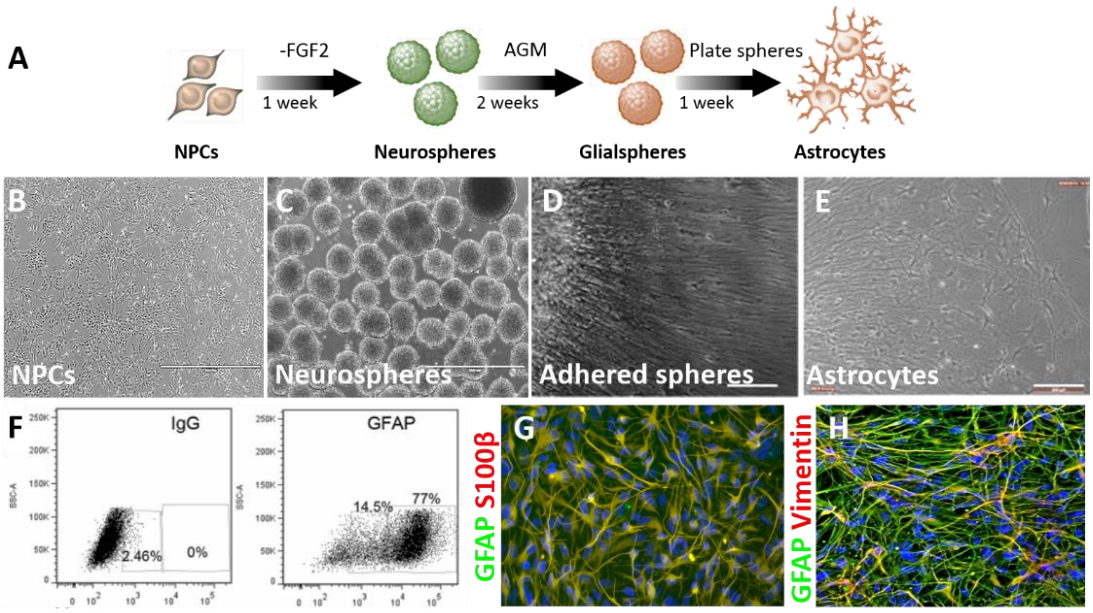


Figure 3-14 Schematic timeline describing astroglia generation from NPC lines.

A) Astroglia differentiation timeline. B) NPCs. C) Neurospheres in suspension rotary culture prior to AGM treatment. D) Adhered glial spheres. E) Astroglia migrating outward along radial extensions from adhered spheres. F) FACS analysis of GFAP reporter expression in NPC-derived astroglia (taken from Figure 4-2D, in Press at PNAS). G) Co-localization of immunostaining for GFAP and S100β. H) Immunostaining for GFAP and vimentin.

3.3.2.7 Generation of enriched neurons from NPC lines

Our lab routinely generates functional cortical neurons from NPC lines derived from human ES and iPS cells (Griesi-Oliveira et al., 2015; Vessoni et al., 2016). In this study we included an additional magnetic-activated cell sorting (MACS) step to further enrich neuronal populations for co-culture. To initiate neural differentiation in nearly confluent NPC cultures, bFGF22 was withdrawn and replaced with 5 µM Y-27632 for two days. Neurogenesis proceeded in NG medium and neural cultures matured for five

weeks. Next, neurons were enriched as needed (Figure 3-15) using MACS cell separation, as recommended by manufacturer (Miltenyi Biotec), to negatively select CD44+ and CD184+ cell populations. Enriched neurons were then immediately used for co-culture assays.

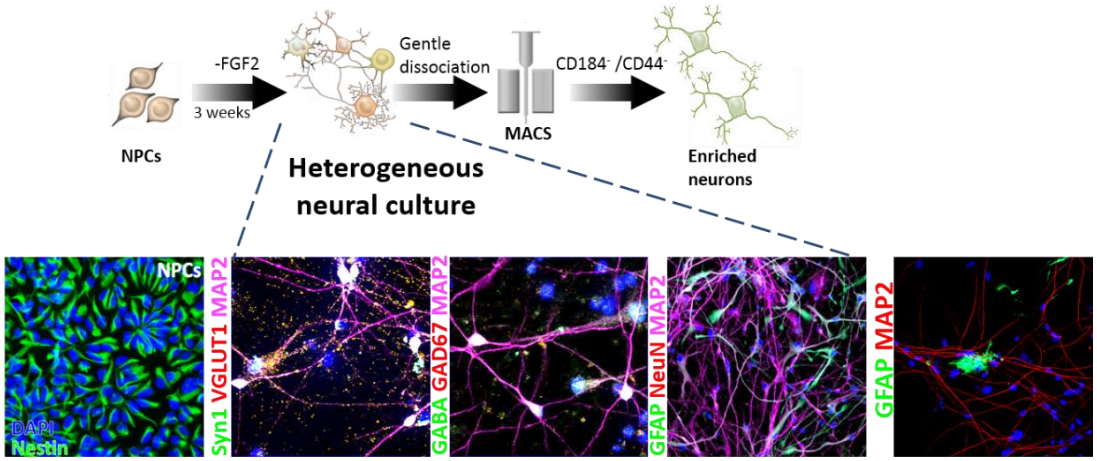


Figure 3-15 Schematic timeline for neuronal differentiation and enrichment from NPC lines.

Neural differentiation and enrichment by negative selection of $CD184^{+}$ and $CD44^{+}$ cells via MACS cell separation.

3.3.2.8 Neural co-cultures

Astroglia conditioned medium (ACM) was prepared by adding 9 mL NBA to a pre-rinsed confluent 10 cm astroglia culture dish for 24 hrs. ACM was then centrifuged at 200 g for 3 min to remove cell debris, and immediately loaded directly onto enriched neuronal cultures three times per week. To maintain astroglia phenotype, AGM and NBA medium was alternated every other day for up to one week.

For preliminary contact co-culture study, astroglia were enzymatically dissociated and re-plated at 25 $x10^3$ cells/cm^2 in 1:1 AGM. The next day, neurons were enriched via MACS as described above and plated onto astroglial feeders (or fibroblast

controls) at plating 2:1 ratio in 100% NBA medium, after rinsing the feeders once with HBSS. NBA medium was exchanged 2x per week.

For *MECP2* isogenic co-culture studies, astroglia and neurons were prepared as described above with two exceptions: (1) neurons were re-plated at 5:1 ratio in NBA medium (2) supplemented with 0.5% horse serum (DH-05, Omega Scientific).

3.3.2.9 Microelectrode array recording and analyses

MEA acquisition was carried out similarly as described in 3.2.2.6 with the following noted exceptions. These studies were carried out in 12-well plates on platinum coated MEAs. For pre-coating, polyethyleneimine was prepared in 8.4 pH borate buffer as recommended by Axion. Randomization of wells was implemented to accommodate potential non-random noise in the multiwall system. The following custom script was provided by Axion to run in debug mode to open up the bandwidth range from 0.1 Hz to 5 kHz:

```
setdac HighPass .1Hz;
setdac Pre_HighPass -p .1Hz;
setdac HighPassAmp 5000Hz;
```

Analyses were performed using Axion 1.9, Neural Metric Tool 1.0, or in MATLAB with custom scripts as indicated.

3.3.2.10 Immunocytochemistry & Synapse density assay

Cells were plated on glass coverslips pre-coated with Matrigel (ESC and iPSC colonies) or 100 µg/ml of PO and 10 µg/ml of laminin (NPCs and astroglia) and fixed with 4% paraformaldehyde for 10 minutes at room temperature, then permeabilized (0.1% TritonX in PBS). Neural co-cultures were fixed in ice-cold methanol for 10

minutes. Cytology samples were then blocked (3.5% BSA in PBS), cells were incubated with primary antibodies (see list below), followed by Alexa Fluor-conjugated secondary antibodies (Life Technologies). Cell nuclei were treated with DAPI, and immunofluorescence images were generated with a Zeiss Apotome epifluorescent microscope (Carl Zeiss, Oberkochen, Germany). Primary antibodies used were: Map2 (ab5392, Abcam), GFAP (Z0344, DAKO) or (ab53554, Abcam), NeuN (MAB377), Synapsin I (AB1543p, Millipore), Nestin (MA1-46100, Thermo Scientific), HOMER1 (160003 or 160011, Synaptic Systems); VGLUT1 (135311, Synaptic Systems), GABA (4819S, Cell Signalling), GAD67 (ab11070, Abcam), and vimentin (3932, Cell Signalling or 55013, BD Pharmingen). For synapse density analysis, 1.25 x 10^5 Enriched neurons, and co-cultures with astrocytes or fibroblast feeders were plated on pOrn/Ln pre-coated 12 mm cover glass. After one or two weeks of co-culture, cells were fixed, stained for Synapsin I, HOMER1, and MAP2 and then 3D z-stack image data sets were generated using a Zeiss Apotome under a 63X oil-immersion objective in the Apotome Z-stack mode (19 slices with 0.31 interval). 3D models were rendered using Imaris 7.6. Synapse density was calculated as follows: The number of synapses (Synapsin I co-localizing to HOMER1, center-to-center of 3D rendered diameter < 1 µM) with SYN1 puncta center located within a distance having a ratio of 1:2 of the neurite filament radius (MAP2). Synapse density was assessed per 50 µm length of the MAP2 filaments. Synapse density was averaged for ten to fourteen fields per condition, of varying neuronal densities reconstructed in 3D via Imaris software. Cell soma were manually removed from analyses.

3.3.3 Results

3.3.3.1 Contact neural co-culture supports more complex activity

We differentiated ctr83 iPSCs into astroglia described in the materials and methods section. We prepared separate confluent astroglial cultures in pOrn/Ln coated 10 cm tissue culture dishes for collection of 24 hr astroglial conditioned medium (ACM) immediately prior to ACM neuronal group medium exchanges.

We then differentiated H9 ESCs into heterogeneous cortical neural cultures as previously described (Griesi-Oliveira et al., 2015; Vessoni et al., 2016). Briefly, we initially differentiated ESCs into NEBs in suspension cultures followed by dual SMAD inhibition. Next, adhered NEBs gave rise to neural rosettes which were then dissociated to generate NPCs Figure 3-2. NPCs were further differentiated into neural cells by culture in NG for four weeks, followed by ongoing culture in NBA medium. Neural cultures gave rise to neurons and astrocytes as evidenced by non-localized MAP2 and GFAP staining, respectively (Figure 3-15 and Figure 3-20). Neural cultures were dissociated and further enriched for neurons via MACS to negatively select $CD44^{+}/CD184^{+}$ cells (Figure 3-15). Cells were immediately plated on either a feeder layer of astroglia (2:1), or directly onto PEI/Ln pre-coated microelectrode array (MEA) substrates which allow temporal mapping of action potentials. Contact astroglial co-cultures and one group of enriched neurons were provided fresh NBA medium, while the second group of enriched neurons were provided 24 hr ACM and maintained for six additional weeks in culture. We analyzed neuronal activity of neuronal networks. Representative bright field images of enriched neurons and contact co-cultures at two weeks are exhibited in Figure 3-16A. Representative temporal raster plots illustrating timestamps of spikes over three minutes of continuous recording two weeks after re-

plating are shown in Figure 3-16B for enriched neurons in NBA or ACM and contact astroglial co-cultures. Results show that all groups spontaneously generated action potentials confirming the presence of functional neurons. However, comparing either enriched neuronal group to contact co-cultures reveals overall spike number was substantially lower in the absence of astroglia (Figure 3-16C).

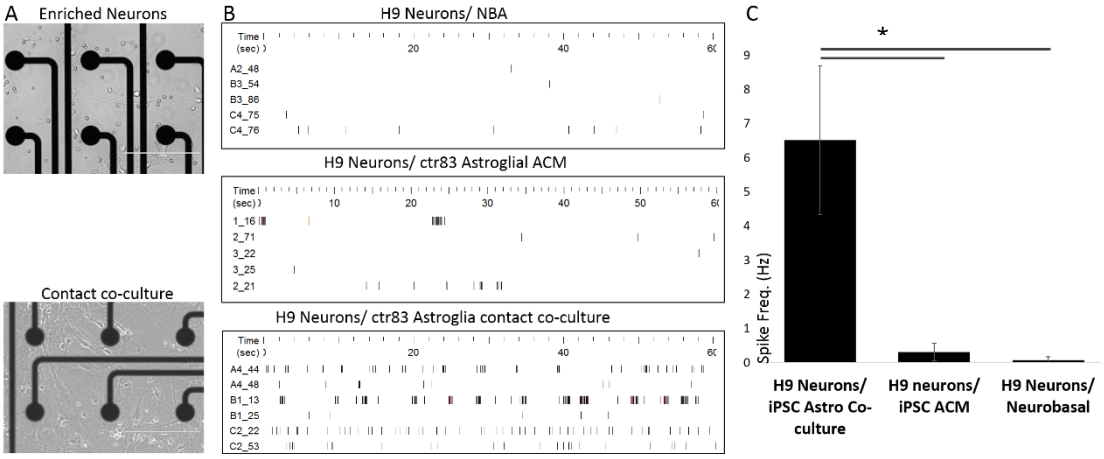


Figure 3-16 Neuronal activity is enhanced early by astroglia contact co-culture after two weeks.

A) Representative bright field images of enriched neurons (Upper) and astroglial contact co-culture (Lower) demonstrating similar neuronal MEA coverage, Scale bar: 300 µm. B) Representative temporal raster plots of spike activity for enriched neurons in NBA (Upper) in ACM (Middle) and astroglial co-cultures Lower). C) Average spike rate analyzed from three wells per condition two weeks after re-plating. * indicates $p < 0.001$.

All temporal raster plots are shown in Figure 3-17A illustrating timestamps of spikes recorded continuously during several two to five minute sessions over a cumulative period spanning six weeks post re-plating for enriched neurons in NBA or ACM and contact astroglial co-cultures. Comparing the enriched neuronal group in NBA to either the ACM group or contact co-cultures reveals cumulative spike activity number was substantially lower in the enriched neuronal group maintained in non-conditioned NBA medium (Figure 3-17B). Less remarkable, but motivation for further

study, the direct co-cultures trended with more cumulative activity than enriched neurons treated with conditioned medium, but at the power of this experiment the difference was not significant (Figure 3-17B).

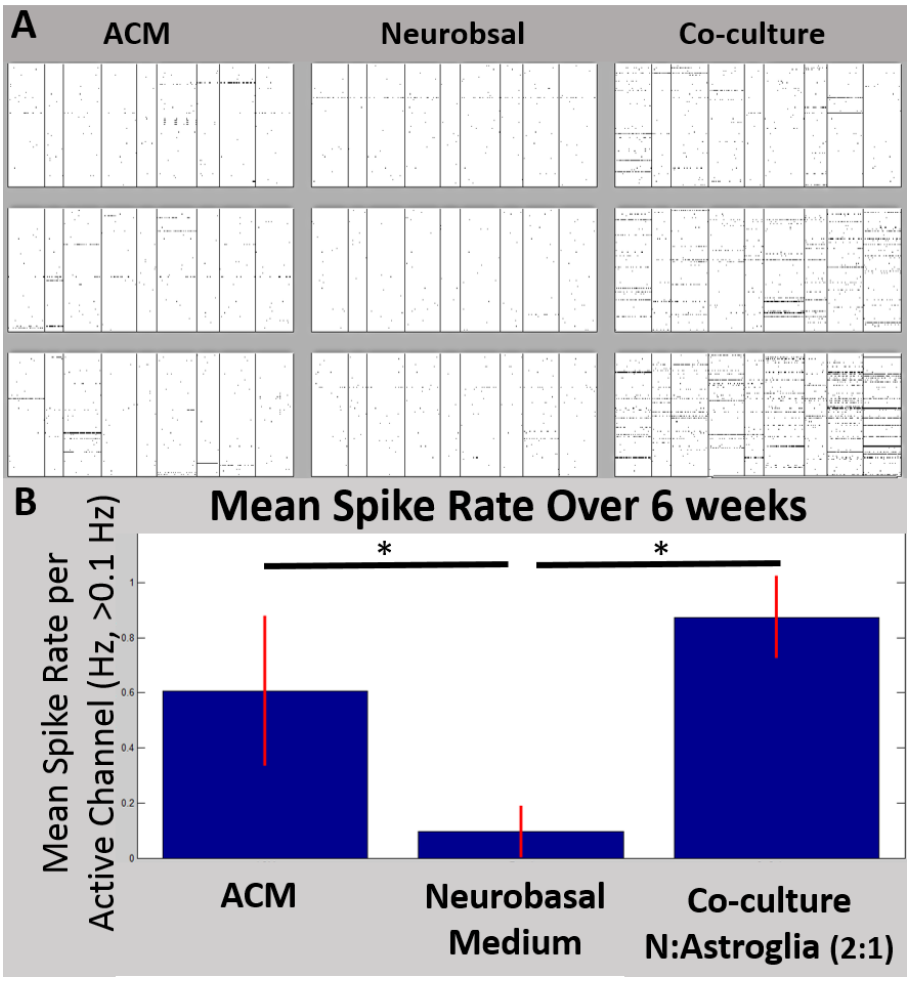


Figure 3-17 Astroglia and ACM promote cumulative neuronal activity over time.

A) Temporal raster plots of spikes recorded from three wells per condition at nine sessions over six weeks; stitched together and separated by vertical black lines. Varying widths indicate time scale. B) Mean cumulative spike rate of active channels (active > 0.1 Hz), per condition over all sessions in a six week period. * represents significant differences according to two way anova.

3.3.3.2 Neuronal co-localized synapse density is increased by astroglial co-culture and ACM

We also quantified synapse density via immunofluorescence by co-immunostaining Synapsin I (pre-synaptic protein) and HOMER1 (post-synaptic protein) on Map2 positive processes (neuronal filament marker). Our data showed that enriched neurons re-plated without a feeder layer and grown in fresh NBA medium have significantly reduced synapse density when compared to similar neuronal cultures supplemented with ACM or direct astroglial co-cultures (Figure 3-18), strongly suggesting that astroglia are necessary for synapse formation, maintenance or a combination in human neurons. Interestingly, despite ACM groups exhibiting lower network activity, their trend for synapse density was nearly double compared to direct co-culture groups. Taken together these data supported that direct neural co-cultures consistently outperformed enriched neuronal cultures alone, and therefore were sufficient to probe the role of astroglial MeCP2 in neural networking.

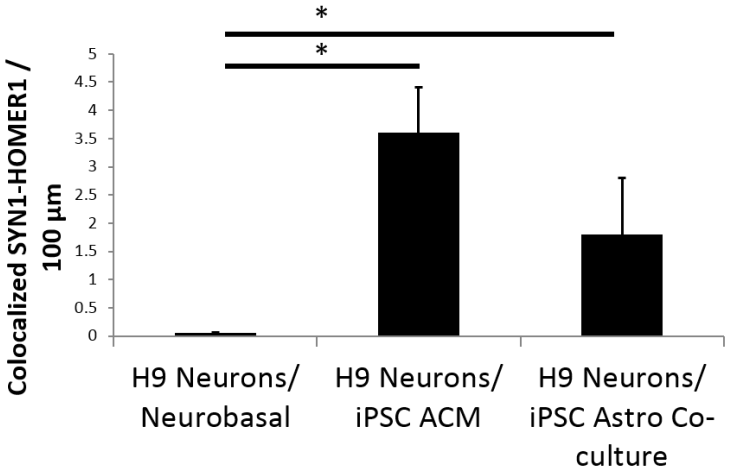


Figure 3-18 Astroglial co-culture and ACM increase neuronal co-localized synapse density.

Synapse density of co-localized Synapsin 1 (pre-) and HOMER1 (post-) synaptic proteins per 50 um of neuronal filaments. * indicates $p < 0.01$.

3.3.3.3 Neurons exhibit limited functionality and diminished network activity co-cultured with MecP2-deficient astroglia

We analyzed control neuronal network activity co-cultured on separate feeder layers of MECP2 isogenic ESC-derived astroglia, or on subcultured primary fibroblasts (cell source of control iPSCs used to generate neurons for this experiment) on MEA substrates. Enriched ctr83-derived neuronal networks grown on MEAs supported by feeder layers of either control human primary fibroblasts or astroglia derived from MeCP2-deficient ESC lines demonstrated greatly reduced electrophysiological activity and limited network synchrony compared to those co-cultured on astrocytes derived from isogenic control ESCs (Figure 3-19). Figure 3-19A depicts a heatmap generated by Axion's Neural Metric Tool represents differential activity between wells and groups as defined by the number of active electrodes (>0.1 Hz). The control neurons spontaneously generated action potentials in most wells, even in those for which the spike frequency was negligible, indicating presence of functional neurons, however, results show that activity is greatly diminished in co-cultures with MeCP2-deficient astroglia or with fibroblasts. Wells with only astroglia or fibroblasts did not exhibit activity. Neuronal networks co-cultured with control astroglia demonstrated varying network wide activity (Figure 3-19D), and no well-wide bursting was observed for other groups, indicating astroglial MeCP2 is necessary for synchronous neuronal network activity, connectivity, or both.

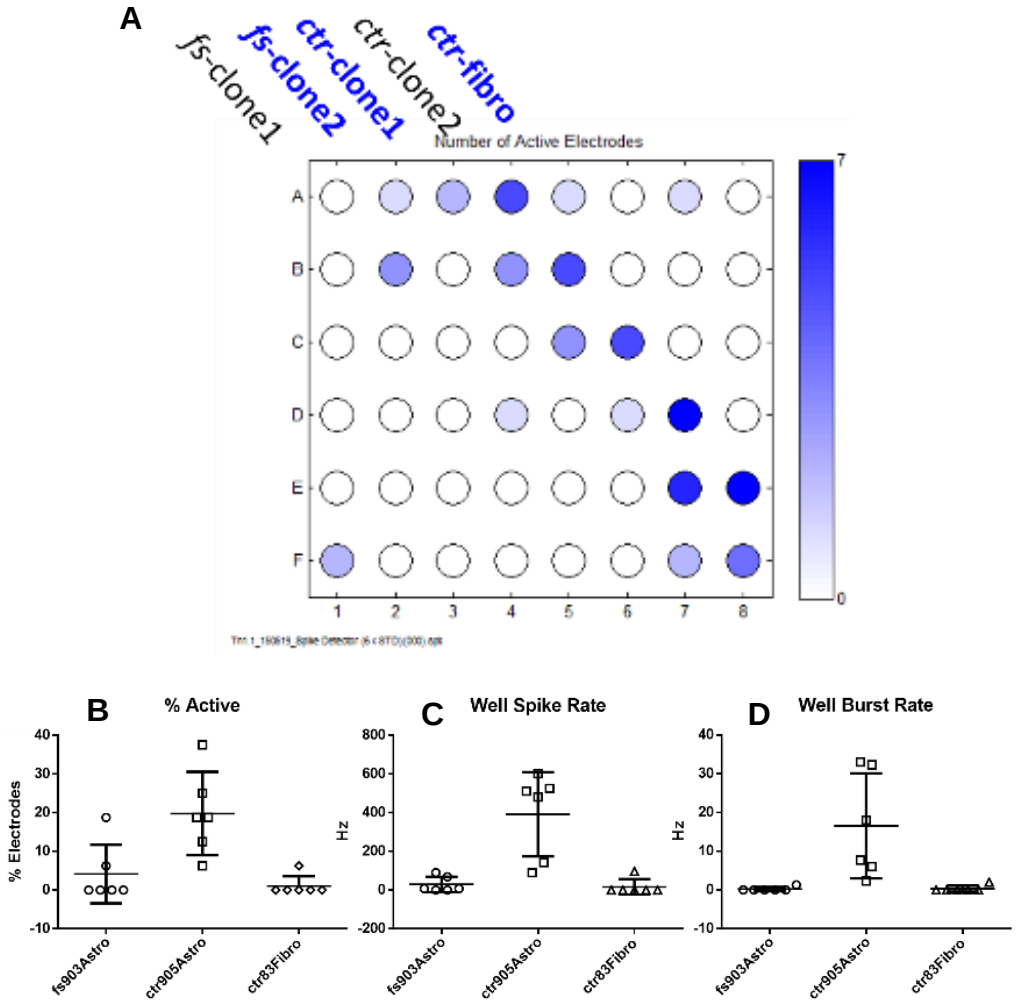


Figure 3-19 Neural activity is diminished by MeCP2-deficient astroglia.

A) Heat map generated by Axis2.0 software representing the number of active electrodes in each well. Samples were plated in a checkerboard arrangement. Figure unlabeled wells exhibiting no activity contained fibroblasts or astroglia without neuronal co-culture. (spiking > 0.1 Hz) B) Plot of mean percent active electrodes per condition. C) Plot of mean well spike rate. D) Plot of mean well burst rate.

3.3.3.4 Neuronal excitatory puncta density is not affected by MeCP2-deficient astroglia

We quantified excitatory synaptic puncta density on neurons in co-culture via immunofluorescence by immunostaining VGLUT1 (pre-synaptic protein) and Map2 positive processes (neuronal filament marker, Figure 3-20). Isogenic *MECP2* control ESC-derived NPC lines were differentiated into heterogeneous neural cultures followed by MACS neuronal enrichment. Astroglia were separately differentiated from MeCP2-difficient or isogenic control ESC-derived NPCs. Primary human fibroblasts were used as an additional control feeder layer. Enriched neurons were re-plated at 5:1 on pre-adhered feeder layers. Using Imaris we quantified excitatory puncta density. Surprisingly, our data showed no difference in presynaptic excitatory puncta for neurons co-cultured on either *MECP2* isogenic group of astroglia, nor on fibroblasts (Figure 3-20).

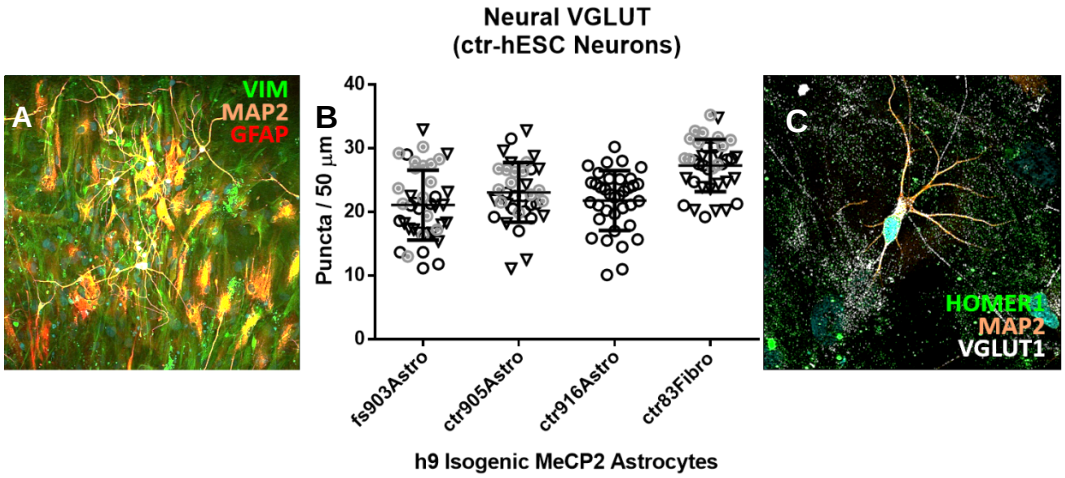


Figure 3-20 Neuronal glutamatergic pre-synaptic puncta density unaffected by feeder cell type.

A) Illustrative image of neurons (MAP2) co-cultured on a feeder layer of astrocytes (GFAP & VIM) B) Quantification of VGLUT1 puncta per 50 um of MAP2 positive neurites. Anova analyses revealed no significance between groups. C) Illustrative image of VGLUT1 puncta corresponding with neuronal filaments (MAP2), as evidenced by epifluorescence microscopy.

3.3.3.5 Neurons have reduced synapse density co-cultured with MeCP2-deficient astroglia

We next quantified synapse density via immunofluorescence by co-immunostaining Synapsin I (pre-synaptic protein) and HOMER1 (post-synaptic protein) on Map2 positive neurites (neuronal filament marker), represented in Figure 3-21B. Briefly, enriched ctr83-derived neuronal networks were co-cultured on separate feeder layers of MECP2 isogenic ESC-derived astroglia, or on subcultured primary human fibroblasts. Our data showed that neurons have significantly reduced synapse density when co-cultured with MeCP2-deficient astroglia compared to co-cultures of control astroglia or fibroblasts (Figure 3-21A). However, the latter two co-culture conditions resulted in similar neuronal synapse density. Together these data suggest that, while MeCP2-deficient astrocytes have a significantly negative effect on synapse density, control astroglia do not influence synapse density any more than fibroblast co-cultures at two weeks post-re-plating.

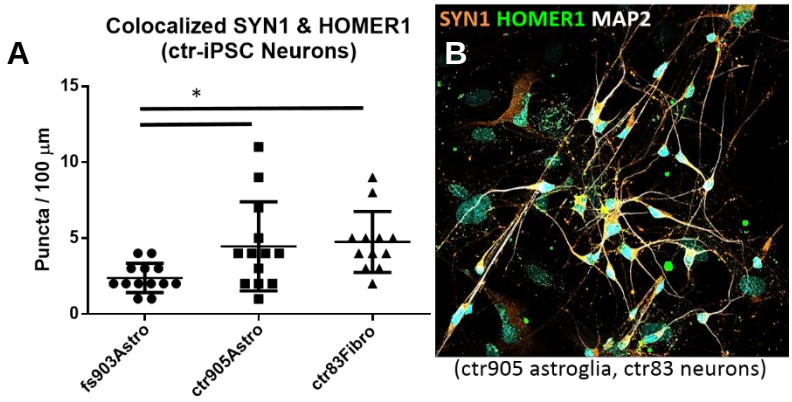


Figure 3-21 Neuronal co-localized synapse density is adversely affected by MeCP2-deficient astroglia.

A) Synapse density of co-localized Synapsin 1 (pre-) and HOMER1 (post-) synaptic proteins per 50 µm of neuronal filaments. * indicates $p < 0.05$. B) Illustrative image of neuronal synapses consisting of SYN1 co-localized with HOMER1 corresponding with neuronal filaments (MAP2), as evidenced by immunofluorescence.

3.3.4 Summary

Astroglia perform a wide range of functions including the modulation of neuronal synapses (Bacci et al., 1999; Freeman, 2005; Ullian, Christopherson, & Barres, 2004) necessary for neural networking and communication. RTT mouse models have demonstrated partial rescue upon re-expression of *Mecp2* preferentially in astrocytes (Lioy et al., 2011). Human iPSC models have previously demonstrated morphologic and single-cell electrophysiological neuronal phenotypes in genetically unaffected neurons caused by exposure to RTT astroglia (Williams et al., 2014), including evidence of transferring mutated MeCP2 into neurons via gap junctions (Maezawa et al., 2009). Although some pieces of the puzzle have been described, the story is not complete. We sought to further delve into the nature and extent of astroglial MeCP2 effects in human neural development and networking. In this study we examined the

impact of astroglial MeCP2 on neural network electrophysiology using isogenic stem cell models. We separately generated isogenic *MECP2* astroglia from sublines of an extensively characterized human ESC line genetically edited to include a nonsense *MECP2* mutation, and neurons from iPSC control NPC lines. Heterogenetic co-cultures demonstrate that MeCP2-deficient astrocytes cause significant neurophysiological differences on co-cultured neuronal networks when compared to isogenic control astroglia. Our findings demonstrate the ability to reconstitute a complex neuronal-astroglial system to distinguish the contribution of specific cell types to RTT pathology.

3.4 Conclusions

In conclusion, we provide an alternative to current *in vitro* and *in vivo* CS models by generating human neurons and neural cultures from human CS donor-derived iPSCs. These neural populations show transcriptional dysregulation of several pathways including the GH/IGF-1 pathway, reduced network synchrony and reduced synapse density. Our results prove feasibility and demonstrate utility of this new *in vitro* human model of CS neuropathology; further, our discovery of GH/IGF-1 dysregulation in disease-appropriate neural tissue provides a specific potential therapeutic target.

Additionally, I provided an important update to our model of neural development. Combining recently accessible isogenic stem cell methods with MEA technology has allowed us to begin investigating cell-type specific contributions to complex networking in functional neural co-cultures. Astroglia, the most prevalent cell type in the brain, exhibited non-autonomous effects on both physical and electrophysiological aspects of neuronal networks responding to either astroglial conditioned medium or direct co-culture. Further, MeCP2-deficient astroglia adversely effected control neuronal network synapse density and activity in direct co-cultures. Overall our results emphasize the necessity and value of increased sophistication in brain disease models.

3.5 Acknowledgements

Part of Chapter 3.1 and the contents of Chapter 3.2 were adapted for Human Molecular Genetics and published as “Cockayne Syndrome-derived neurons display reduced synapse density and altered neural network synchrony**.”** Vessoni AV, Herai RH, Karpiak JV, Leal A, Trujillo C, Quinet A, Menck CFM, Muotri AR. Human Molecular

Genetics, 2016. Published online Jan 4, doi:10.1093/hmg/ddw008. The dissertation author was a main contributor and co-author of this work.

Chapter 4

Three-dimensional scaffolds accelerate *in vitro* neuronal differentiation & laminar co-cultures reveal new neurophysiological phenotypes in Rett Syndrome

Chapter 4

4.1 Abstract

Probing a wide range of cellular phenotypes in neurodevelopmental disorders using patient-derived neural precursor cells (NPCs) can be facilitated by three-dimensional (3D) assays, as two-dimensional (2D) systems cannot entirely recapitulate the arrangement of cells in the brain. Here, we developed a novel 3D migration and differentiation assay in layered hydrogels to examine how these processes are affected in neurodevelopmental disorders, such as Rett syndrome (RTT). Our soft 3D system mimics the brain environment and accelerates maturation of neurons from human iPSC-derived NPCs, yielding electrophysiologically active neurons within just three weeks. Using this platform, we revealed a genotype-specific effect of MeCP2 dysfunction on iPSC-derived neuronal migration and maturation (reduced neurite outgrowth and fewer synapses) in 3D layered hydrogels. Thus, this 3D system expands the range of neural phenotypes that can be studied *in vitro* to include those influenced by physical and mechanical stimuli or requiring specific arrangements of multiple cell types.

4.2 Brief introduction and rationale

Neuronal migration and maturation is a key step in brain development. Defects in this process have been implicated in many disorders, including autism (Marchetto et al., 2010; Wegiel et al., 2010) and schizophrenia (Deutsch, Burket, & Katz, 2010). Thoroughly understanding how neural precursor cell (NPC) migration is affected in neurodevelopmental disorders requires a means of dissecting the process using cells with genetic alterations matching those in patients. Existing *in vitro* assays of migration generally involve measurement of cell movement across a scratch or gap or through a

membrane towards a chemoattractant in two-dimensional (2D) culture systems. Although widely used, such assays may not accurately reflect *in vivo* differences, as neuronal migration is tightly regulated by physical and chemical cues in the extracellular matrix that NPCs encounter as they migrate.

in Vitro three-dimensional (3D) culture systems offer a solution to these limitations (DeForest & Tirrell, 2015; Dvir et al., 2011; S Khetan et al., 2013; Musah et al., 2012; Otsuji et al., 2014; Zorlutuna et al., 2012). Compared to 2D culture, a 3D arrangement allows neuronal cells to interact with many more cells (Zorlutuna et al., 2012); this similarity to the *in vivo* setting has been shown to lengthen viability, enhance survival, and allow formation of longer neurites and more dense networks in primary neurons in uniform matrices or aggregate culture (Bellamkonda et al., 1995; H. K. Choi, Won, & Heller, 1993; Horie & Akahori, 1994; Lampe, Antaris, & Heilshorn, 2013; Peretz et al., 2007). Indeed, 3D culture systems have been used to study nerve regeneration, neuronal and glial development (Leipzig & Shoichet, 2009; J Mariani et al., 2015; Jessica Mariani et al., 2012; A Odawara et al., 2014; Pasca et al., 2015; Seidlits et al., 2010), and amyloid-β and tau pathology (S. H. Choi et al., 2014). Thus, measuring neuronal migration through a soft 3D matrix would continue this trend towards using 3D systems to study neuronal development and pathology.

We sought to develop a 3D assay to examine potential migration and neuronal maturation defects in Rett syndrome (RTT), a genetic neurodevelopmental disorder that affects 1 in 10,000 female children in the U.S and is caused by mutations in the X-linked methyl-CpG-binding protein-2 (*MECP2*) gene (Amir et al., 1999). Studies using induced pluripotent stem cells (iPSCs) from RTT patients in traditional 2D adherent culture have revealed reduced neurite outgrowth and synapse density, as well as

altered calcium transients and spontaneous postsynaptic currents (Marchetto et al., 2010). However, 2D migration assays have been unable to reveal potential defects in this developmental process, which could be affected since MeCP2 regulates multiple development-related genes (Carouge et al., 2010; W. G. Chen et al., 2003). Migration of RTT iPSC-derived NPCs has not previously been studied.

Using a novel 3D tissue culture system that allows creation of laminar architectures, we studied differences in migration of MeCP2-mutant *vs.* control iPSC-derived NPCs. This approach revealed migration defects for MeCP2-mutant NPCs induced by either astrocytes or neurons. Further, this 3D system accelerated maturation of neurons from human iPSC-derived NPCs, yielding electrophysiologically active neurons within just three weeks. With mature neurons derived from RTT patients and controls, we further confirmed defective neurite outgrowth and synaptogenesis in MeCP2-mutant neurons. Thus, this 3D system enables study of morphological features accessible in 2D system as well as previously unexamined phenotypes.

4.3 Materials and methods

4.3.1 Synthesis of hyaluronic acid methacrylate (HAMA)

Hyaluronic acid methacrylate (HAMA) was prepared following a modified version of reported procedures (Hachet et al., 2012; Messager et al., 2013). Hyaluronic acid (91-175 kDa, 1 g, 2 wt%) was suspended in ultrapure water (50 mL) and the resulting mixture was stirred overnight in a cold room at 4 °C until completely solubilized. Dimethylformamide (DMF) (33.5 mL) was then added to obtain 3:2 water/ DMF and the resulting mixture was stirred vigorously in an ice bath at 0 °C. Methacrylic anhydride (0.74 mL, 5 mmol) was added dropwise over 2 hr at 0 °C while pH was

maintained between 8 and 9 by addition of 0.5 M NaOH, and the reaction was stirred overnight at 4 °C. NaCl (2.4 g, 41 mmol, 0.5 M) was then added to stop the reaction. The polymer was precipitated in cold ethanol (50 mL) and the white suspension was stirred in an ice bath for 30 min. The supernatant was removed by centrifugation at 5000 x g for 5 min. The resulting white solid was dissolved in ultrapure water (50 mL) and purified by dialysis (Float-A-Lyzer® G2 10 mL, 20 kDa, Spectrum Labs) against water for three days (water was changed every 8-10 h). Purified HAMA was recovered by freeze-drying (810 mg). The degree of methacrylation (DM) was determined by 1H-NMR (600 MHz, D2O, 298 K) by integration of the methacrylate proton signal at 5.7 ppm or 6.2 ppm relative to the acetyl protons signal of HA at 2 ppm; DM=17±1%.

4.3.2 Synthesis of lithium acylphosphonate (LAP) photoinitiator

The initiator was synthesized in a two-step process as described in the literature (Fairbanks et al., 2009; Majima, Schnabel, & Weber, 1991). 2,4,6-Trimethylbenzoyl chloride (3.2 g, 2.9 mL, 17.5 mmol) was added dropwise to dimethyl phenylphosphonite (2.98 g, 2.8 mL, 17.5 mmol) at room temperature (RT) under argon and reacted via a Michaelis-Arbuzov reaction. The reaction mixture was then stirred for 18 h, and a solution of lithium bromide (6.2 g, 70 mmol) in 2-butanone (100 mL) was added. The resulting mixture was then stirred at 50 °C for 10 min. A white precipitate formed and the resulting suspension was stirred at RT for 4 h and then filtered. The filtrate was washed 3 times with 2-butanone to remove unreacted lithium bromide and dried under high vacuum to yield LAP as a white powder (4 g, 80%). 1H NMR (600 MHz, D2O) δ 7.71 (dd, 2H, J = 7.9 Hz, 7.5 Hz), 7.56 (t, 1H, J = 7.5 Hz), 7.46 (t, 2H, J = 7.9 Hz), 6.88 (s, 2H), 2.23 (s, 3H), 2.01 (s, 6H).

4.3.3 Fluorescent labeling of HAMA

HAMA (100 mg, DM = 17±1%) was dissolved in ultrapure water (10 mL), and EDC (0.2 mg, 1.33 μmol), NHS (0.15 mg, 1.33 μmol) and Alexa Fluor® 647 hydrazide (0.2 mg, 0.17 μmol) were added. The resulting mixture was stirred overnight in the dark under argon at room temperature, then transferred to a dialysis membrane (Float-A-Lyzer® G2 10 mL, 20 kD, Spectrum Labs) and dialyzed against water for three days (water was changed every 8-10 h). The purified, fluorescent-labeled polymer HAMA-Alexa647 was recovered by freeze-drying (87.5 mg).

4.3.4 Fabrication and characterization of 3D hydrogel

Hydrogels were formulated from HAMA (17±1% methacrylation) with the photoinitiator LAP under UVA irradiation (average intensity of 2.5mW/cm2, broadband UV centered at 365 nm; Bayco, UVR-9000, Wylie, TX). Varying HAMA concentrations and addition of various adhesion molecules identified a formulation supporting neuronal differentiation and migration: 1% (w/v) HAMA gel and 0.032% (w/v) LAP containing laminin (8 μg/mL). Cells were seeded at 15×10^6 /mL in the HAMA solution, which was transferred into 5 mm × 5 mm × 400 μm rubber molds and UV-irradiated for 60 s, 90 s or 120 s to crosslink. An atomic force microscope (AFM) was used to determine the modulus.

4.3.5 Atomic force microscopy (AFM)

Elastic modulus was measured via indentation using an MFP-3D-Bio (Asylum Research) atomic force microscope (AFM) with a 45 μm-diameter polystyrene spherical tip (Novascan) with a nominal spring constant of 0.03 N/m. Hydrogels were mounted

on glass slides and kept hydrated in PBS. The spherical probe was indented into the sample with approach and retraction velocities of 2 μm/s and 20 μm/s with a force trigger of 2 nN. Indentation force curves were analyzed using custom code in Igor Pro (Wavemetrics), and elastic moduli were computed using a linearized Hertz model (Ramalingam, 2012).

4.3.6 Scanning electron microscopy (SEM)

Hydrogels were placed on a glass coverslip and excess moisture was removed. Hydrogels were next flash-frozen by immersion in liquid nitrogen, cryo-fractured using a scalpel blade, and lyophilized overnight. Freeze-dried hydrogel fragments were placed on conductive copper tape on an SEM sample holder, sputter-coated with gold (Cressington 108Auto Sputter Coater), and imaged using a field emission SEM (Agilent 8500 FE-SEM) at 1 kV acceleration.

15 random low magnification micrographs were obtained from each specimen. Micrographs were analyzed for the quantity of synapses. Spine synapses were identified by an electron dense region associated with vesicles pre-synaptically and contained a spine apparatus with post-synaptic densities as described previously (Bamji et al., 2003). Approximately 15 electron micrographs (324 μm^2) per sample were analyzed in a blinded fashion for total synapse number per area (synapse #/324 μm^2).

4.3.7 Transmission electron microscopy (TEM)

Hydrogels were fixed in 0.15 M cacodylate buffer containing 2.5% glutaraldehyde, 2% paraformaldehyde and treated for 1 h with 1% OsO4. Fixed gels were then dehydrated in solutions containing increasing concentrations of ethanol,

negatively stained with 2% uranyl acetate and embedded in durcupan resin at 60 °C. Thin sections of 70-80 nm were cut with a diamond knife on a Leica ultramicrotome and collected on 300 mesh grids. Sections were stained with 0.3% lead citrate for 1 min and imaged using a transmission electron microscope (FEI Tecnai Spirit G2 BioTWIN) at 80 kV.

4.3.8 NPC differentiation and culture

Fibroblasts from male RTT (Q83X and N126I) patients and their fathers (WT83 and WT126) were reprogrammed and differentiated into NPCs as previously described (Griesi-Oliveira et al., 2015). Two different pairs of control iPSCs and RTT iPSCs were used in our studies to mitigate line-to-line variation. iPSC colonies were plated on Matrigel-coated (BD Biosciences) plates and maintained in mTeSR1 media (Stem Cell Technologies) for 5 days, after which media was changed to N2 (Dulbecco's modified Eagle's medium (DMEM)/F12 media supplemented with 1X N2 supplement (Life Technologies) and 1 µM dorsomorphin (Tocris, Ellisville, MO, USA)). After 2 days, colonies were removed and cultured in suspension as embryoid bodies for 2-3 weeks using N2 media with dorsomorphin. Embryoid bodies were then gently dissociated with Accutase (Gibco), plated on Matrigel-coated dishes and maintained in DMEM/F12 supplemented with N2, B27, and basic fibroblast growth factor (bFGF2) (Dulbecco's modified Eagle's medium/F12 media supplemented with 0.5X N2, 0.5X B27 supplements, 20 ng/mL bFGF2 and 1% penicillin/streptomycin). Rosettes emerging after 3 or 4 days were manually selected, gently dissociated with Accutase and plated in dishes coated with 10 µg/mL poly-ornithine and 5 µg/mL laminin (pOrn/Ln). NPCs were maintained in DMEM/F12 with N2, GEM21 and bFGF2. Moreover, we have also

generated *MECP2*-mutant isogenic cell lines using CRISPR/Cas9 genome editing (manuscript in preparation). Isogenic stem cell models of RTT were generated by a frame-shift mutation in *MECP2* (similar to that found in one RTT donor) in H9 ESCs. Additionally, we rescued a patient cell line by reversing an early stop codon mutation (Q83X), restoring MeCP2 protein levels to normal (rQ83X) using the CRISPR/Cas9 genome editing (manuscript in preparation). Number of clones from iPSCs used in each experiment in this study is listed in Table 4-1.

Table 4-1 Number of clones from iPSCs used in each experiment.

The number indicates the times a clone was used for that particular method.

	Subjects											
	WT83		Q83X		H9 - ESC	ESC - K82*fs*	Q83X - C2	rQ83X	WT126		N126I	
Experiments/clones	*C1*	*C2*	*C1*	*C2*	*C1*	*C1*	*C1*	*C1*	*C1*	*C2*	*C1*	*C2*
NPC staining	2	2	2	2	2	2	2	2	2	2	2	2
NPC FACS	2	2	2	2	2	2	2	2	2	2	2	2
Neuron differentiation	3	3	3	3	3	3	3	3	3	3	3	3
Astrocyte differentiation	3	3	3	3	3	3	3	3	3	3	3	3
Neuron MACS	3	3	3	3	3	3	3	3	3	3	3	3
Astrocyte FACS	3	3	3	3	3	3	3	3	3	3	3	3
Neuron /NPC migration	3	3	3	3	3	3	3	3	3	3	3	3
Astrocyte /NPC migration	3	3	3	3	3	3	3	3	3	3	3	3
Q RT-PCR	3	3										
TEM	3	3										
Electrophysiology	3	3	3	3								
Western blotting	3	3										
Immunostaining	3	3	3	3	3	3	3	3	3	3	3	3

4.3.9 Astrocyte differentiation

Astrocytes were obtained by allowing NPCs to form neurospheres. bFGF2 was removed, and Rho-associated protein kinase (ROCK) inhibitor was added for 48 h to induce neuronal differentiation. Spheres were maintained under rotation in neuronal

medium for 1 week followed by 2 weeks in astrocyte growth medium (AGM, Lonza) prior to plating. Spheres were maintained for astrocyte differentiation and later removed to enrich for astrocytes.

4.3.10 Neuronal differentiation

In adherent cultures, NPCs were differentiated into neurons by adding 10 µM ROCK inhibitor (Y-27632, Calbiochem, La Jolla, CA, USA) in the absence of bFGF2. In 3D hydrogels, NPCs were encapsulated prior to polymerization and cultured in NG medium with Rock inhibitor for 24 h. Medium was changed every other day. To examine whether 3D differentiated neurons were functionally mature, cells differentiated for 3 weeks in hydrogels were transferred to glass slides after digestion using hyaluronidase (2000 units/mL) overnight. After 4 days of monolayer culture on slides, electrophysiological activity of eGFP-positive cells was examined. As hyaluronidase may affect neuronal function, 2D differentiated neurons were also treated with hyaluronidase for direct comparison.

4.3.11 Lentivirus preparation and infection

The lentiviral vector was derived from HIV-1 (Invitrogen, Carlsbad, CA, USA). The Syn::eGFP and GFAP::tdTomato vectors were obtained by cloning the synapsin-1 promoter (a gift from Dr. G. Thiel, Hamburg, Germany) or the GFAP promoter into the vector (Marchetto et al., 2010). CMV::eGFP and CMV::tdTomato vectors were obtained by cloning eGFP or tdTomato under the CMV promoter into the lentivirus backbone. Lentivirus (Lentiviral Expression System, Invitrogen) was produced according to the manufacturer's instructions. The destination plasmid was co-

transfected with the mixture of packaging plasmids into 293FT cells (Invitrogen) using polyethylenimine. The medium was replaced 8 h after transfection with Dulbecco's modified Eagle's medium containing 5% fetal bovine serum. After 3 days, viral particles in the supernatant were collected, filtered through 0.45 μm filters (Millipore, Corning, NY, USA), and concentrated by high speed centrifuge (20,000 rpm, 2 h, 4 °C). Virus solution was stored in aliquots at −80 °C until use.

4.3.12 Western blotting

Protein extracts from differentiated cells were resolved on 10% SDS-PAGE gels and transferred to nitrocellulose membranes, which were probed with rabbit polyclonal antibody against eGFP (sc-8334; Santa Cruz, 1:1000) or rabbit polyclonal antibody against Hsp90 (sc-33755; Santa Cruz, 1:1000). Membranes were subsequently probed with a horseradish peroxidase-conjugated secondary antibody and developed using an ECL detection kit (Amersham Biosciences, Pittsburgh, PA).

4.3.13 Quantitative real-time PCR

Real-time PCR was performed as previously described (Marchetto et al., 2010). Briefly, total RNA was purified from ESCs using an RNeasy Mini kit (Qiagen, 74106). Total RNA (1 μg) was reverse-transcribed into cDNA and analyzed by quantitative real-time PCR using FastStart Universal SYBR Green Master (ROX) (Roche, 04 913 850 001). Primer sequences are listed in Table 4-2. The average threshold (Englund, Björklund, & Wictorin, 2002) was determined for each gene and normalized to GAPDH.

Table 4-2 Sequence of primers used in qPCR experiments.

Gene	Primer F	Primer R
Nestin	CTGCTACCCTTGAGACACCTG	GGGCTCTGATCTCTGCATCTAC
MAP2	CTCAGCACCGCTAACAGAGG	CATTGGCGCTTCGGACAAG
Ctip2	GGTGCCTGCTATGACAAGG	GGCTCGGACACTTTCCTGAG
Syn I	AGTTCTTCGGAATGGGGTGAA	CAAACTGCGGTAGTCTCCGTT
VGluT1	CTGGGGCTACATTGTCACTCA	GCAAAGCCGAAAACTCTGTTG
GAPDH	CATGAGAAGTATGACAACAGCCT	AGTCCTTCCACGATACCAAAGT

4.3.14 Flow cytometric analysis

hNPCs were fixed, permeabilized, and stained with specific antibodies using standard procedures and analyzed using a Becton Dickinson LSR-II and FACS Diva software as previously described (Marchetto et al., 2010). Differentiated astrocytes expressing GFAP::tdTomato were digested using papain and DNase (Worthington Biochemical Corporation) at 37 °C for 30 min and tdTomato-positive cells were sorted using BD Influx.

4.3.15 Immunostaining and imaging

Cells (either cultured on pOrn/Ln coated coverslips or in hydrogels) were fixed with 4% paraformaldehyde in phosphate-buffered saline (PBS) for 15 min at RT. After three washes with PBS, cells were incubated in 0.1% Triton X-100 in PBS for 15 min at RT. After blocking with 1% BSA in PBS for 2 h at RT, cells were incubated with either anti-Nestin (ab51755, Abcam, 1:500), anti-Sox1 (AF3369, R&D, 1:100), anti-Sox2 (2748S, Cell Signaling, 1:500), anti-PAX6 (HPA030775, Sigma, 1:100) anti-Map2 (ab5392, Abcam, 1:500), anti-Tuj1 (T8660, Sigma, 1:500), anti-Syn1 (ab1543p,

Abcam, 1:500), anti-Ctip2 (Ab18465, Abcam, 1:500), anti-Tbr1 (Ab31940, Abcam, 1:250), anti-GAD1/GAD67 (MAB5406, Abcam, 1:500), anti-GABA (A0310, Sigma, 1:500), anti-vGlut1 (135.311, Synaptic system, 1:500), anti-TH1 (SC-14007, Santa Cruz, 1:500), anti-GFAP (Z033429-2, Dako, 1:500) or anti-S100β (NBP1-41373, Novus Bio, 1:500) overnight at 4 °C, followed by washing and incubating with the secondary antibody for 45 min in the dark at RT. Coverslips were mounted on glass slides using Vecta shield mounting medium for fluorescence. Stained cells were examined using an Olympus (FV1000) confocal microscope.

4.3.16 Migration assay

Two-layered 3d hydrogel scaffolds, in which NPCs infected with lentivirus encoding a fluorescent reporter were loaded in the lower layer containing 5% iodixanol and sorted astrocytes or 2D differentiated neurons infected with indicated lentivirus encoding a fluorescent reporter were loaded in the upper layer, were crosslinked by UVA irradiation (see Hydrogel fabrication). Hydrogels containing astrocytes were cultured either in NG or AG medium and those containing neurons were cultured in NG medium. Hydrogels were swollen in medium for 12 hours. This day is termed as “0 day”. Live-cell images of the region where the two layers interface were acquired using an Olympus confocal microscope. Z-stacks were reconstructed using Imaris software. The width of the region containing both NPCs and astrocytes (or neurons) was measured by marking the furthest migrated cell of each type with a horizontal line and quantifying the distance between them.

4.3.17 Electrophysiology

For 3D differentiated neurons, we differentiated for three weeks and transferred them to glass slides by digesting hydrogels using hyaluronidase (2000 units/mL) overnight. After four additional days of culture on slides, electrophysiological activity of individual neurons was examined. Patch clamp recording was performed on single neurons re-plated in monolayer cultures using an Axopatch 200B amplifier. Whole-cell patch clamp recordings were performed from cells co-cultured with mouse astrocytes after 3 weeks of differentiation for sEPSC (Marchetto et al., 2010). Neurons were identified by Syn1::eGFP fluorescence. All experiments were performed at RT. Patch pipettes (5-8 MΩ) contained 150 mM KCl, 5 mM NaCl, 1 mM MgCl2, 2 mM ethylene glycol tetraacetic acid (EGTA)-Na, 10 mM HEPES at pH 7.2. The extracellular solution contained 125 mM NaCl, 3 KCl, 10 mM glucose, 26 mM NaHCO3, 1.2 mM NaH2PO4, 2 mM CaCl2 and 1 mM MgCl2. 1 µM TTX was bath-applied following dilution into the external solution from concentrated stock solutions. All data were acquired with pClamp 10.0 software and analyzed with MATLAB v2009b.

4.3.18 Statistical analysis

For all viability experiments, a two-tailed Student's t-test was used to evaluate statistical significance, which was noted when *$p < 0.05$, ** $p < 0.01$ or *** $p < 0.005$.

4.4 Results

4.4.1 Modular design of layered hydrogels for migration of iPSC-derived NPCs

We developed a novel and simple assay measuring migration through a soft 3D matrix of hyaluronic acid to better imitate the physical environment within the brain.

This 3D hydrogel-based migration assay relies on density gradient multilayer polymerization (DGMP, (Joshi-Barr et al., 2013; Karpiak et al., 2012)), which consists simply of mixing small-molecule density modifiers with prepolymer-containing cell suspensions and gently layering them with a syringe. The prepolymer in these studies was hyaluronic acid methacrylate (HAMA, 17±1% methacrylation); varying UVA irradiation time yielded hydrogels of variable stiffness (Figure 4-1A & B). Hydrogels with stiffness around 100 Pa and pore size around 10 μm were used (Figure 4-1C). By recreating cell-cell interactions, 3D layered structures enable the formation of tissue-mimetic architectures and promote more realistic physiological responses than conventional 2D culture. We used the layered hydrogel model to investigate the migration of NPCs towards different neuronal cell types: NPCs, astrocytes, or neurons (Figure 4-1D). As astrocytes have been shown to promote neural migration (Mason et al., 2001), we first evaluated NPC migration toward these cells. Human NPCs were derived from human non-affected control iPSC lines (WT83) and infected with lentivirus expressing green fluorescent protein (eGFP) under the control of the cytomegalovirus (CMV) promoter to track migration by microscopy. Immunofluorescence and flow cytometry confirmed expression of progenitor markers Nestin, Sox1, Sox2 and PAX6 (Figure 4-2A & B). Human astrocytes were generated from differentiated human NPCs and infected with lentivirus expressing tdTomato under the control of the glial fibrillary acidic protein (GFAP) promoter, then enriched by flow cytometry for tdTomato-positive cells (Figure 4-2C & D). Immunofluorescence confirmed expression of astrocyte markers, GFAP and S100 calcium-binding protein β (S100β, Figure 4-2E). Migration

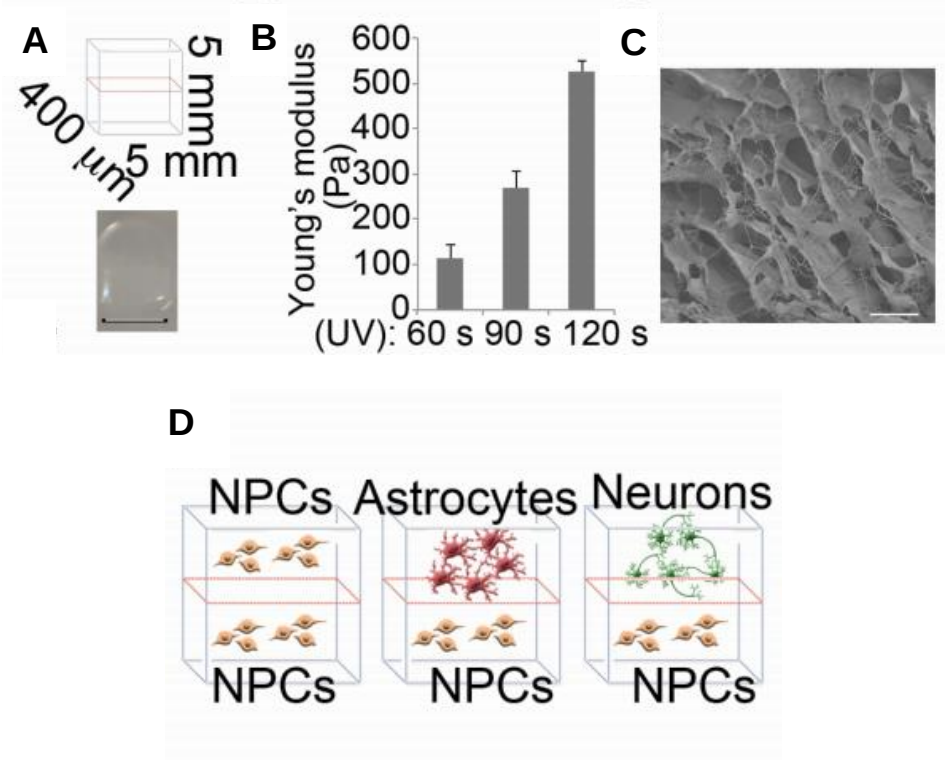


Figure 4-1 Setup of layered hydrogels to study migration of human iPSC-derived NPCs.

A) Bright-field image of two-layered hydrogels. Scale bar, 5 mm. B) Compressive moduli of HAMA hydrogels measured by AFM following varying UV exposure time. C) Scanning electron microscopy (SEM) imaging of HAMA hydrogels. Scale bar: 10 µm. D) Schematic representation of a two-layered hydrogel assay of NPC migration towards NPCs, astrocytes, or neurons.

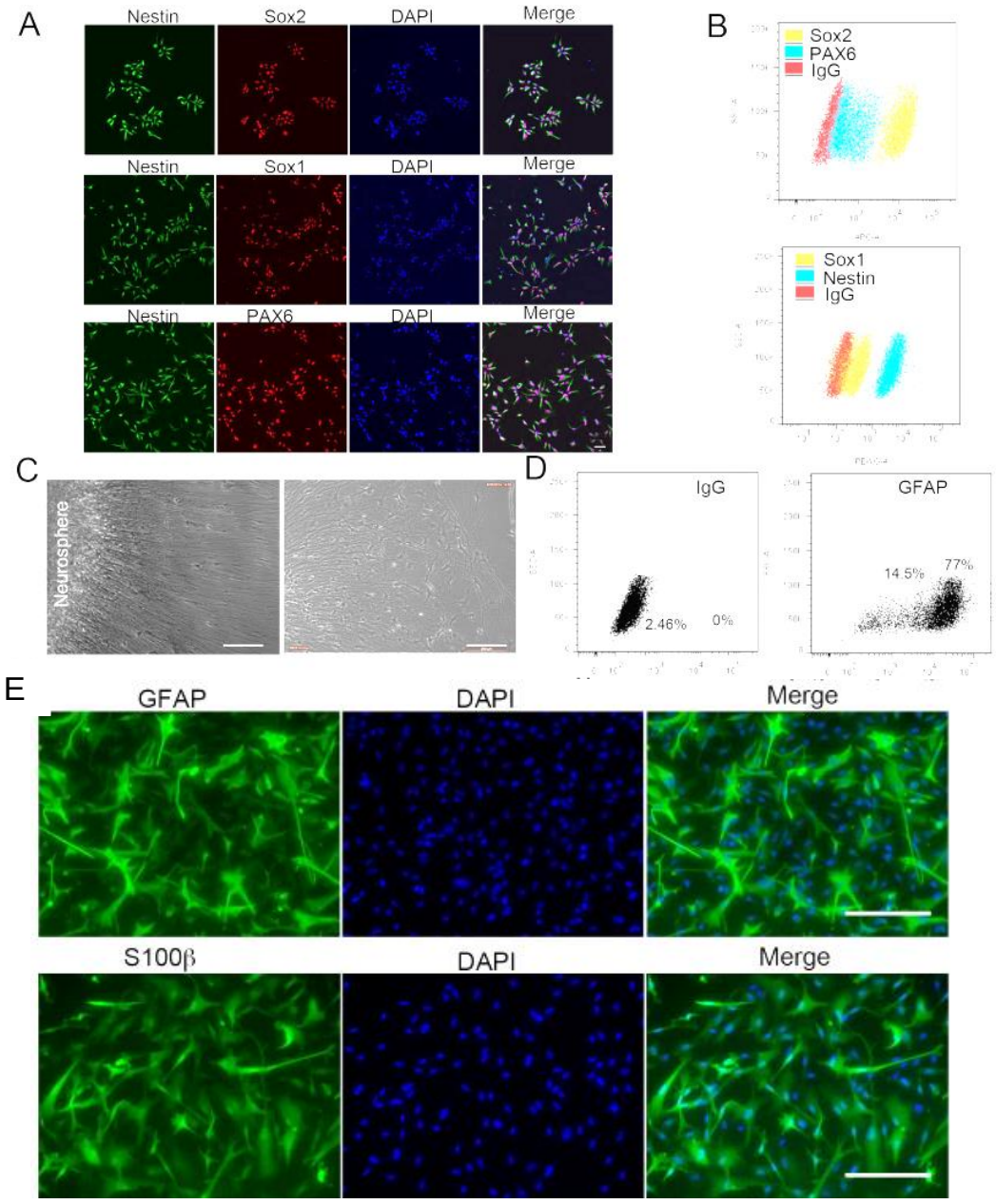


Figure 4-2 Characterization of NPCs and astrocytes derived from iPSCs.

A) Representative immunofluorescence of WT83 NPCs stained for Nestin, Sox2, Sox1, PAX6 and DAPI. Scale bar: 50 µm. B) FACS analysis of PAX6, Sox2, Nestin and Sox1 expression in WT83 NPCs. C) Representative images of NPC-derived astrocytes migrating from a neurosphere. Scale bar: 200 µm. (D) FACS analysis of GFAP expression in NPC-derived astrocytes. E) Representative image of NPC-derived astrocytes immunostained for GFAP and S100β. Scale bar: 100 µm.

was examined in two-layered hydrogels containing sorted GFAP::tdTomato-positive astrocytes in the top and CMV::eGFP-positive NPCs in the bottom layer, cultured in either neuronal growth medium (NG) or astrocyte culture medium (AG), respectively. After three days, we observed dramatic NPC migration towards astrocytes (Figure 4-3A and B). Using real-time fluorescence microscopy, we showed NPC migration towards astrocytes in a time-dependent manner (Figure 4-3C). To further confirm that NPCs in the bottom layer were migrating toward astrocytes, we used fluorescence-labeled HAMA to identify the top layer in our 3D migration assay. We found that GFAP::tdTomato-positive astrocytes remained in the fluorescence-labeled top layer, while CMV::eGFP-positive differentiating NPCs migrated into it (Figure 4-3D).

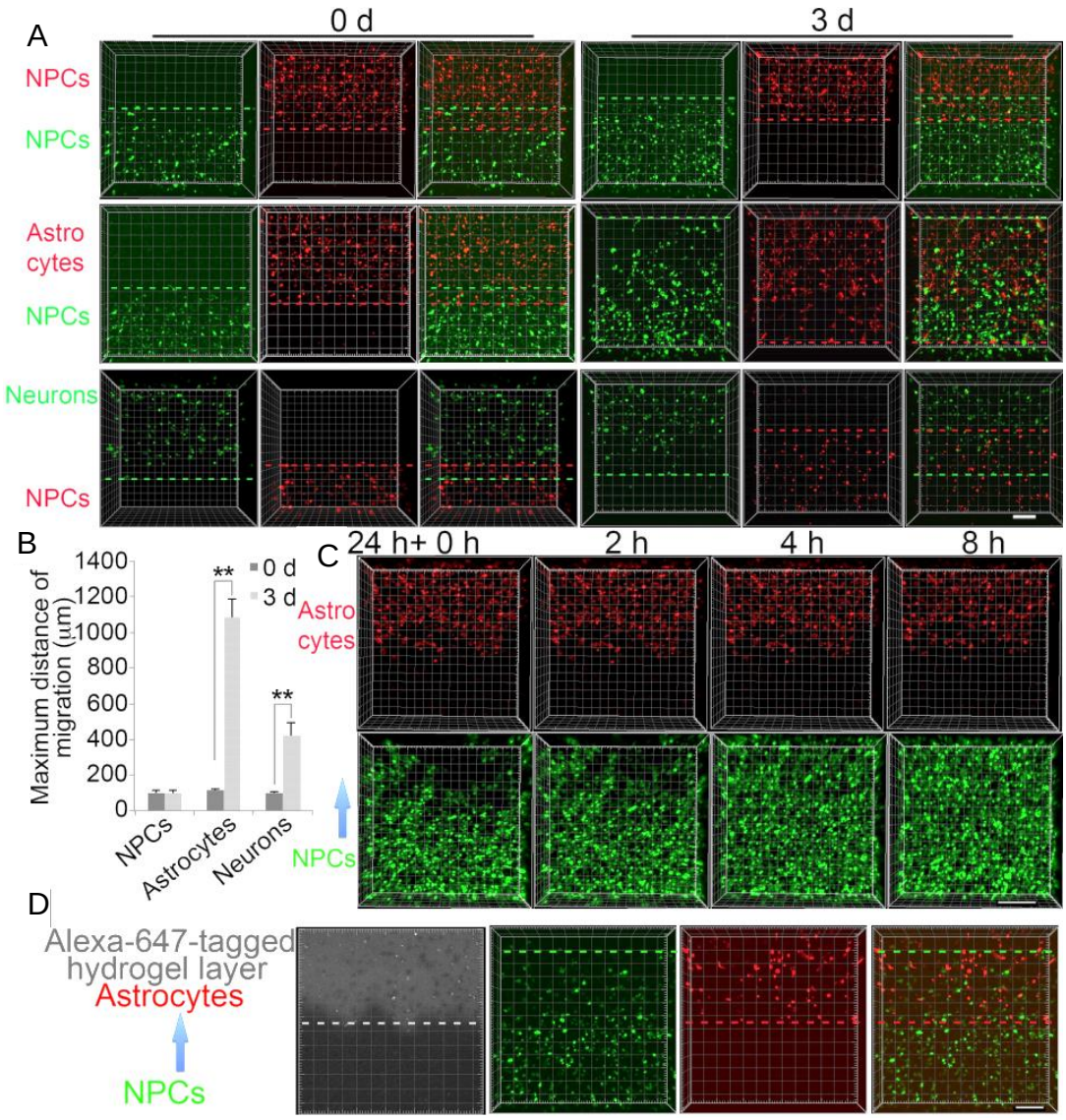


Figure 4-3 Layered hydrogels to study migration of iPSC-derived NPCs.

A) Representative images of NPC migration induced by NPCs, astrocytes, or neurons for indicated times. Dashed lines identify the max migration of each cell type; distance between red and green dashed lines indicates maxi migration distance. B) Quantification of max migration distance induced by NPCs, astrocytes or neurons. Bars represent means; *$p < 0.05$ and **$p < 0.01$. (n=3). C) Time-lapse images of NPC migration induced by astrocytes for 8 h. D) Representative images of NPC migration induced by astrocytes for 1.5 days. Alexa647-labeled HAMA identifies the top layer. ALL scale bars: 200 μm.

We further evaluated NPC migration induced by neurons in our 3D system. Human neurons positive for the neuronal markers β-III-tubulin (Tuj1) and Map2 (Figure 4-4A) were generated from differentiated human NPCs as described (Marchetto et al., 2010) and enriched by magnetic-activated cell sorting for CD44 and CD184 double-

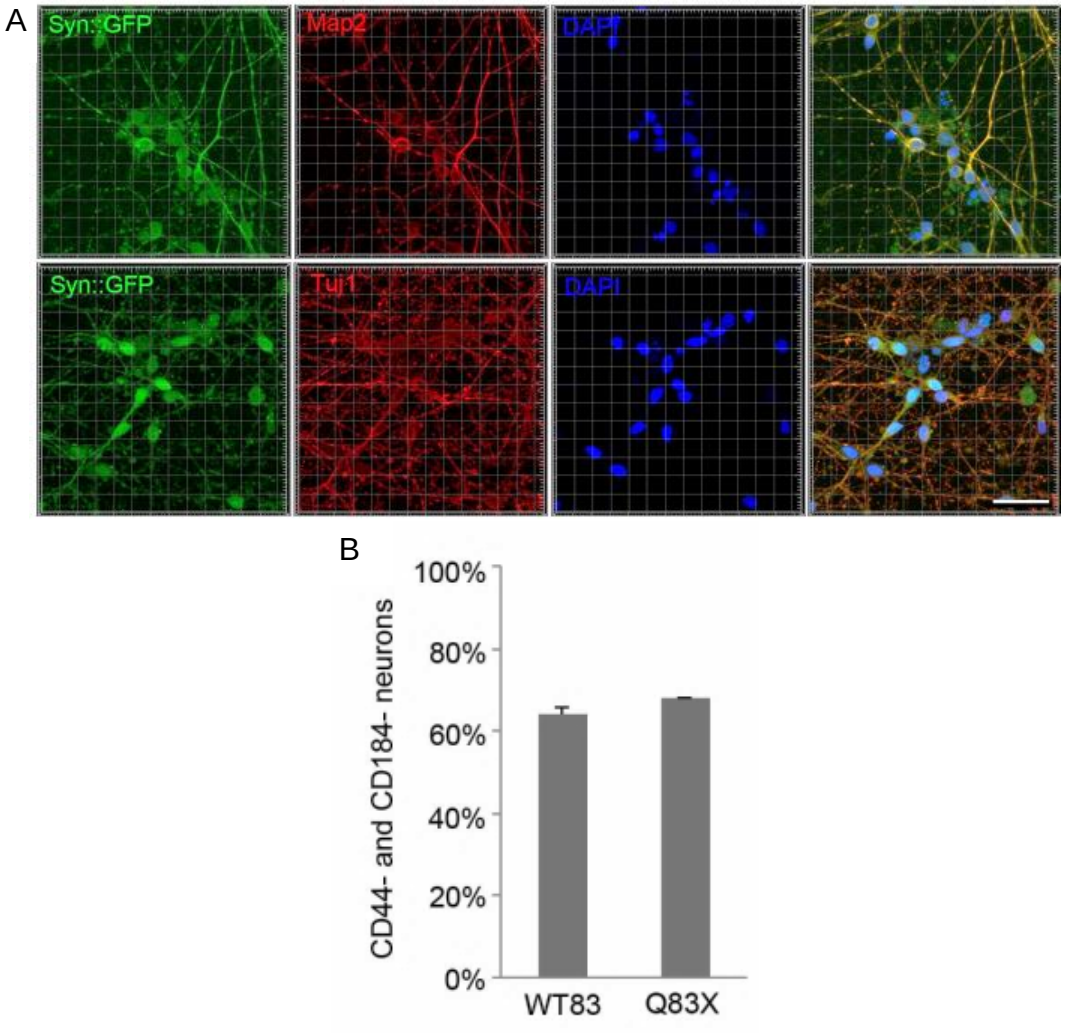


Figure 4-4 Characterization of NPC-derived neurons.

A) Representative image of NPC-derived neurons in 2D immunostained for Tuj1 and Map2 (red), expressed Syn::eGFP and stained with DAPI (blue). Scale bar, 30 μm. B) Magnetic-assisted cell sorting analysis of NPC-derived CD44- and CD184-negative neurons.

negative cells (Figure 4-4B). CD44 and CD184 were cell-surface markers for the isolation of neurons derived from human pluripotent stem cells (Yuan et al., 2011). These neurons were seeded in the top and CMV::tdTomato NPCs in the bottom layer. We observed NPC migration induced by neurons after three days of co-culture (Figure 4-3A & B). On the contrary, when NPCs were seeded in both layers, NPCs in the bottom layer did not migrate (Figure 4-3A & B). Taken together, this 3D assay measures NPC migration towards either astrocytes or neurons.

4.4.2 Defective migration of NPCs derived from RTT- iPSCs

With this 3D migration system, we sought to examine whether MeCP2 mutations found in RTT patients affect neuronal migration, as MeCP2 regulates multiple genes involved in this process (Carouge et al., 2010; W. G. Chen et al., 2003). Further, mutations in one of these, cyclin-dependent kinase-like 5 (CDKL5), have been identified in patients with RTT (Scala et al., 2005); knockdown of CDKL5 in rats causes delayed neuronal migration (Q. Chen et al., 2010). Despite the current consensus that RTT does not involve migration defects (Neul & Zoghbi, 2004), this process may be affected in some RTT-affected individuals.

We compared migration of NPCs derived from RTT patients and their parental controls (Marchetto et al., 2010). First, we employed NPCs derived from a male RTT patient (Q83X) and his non-affected father's iPSC lines (manuscript in preparation). Migration was examined in two-layer hydrogels containing sorted GFAP::tdTomato-positive astrocytes in the top and CMV::eGFP-positive NPCs in the bottom layer. Q83X NPC migration towards Q83X astrocytes was retarded approximately 70% compared to WT83 NPCs towards WT83 astrocytes, indicating a migration defect (Figure 4-5A &

C). At the meantime, Q83X NPCs migration towards WT83 astrocytes was still retarded approximately 40% comparing to WT83 NPCs migration towards WT83 astrocytes, indicating intrinsic defect of Q83X NPCs migration itself, while WT83 NPC migration towards Q83X astrocytes was also approximately 55% retarded comparing to WT83 NPC migration towards WT83 astrocytes, indicating defect of Q83X astrocytes chemoattraction. (Figure 4-5A & D). Thus, the phenotype appears to reflect both slower intrinsic migratory ability of Q83X NPCs and impaired chemoattraction by Q83X astrocytes. We further evaluated WT83 and Q83X NPC migration induced by neurons. Q83X NPC migration towards neurons was also retarded compared to WT83 NPCs (Figure 4-5B & E). Taken together, RTT NPCs carrying the Q83X variant of MeCP2 migrate shorter distances towards either astrocytes or neurons.

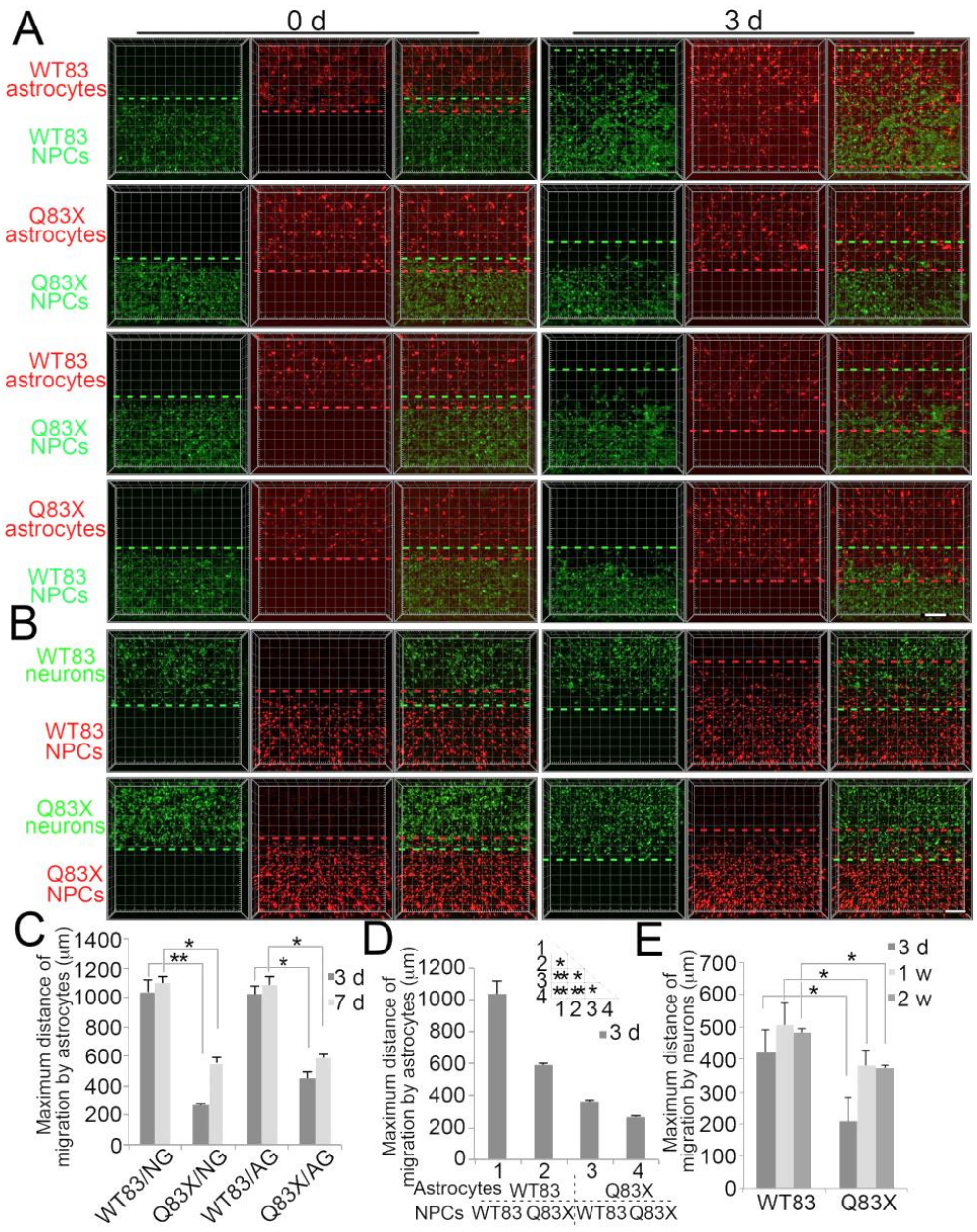


Figure 4-5 Defective migration of Q83X NPCs towards astrocytes or neurons.

A) Representative microscopy images of WT83 and Q83X NPC migration induced by WT83 or Q83X astrocytes for indicated times. Scale bar, 200 μm. B) Representative microscopy images of WT83 and Q83X NPC migration toward neurons for indicated times. Scale bar, 200 μm. C) & D) Quantification of maximum migration distance induced by astrocytes. Bars represent means; *p < 0.05 and **p < 0.01. (n=3). E) Quantification of maximum migration distance toward neurons. Bars represent means; *p < 0.05. (n=3).

To rule out the influence of genetic factors besides the MeCP2 Q83X mutation as a cause of this phenotype, we used isogenic stem cells (manuscript in preparation) carrying a frame-shift mutation in the MeCP2 gene in a human embryonic stem cell (ESC) line (ESC-MeCP2 mutation). Similar migration assays using NPCs derived from these cells validated the defect in migration towards both astrocytes (Figure 4-6A & E) and neurons (Figure 4-6C & F). Additionally, we rescued a patient cell line with an early stop codon mutation (Q83X), restoring MeCP2 protein levels to normal (rQ83X). The defects in migration towards both astrocytes (Figure 4-6B & E) and neurons (Figure 4-6D & F) were rescued when MeCP2 was restored in the cells (rQ83X). These results suggest that MeCP2 mutation impairs cell-induced migration in 3D hydrogels.

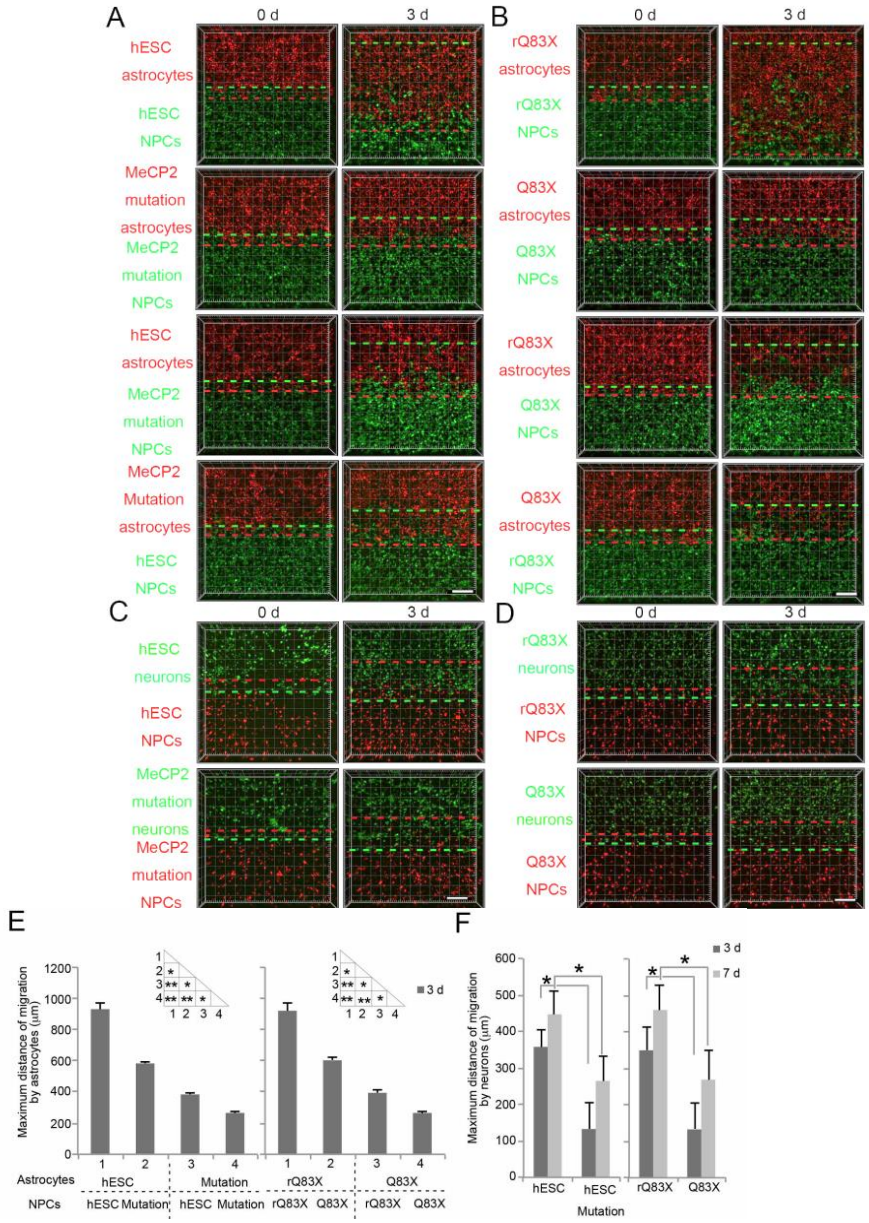


Figure 4-6 ESC isogenic *MECP2* matched NPCs mimic RTT migration defect.

A) Representative images of MeCP2-mutated or control ESC-derived NPC migration toward astrocytes. B) Representative images of Q83X donor or CRISPR-rescued Q83X (rQ83X)-derived NPC migration toward astrocytes. C) Representative images of MeCP2-mutated or control NPC migration toward neurons. D) Representative images of Q83X or rQ83X-derived NPC migration toward neurons. ALL Scale bars: 100 μm. E) Quantification of max astrocyte-induced migration. Bars represent means; *p < 0.05 and **p < 0.01 (n=3). F) Quantification of max neuron-induced migration. *p < 0.05 (n=3).

To further confirm the migration defects caused by dysfunction of MeCP2, we repeated the 3D migration assay with NPCs derived from another male RTT patient (N126I) and his non-affected father's iPSC lines. Migration was examined in two-layer hydrogels containing sorted GFAP::tdTomato-positive astrocytes in the top and CMV::eGFP-positive NPCs in the bottom layer. Similar migration defect due to both slower intrinsic migratory ability of N126I NPCs and impaired chemoattraction by N126I astrocytes was found (Figure 4-7A & C). We further evaluated WT126 and N126I NPC migration induced by neurons. N126I NPC migration towards neurons was also retarded compared to WT126 NPCs (Figure 4-7B & D). Taken together, RTT NPCs carrying the N126I variant of MeCP2 mutation migrate shorter distances towards either astrocytes or neurons.

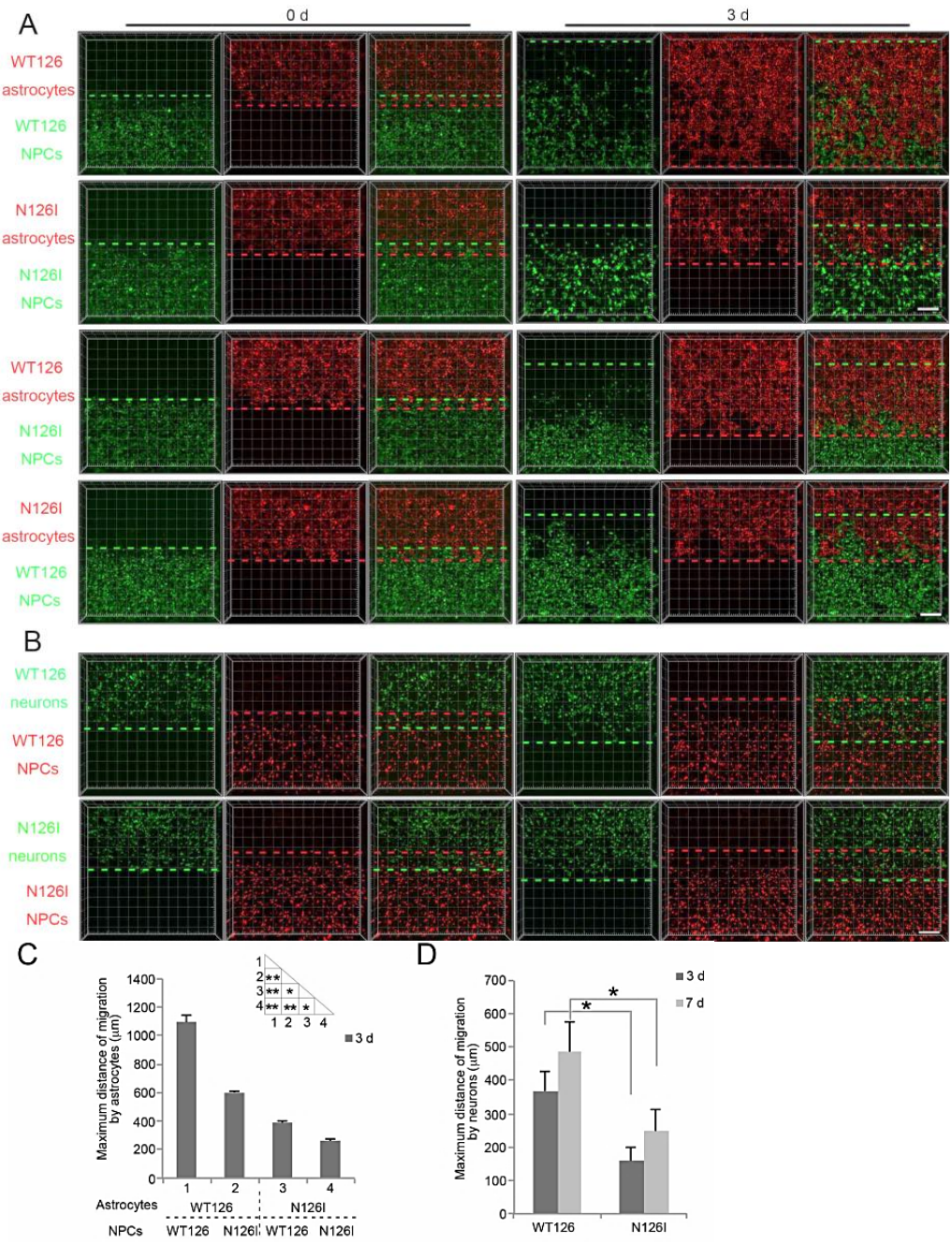


Figure 4-7 Defective migration of N126I NPCs towards astrocytes or neurons.

A) Representative images of WT126 and N126I NPC migration induced by astrocytes for indicated times. B) Representative images of WT126 and N126I neuron-induced NPC migration for indicated times. ALL scale bars: 200 μm. C) Quantification of max astrocyte-induced migration. Bars represent means; *p < 0.05 and **p < 0.01 (n=3). D) Quantification of max neuron-induced migration. Bars represent means; *p < 0.05 (n=3).

4.4.3 Three-dimensional hydrogel culture accelerates neuronal differentiation of human iPSC-derived NPCs

As an initial step towards investigating RTT pathophysiology, we generated mature neurons from human iPSC-derived NPCs in our 3D culture system. NPCs were infected with lentivirus expressing eGFP from the neuron-specific synapsin-1 (Syn) promoter and differentiation was followed by monitoring eGFP fluorescence. Control iPSC-derived Syn::eGFP NPCs (WT83) expressing Nestin, Sox2, Sox1 and PAX6 (Figure 4-2A & B) were seeded in 3D hydrogels. Expression of eGFP, indicating neuronal differentiation, was detectable within only two days (Figure 4-8A). After one week of culture in the hydrogel, neurite outgrowth from NPCs was already clearly visible, and neurites > 100 µm were apparent throughout the thickness of the hydrogel by week two (Figure 4-8A). These cells were positive for neuronal markers such as Tuj1 and microtubule-associated protein 2 (Map2). Moreover, we also observed synapsin puncta outlining Map2-positive neurites (Figure 4-8B). When compared to 2D culture, the density of syn1-positive puncta in 3D culture was significantly higher after 3 weeks culture and was even more significant after 6 weeks culture (Figure 4-8C). To further confirm formation of synapses, we examined ultrastructure. Electron microscopy revealed typical synaptic vesicles and postsynaptic densities after three weeks of differentiation in 3D hydrogels but only large clear vesicles (CV) at the same time in 2D culture. Only after 6 weeks of differentiation in 2D culture did the postsynaptic densities appear. The density of synapses was significantly higher in 3D culture compared to 2D culture after both 3 weeks and 6 weeks of differentiation (Figure 4-8D).

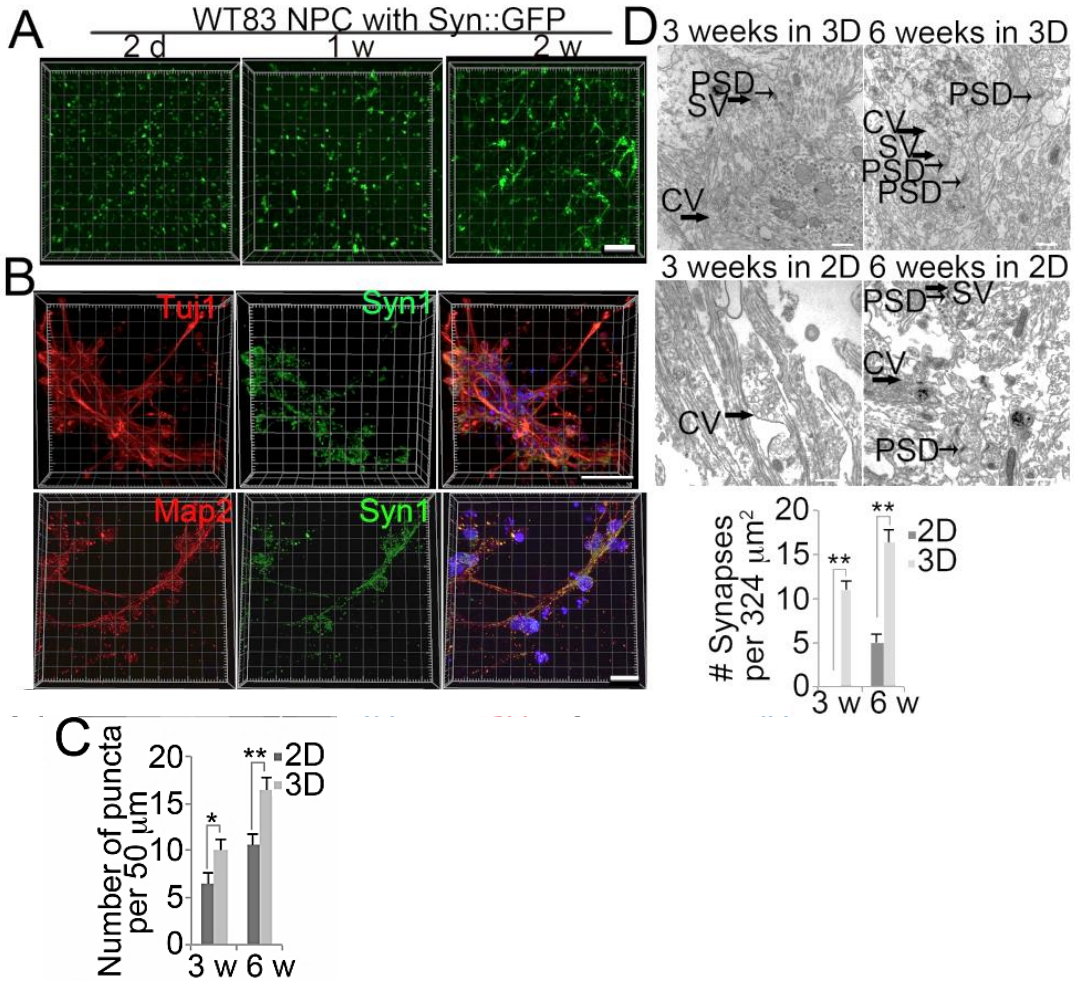


Figure 4-8 Rapid structural maturation of human neurons in 3D hydrogels.

A) Representative images of human iPSC-derived NPCs infected with Syn::eGFP lentivirus after neuronal differentiation for indicated times in 3D hydrogels. Scale bar: 200 µm. B) Representative images of human iPSC-derived neurons stained for Tuj1 or Map2 (red), Syn1 (green), and DAPI (blue) in 3D hydrogel. Scale bar: 60 µm. C) Quantification of Syn1 puncta on Map2 neurites. Bars represent means of 50 neurons per condition; *$p < 0.05$ and **$p < 0.01$. (n=3). D) Representative images of ultrastructural investigation of synaptogenesis by transmission electron microscopy in control NPCs differentiated in 3D or 2D system at indicated times. Scale bar, 500 nm. CV, large clear vesicle; SV, synaptic vesicle; PSD, post-synaptic density. Quantification of Synapse #. Bars represent means; **$p < 0.01$ (n=3).

To examine whether 3D differentiated neurons were functionally mature, we transferred them to glass slides by digesting hydrogels containing NPCs expressing

Syn::eGFP and differentiated for three weeks using hyaluronidase (2000 units/mL) overnight. After four days of culture on slides, electrophysiological activity of isolated eGFP-positive cells was examined. Pre-digestion of 3D hydrogel is to facilitate recording and allow direct comparison to 2D differentiated neurons. 2D differentiated neurons were also treated with hyaluronidase and re-plated prior to recording. In response to steps of depolarizing current, only neurons differentiated in 3D hydrogels but not in 2D culture for three weeks fired trains of action potentials (Figure 4-9A). Further, whole-cell voltage clamp recordings performed before and after application of 1 µM tetrodotoxin (TTX) revealed functional voltage-activated sodium and potassium channels in 3D differentiated cells, but not in 2D culture, indicating fast maturation of 3D cultured cells (Figure 4-9B & C). In addition, we detected whether 3D differentiated neurons expressed functional glutamate and GABA receptors. Bath application of the neurotransmitter glutamate (100 µM) transiently induced an inward current, and these events were blocked by 20 µM 2,3-dihydroxy-6-nitro-7-sulfamoyl-benzo[f]quinoxaline-2,3-dione (NBQX) and 50 µM D-aminophosphonovalerate (APV), indicating the presence of functional glutamate receptors (Figure 4-9D). Transient currents were also observed following 10 µM ɣ-aminobutyric acid (GABA) bath application, indicating the presence of functional GABA receptors, as these events were blocked by 50 µM picrotoxin (Figure 4-9E). All these results suggest that NPC-derived neurons differentiated in 3D hydrogels for only three weeks are functionally mature.

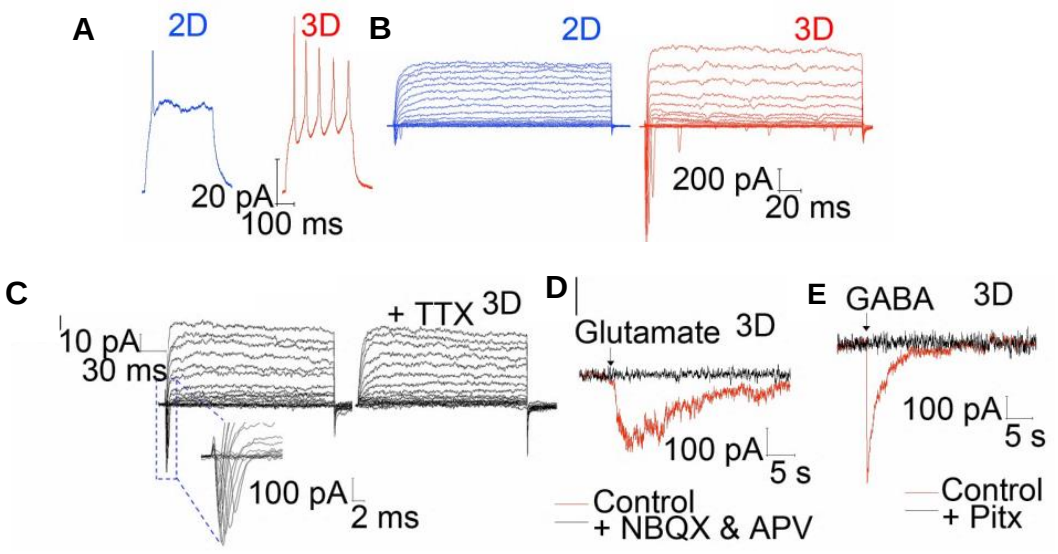


Figure 4-9 Rapid functional maturation of human neurons in 3D hydrogels.

A) Representative whole-cell current-clamp recordings of human iPSC-derived neurons after 3 weeks' differentiation in 3D or 2D system. Spiking activity was examined following current injection. B) & C) Representative voltage clamp recording of a neuron held at -75 mV and then stepped to a series of voltages (−80 to +20 mV) in 5 mV increments. TTX, 1 μM tetrodotoxin. D) Response to glutamate in the presence and absence of the glutamate receptor blockers 20 μM NBQX and 50 μM APV. E) Response to GABA in the presence and absence of 50 μM picrotoxin (Pitx).

We further compared neuronal differentiation of Syn::eGFP-expressing NPCs cultured either in 2D adherent culture or 3D hydrogels. By real-time PCR, the NPC marker Nestin was dramatically downregulated in 3D cultured but not in 2D cultured cells, while neuronal markers, such as Syn1, vGlut1, CTIP2 and Map2 were elevated in both. However, mRNA expression of these neuronal markers in 3D cultured cells was significantly greater than that in 2D culture (Figure 4-10A). Consistently, Syn promoter-driven eGFP expression in 3D culture was also higher than in 2D culture (Figure 4-10B), indicating greater neuronal differentiation.

To examine the proportion of NPCs that differentiate into neurons vs. astrocytes in 3D and 2D culture, we infected iPSC-derived NPCs with both lentiviral Syn::eGFP

and GFAP::tdTomato (GFAP is an astrocyte marker). While in 2D culture 10% of cells were GFAP-positive at two weeks' differentiation, few GFAP-positive cells were detected in 3D culture at this time point. At five weeks, 2D cultures contained 26% GFAP-positive cells versus only 3.5% in 3D culture (Figure 4-10C & D). Further, a greater proportion of 3D than 2D cultured cells were double-negative for CD44 and CD184 (85% vs. 63%; Figure 4-10E), cell-surface markers used to isolate neurons derived from human pluripotent stem cells (Yuan et al., 2011). These results show that differentiation of iPSC-derived NPCs in 3D hydrogels favors neuronal over glial differentiation and accelerate maturation of neurons compared to 2D culture.

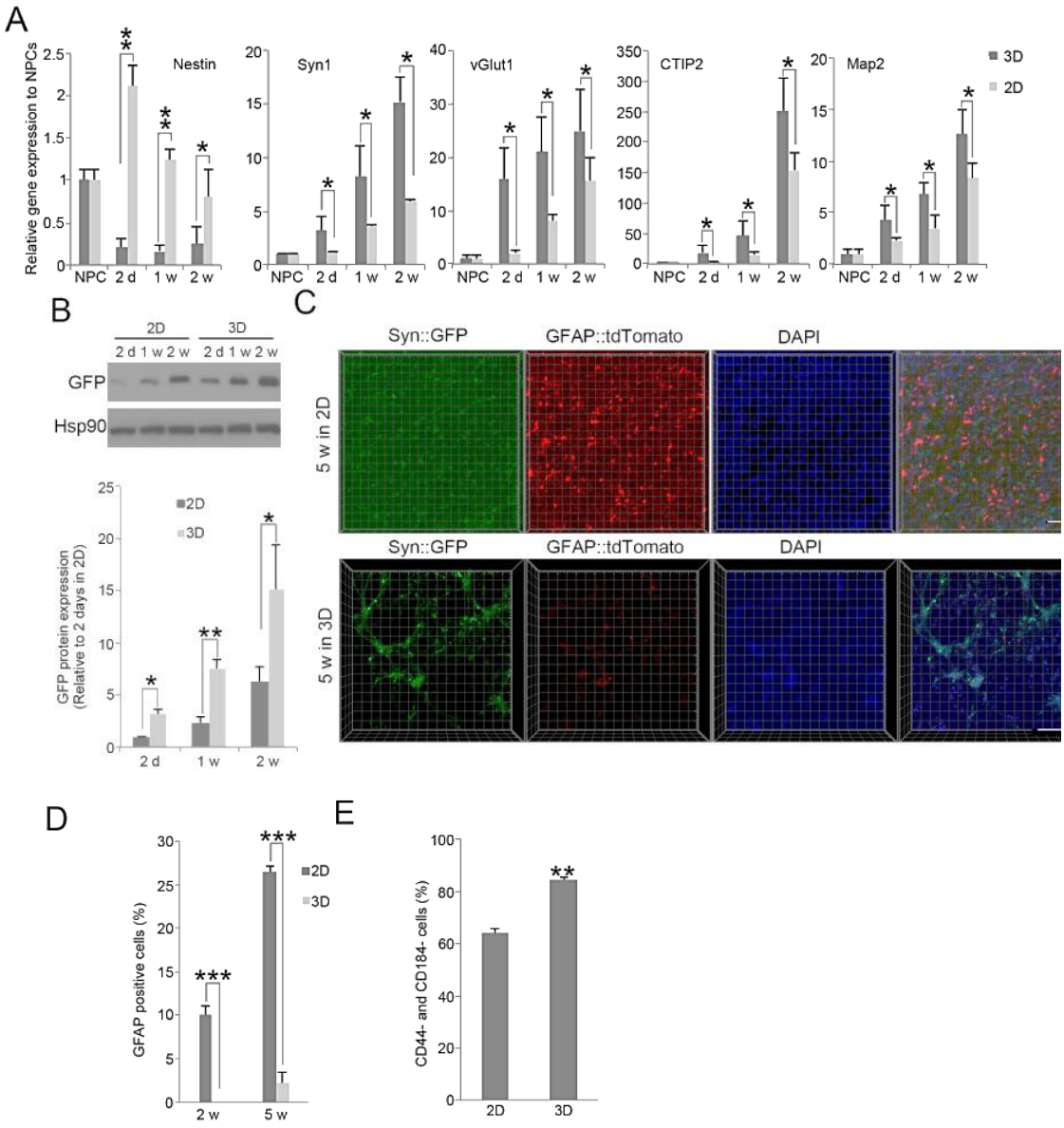


Figure 4-10 Neuronal differentiation in 3D versus in 2D system.

A) mRNA expression of NPC (Nestin) and neuronal marker genes (*SYN1*, *VGLUT1*, *CTIP2* and *MAP2*) in cells cultured either in 3D or in 2D system. Bars represent means; *$p < 0.05$ and **$p < 0.01$. (n=3). B) Syn1 promoter-driven eGFP protein expression after differentiation in 3D or 2D system. C) Representative images of cells infected with lentivirus expressing both GFAP::tdTomato and Syn1::eGFP after neuronal differentiation at 5 weeks in 3D or 2D system. D) Quantification of GFAP-positive cells after differentiation in 3D or 2D system. Bars represent means; ***$p < 0.005$. (n=3). E) Quantification of CD44 and CD184 double-negative cells after differentiation in 3D or 2D system. Bars represent means; ** $p < 0.01$. (n=3).

Next, we directly tested whether there was any bias for differentiation into specific neuronal subtypes. In our 3D system, neurons were cultured in NG medium, which is widely used for differentiation of human cortical neurons (Griesi-Oliveira et al., 2015; Marchetto et al., 2010). Thus, we used TBR1 and vGluT1 to determine the proportions of cortical excitatory neurons, GABA and GAD1/GAD67 (the GABA synthetic enzyme) for GABAergic inhibitory neurons, CTIP2 (also known as BCL11B) for layer V/VI neuron, and TH1 for dopaminergic neuron (Figure 4-11, (J Mariani et al., 2015)). Most importantly, there was no significantly difference in different subtype

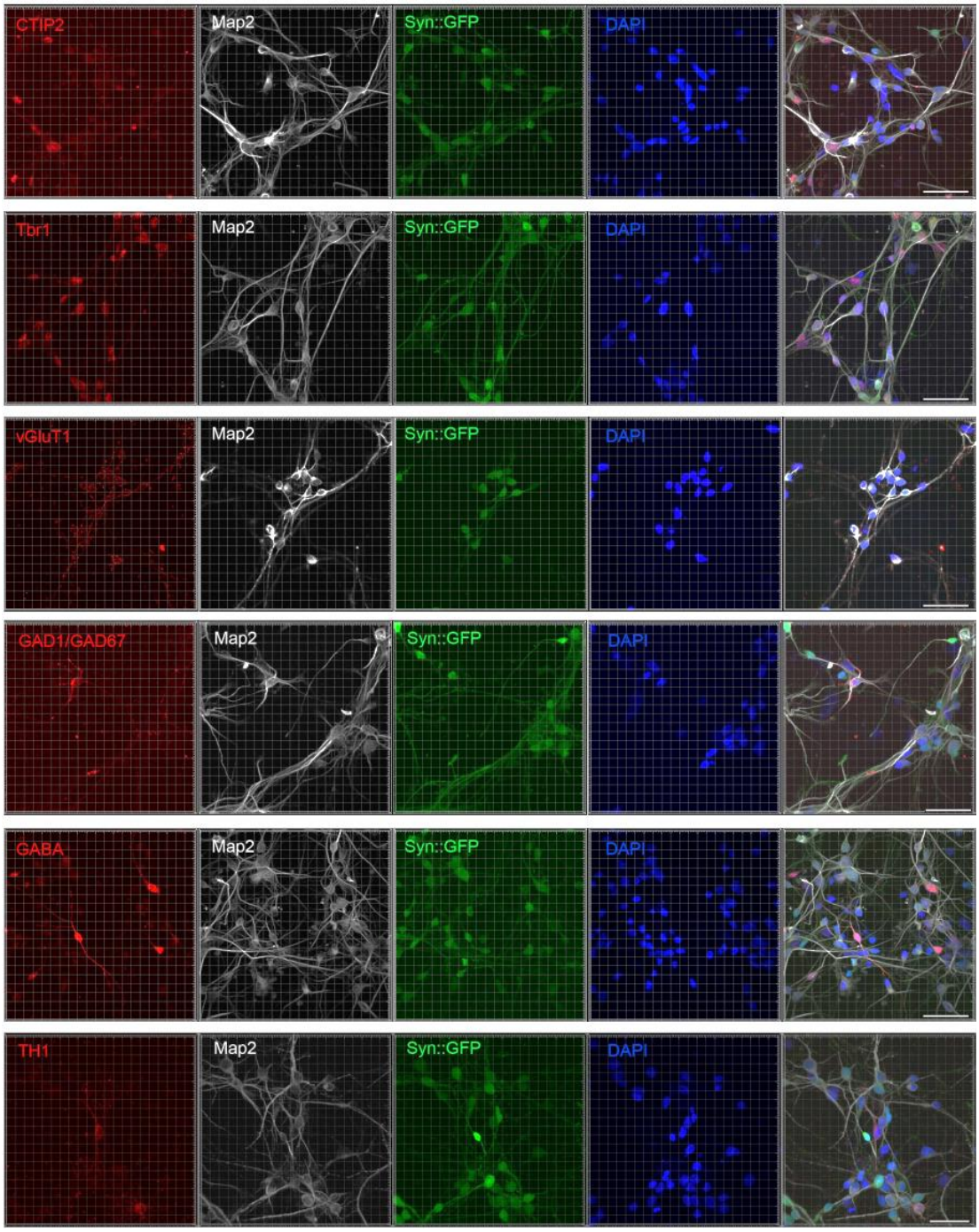


Figure 4-11 Representative images of WT83 neurons in 3D hydrogel.

Immunostained for CTIP2, Tbr1, vGlut1, GAD1, GABA, TH1 (red) and Map2 (white), expressed Syn::eGFP (green) with DAPI (blue). Scale bar: 50 μm.

populations between 3D cultured and 2D cultured neurons (Figure 4-12).

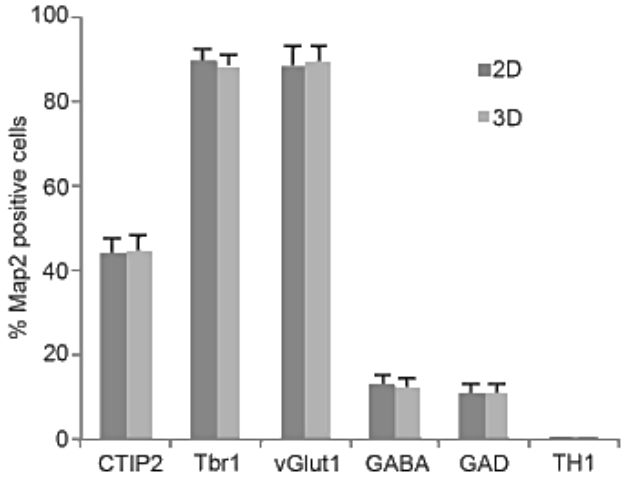


Figure 4-12 Neuronal subtypes in 3D versus 2D system.

Quantification of inhibitory (GABA+, GAD1+), excitatory (vGlut1+, Tbr1+) neurons, layer V/VI (CTIP2+) neurons and dopaminergic (TH1+) neurons in Map2 positive neurons. Bars represent means (n=3).

Hydrogel scaffold mechanical properties and presentation of biochemical cues can simulate the *in vivo* environment of the brain (McKinnon, Kloxin, & Anseth, 2013). Most importantly, the defined elastic modulus range of our hyaluronic acid methacrylate (HAMA) hydrogels is consistent with native neural microenvironments (50-250 Pa), which is important for directing neural survival and axonal outgrowth (Flanagan et al., 2002; Lu et al., 2006). We carefully tuned the mechanics of our system to accurately represent the *in vivo* condition. For example, we expected that scaffold elasticity influences extent of neurite outgrowth for differentiating NPCs. We tested our hypothesis by tracking extension length as a function of varied elastic moduli over a biologically relevant range. As shown in Figure 4-1B, altering the UVA irradiation time at 60s, 90s or 120s resulted in HAMA hydrogel matrices with elastic moduli of 130 Pa, 260Pa and 520 Pa respectively. Neurons differentiated within more elastic 130 Pa

scaffolds exhibited greater neurite outgrowth compared to those differentiated within less elastic, 260 Pa and 520 Pa, scaffolds (Figure 4-13). These data illustrate our effort to identify and optimize scaffold conditions critical to our 3D neural model of migration, differentiation and neurite outgrowth.

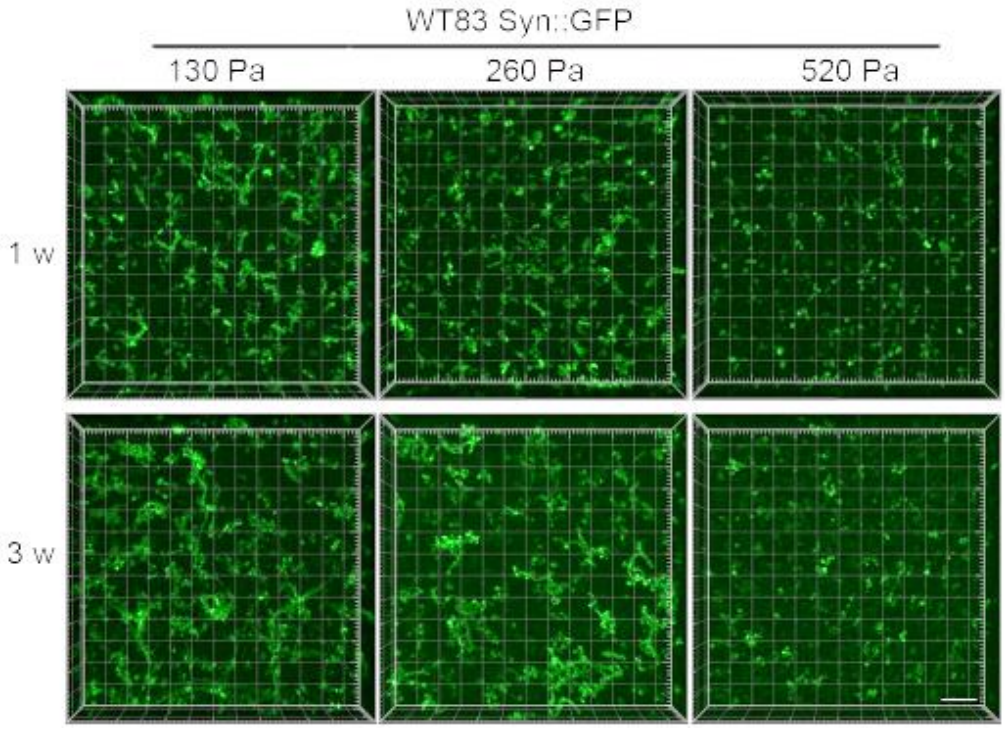
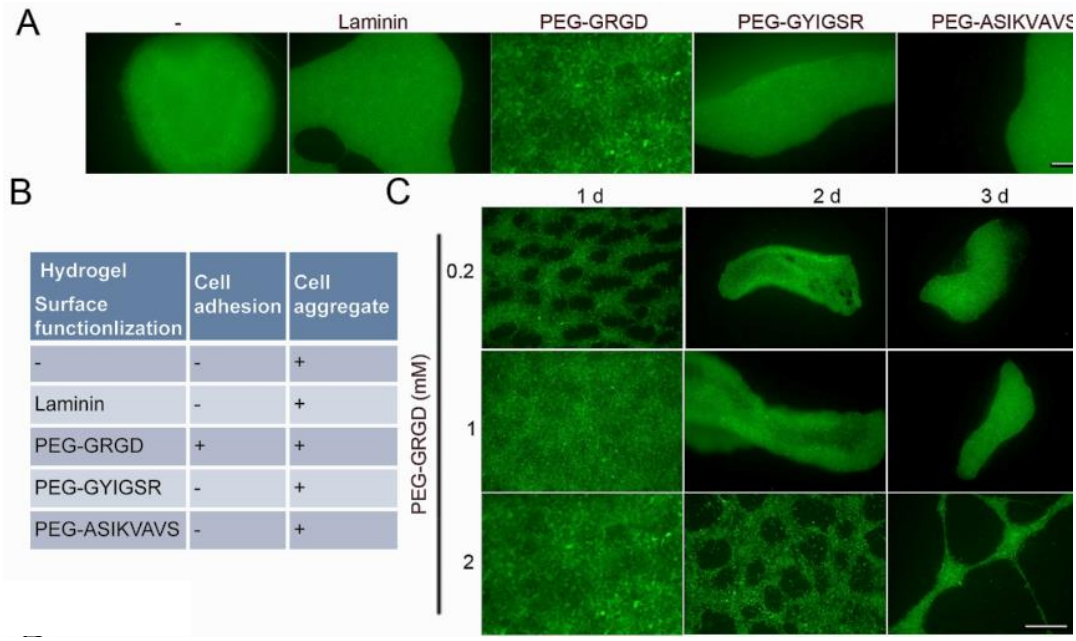


Figure 4-13 Effects of hydrogel mechanical properties on differentiation and neurite outgrowth in 3D.

Representative images of cells infected with lentivirus expressing Syn::eGFP after neuronal differentiation at 1 and 3 weeks in 3D hydrogels of three different moduli. Scale bar: 200 μm.

Cell adhesion, spreading and locomotion on 2D substrates is inversely proportional to substrate elasticity for a wide range of elastic moduli (Pelham Jr. & Wang, 1997). Native extracellular matrix elasticity is tissue-dependent; however, cells are typically rounded, minimally adhesive, growth arrested and prone to apoptosis when grown on soft 2D matrices (Kocgozlu et al., 2010; Wells, 2008). For this study,

we designed a scaffold to mimic native mechanical and biochemical properties of the developing CNS (Flanagan et al., 2002; Lu et al., 2006). Not surprisingly, our initial efforts to cultivate NPCs and astrocytes on 2D soft material substrates were unsuccessful. Encapsulating and absorbing laminin into 2D HAMA hydrogels failed to promote attachment and spreading. Instead, NPCs quickly aggregated and detached as spheres (Figure 4-14A & B). It has been reported that cell adhesion peptides and proteins engineered into hydrogels promote neuronal differentiation and outgrowth (McKinnon et al., 2013; Silva et al., 2004). Likewise, we covalently cross-linked potent integrin-binding adhesion ligands into the HAMA hydrogel surface, specifically RGD, YIGSR and IKVAV, to compliment the innate CD44-binding property of hyaluronic acid. acryloyl-PEG3400-GRGD, acryloyl-PEG3400-GYIGSR and acryloyl-PEG3400-ASIKVAVS were custom ordered (21st Century Biochemical and Laysan, Bio). We tested cell adhesion on ligand-functionalized 2D HAMA hydrogels twelve hours after initial seeding. RGD peptide, but not YIGSR or IKVAV, promoted initial NPC attachment (Figure 4-14A & B). Further, we optimized the RGD concentration-dependent initial adhesion and spreading (Figure 4-14C). Despite initial NPC attachment, NPCs only adhered to optimized RGD-HAMA surfaces for two days before aggregating, and ultimately detached after three days (Figure 4-14C). Within the initial two-day period,



Hydrogel Surface functionlization	Cell adhesion	Cell aggregate
-	-	+
Laminin	-	+
PEG-GRGD	+	+
PEG-GYIGSR	-	+
PEG-ASIKVAVS	-	+

Figure 4-14 2D soft hydrogel NPC attachment and neural induction.

A) Representative images of WT83 NPCs 12 hr after neural induction on 2D hydrogels. Laminin or 2 mM PEG-GRGD, PEG-GYIGSR or PEG-ASIKVAVS was incorporated during fabrication of HAMA hydrogels. B) Summary of adhesion and aggregation of NPCs on 2D hydrogel surface. C) Representative images of WT83 NPCs after neural induction on 2D soft hydrogel surface with 0.2 mM, 1 mM or 2 mM PEG-GRGD. All scale bars: 500 μm.

using time-lapse fluorescence microscopy, we observed no NPC migration towards discretely co-cultured astrocytes on 2D RGD-HAMA substrates (Figure 4-15A & C). Identical functionalization in 3D RGD-HAMA scaffolds had no adverse effect on encapsulated astrocyte-induced NPC migration over the same time period (Figure 4-15B & C). To further test the hypothesis that astrocyte-guided migration was, at least

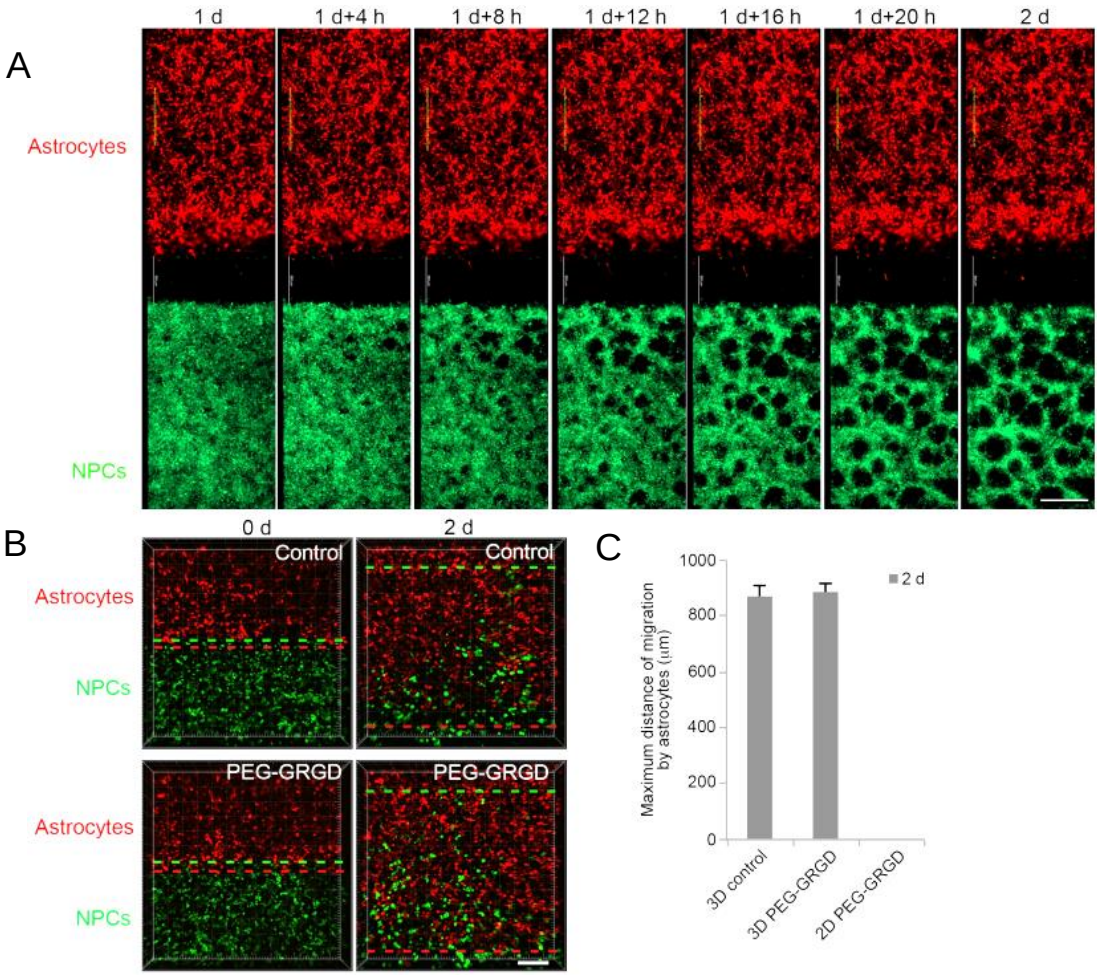


Figure 4-15 2D soft hydrogel neural induction and migration assay.

A) Time-lapse images of NPC migration induced by astrocytes for 2 days on 2D soft hydrogel substrate. Scale bar: 500 μm. B) Representative images of NPC migration induced by astrocytes in 3D hydrogel with or without 2 mM aPEG-GRGD for indicated times. Scale bar: 200 μm. Dotted lines identify the furthest travel distance for each indicated cell type; distance between red and green dotted lines is the maximum migration distance. C) Quantification of mean maximum migration distance induced by astrocytes (n=3).

in part, due to gradients of released chemotactic cues uniquely captured within the 3D scaffolds we set up identical functionalized gels in 3D RGD-HAMA scaffolds and supplemented the normal maintenance medium with either concentrated astrocyte conditioned medium (CM) pre-incubated with astrocytes or concentrated astrocyte

growth medium (AG) incubated without astrocytes, both groups sans FBS. CM disrupted chemotactic gradients and consequently substantially reduced encapsulated astrocyte-induced NPC migration compared to equally concentrated AG supplementation (Figure 4-16).

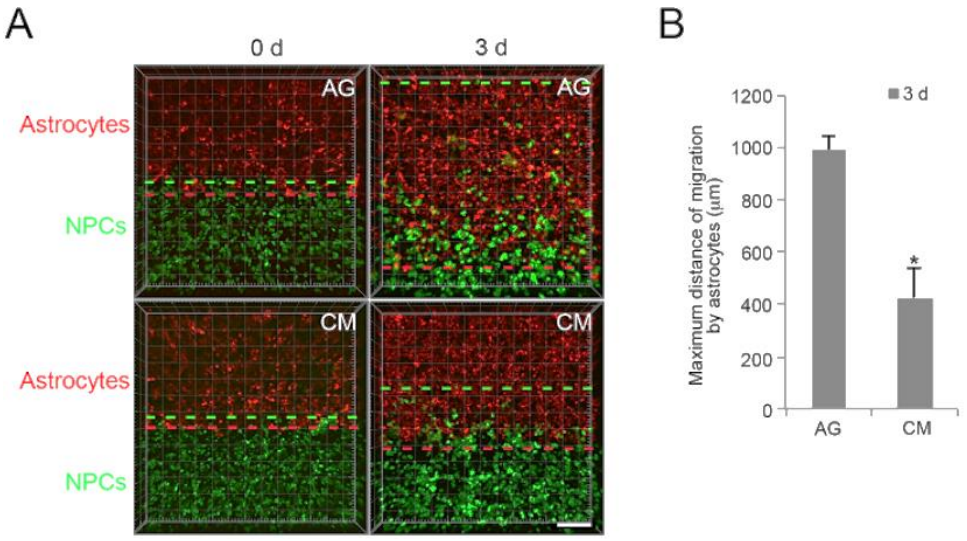


Figure 4-16 Astrocyte conditioned medium disrupts astrocyte-induced chemotaxis.

A) Representative images of NPC migration induced by astrocytes in 3D hydrogels supplemented with either concentrated astrocyte growth medium (AG) or concentrated astrocyte conditioned medium (CM) for 3 days. Scale bar: 200 μm. Dotted lines identify the furthest travel distance for each indicated cell type; distance between red and green dotted lines is the maximum migration distance. B) Quantification of mean maximum migration distance induced by astrocytes (n=3). *$p < 0.05$

4.4.4 Reduced neurite outgrowth and synapse density in RTT neurons in 3D hydrogel

Reduced dendritic arborization has been observed both in RTT patient cortex (Armstrong et al., 1995) and in some MeCP2 mutant mice (Kishi & Macklis, 2004; Stuss et al., 2012), but whether this results from reduced branching during development or from a failure of dendrite maintenance remains unclear. Similarly, disorganization of axons within cortical layers has been observed both in patients and animal models

(Belichenko et al., 2009; Ronnett et al., 2003). The underlying mechanism behind dendritic arborization could be most easily studied *in vitro* using human neurons generated from patient iPSCs. We therefore compared neurite outgrowth between MeCP2 Q83X neurons derived from RTT patient iPSCs and control neurons derived from a parent's iPSCs in our 3D hydrogel system. Neurite outgrowth in Q83X neurons was much slower, producing much shorter neurites than WT83 (Figure 4-17A - C). The difference became apparent at as early as day three and remained significant throughout 42 days of culture (Figure 4-17A - C). To further confirm this difference, we used immunostaining to detect Syn-positive puncta along Map2-positive neurites. Syn puncta were far less dense in Q83X neurons than controls (Figure 4-17D & E), confirming our prior findings in 2D culture (Marchetto et al., 2010). To further study the maturation defect, we recorded spontaneous excitatory postsynaptic currents (sEPSCs) as a way of measuring intercellular connectivity and network formation (Figure 4-17F). Cumulative probability plots of amplitudes and inter-event intervals of spontaneous postsynaptic currents revealed that RTT neurons have a significant decrease in frequency when compared to WT neurons (Figure 4-17F). Defective

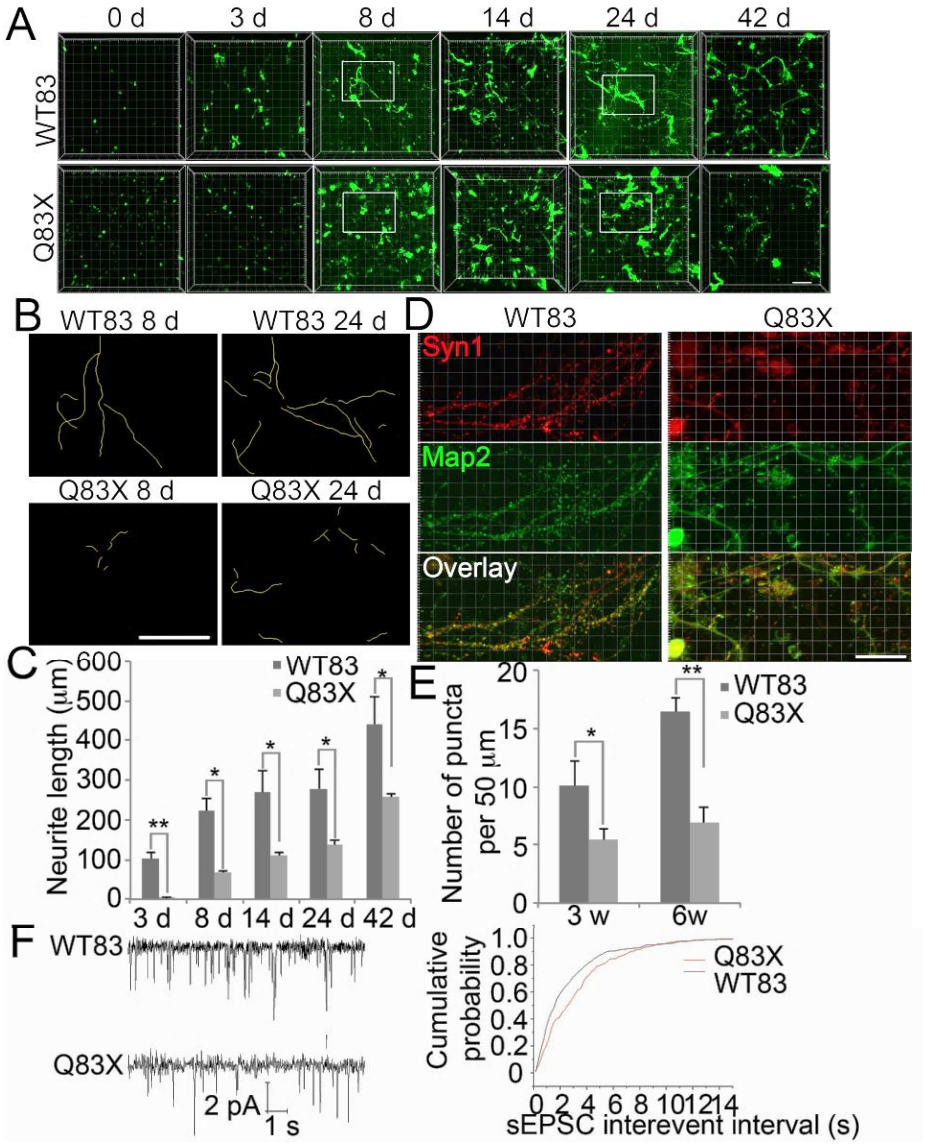


Figure 4-17 Defective maturation of *MECP2*$^{-/y}$ Q83X neurons in 3D hydrogel.

A) Representative images of WT83 and Q83X cells after neural differentiation in 3D hydrogels. Scale bar: 200 μm. B) Neuronal tracing comparing WT83 and Q83X neurons at day 8 and day 24 after neural induction. C) Quantification of neurite length. Bars represent means of 50 neurons per condition; *$p < 0.05$ and **$p < 0.01$ (n=3). D) Representative images of WT83 and Q83X neurons showing Syn1 puncta on Map2-positive neurites. Scale bar: 20 μm. E) Quantification of Syn1 puncta on Map2 neurites. Bars represent means of 50 neurons per condition; *$p < 0.05$ and **$p < 0.01$. (n=3). F) Spontaneous activity of WT83 and Q83X neurons. Cumulative probability plot of inter-event intervals ($p < 0.05$) of sEPSCs from WT83 (black) and Q83X (red) neurons (n=5).

neurite outgrowth Figure 4-18A & C and a lower density of Syn puncta in Q83X neurons was confirmed using neurons generated from *MECP2* isogenic ESC-derived NPCs (Figure 4-18B & D).

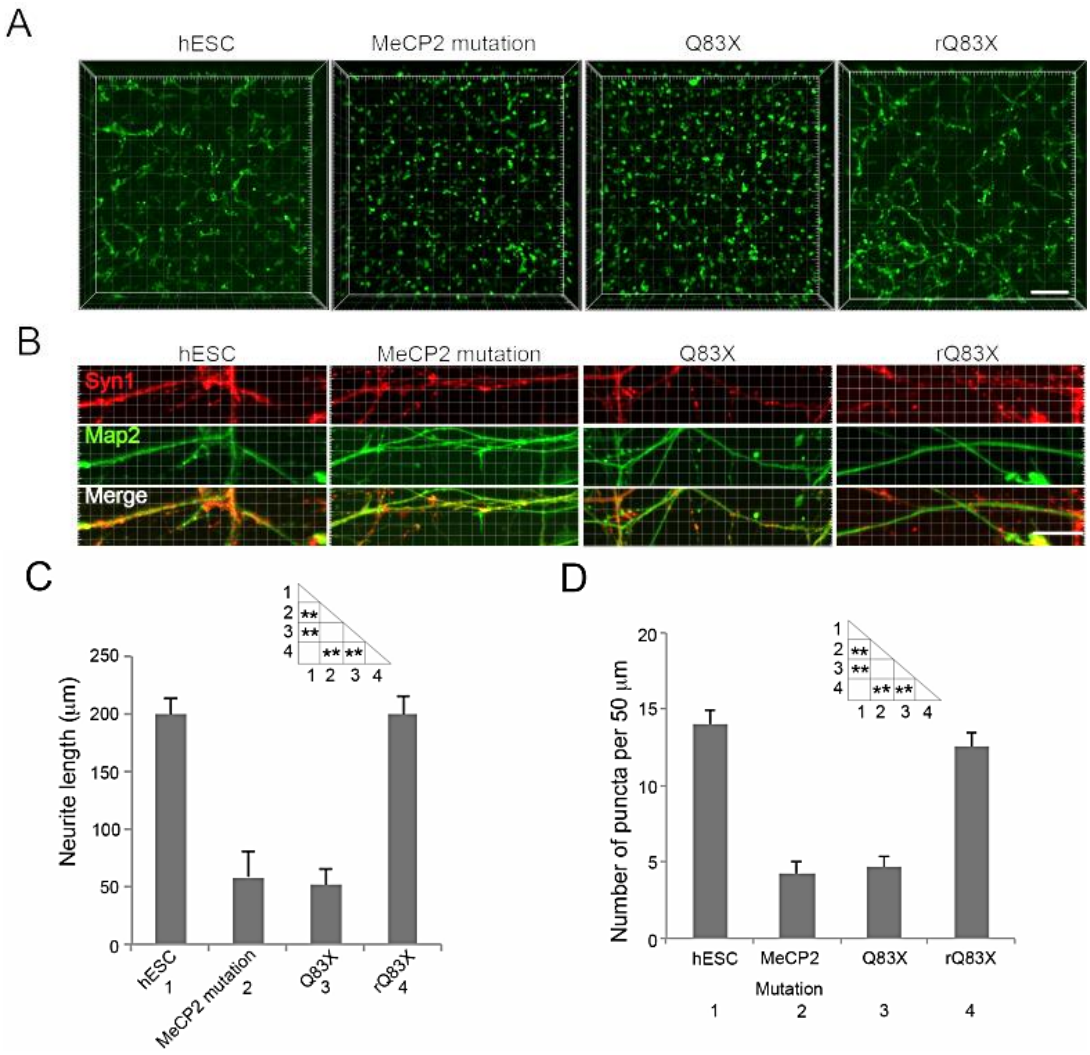


Figure 4-18 Isogenic *MECP2* ESC derived neurons verify RTT neural defects in 3D.

A) Representative images of isogenic ESC-derived neurons after neural differentiation in 3D. Scale bar: 50 µm. B) Representative images of ESC-derived neurons showing Syn1 puncta on Map2-positive neurites. Scale bar: 20 µm. C) Quantification of neurite length after neural induction in 3D. Bars represent means; **p < 0.01 (n=3). D) Quantification of Syn1 puncta on Map2 neurites. Bars represent means of 50 neurons per condition; **p < 0.01 (n=3).

To further validate the reduced neurite outgrowth and synapse number caused by dysfunction of MeCP2, we used the NPCs derived from another male RTT patient (N126I) and his non-affected father's iPSC lines. Neurite outgrowth in N126I neurons was much slower, producing much shorter neurites than WT126 (Figure 4-19A & C). Next, we used immunostaining to detect Syn-positive puncta along Map2-positive neurites. Syn puncta were far less dense in N126I neurons than controls (Figure 4-19B & D). Taken together, our data confirm previous observations of reduced neurite outgrowth and synapse density in RTT neurons.

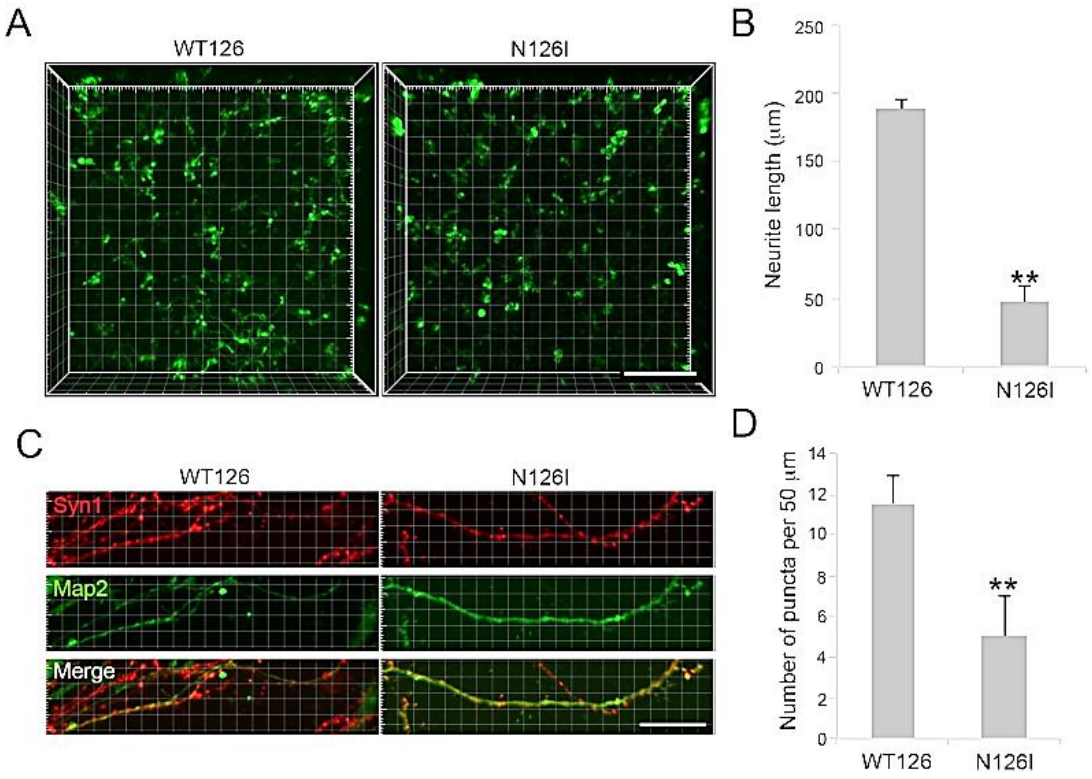


Figure 4-19 Defective neurite outgrowth and synapse density in *MECP2*$^{-/y}$ N126I neurons in 3D.

A) Representative images of WT126 and N126I cells after neural differentiation in 3D. Scale bar: 200 µm. B) Quantification of neurite length. C) Representative images of WT126 and N126I neurons showing Syn1 puncta on Map2-positive neurites. Scale bar: 20 µm. D) Quantification of Syn1 puncta on Map2 neurites. Bars represent means of 50 neurons per condition; **p < 0.01 (n=3).

4.5 Summary

In this study, we describe a novel 3D system for manipulating neuronal migration and differentiation in NPCs from humans with neurological disease. This system allowed us to discover a defect in migration in NPCs carrying mutation in MeCP2 versus control. Importantly, the 3D hydrogel system described here allows faster maturation of NPCs, suggesting that this approach could expedite the pace of

research using iPSCs to study several neurodevelopmental and neurodegenerative disorders.

While migration of human-derived NPCs has been examined in 3D hydrogel by transplantation into adult rat brains (Englund et al., 2002), no method has yet been developed to study 3D migration of human-derived NPCs *in vitro*. Though NPC migration may be assessed using chemotaxis chambers, such assays may not accurately reflect *in vivo* differences, as cells can also migrate through aqueous media across membranes rather than specifically along a 3D matrix. The most common *in vitro* approach for studying 3D migration, co-culture with tissue pieces or heterogeneous cell aggregates expressing secreted neurotrophins, has only been applied to tissue explants (Gil & del Rio, 2012). Our system provides better spatial control and may be more suited to observing single cells than tissue explant cultures.

Rapid generation of neurons in 3D hydrogels could result from several mechanisms. (1) Close matching of the physical properties of the brain (the elastic modus of soft, neurite-supportive hydrogels (100 Pa) is similar to that of brain tissue (Flanagan et al., 2002; Gefen & Margulies, 2004)) may accelerate differentiation. Materials whose mechanical properties closely mimic those of the *in vivo* extracellular matrix (ECM) of a particular soft tissue have been shown to promote differentiation of progenitor cells into the mature phenotypes inherent to that tissue (A. J. Engler et al., 2006; P C Georges et al., 2006; Yang et al., 2014). (2) The 3D scaffold may allow generation of mechanical force by NPCs in response to their environment (Seidlits et al., 2010). (3) The 3D environment provides a high surface area for growth and migration (Schultz, Kyburz, & Anseth, 2015), which can be tuned to support other cell

behaviors, such as differentiation or maturation. *in Vivo*-like cell-cell interactions may lead to more realistic gene expression and cellular behavior.

We synthesized cross-linkable HA with the intention to exploit the innate bioactive properties of this high molecular weight glycosaminoglycan naturally abundant in the brain. HA plays a prominent structural role in brain ECM (Bignami et al., 1993) and is upregulated along NPC migratory routes in the developing brain (Lindwall et al., 2013). Many non-neuronal neural cell types express HA receptor CD44, including NPCs and astrocytes (Lindwall et al., 2013). Notably, momentary cellular focal adhesions are less stable during HA/CD44 ligation in HA matrices alone compared to α/β integrin-mediated ligation in the added presence of potent ECM ligands such as RGD peptide (Y. Kim & Kumar, 2014). We encapsulated laminin protein, another key neural ECM component that comprises such ligands, within our HAMA scaffolds to support viability of neural cells. Laminin especially promoted neurite dynamics in differentiating neurons, which cease to express CD44. However, since we did not covalently bind laminin to the matrix, it likely did not significantly contribute to anchorage-dependent NPC locomotion. Native neural ECM varies in character and distribution, with unique molecular structure surrounding a wide variety of neurons (Dityatev & Schachner, 2003). ECM affects both the differentiation efficiency and the derived cell function of developing neural cells (Y. Li et al., 2013; W. Ma et al., 2008). Physically entrapping ECM proteins, such as collagen, laminin, or fibronectin in the synthetic hydrogels has been shown to promote NPC differentiation (Blewitt & Willits, 2007; Hersel, Dahmen, & Kessler, 2003). Although we demonstrated that HAMA hydrogels with laminin only is sufficient to induce NPC differentiation, additional cell

adhesion cues might further enhance biomimicry in our 3D system. Thus, it is intriguing for us to fully assess the function of additional ECM components in our future work.

4.6 Conclusions

Three-dimensional systems enable the formation of tissue-mimetic architectures and promote more realistic physiological responses than conventional 2D cell and tissue cultures. Here we reported a novel laminar 3D culture system to assay migration and maturation of human iPSC-derived NPCs to reveal a genotype-specific effect of MeCP2 dysfunction on iPSC-derived neural cell migration and maturation in 3D layered hydrogels. Using this platform, we identified a migration defect in MeCP2-mutant iPSC-derived NPCs and confirmed previous observations that neurons derived from these cells have reduced neurite outgrowth and fewer synapses. In addition, 3D hydrogel culture accelerates neuronal differentiation of iPSC-derived NPCs. In this study we validated our 3D hyaluronic acid scaffold based approach with two unrelated male RTT iPSC models and further verified our results with an induced isogenic *MECP2* human ESC neural model.

In conclusion, our hydrogel-based assay of neural migration reveals a defect in NPCs derived from two rare male RTT iPSC donors as well as in NPCs from a CRISPR/Cas9-induced *MECP2* ESC model, compared to respective controls. In addition to cell autonomous NPC migration defects, we report astroglial, and to a lesser extent neuronal, non-autonomous effects on NPC chemotaxis through novel laminar 3D hydrogels. Further, this hyaluronic acid hydrogel system facilitates neuronal differentiation and maturation, reducing the time needed to generate functional neurons from between five and six weeks for conventional monolayer systems, as demonstrated

previously and as described in detail in Chapter 3 and Chapter 4 of this dissertation, to just three weeks in 3D as demonstrated by mature synapse formation and individual neuronal electrophysiology. Employing this method to examine migration and differentiation of NPCs derived from donor iPSCs yields more biologically relevant and reliable results than other approaches, as cells move through a soft biomimetic matrix rather than across a hard surface or through an inert membrane. Further, it allows investigation of responses to various cytoarchitectural and biochemical cues without employing less controlled neurosphere cultures or organoids, which can be time-consuming and often difficult to interpret especially when trying to identify cell type-specific contributions to complex phenomena. This system could also be used to screen drug candidates for their ability to restore disease-associated defects in migration or other phenotypes more appropriately studied in 3D systems such as neuronal circuits and more complex networks.

4.7 Recognitions

The authors gratefully acknowledge the NIH New Innovator Awards (DP2OD006499 and DP2OD006495), NIH grants 5R01EY024134-02, R01MH094753, R01MH103134, U19MH107367, the California Institute for Regenerative Medicine (CIRM) TR2-01814 and TR4-06747, the International Rett Syndrome Foundation (IRSF grant# 2915 and grant# 2925), a NARSAD Independent Investigator Grant to A.R.M, and King Abdulaziz City for Science and Technology (through the KACST-UCSD Center for Excellence in Nanomedicine and Engineering) for funding.

4.8 Acknowledgements

The contents of Chapter 4 were adapted for the Proceedings of the National Academy of Sciences and are currently in press as “Layered hydrogels accelerate iPSC-derived neuronal maturation and reveal migration defects caused by MeCP2 dysfunction.” Zhang Z-N, Freitas BC, Qian H, Lux J, Acab AJ, Trujillo C, Herai R, Nguyen Huu VA, Wen JH, Joshi-Barr S, Karpiak JV, Engler AJ, Fu X-D, Muotri AR, Almutairi A. The dissertation author was a main contributor and co-author of this work.

Chapter 5

Discussion of the thesis

5.1 Hypothesis and goals

The human brain is complex. Brain development is a highly ordered process involving multiple cell types and highly orchestrated spatiotemporal migration, differentiation and ECM-mediated laminar functionalization. Genetic brain diseases either perturb this process, degrade the neural environment or a combination of both. Isogenic stem cell models provide a means to investigate cell-type and biomolecular contributions, especially in monogenetic disorders; however, traditional *in vitro* monolayer models lack the sophistication of *in vivo* neural development, not to mention the ability to reveal potentially subtle neuropathophysiology. Conversely, the biological intricacy of animal models and recently described 3D organoid cultures, makes it difficult to decouple cell-type specific effects due to complex, multi-cellular interactions. Additionally, the issue of consistency has not yet been appropriately addressed for practical application of organoid culture systems. Further complicating the challenge of modeling human disease, animal models often fail to represent human pathology, especially with regard to neurological diseases. **I hypothesized that a tunable stem cell based 3D laminar co-culture model could better represent cytoarchitecture of *in vivo* neural environments, and therefore provide an accessible and potentially more accurate research tool than animal or 2D models of brain disease.** Such a system could potentially drive earlier diagnoses and better outcomes for individuals with identifiable disease-causing genetic mutations. The model could be used to safely test individualized treatment methods, and more broadly, could provide a template for the development of implantable therapies or regenerative approaches for diseased or injured tissues. **The goal of this thesis was to develop screenable stem cell-based systems using 3D bioengineered scaffolds to better model brain**

development and thereby provide better insight into genetic perturbations of this process. To accomplish this goal, test my hypothesis and advance ***our overarching goal of understanding brain disease and neural development***, we exploited my tissue engineering background establishing a highly tunable cell-compatible multilayer hydrogel scaffold (Chapter 2) while concurrently characterizing functional co-cultures of distinct neural cell subtypes derived from iPSC and isogenic stem cell models of monogenetic neurologic disorders (Chapter 3). I then combined these two systems, ultimately supporting my hypothesis and accomplishing the central goal of the thesis, to reveal previously undetected neurophysiologic RTT phenotypes in a 3D *in vitro* model of neurodevelopment (Chapter 4). The broader impact of this research in the context of developmental biology, regenerative medicine and disease modeling is that the compartmentalized 3D tissue scaffolds and isogenic stem cell co-culture approaches herein described can potentially be adapted to emulate *in vivo* cytoarchitectures of any human tissue, in addition to the brain and CNS, bridging gaps between traditional *in vitro* monolayer disease models, animal models and human clinical relevance.

5.2 Summary of principal findings

Current monolayer cell-based systems fail to recapitulate much of *in vivo* neural development; therefore, 3D modeling of brain development is critical. The main goal of my thesis was to develop 3D *in vitro* stem cell-based models to study brain disease. The underlying hypothesis was that 3D neural co-culture models would more accurately recapitulate neural development and brain cytoarchitecture, thereby facilitating better insight into the pathology of neurological disorders. Ultimately, I

accomplished my goal developing a screenable 3D model of neural development and successfully supported my hypothesis by revealing aspects of RTT not obvious in common monolayer systems. In pursuit of my goal, I achieved several scientific advancements and discoveries summarized below.

I developed a novel and highly adaptable tissue scaffold method, density gradient multilayer polymerization (DGMP, Chapter 2 section 2.2 & Appendix B), to engineer complex *in vitro* tissues. We first validated the utility of DGMP for disease modeling in a gradient substrate-mediated *in vitro* cellular model of wound healing (Chapter 2 section 2.3). Results from this study demonstrated that haptotactic cellular response, pertinent at the interface between healthy and fibrotic tissue, is limited by substrate adhesiveness. Perhaps more notably, we reported that although both mesenchymal stem cells (MSCs) and fibroblasts home to damaged tissue to aid in repair, fibroblasts may be more responsive to ligand gradients. Following this study, I shifted focus to neural modeling, developing a hyaluronic acid methacrylate (HAMA) based scaffold viable for both the maintenance and differentiation of iPSC-derived NPCs (Chapter 2 section 2.4 & Appendix A). As I was optimizing this 3D neural tissue scaffold, I worked in parallel on establishing a microelectrode array (MEA) platform to screen neural networking in a monolayer model of Cockayne Syndrome (CS, *ERCC6*), a devastating neurodegenerative disorder.

Applying our established *in vitro* monolayer neural development model, previously described to study RTT (Marchetto et al., 2010), we reported the first, to our knowledge, iPSC-derived neural networks from CS donors. In this study I validated a MEA platform to screen early functional deficits in a neurodevelopmental model of CS, a neurodegenerative brain disease (Chapter 3 section 3.2). In addition to altered

network electrophysiology and reduced synapse density (which are both nonexistent in CS fibroblasts), striking transcriptional dysregulation was revealed by RNA-seq analysis of CS neural cultures that contrasts with fibroblast models (Newman et al., 2006; Y. Wang et al., 2014). This result could be due to either a greater dysregulation in neurons compared to fibroblasts, or due to microarray technology from those studies providing less coverage. Notably, we discovered impaired transcription of the GH/IGF-1 signaling pathway, and verified the results by qPCR for *IGF1* and *STAT5.* Remarkably, robust bioinformatics analysis suggested miRNA and *TGFB1* as potential contributors to this transcriptional dysregulation, providing strong rationale for future studies.

While carrying out the CS experiments, I used one of the control iPSC lines from that study to develop neural co-culture systems of separately derived astroglia and enriched neurons. I first evaluated the effects of direct contact co-cultures on neural networking compared to astroglial conditioned medium (ACM) or untreated enriched neurons. Based on these results, I implemented direct contact co-cultures to decouple astroglial and neuronal effects in our reported monolayer model of RTT, facilitated by isogenic *MECP2* matched stem cell lines (Chapter 3 section 3.3). I reported greatly diminished electrophysiological activity in control neuronal networks co-cultured with either MeCP2-deficient astroglia or fibroblasts compared to control astroglia. I also reported a significant reduction of neuronal synapse density in co-cultures with MeCP2-deficient astroglia compared to both fibroblast and control astroglia; however, excitatory presynaptic VGLUT1 puncta density was unaffected. The former results compliment previously reported isolated neuron electrophysiological deficits and morphogenic changes caused by MeCP2-deficient astroglia in neural co-cultures *in vitro.*

Finally, combining these tools I developed, 3D tissue culture scaffolds and stem cell derived neural co-cultures, we constructed more sophisticated neural development models (Chapter 4). *In vitro* neural development, as traditionally measured by synaptic maturation, cellular morphometrics and isolated neuronal electrophysiology of differentiating iPSC-derived NPCs, was accelerated in optimized 3D HAMA scaffolds compared to monolayer cultures. Further, using our novel DGMP method to construct 3D laminar co-cultures of neural cell subtypes derived from isogenic *MECP2* stem cell models, we reported for the first time, diminished chemotaxis in *MeCP2*-deficient NPCs. This subtle migration deficit was further exacerbated by MeCP2-deficient astroglia compared to control astroglia. Interestingly, migration deficits were also observed in unaffected NPCs co-cultured with MeCP2-deficient astroglia further supporting previous reports of astroglial non-autonomous effects in RTT.

5.3 Scaffold and stem cell based approaches to building functional brain models

Recently, a group of scientists met at Cold Spring Harbor in New York to discuss ongoing efforts to advance cell-based models of brain disease (Brennand et al., 2015). They agreed that, to advance the field of personalized *in vitro* modeling, efforts must focus on building functional neural complexity *in vitro* by combining multiple defined cell subtypes and spatiotemporal arrangements that mimic *in vivo* cytoarchitecture, followed by higher level analyses of complex neural circuitry. In this thesis, I proposed adapting genetic stem cell systems to explore cell-type specific functional and molecular contributions in mutation-specific brain models. Additionally, given the complexity of the human brain, I hypothesized that 3D *in vitro* modeling of neural

development is critical to understanding often subtle developmental and functional dysregulation. Recent tissue engineering approaches offer viable solutions to building complex tissues for *in vitro* investigation and potential therapeutic screening. And, emergent MEA technology allows multilevel neural network characterization. I further hypothesized that screenable 3D hydrogel scaffolds designed to mimic neural extracellular matrix would better support neural differentiation and development of human stem cells and elucidate tissue-specific pathological processes that have otherwise remained obscure in traditional *in vitro* models of brain disease (Figure 5-1).

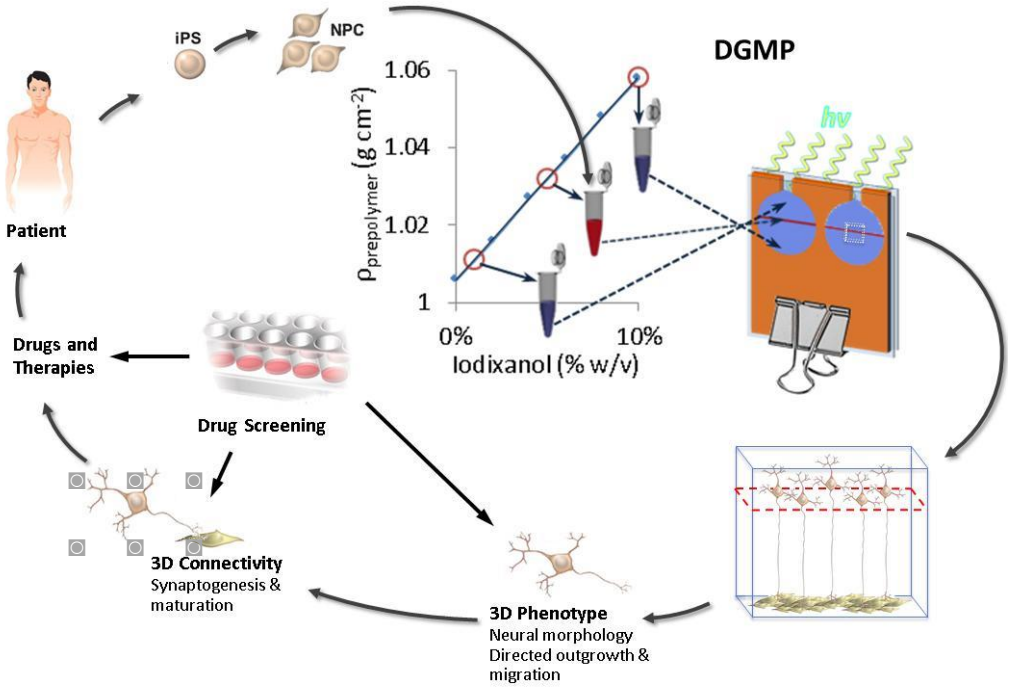


Figure 5-1 Application of DGMP to model brain disease.

Somatic cells from RTT donors and controls are reprogrammed to iPSCs, then directed to become NPCs or other mature neural cells and encapsulated within a discrete layer of a DGMP hydrogel tissue scaffold. 3D organization enables study of directed neurite outgrowth and migration, and facilitates examination of morphological phenotypes including process branching and spine density/volume/maturation, as well as synapse formation (by immunostaining). Incorporating additional neural subtype cell layers (e.g., astroglia) allows distinction between autonomous and non-autonomous aspects of the disease. MEA technology enables network analyses at the circuit and network level. Once a novel disease-related phenotype is identified, the system may be used to screen candidate drugs.

5.3.1 3D laminar scaffolds to engineer complex *in vitro* tissue

Towards testing my hypothesis, I invented a new cell-compatible laminar scaffold fabrication method (DGMP) and first demonstrated its simple utility using synthetic hydrogels (Figure 2-1). Hydrogels comprise networks of cross-linked or intertwined polymer chains of natural or synthetic origin. Due to their significant water

content and structural tunability (Figure 2-6), hydrogels can be designed to mimic biophysical characteristics of native human tissue, and serve as highly effective matrices for tissue culture (Figure 2-8). Cellular morphology, fate and functionality within hydrogels (Figure 2-12) depend on cell type arrangement (Figure 2-8C), presentation of biophysical (Figure 2-7) and biochemical cues by covalent attachment (Figure 2-2) or encapsulation (Figure 2-10 and Figure 2-11), geometry (Figure 2-9) and mechanical properties (Figure 2-13E) of the hydrogel. DGMP facilitates such patterning and tunability using viable cell-compatible technology yielding robust results. I first applied the DGMP method to study cellular haptotaxis (substrate mediated migration) of mesenchymal stem cells (Figure 2-16, left and Figure 2-17) and fibroblasts (Figure 2-16, right and Figure 2-18) in a monolayer wound healing model using adhesive gradients bound within synthetic hydrogel substrates (Figure 2-13). This study validated the utility of DGMP to generate a disease-relevant tissue model revealing haptotaxis dependence on cell type and substrate adhesiveness.

5.3.2 Three dimensional HAMA scaffolds support NPCs and accelerate *in vitro* neural differentiation

In preparation of building complex 3D *in vitro* brain models I developed and verified neural tissue culture compatible hyaluronic acid based hydrogel scaffolds. I synthetically methacrylated commercially available hyaluronic acid as indicated by sharp peaks at 5.75 and 6.19 ppm on the ^{1}H-NMR spectrum (Figure 2-26A) and optimized polymerization parameters to mimic mechanical stiffness of neural tissue (Figure 2-26B). Finally, I encapsulated human iPSC-derived NPCs under DGMP conditions and monitored viability, outgrowth, multipotency and neural differentiation

capacity upon bFGF22 withdrawal (Figure 2-27A-D). We observed accelerated NPC differentiation and *in vitro* neural development in 3D HAMA scaffolds compared to those in monolayer cultures confirmed by synaptic maturation (Figure 4-8), isolated neuronal electrophysiology (Figure 4-9), and expression profiles (Figure 4-10A & B). Further, our results showed that differentiation of iPSC-derived NPCs in 3D hydrogels favors neuronal over glial differentiation (Figure 4-10C-E).

5.3.3 iPSC and co-culture models to study neural development

The Muotri Lab published one of the first iPSC studies used to model neural development *in vitro* (Marchetto et al., 2010). Since that report, the neuroscience community has been applying, and improving upon, this model (and others) to study multiple neurodevelopmental and neurodegenerative brain diseases. My first practical application of this model was to study neural networking in CS (Chapter 3 section 3.2). I established multi-well MEA assays to begin looking at higher network-level neural activity in our monolayer neural model (Figure 3-9), as well as synapse density assays to assess co-localized signature pre- and post-synaptic proteins. For this study we primarily used iPSC lines generated via non-integrative Sendai viral reprograming of long-term commercially cryopreserved fibroblasts with the exception of one control line. “WT83,” also referred to in this manuscript as “ctr83,” is a standard control iPSC line in the Muotri Lab originally generated via retroviral reprograming of primary fibroblasts recovered from a skin biopsy obtained specifically for our lab repository.

To begin addressing the challenge of defining distinct brain cell states I characterized neural co-cultures comprised of separately differentiated astroglia and enriched neurons from the ctr83 iPSC line (Figure 3-10). Since this project started,

several robust astroglial differentiation protocols have been reported (C. Chen et al., 2014; Haidet-Phillips et al., 2013; Williams et al., 2014). However, to probe astroglial roles in neural development and disease for this thesis I used a simple alternative method to generate enriched populations of astroglia from NPCs described in detail in Chapter 3 section 3.3.2.6. While there is batch-to-batch variability and resultant glia are in an activated state due to serum-supplemented Astrocyte Growth Medium (AGM) during differentiation, with some morphologic screening to eliminate non-glial cell contamination I generated large quantities of enriched GFAP expressing astroglia (Figure 3-14 and Figure 4-2D & E) suitable for neural co-cultures (Figure 3-20A and Figure 4-3A 2nd row & B-D). Additionally, to moderate potential effects from non-neuronal cells resulting from our routine neural differentiation protocol, we introduced an enrichment procedure. Using MACS to negatively select cells expressing CD44 and CD184 from the heterogeneous neural population (Figure 3-15), I generated enriched populations of neurons suitable for co-culture (Figure 3-16, Figure 3-20C and Figure 4-3A 3rd row). To set up neural co-cultures, I pre-plated astroglia overnight in AGM:NBA media (1:1) to promote adhesion and viability, followed by neuronal co-plating in 100% NBA medium at 2:1 or 5:1 seeding ratio, as indicated. Alternatively, I produced astrocyte conditioned NBA medium (ACM) from over-confluent astroglial cultures to determine sufficient conditions necessary to study astroglial effects in neural development and networking.

5.3.4 Functional monolayer neural co-cultures from iPSCs demonstrate astroglial non-autonomous effects in neuronal networks

The ability to decouple cell-type specific roles in complex neural networks is an important update to our model of neural development. Combining this stem cell-derived co-culture approach with MEA technology and an advanced synapse density assay has allowed us to begin investigating astroglial contributions to in functional neural development. Not surprisingly, we reported that astroglia, the most prevalent cell type in the brain, exhibited non-autonomous effects on both physical and electrophysiological aspects of neuronal networks. The experiments demonstrated significant increases in connectivity measured in neural networks in response to both ACM and direct co-culture compared to enriched neurons alone. Interestingly, the ACM treatment group trended nearly double the synapse density of direct co-cultures two weeks after co-plating, while exhibiting only a fraction of the electrophysiological activity. However, this substantial difference lost significance when considering cumulative results over six weeks. Due to the robustness and consistency of direct contact co-cultures demonstrated in this iPSC system, I proceeded with this approach for the remainder of the thesis. Overall our results emphasize the necessity and value of investigating cell-type contributions to neural development.

5.4 Monolayer iPSC derived neural networks reveal altered neuronal connectivity in CS

In vitro stem cell based disease models reveal important tissue-specific effects and advance our fundamental understanding of human disease, as well as potentially lead to development of targeted diagnostics and therapeutics. In this dissertation I

described the first functional neural model of Cockayne syndrome created from human donor-derived iPSCs. Previous studies using human somatic cells are unable to reveal functional neural aspects, and murine models fail to recapitulate key neural phenotypes of this devastating neurodegenerative disorder (Brace et al., 2013; Van der Horst et al., 1997). We studied neural cell and transcriptional contributions in CS in our monolayer heterogeneous neural development model.

5.4.1 First report of neural cells derived from Cockayne Syndrome donor iPSCs

Cockayne Syndrome iPSCs lacking *ERCC6* were previously established (Andrade et al., 2012) via retroviral reprograming, but it remained to be determined whether neural differentiation was possible, especially since transdifferentiation from fibroblasts had previously failed (Y. Wang et al., 2014). For this study we reprogrammed CS fibroblasts via a non-integrative Sendai virus method (Figure 3-1). Control iPSCs were either derived from primary tissue banked at the same commercial repository and donor matched for age and gender, or previously derived from live donor skin biopsies and banked in the Muotri Lab repository. Of the two controls retrieved from our repository, one was age and gender matched and one was unmatched. By adapting our previously published RTT model we then successfully established NPC lines (Figure 3-2) and were able to demonstrate corticogenesis from monolayer cultures using both CS and control iPSC lines (Figure 3-3).

5.4.2 MEA platform reveals altered CS neuronal functionality and connectivity

To assess whether MEA technology could be applied to study impaired neural network electrophysiology, neural differentiation was performed directly on multi-well

MEA substrates (Figure 3-9A). After five weeks, signature neurophysiological waveforms were observed in both CS and control cultures (Figure 3-9C) demonstrating functional neurons, however overall activity was significantly reduced in CS cultures (Figure 3-9D). Network synchrony was assessed (Figure 3-9B) as well as synapse density (Figure 3-8A & B) revealing significant connectivity deficiencies in CS networks (Figure 3-9E and Figure 3-8C, respectively).

5.4.3 Altered transcriptional pathways in CS neurons reflect processes essential for neural function & miRNA may contribute to neuropathology

We were initially uncertain whether disease phenotypes could be consistently observed in short-term *in vitro* neural cultures of this neurodegenerative disorder. Once robust phenotypes were established, we compared gene expression of CS neural cultures with controls (Figure 3-5 and Figure 3-6) revealing several dysregulated pathways related to neuronal function. Notably, morphology of the nervous system, axonogenesis, action potential of neurons, long term potentiation and neurotransmission were downregulated (Table 3-3). Although the implication of miRNA dysregulation in CS needs to be clarified in future work, we report miRNA as potential candidates contributing to transcriptional dysregulation in CS cells (Table 3-5). We also show that, contrary to previous reports from studies involving human primary fibroblasts models (Newman et al., 2006; Y. Wang et al., 2014), this model revealed transcriptional dysregulation in the Growth Hormone/Insulin-like Growth Factor-1 (GH/IGF-1) pathway compared to controls. Now that we have revealed dysregulation of key components of the GH/IGF-1 pathway in CS neurons, and given preclinical success of human IGF1 treatment in autism-related disease models of RTT (Khwaja et al., 2014; Marchetto et

al., 2010; Pini et al., 2012) (Marchetto et al., 2010) and Phelan-McDermid Syndrome (Shcheglovitov et al., 2013), investigating the potential effects in our newly established CS model may also be of compelling clinical interest.

5.5 Monolayer neural co-cultures from isogenic *MECP2* stem cells reveal astroglial non-autonomous phenotypes in RTT

Rationally designed *in vitro* disease models reveal important cell-type specific effects in complex systems and advance our fundamental understanding of human disease, as well as potentially lead to development of targeted diagnostics and therapeutics. Previous xenogenous studies strongly support a role for astroglia in RTT (Lioy et al., 2011; Maezawa et al., 2009; Williams et al., 2014). I characterized a CRIPSR/Cas9 generated isogenic matched human *MECP2* ESC model. I then studied the effect of astroglial MeCP2 on neural networking in an all human monolayer neural co-culture of control iPSC-derived neurons with separately derived isogenic matched *MECP2* astroglia.

5.5.1 Generating an isogenic matched *MECP2* ESC model

We applied CRISPR/Cas9 genomic editing to disrupt MECP2 in the extensively studied H9 human ESC line. We introduced a single nucleotide deletion at the lysine 82nd residue of exon 3, resulting in a nonsense frame shift with multiple early stop codons (K82*fs*, Figure 3-11A). We verified either total loss (Figure 3-11C) or total presence of MeCP2 in clonally expanded ESC sub-lines, suggesting robust X-inactivation occurs prior to clonal selection. Then we established NPC lines from both “RTT” and “ctr” sub-lines.

5.5.2 Neuronal activity and connectivity is diminished by MeCP2-deficient astroglia

I next established heterogenetic ESC astroglial and enriched iPSC neuronal co-cultures using CRISPR/Cas9-generated isogenic matched *MECP2* ESC lines to study astroglial MeCP2. Co-cultures of neurons with astroglia or fibroblast controls were grown directly on MEA substrates for network activity analyses or on cover glass for synapse density studies as described above, initially plated at 5:1 neuron to feeder cell ratio. I reported greatly diminished neuronal activity in both MeCP2-deficient astroglia and fibroblast co-cultures compared to those co-cultured with control astroglia after two weeks (Figure 3-19A & B). Synchronized activity was only measureable in neurons supported by control astroglia (Figure 3-19C). Interestingly, I observed similar excitatory presynaptic VGLUT density for all groups (Figure 3-20). Synapses were assessed by geometric co-localization of synapsin I and HOMER1 within defined proximity to MAP2 immunostained neural dendrites using IMARIS software. I report significant reduction of synapse density in the presence of MeCP2-deficient astroglia compared to both controls suggesting a negative non-autonomous effect caused specifically by the *MECP2* mutated astroglia (Figure 3-21). The outcome of fibroblast feeders promoting synapse densities similarly to control astroglia was unexpected. This connectivity may not be functional given the electrophysiology results, but provides rationale for additional study.

5.6 3D neural development models reveal neuronal maturation deficits and altered chemotaxis in RTT

To assess whether 3D scaffold technology could be applied to reveal neuropathophysiological phenotypes, we first evaluated neural differentiation of NPCs

in 3D. Once we observed phenotypic differences in Q83X compared to paternal control in 3D, we characterized additional male RTT and control NPC lines to test consistency across models. We generated iPSC lines from donor fibroblasts carrying a unique *MECP2* defect, N126I, and the corresponding unaffected paternal control, WT126. We also characterized a second isogenic matched *MECP2* pair, reversing the Q83X mutation in an iPSC subline, rQ83 (Table 4-1). NPCs, astroglia and neurons were separately generated (Figure 4-2A & B, Figure 4-2C-E, and Figure 4-4, respectively). Then, to accomplish the main goal of my thesis, I applied DGMP to separately encapsulate isogenic matched pairs of *MECP2* iPSC or ESC derived astroglia or neurons co-cultured with NPCs within laminar HAMA hydrogels optimized to facilitate migration and outgrowth (Figure 4-1 and Figure 4-13).

5.6.1 Reduced synapse density and maturation in MeCP2-deficient 3D neural tissue constructs

We reported defective maturation of RTT neurons in 3D hydrogels. We observed reduced neurite outgrowth, excitatory synaptic puncta density and frequency of postsynaptic currents from differentiated Q83X NPCs compared to paternal controls (Figure 4-17). Neurite outgrowth and synaptic phenotypes were reversed in isogenic controls (Figure 4-18), and present in a second MECP2 defect, N126I (Figure 4-19), demonstrating consistency across iPSC-derived RTT models.

5.6.2 Generating an isogenic matched *MECP2* iPSC model

To provide additional power to this study, I characterized a second pair of CRISPR/Cas9-generated isogenic matched stem cell lines. Distinct from the ESC-

derived isogenic pair initially developed for the preliminary monolayer neural co-culture studies, the second pair is a reversal of the RTT-causing Q83X mutation in our earlier described male RTT donor derived iPSC line (Figure 3-12). iPSCs were previously derived from live donor skin biopsies banked in the Muotri Lab repository and CRISPR/Cas9 genomic editing was outsourced to Applied StemCell.

5.6.3 Deficits in NPC migration and non-autonomous astroglial effect in RTT

We were able to examine cell type-specific effects of MeCP2 on developmental NPC migration. Notably, in addition to the inherently reduced capacity for migration of MeCP2-deficient NPCs (Figure 4-5A 1st *vs*. 3rd rows & D, and Figure 4-6A & B 1st *vs*. 3rd row & E), we report consistent non-autonomous effects from co-cultured MeCP2-deficient astroglia in our 3D model of neural development (Figure 4-5A 1st *vs*. 4th row & C-D, and Figure 4-6A & B 1st *vs*. 4th rows & E). This phenomenon escaped observation in 2D cell culture on similar scaffolds (Figure 4-15). This reduced migration is likely influenced by chemotactic gradients captured in the 3D scaffolds. I designed 3D and 2D experiments on similarly soft HAMA substrates to test this.

Unfortunately, without additional adhesive cues, our HAMA substrates did not support 2D NPC adhesion. We therefore covalently incorporated additional integrin binding peptide motifs into the HAMA scaffolds to promote attachment (Figure 4-14A & B). Unfortunately, even optimized RGD scaffolds only supported up to three days of attachment which is not long enough to test neural induction (Figure 4-14C). Co-cultures on 2D HAMA substrates did not reveal astroglial-mediated NPC migration (Figure 4-15A) compared to co-cultures in 3D RGD-HAMA scaffolds (Figure 4-15B and C). We also report partially disrupted NPC migration when 3D neural co-cultures were

treated with concentrated ACM (Figure 4-16). Together these data suggest the mode of NPC migration is chemotactic and that soluble gradients captured by HAMA hydrogels are generated by adjacently encapsulated astroglia.

5.6.4 Consistency of iPSC and ESC MeCP2 phenotypes

Our functional analyses of the Q83X and N126I iPSC-derived NPCs and induced neural cultures were unbiased. Characterizing fundamental neuronal parameters of these 3D cultured cells revealed that, similar to previous reports, *in vitro* differentiated *Mecp2*-deficient neurons exhibit abnormal connectivity, electrophysiology and morphometrics. Results across affected sublines, paternal and isogenic controls agree with published data generated from 2D models.

The previously unreported chemotaxis phenotypes observed in both RTT iPSC groups were further confirmed using CRISPR/Cas9 generated isogenic *MECP2* matched pair of ESCs. Our cumulative data across all three models confirms this robust phenotype, and further, the relevance of modeling neural development in 3D. These discoveries will likely drive similar investigations into 3D co-cultures for other neurological disease models, such as astroglia:neurons for CS and muscle:neurons to mimic the neuromuscular junction for ALS.

5.7 Future perspectives

The immediate next steps would be to continue developing and combining the approaches I have established during my thesis and applying them to *in vitro* neural models of development and disease. Specifically, further investigations into the

hierarchical complexity of neural network behavior is necessary and investigations into additional neural cell subtypes with regard to neural development and disease.

5.7.1 Isogenic stem cell co-culture system as a model of non-cell autonomous disease pathology

Decoupling cell-type specific contributions in complex neural tissue remains a considerable challenge. In this dissertation I establish viable neural co-cultures applied in both monolayer and 3D systems. While the deficits we observed in NPC chemotaxis and (primarily) cortical excitatory neurons are modulated by astroglia, it remains to be seen whether similar alterations in neurophysiology are differentially present in other stem cell derived neuronal subtypes.

5.7.2 Adapting the DGMP 3D laminar co-culture model for multiple tissues and diseases

Since all living human tissues exhibit higher complexity than what is presented in equally distributed monolayer cell culture, I expect the 3D laminar scaffold approach described herein to be of tremendous value to studies of many other tissues affected by disease. The DGMP method is highly adaptable as demonstrated by dissimilar models described throughout this dissertation, e.g. a wound healing model in Chapter 2 section 2.3 and models of neural chemotaxis and development in Chapter 4. This research has great potential to significantly impact the fields of developmental biology, regenerative medicine and disease modeling.

5.7.2.1 Network and circuit studies in 3D

Another group using similar approaches analyze 3D patterned neural networks and reported both synchronous and discordant oscillations in different neuronal populations patterns as measured by intracellular Ca^{2+} imaging (Aoi Odawara et al., 2013b). Separately, this group measured signal propagation time between 3D patterned networks via MEA (Aoi Odawara, Gotoh, & Suzuki, 2013a). Signal propagation times were on the order of *in vivo* network behavior and their evidence suggests an ability for investigating complex network activity in 3D co-cultures; however, oscillation patterns reported in the former study are far more interesting to us. The Suzuki group's work compliments what I have reported here and importantly, provides interesting proof-of-principle data prompting further investigation in the context of brain disease. In this dissertation I separately pattern neural co-cultures in 3D and analyze electrophysiology in 2D on MEA substrates. Interestingly, we did not observe robust oscillations in monolayer cultures (Figure D-2). An obvious next step is to combine these approaches to examine higher order neural networks in 3D with higher resolution than intracellular Ca^{2+} imaging.

5.7.3 Enhanced analyses of MEA electrophysiological data for potential clinical translation for epilepsy

CDKL5 is a monogenic X-linked neurodevelopmental disorder widely considered an atypical early onset seizure variant of RTT. In Appendix C I describe an ongoing study involving an isogenic iPSC-derived *CDKL5* neural model generated via X-inactivation in female donor cell lines. I report altered electrophysiology in network behavior and neuronal bursting rates in *CDKL5* neural networks derived from a single

donor compared to controls (Figure C-2). Additionally, I initiated a comparative electrophysiology study comparing *in vitro* MEA data to atypical RTT donor EEG data (Figure C-4). The potential impact of this translational multidisciplinary approach could revolutionize personalized medicine for epileptic brain diseases. This important work will be continued by the Muotri Lab, in collaboration with the Voytek Lab.

5.7.4 API screening platform using MEA network electrophysiology phenotypes as a readout

CDKL5 neural cultures will also serve as an *in vitro* epileptic model to screen potential therapeutic active pharmaceutical ingredients (APIs) using MEA technology to determine electrophysiological readouts. In Appendix D I describe a pilot study I performed using control ESC-derived neural cultures and report baseline recoverable *in vitro* effects of cannabinoid APIs, a potential therapy for epilepsy currently entering clinical trial (Figure D-1). Based on these pilot studies, future work will continue to focus on the MEA platform as a screen for epileptic therapeutic agents.

5.8 Conclusions

Challenges for personalized *in vitro* modeling of complex diseases remain. I took the opportunity of my PhD thesis to establish and explore several emergent technologies in effort to address some of these challenges for modeling brain disease, specifically for Cockayne Syndrome (CS) and Rett Syndrome (RTT). iPSC technology, now well established, can assist in challenging long established dogma resulting from studies involving cell types not directly affected by disease. We demonstrated this by reprogramming banked fibroblasts obtained from CS donors into iPSCs, differentiating

them into disease-relevant neural cells, and then revealing transcriptional phenotypes not observed in previous somatic cell models. Emergent MEA technology also revealed early developmental deficits of this neurodegenerative disease not previously described. With the advent of CRISPR/Cas9 genomic editing, it is becoming routing to develop isogenic matched stem cell models to study monogenetic disorders. I used this approach to establish isogenic *MECP2* neural co-cultures, allowing me to decouple NPC, astrocyte and neuronal specific aspects in RTT. Further, 3D scaffold based tissue models offer biomimetic complexity unmatched in monolayer systems. I describe a novel 3D cell scaffold fabrication method facilitating the construction of spatially controlled complex tissue. Using this method to construct neural co-cultures, I revealed previously unobserved chemotaxis phenotypes in RTT.

The findings from the studies presented in this dissertation demonstrate that detailed characteristics of neuron function and contributions from neural subtype can be extensively studied *in vitro*. I describe stem cell and scaffold based approaches to brain disease modeling and provide proofs-of-principle for similar evaluations of related or non-related human diseases. Further, I expect the tissue engineering-inspired methods described herein will have a broad impact in the context of developmental biology, regenerative medicine and disease modeling. The described 3D tissue scaffolds and isogenic stem cell co-culture approaches can be adapted to emulate *in vivo* cytoarchitectures of any human tissue, potentially offering new insights into disease and providing screening platforms towards more efficient development of therapeutic solutions.

Appendix A

Published US Patent Application 13/794,546: Single step polymerization of covalently bound multilayer matrices

Appendix A

A.1 Abstract

A method is provided for forming complex tissue using density gradient multilayer polymerization (DGMP) to form strong hydrogels with smooth transitions between layers. The multicompartment hydrogel is formed by co-dissolving a polymer precurser with a constituent in multiple solvent fractions to a create prepolymer solutions with different densities, layering the prepolymer solutions on top of each other from high to low solvent density, and irradiating the prepolymer solutions to form a polymer. The hydrogels may be used as biomimetic matrices.

A.2 Related U.S. Application Data

This application claims the benefit of priority under 35 U.S.C. §119(e) of U.S. Provisional Application Serial No. 61/609,300, filed March 10, 2013, and entitled SINGLE STEP POLYMERIZATION OF COVALENTLY BOUND MULTILAYER MATRICES, which is incorporated herein by reference in its entirety as if set forth in full.

A.3 Government rights

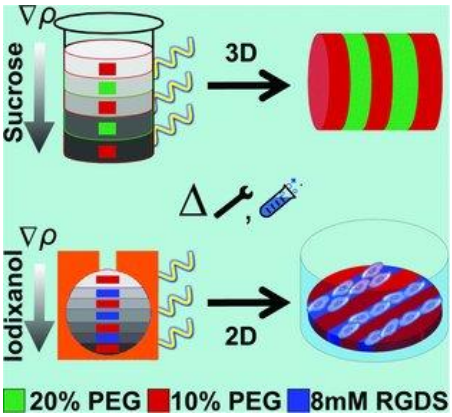
This invention was made with government support under Grant No. DMR1006081, awarded by the National Science Foundation. The government has certain rights in the invention.

A.4 Field of the invention

The present invention relates to a method for creating complex tissue. More specifically, the present invention provides a new method known as “density gradient

multilayer polymerization (DGMP)", which uses inexpensive reagents to form strong hydrogels with smooth transitions between layers. These novel hydrogels may be used as biomimetic matrices.

A.5 Background of the invention



Visual Abstract (Karpiak et al., 2012) For full background reference dissertation Chapter 2 section 2.2 - DGMP method for creating complex tissue.

A.6 Summary of the invention

The inventive method allows for conventional single step polymerization of multi-compartment polymer matrices. The described method is further unique in that the number of compartments is not limited by the procedure. Moreover, structural integrity is not compromised between layers or across gradients due to partial or incomplete interfacial integration. Properties of the resultant multilayer substrate are fully modulated by predetermination of discrete precursors separated by adjacent solvent liquid phase density dissimilarity and settling time of the solvent gradient. Additionally, the method is versatile, simple, requires ordinary adaptable reagents without additional heating or cooling steps, and is fully amenable to complimentary

techniques, including competitive methods, to further direct multi-scale polymer matrix architecture.

In one aspect of the invention, solutions of the components of each layer, including polymers, are mixed with varying concentrations of a common inert reagent to control density. The solutions are layered so that the difference in density segregates each solution, and then polymerized to form a gel. The structure of each layer can be altered by varying the concentration of polymers, and the discreteness of the transition between layers can be altered by allowing the solutions to diffuse.

This method, termed Density Gradient Multilayer Polymerization (DGMP), exploits phase separations between liquids of varying density to create layers of distinct structure and chemical composition. Briefly, serial concentrations of an inert density modifier, such as sucrose or iodixanol, are co-dissolved with a prepolymer (such as bisacrylamide and acrylamide or biocompatible c(PEGda)), crosslinkers, and ligands, proteins or cells.

Next, these prepolymer solutions are gently layered on top of each other in order of decreasing density. Varying the initial concentrations and types of each of these agents in each layer allows structures and chemical properties to be tailored. Varying the settling time before polymerization (t_S) adjusts the smoothness of gradients between layers. Bulk polymerization yields a multicompartment hydrogel. Finally, the density modifier is removed, resulting in multiphase hydrogels that are structurally uninterrupted at interfaces of chemically and mechanically diverse layers.

Density gradient multilayer polymerization allows engineering of multiple properties, either separately or combinatorial, into discrete or gradient phases of a structurally continuous polymer-based scaffold. Non-limiting tunable properties include:

covalently bound or encapsulated functional motifs and/or proteins; encapsulated cell type, ratio, density, and organization; minimally manipulated Human Cells, Tissues, and Cellular and Tissue-Based Products (HCT/Ps); matrix swellability, porosity, mechanical stiffness, macro, micro and nano-scale architectures; and responsiveness to cues such as pH, reactive oxygen species, light, enzymatic degradation, temperature.

The polymer based scaffolds/gels can also be formulated in different shapes to further control the release of encapsulated materials. This can be achieved via the gradient, multilayer, or combined systems in a flat gel, 3-dimensional gel, or a rolled gel.

In one aspect of the invention, a polymer precursor with a predetermined property is organized in discrete phases by static density gradient separation. Briefly, multilayer solvents are separately prepared via sequential dilution of a density modifier, such as sugar, salt, or iodixanol (in cases of aqueous precursors). Precursor constituents are dissolved separately, or in combination, in a solvent preparation corresponding to the desired layer, in order of density. Solvents are sequentially added to vessel of desired geometry. After a settling duration, precursors are polymerized to form a multi-compartment polymer matrix.

Due to the tissue like properties, this invention has many applications in tissue engineering. It allows for full control of each layer’s content in multilayer gels. Additionally it can function as an inductive/conductive multilayered scaffold to drive differential cellular behavior. It can be used to create patterned features throughout the gel or in patterns to better mimic certain biological tissues or niche scenarios.

It also has potential applications in therapeutic drug release and delivery. Due to the flexibility and multilayer capability, drug release and delivery can be modulated and controlled. Drugs can be released through controlled diffusion or actively using stimuli responsive polymers within separated compartments.

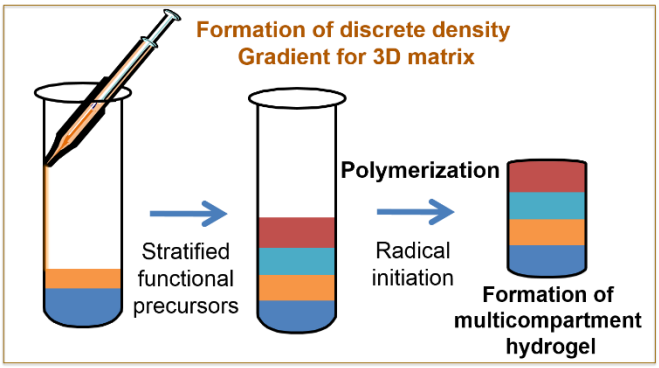
There is also potential to apply this technology to drug discovery. For example, it can be used to model diseases using human cells to facilitate investigation of migration, polarization, differentiation, and intercellular communication, among other phenomena, in a more *in vivo* like setting.

Outside of life sciences, potential commercial applications include multilayered processed food items or the preservation of foods with coatings in the food industry.

A.7 Detailed description

DGMP exploits phase separations between liquids of varying density to create layers of distinct structures and chemical compositions. Briefly, serial concentrations of an inert density modifier, such as sucrose or iodixanol, are co-dissolved with prepolymer (such as bisacrylamide and acrylamide or biocompatible c(PEGda)), crosslinkers, and ligands or proteins (Figure 2-1A & B). Next, these prepolymer solutions are gently layered on top of each other in order of decreasing density. Varying the initial concentrations and types of each of these agents in each layer allows structures and chemical properties to be tailored. Varying the settling time before polymerization (t_S) adjusts the smoothness of gradients between layers. Bulk polymerization yields a multicompartment hydrogel. Finally, the density modifier is removed, resulting in multiphase hydrogels that are structurally uninterrupted at interfaces of chemically and mechanically diverse layers.

Reagents are chosen for their suitability for this application. Sucrose is a highly soluble density modifier with a linear relationship between concentration and density (Figure 2-1A). Iodixanol, the main ingredient of Optiprep, is a nonionic, iso-osmotic density modifier currently used in viable cell purification (Brewer & Torricelli, 2007; Graziani-Bowering et al., 1997). Polyethylene glycol and polyacrylamide (PAM)-based hydrogels are well-suited for cell culture applications because they are biologically inert, so they are resistant to non-specific protein adsorption and cell adhesion (Peng et al., 2011; J. Tang et al., 2010), enabling precise engineering of desired biofunctionality through the covalent addition of ligands such as RGD peptide (Lutolf & Hubbell, 2005; Peppas et al., 1999; Roberts et al., 2012; Zhang et al., 2010). With these components, DGMP produces structurally continuous multilayer hydrogels for tissue engineering. Furthermore, the method can be adapted to varying mold shapes, sizes, and materials (**Figure 2-1**B).



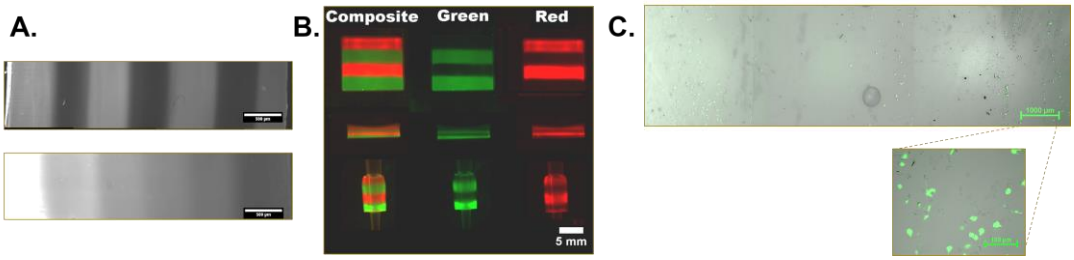
Patent Figure 17 A schematic of the adaptable DGMP method to pattern discrete or continuous features within an uninterrupted hydrogel matrix in a single polymerization step.

Existing techniques, including sequential photopolymerization, may yield networks that are susceptible to delamination under mechanical stress (Calvert,

Frechette, & Souvignier, 1998; Kuckling & Pareek, 2008; Weber et al., 2007). This mechanical instability is due to discontinuity at layer interfaces. Field emission scanning electron microscopy (FESEM) of architecturally varied PEGda layers reveals enhanced continuity at the interface of hydrogels fabricated by DGMP when compared to sequential polymerization (Figure 2-6A compared to Figure 2-6B).

This enhanced continuity can also be observed macroscopically in five-layer PAM hydrogels (Figure 2-6C compared to Figure 2-6D). Moreover, perpendicular compression testing revealed that PAM hydrogels fabricated via DGMP outperform analogous sequentially polymerized hydrogels (Figure 2-6E compared to Figure 2-6F).

Biomimetic tissue engineering also requires fabrication of not only discrete multicompartment gels but also gradients of varying degrees. To demonstrate the ability of DGMP to produce a variety of gradients, both smooth and sharp, between layers with different structures, we initially created biphasic matrices with 7% and 1% (w/w) PAM precursor using sucrose solutions of distinct densities and varied the settling times. Immediately polymerized hydrogels exhibit discrete compartments, with an abrupt transition, or sharp gradient, with different susceptibilities to swelling (Figure 2-6G, left). However, as t_S is incrementally increased prior to bulk polymerization, the lower layer becomes less susceptible to swelling (Figure 2-6G, from left to right). This illustrates that increasing settling time increases the graduation in mechanical transition.



Patent Figure 20 Biologically relevant adaptability.

A) PEGDA hydrogels with encapsulated BSA-594 in alternate or adjacent stepwise dilutions. B) Various geometries of polyacrylamide hydrogels with alternately incorporated fluorescein & rhodamine B for visualization. C) Five-layer PEG hydrogel substrates with A-PEG-RGDS incorporated into alternating layers via DGMP promotes patterned adhesion of HeLa:CMV-eGFP cells.

To determine whether DGMP allows spatial restriction of biological cues, we designed a simple experiment in which the biological cue would allow cell adhesion; whether the cues were separated would be obvious from whether cells attached. We fabricated tissue culture compatible two-dimensional (2D) substrates with alternating layers of covalently bound aPEG-RGDS labeled with Alexa Fluor 350 (to help visualize patterning) and seeded them with C2C12 myoblasts (Figure 2-8A and Figure 2-8B).

We developed a small scale manufacturing technique using iodixanol concentration gradients to construct these multilayer disc-shaped PEGda hydrogels specifically for tissue culture with standard well plates (Figure 2-1B). Briefly, molds were cut from 0.8 mm silicone sheets sized to fit between glass slides and used to construct seven-layer PEGda substrates via iodixanol DGMP. The tissue-culture discs swelled, were sterilized, and then seeded with C2C12 myoblasts (Figure 2-8B).

It was observed that adhered cells co-localized with covalently grafted RGDS peptide, visualized by alternating substrate fluorescence (Figure 2-8C). Furthermore, we were able to photoencapsulate C2C12 myoblasts by photopolymerization of the solutions, containing these cells, to form gels in the presence of 35% (w/v) iodixanol.

Briefly, 500,000 cells cm-3 were photoencapsulated in single compartment PEGda hydrogels with 8 mM RGDS and expanding cell colonies were confirmed viable by calcein-AM live stain after two weeks in culture (Figure 2-12). These results show that the iodixanol DGMP method allows fast, simple fabrication of hydrogel scaffolds with spatially defined active biological cues.

To determine whether this method allows spatial control of discretely arranged proteins, we created matrices in which small molecules (fluorescein-o-acrylate or rhodamine B) were bound (Figure 2-9A - C) or protein was encapsulated (Figure 2-8D and Figure 2-10A & B). Bovine serum albumin (BSA) was encapsulated in alternate layers (Figure 2-10A) or in discretely stepped gradients (Figure 2-10B). Further, we modulated smooth protein cross-gradients in PEGda hydrogels by increasing t_S after layering sucrose solutions of ovalbumin conjugated to Alexa Fluor 488 (OVA-488, 4mg mL^{-1}; Figure 2-8D, top) and BSA conjugated to Alexa Fluor 594 (4mg mL^{-1}; Figure 2-8D, bottom). Longer t_S resulted in progressively graduating protein concentration profiles.

Accurately modeling diseases using human cells requires 3D *in vitro* culture systems that mimic the degree and nature of variation found *in vivo*: both structural and biochemical, allowing cells to integrate multiple signals from various directions. Not only could such systems be used to create models of layered tissues, but they could also facilitate investigation of migration, polarization, differentiation, and intercellular communication, among other phenomena, in a more *in vivo*-like setting. Unfortunately, such variation in 3D hydrogel matrices is difficult to generate; current methods to create multilayer or gradient hydrogels involve complex instrumentation that requires technical skill.

Naturally, this has limited the use of such methods to engineering groups, which is unfortunate, as life science labs far outnumber bioengineering labs. The existing techniques that allow construction of multilayer matrices include additive photopatterning (V. A. Liu & Bhatia, 2002), laser scanning lithography (Mariah S Hahn et al., 2006), printing (Boland et al., 2006), and sequential functionalization (Kizilel et al., 2006).

Additional techniques offer spatial control of chemical or mechanical gradients, including gradient makers (Chatterjee et al., 2010) and microfluidics (Cosson et al., 2009).

An intuitive approach to generate multilayer hydrogels that does not require specialized instruments is serial addition of layers (T. K. Kim et al., 2003), but this creates barriers to diffusion and mechanical weakness at interfaces, and because of repeated UV exposure or cycles of temperature changes, may damage encapsulated cells.

To develop assays for migration, neurite outgrowth, and synaptogenesis, enabling the comparison of iPSC-derived NPCs and neurons generated from Rett syndrome (RTT) patients to those from controls. Because of the adaptability of DGMP, these assays may be modified to suit a variety of neuroscience questions, from the study of responses to specific migratory cues by a particular cell to screening drug candidates for their ability to rescue disease-associated defects in neural organization.

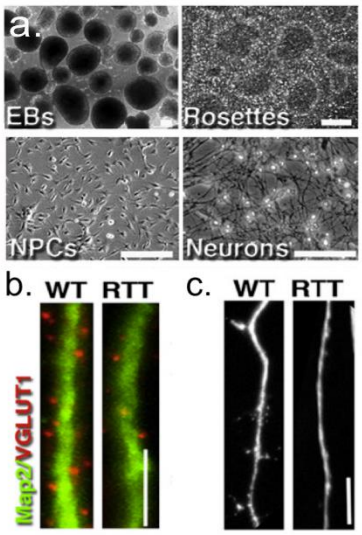
Current technologies for organizing cells, matrix components, and biochemical cues in 3D are complicated and require expensive equipment. Thus, their use is limited to only a few labs. This narrow application means that other labs must either limit their research questions to those addressable in 2D cell culture or in animals. To study brain

disorders, the most appropriate animal models are mice or rats, which can be expensive, and more importantly often yield results that do not correlate with those in human cells. The invention described herein (Figure 5-1) bridges the gap between studies in animal models and previous investigations using human iPSC-derived neurons cultured on flat surfaces.

The brain is complex, containing billions of interconnected neurons, forming trillions of individual connections. Its development occurs through the presentation of molecular, structural, and environmental cues presented at precise times in three dimensions. As such, modeling human brain development *in vitro* presents major challenges. The unavailability of live human neurons for research had until recently represented a major obstacle in the understanding of human brain development. While brain imaging has revealed important macroscale insights, such as increased numbers of neurons in autistic patients (Rapin et al., 2006), understanding local circuit development is also important for understanding neurological disease. In addition, while animal models are an important tool, they often do not recapitulate human phenotypes, and have been particularly problematic in the case of human neurodevelopmental diseases such as autism.

The development of induced pluripotent stem cell (iPSC) technology overcame some of these limitations, but the lack of methods to organize neurons in 3D has limited observable phenotypes to mostly individual characteristics, such as morphology and spontaneous electrical activity. iPSCs have enabled the generation of neurons from patients (Patent Figure 9A), allowing our recent investigation of RTT pathology, one of the first to use this breakthrough system to study neurodevelopmental disorders (Marchetto et al., 2010).

Studying RTT, which affects 1:10,000-1:22,000 births, may reveal mechanisms involved in other autism spectrum disorders. RTT is especially amenable to study because its genetics are relatively simple: it is caused by mutations in methyl CPG-binding protein 2 (MeCP2). Our investigation revealed reduced numbers of synapses and dendritic spine density (Patent Figure 9A - C), as well as altered calcium transients and spontaneous postsynaptic currents, in RTT patient-derived neurons compared to familial controls (Marchetto et al., 2010).



Patent Figure 9 Characterization of iPSC-derived neurons. A) Representative images depicting morphological changes during neurogenesis. Scale bar: 100 µm. B) Compared to WT, RTT neurons displayed impaired connectivity with reduced synapses and C) and spine density. Scale bar: 5 µm.

Excitingly, we were also able to demonstrate that IGF-1, which reverses some RTT phenotypes in mice, rescued the synapse number defect. However, given the limitations of 2D culture, we were unable to assess either cell volume, which may be altered given RTT patients' microcephaly, or migration. By combining human iPSC technology with 3D biomaterial engineering, we seek to advance the field of human *in*

vitro modeling and generate a novel model of human brain development for to the study of disease.

This system could be relevant to any neurodevelopmental disorder: not only monogenic disorders (e.g., RTT, Angelman, and Timothy syndrome), but also those with more complex inheritance such as other autism spectrum disorders. As the assays may reveal novel deficiencies in NPCs or neurons from patients with any of these disorders, this work enables the creation of several means of screening drugs. Our model should reveal a wider range of differences than apparent in 2D culture and thus should identify more drug leads, providing a powerful screening tool.

In conclusion, we introduce a novel multilayer single step polymerization technique that separates phases by solvent density. This method is accessible, versatile, and facilitates control of discrete, as well as continuously graduated, mechanical and chemical interfaces within structurally uninterrupted hydrogel networks. Although we demonstrated this technique in photopolymerized model hydrogel scaffolds, this simple method can be applied to any polymer system. We apply a sucrose DGMP method to spatially control mechanics, encapsulated proteins, and covalently bound small molecules within hydrogel matrices. We use iodixanol DGMP to pattern bioactive peptides and cells on 2D tissue culture substrates.

Importantly, the range of geometries and feature sizes presented throughout this communication were fabricated with common laboratory equipment and reagents. This powerful and adaptable technique is compatible with a range of polymer types (including those suitable for *in vivo* applications, such as hyaluronic acid) and solvents, as iodixanol is also compatible with organic solvents. DGMP could be combined with a

multitude of current fabrication paradigms to increase the complexity of matrices for tissue engineering, controlled drug delivery, or biological investigation.

A.8 Experimental methods

A.8.1 Cell Maintenance

C2C12 murine myoblasts (AATC) were maintained in Dulbecco's Modified Eagle's Medium supplemented with fetal bovine serum (10% v/v) and penicillin/streptomycin (1% 100X v/v) at 37ºC/5% CO2/95% relative humidity. Cell culture reagents were obtained from Life Technologies.

A.8.2 Fluorescently labeled aPEG-RGDS Synthesis

aPEG-RGDS-350 was synthesized with slight modifications to a previously described procedure (J.C. & J.L., 2010). Briefly, RGDS peptide (American Peptide, Arginine-Glycine-Aspartic Acid-Glycine) was conjugated to PEG (MW 3400 g mol^{-1}) by reaction with aPEG-SCM (Laysan Bio, SCM: Succinimidyl Carboxymethyl) at 1.2:1 molar ratio in the presence of DIPEA at 1.2:2 molar ratio overnight in DMSO under argon at room temperature. aPEG-RGDS was purified by dialysis, lyophilized and confirmed via matrix-assisted laser desorption/ionization time-of-flight mass spectrometry (MALDI-TOF) in universal matrix (Sigma) (Figure 2-2) and 1H-NMR in D2O (Figure 2-3).

An equimolar amount of Alexa Fluor 350 carboxylic acid, succinimidyl ester (Molecular Probes) was then added to aPEG-RGDS dissolved in DMF overnight in DMSO under argon at room temperature and purified by dialysis, lyophilized and stored under argon at -20°C.

A.8.3 Multilayer Hydrogel Fabrication

For 3D sucrose DGMP (Figure 2-1A): aqueous solutions of ethylene glycol diacrylate (Dajac Labs, MW 4000 g mol^{-1}; 10%, 15%, or 20% w/v; Figure 2-6A & B and Figure 2-8D) or acrylamide (Promega; 10% w/v; Figure 2-6C - G) were separately prepared in water. Precursor densities were individually modified with serial concentrations (0-50% w/v) of sucrose.

Each solution was gently layered in transparent cylindrical polypropylene molds made from modified syringes (Figure 2-6A - G) or in hydrophobic silanated (Sigmacote, Sigma) glass Pasteur pipettes (Figure 2-8D). For 2D iodixanol DGMP (Figure 2-1B): aqueous precursor monomer solutions of ethylene glycol diacrylate (15% w/v, Figure 2-8A - C) were separately prepared in Dulbecco‘s phosphate buffered saline (w/ Ca/Mg, HyClone). Precursor densities were modified with serial concentrations (5-40% w/v) of iodixanol (Axis-Shield OptiPrep, 60% iodixanol in water).

Each solution was gently layered in molds made from 0.8 mm thick silicone spacers cut with 10 mm and 8 mm biopsy punches (Acuderm) and sandwiched between hydrophobic silanated glass slides (Figure 2-8A). For all precursor solutions, Durocur 2959 photoinitiator (Gibco) was held constant (10 µl mL^{-1} of 300 mg mL^{-1} in N-vinyl pyrrolidone). Free radical polymerization was photoinitiated under irradiation with 365 nm light for 1 min in a Luzchem Research UV chamber (~2500 mW cm^{-2}) per side unless otherwise noted. Gradients were agitated in ten volumes of PBS for at least two days with two buffer exchanges per day to remove density modifiers, unreacted prepolymer, and photoinitiator.

A.8.4 Structural Stratification

DGMP gradients were compared to sequentially polymerized multi-layer hydrogels, in which precursors identical to those for DGMP were used, both groups were irradiated for 1 min per layer, and the process was not optimized. For microstructural examination (Figure 2-6A & B), bilayer PEGda hydrogels (10% w/v, upper left; 20% w/v, lower right), were snap frozen in N2, lyophilized overnight, and coated with chromium (45 s at 130 mA), then recorded with an FEI XL30 SFEG SEM. For macrostructural examination and mechanical testing (Figure 2-6C - F), five-layer PAM (10% w/v, 1% w/w crosslink) hydrogels were photographed (Figure 2-6C & D) and compressed with a Satec materials testing machine (Figure 2-6E & F).

To examine the effect of graduated transitions on structural properties, PAM mechanical gradients were created in biphasic sucrose gradients by diffusion of bisacrylamide from layers of 7% to 1% (w/w) crosslinker for t_S of 0, 15, 30, 60, 120, and 180 min (Figure 2-6G).

A.8.5 Chemical Stratification

For fluorescence pattern images of PEGda tissue culture discs (Figure 2-8A & C), co-dissolved iodixanol and prepolymer solutions were combined with either methacryloxyethyl thiocarbamoyl rhodamine B (Polysciences, 20 µM) or aPEG-RGDS-350 (8 mM). Precursor solutions were gently layered stepwise into silicone and glass molds, described above, and photopolymerized.

Bioactivity of patterned integrin-binding peptide, RGDS, was evaluated by seeding C2C12 myoblasts (20,000 cells cm^{-2}) onto hydrogel discs. Resulting cell patterns were observed after 24 hr in culture via epifluorescence and phase-contrast

imaging (Zeiss Axiovert 200; Figure 2-6C). Protein gradients in PEGda (15% w/v) were created via biphasic sucrose DGMP by counter-diffusion of OVA-488 (Figure 2-8D, upper) and BSA-594 (Figure 2-8D, lower) for t_S of 0, 30, 90, and 150 min (both proteins initially 4 mg ml^{-1}, Life Technologies).

A.8.6 Photography and image processing

Gross hydrogel images were obtained in a BioRad VersaDoc-4000MP. Color photographs were taken with a Canon Powershot A11000 IS. Individual field fluorescence and transmitted light microscopy images were color composited with Image Pro Plus software. All multi-field images were manually reconstructed with ImageJ software (NIH) using the MosaicJ plugin with all corrections disabled (e.g. blending, smart color, and rotation). Average and line fluorescence intensity profiles were generated with Image J software.

Listed below are several advantages, demonstrated in this study, of the density gradient multilayer polymerization (DGMP) method. DGMP is more versatile and accessible compared to complex alternative methods. Moreover, DGMP allows fast, simple fabrication of structurally uninterrupted complex tissue scaffolds with spatially controlled bioactive chemical and mechanical cues.

- Robust: Structurally uninterrupted interfaces, even for unmatched mechanics.
- Facile & Economical: Single polymerization step & commonly available, inexpensive reagents.
- Tunable: Geometry, matrix porosity, and extra-matrix constituents.
- Scalable: Amenable to complementary methods to further control micro- and nano-architectures & vascularity.

A.8.7 Synthesis of Fluorescently Labeled Acryloyl-PEG-RGDS

1. React the RGDS peptide with acryloyl-PEG-succinimidyl carboxymethyl ester (aPEG-SCM, PEG MW: 3400 g/mol) and N-Ndiisopropylethylamine (DIPEA) at 1.2:1:2 molar ratios in dimethyl sulfoxide (DMSO) under argon at room temperature overnight.
2. Confirm conjugation by matrix-assisted laser desorption/ionization time of flight (MALDI-TOF) mass spectrometry. Add 1 µl of aPEG-RGDS reaction solution to a sample spot on the MALDI target and dry. Prepare a saturated solution of Universal MALDI Matrix in tetrahydrofuran (THF) and vortex for 1 min. Add ~1 µl of this solution to the same sample spot. Repeat the procedure for aPEG-SCM for comparison. Load and analyze. The molecular weight of aPEG-RGDS should be greater than aPEG-SCM (Figure 2-2).
3. To conjugate the fluorophore, add an equimolar amount of Alexa Fluor 350 carboxylic acid (succinimidyl ester), dissolved in a minimal volume of DMSO, to the aPEG-RGDS reaction solution from 1.1 and react under argon at room temperature overnight.
4. Purify aPEG-RGDS-350 by dialyzing (MW 3500 Da) against DI-H2O at 4 °C for 48 hr at 1,000:1 volumetric ratio, exchanging dialysate at least twice per day.
5. Freeze dry the purified aPEG-RGDS-350 in a Labconco Freezone Plus or equivalent freeze dry system and store at -20 °C.

A.8.8 Preparation of a 2D Mold & Fabrication of 2D PEG Gel with Alternating RGDS-350 Layers

1. Prepare hydrophobic glass slides. Place clean glass slides into a glass dish in a vacuum oven. Heat to 80 °C for 30 min to completely dry the surfaces. Place dish with slides in a fume hood and add 250 µl Sigmacote to each slide, gently rocking for 30 sec to coat entire surface. Thoroughly rinse the coated slides with 100% methanol, followed by washing in distilled water, soaking twice for 5 min in at least 10 ml.
2. Cut silicone spacers (0.8 mm thick) with 10 mm biopsy punches.
3. Autoclave the silicone spacers and Sigmacote-treated glass slides.
4. Formulate solutions for each respective layer in individual microfuge tubes by mixing PEG diacrylate (PEGda) precursor (final concentration 15% w/v) with different amounts of iodixanol (60% stock solution in water) to yield varying final concentrations (e.g. 40%, 30%, 20% and 10%), supplementing the remaining volume with phosphate buffered saline (PBS) to obtain solutions of graded densities. In a similar manner, for alternating layers, mix aPEG-RGDS-350 (final concentration 8 mM) with iodixanol and PBS to yield various concentrations (e.g. 35%, 25%, and 15%).
5. Add photoinitiator (2-Hydroxy-4'-(2-hydroxyethoxy)-2-methylpropiophenone, 333mg/ml stock in N-vinyl pyrrolidone) to each solution for various layers (10 µl of stock solution per ml of each layer solution). Photoinitiator is added last to prevent polymerization before layering of the gels in the mold, as it is sensitive to light.
6. Subsequent steps of are performed in a biosafety cabinet to ensure sterility.

7. Filter-sterilize each solution using a sterile 1 ml syringe and 0.2 μm filter. Assemble the mold setup by sandwiching the spacer between two Sigmacote-treated glass slides and secure with clamps placing as depicted in Figure 2-1.
8. Cast the layered gels by adding the most dense solution (e.g. PEGda with 40% iodixanol) first, followed by a less dense solution (e.g. aPEGRGDS-350 with 35% iodixanol). Repeat the alternate layering to achieve several layers of desired composition and densities as shown in Figure 2-1.
9. Irradiate the mold with 365 nm light for 3 min using a portable UVR-9000 lamp. Allow the polymerized gels to cure for 5 min. Remove the clamps, then gently lift the top glass slide and the mold; the stratified DGMP gels remain on the slides. Using a sterile spatula, carefully place the gels in a 50 ml tube containing sterile PBS or culture medium for washing.
10. Wash the polymerized gels in PBS at 1,000:1 volumetric ratio, exchanging buffer at least twice per day to remove the density modifier, photoinitiator, and unreacted polymer. Alternatively, PBS may be exchanged with cell growth medium. Store the DGMP gels in PBS or growth medium for the cell culture experiment outlined in Step 3.
11. To visualize alternating layers, arrange DGMP gel (these gels are not suitable for cell culture) along a ruler on the sample tray of a VersaDoc gel documentation unit. Expose the gels in 350 nm; the exposure time varies depending on the concentration of the fluorophore.

A.8.9 2D Cell Culture on DGMP Gels

1. For gels incorporating RGDS peptide, use adhesion dependent cells, such as C2C12 myoblasts.
2. Gently insert DGMP gels (stored in PBS) into the wells of 48-well cell culture plates using a sterile cell scraper in a biosafety cabinet.
3. Pre-warm growth medium (Dulbecco's modified Eagle's medium or DMEM supplemented with 10% v/v fetal bovine serum and 1% v/v 100X penicillin-streptomycin solution) and PBS in a water bath set at 37 °C.
4. Wash a 60% confluent plate (10 mm) of C2C12 cells three times with PBS. Aspirate off PBS and harvest cells by adding 1 ml of 0.25% Trypsin-EDTA and incubating at 37 °C for 2 min. Re-suspend the cells in growth medium and count cells. Seed the DGMP gel-containing cell culture well with C2C12 myoblasts (20,000 cells/ cm^2). Incubate the cells at 37 °C in 5%CO2/95% relative humidity. Gently exchange medium after 4 hr, careful not to remove lightly adhered cells.
5. After 24 hr, the attachment of C2C12 myoblasts on the RGDS-containing layers of DGMP gels may be confirmed by epifluorescence and phase contrast microscopy (Zeiss Axiovert 200).

A.8.10 Complex, Cell-Laden, Multilayer Hydrogel Matrices

The DGMP method, a breakthrough for its simplicity in creating complex, cell-laden, multilayer hydrogel matrices. Layering, polymerization (by UV exposure if using radically polymerized materials), and initial iodixanol washout all take approximately 25 minutes.

A.8.11 Hyaluronan-Based Hydrogel Matrices

Hyaluronic acid methacrylate (HAMA) was synthesized using the method described in Seidlits SK, et al, The effects of hyaluronic acid hydrogels with tunable mechanical properties on neural progenitor cell differentiation. (Seidlits et al., 2010), with appropriate resulting elastic modulus for neuron culture (Figure 2-26) (Smeds et al., 1999).

As iodixanol may affect matrix elastic modulus, atomic force microscopy (AFM) was performed. Initial results suggest that its effect is concentration independent in the range under investigation (Figure 2-26B). It was also observed that iodixanol minimally affects viability; groups were compared by the ratio of constitutively expressed eGFP to ethidium homodimer-1 staining.

NPCs generated from human iPSCs following informed consent (under protocols approved by the UCSD Institutional Review Board and the Embryonic Stem Cell Research Oversight Committee), generated by transduction of Sox2, Oct4, c-Myc and Klf4. NPCs are produced by dissociating neural rosettes and confirmed by immunocytochemistry against early neural progenitor markers, such as nestin (Figure 2-27C) (Marchetto et al., 2010). NPCs are labeled by infection with a lentivirus carrying the CAG promoter driven eGFP reporter (CAG::eGFP).

Combinations of tethered adhesion peptides and varied encapsulated cell densities are investigated to improve viability and promote neurite extension. A combination of YIGSR, a peptide sequence of laminin responsible for integrin binding, and RGDS, a peptide that binds many integrins, yields the highest 24 hr viability (~80%, Figure 2-27A). This combination also promotes extensive neurite growth by NPCs (Figure 2-27B). Not only do HAMA matrices maintain NPCs (nestin expression, Figure

2-27C), they also support differentiation when soluble BDNF is provided in the media (MAP2 expression, Figure 2-27D).

A.8.12 Development of a 3D scaffold to maintain NPC viability

Cell, adhesion peptide, and photoinitiator concentration, as well as HAMA degree of substitution (DS), are adjusted to establish consistent NPC viability. To maintain NPC multipotency, cells are cultured in an NPC medium with bFGF22, barring differentiation and limiting neurite outgrowth. Percent eGFP positive cells is assessed via FACS analysis. HAMA with varied DS, which affects elastic modulus, is synthesized by adjusting molar ratios of reactants, methacrylic acid, and hyaluronan (Smeds et al., 1999).

Since scaffold elastic modulus affects differentiation (Seidlits et al., 2010) and pore size affects locomotion, hydrogel elastic modulus and pore size are measured for each condition tested. Viability is assessed as in preliminary experiments (Figure 2-27A).

A.8.12.1 Outcomes

A set of permissive (later referred to as “baseline”) conditions that reliably promote cell viability (at least 90% of total encapsulated cells) with little effect on cell spreading, migration, and neurite outgrowth are identified. It is then determined which adhesion cues are required to prevent anoikis and, through fine tuning, what range of crosslinking density allows nutrient transport, cell locomotion, and neurite outgrowth.

Alternative Approaches: If necessary, encapsulation conditions are modified to balance photoinitiator concentration with UVA exposure time, or add cytoprotective

elements such as human serum albumins to enhance encapsulated cell viability. The viability assay we are proposing may be difficult to interpret at late time points due to optically inseparable cell aggregates (Figure 2-26B - D); viability analysis by a DNA-normalized metabolic assay (MTS), or by FACS analysis of dissociated cells following enzymatic digestion can also be considered. Further, if 800 μm thick hydrogels (chosen for ease of handling) are too thick to allow nutrient and oxygen diffusion, thinner constructs are fabricated.

A.8.13 Determination of variables that modulate NPC migration

Many variables influence NPC migration, so focus is applied to those inherent to the matrix itself. The gradients of crosslink densities or concentrations of extracellular matrix derived integrin-binding peptides YIGSR, IKVAV, and RGD, both individually and in combination, are examined. Non-gradient hydrogel matrices serve as controls.

While many cues that promote directional migration of cell bodies may also promote neurite extension in the same direction, cultures are maintained in NPC medium (with bFGF22) to limit outgrowth. In each of these experiments, cells are encapsulated in the middle layer of a HAMA matrix in which adjacent layers contain semi-continuous gradients (Figure 2-28). The cell-loaded layer is fluorescently marked with methacrylated rhodamine-B and match the conditions determined to maintain NPC viability.

Migration is quantified using confocal microscopy at static time points and, when feasible, with time-lapse imaging. NPCs are monitored daily to determine preferential migration up or down gradients of each variable or combination of variables. The total number of cells crossing into adjacent layers and total distance

traveled away from the initial center layer are measured. The combinations of gradients or opposing gradients are further measured to enhance migration (Figure 2-29).

A.8.13.1 Outcomes

A gradient conditions that reliably facilitate cell migration is identified. Contrary to many somatic cell types, NPCs are expected to migrate towards decreasing crosslinking density (HAMA DS), as migration in HAMA has been demonstrated to coincide with hydrogel degradation (Seidlits et al., 2010). We expect NPCs to migrate towards greater concentrations of adhesion peptide (Luo & Shoichet, 2004; Tate et al., 2004).

A.8.13.2 Alternative approaches

If spontaneous migration does not occur, the scaffolds are co-cultured with underlying 2D cultures of astrocytes, which have been shown to promote neural migration (Mason et al., 2001).

Alternately, by tethering to the HAMA macromer (Yu, Dillon, & Bellamkonda, 1999), gradients of proteins that direct NPC migration may be incorporated, e.g. sonic hedgehog (SHH) (Wylie et al., 2011).

If necessary, an additional level of control over combination gradients is employed: the DGMP method can be combined with a gradient grayscale mask method to independently adjust peptide and elastic modulus gradients by exposing DGMP layered prepolymers to variable amounts of UVA (Tse & Engler, 2010).

A.8.14 Creation of organized 3D neural networks

Gradient variables that enhance neurite outgrowth from neurons are identified and, by incorporating a non-adjacent synaptic target cell layer, a model in which cell bodies, axons, and synapses may be easily located and separately analyzed is developed.

This organization simplified a wide array of investigations, such as quantification of synapses and analyses of 3D morphology, e.g. axon packing and alignment. Further, a 3D environment is likely more representative of neural behavior *in vivo*. In order to generate 3D neuronal networks, NPCs are induced to differentiate by switching to medium without bFGF22.

In order to direct oriented neurite outgrowth, gel-inherent variables are considered, and a range of HAMA DS as well as adhesion peptide concentrations are examined. If a gradient of a particular variable, for example IKVAV peptide, directs both neurite outgrowth and cell migration, hydrogel mechanical properties are tailored to fall outside an expected range of migration-permissive elasticity (Hynes et al., 2009).

Neurite outgrowth from eGFP-expressing neurons is monitored daily by confocal microscopy, and, when effective conditions are identified, by time-lapse imaging. To identify the variable, or combination of variables, that best promotes neurite extension, the total number and length of neurites extending out of the baseline layer in experimental matrices are compared to those in control, non-gradient matrices.

A model in which somatic target cells is used to enable the distinction between pre- and postsynaptic cells is developed. Initially, examples of previous mixed-culture systems are followed for the study of synapses, which often employ HEK293 cells heterologously expressing at least one postsynaptic protein, e.g. neuroligin-1 (J.-E. Kim

et al., 2011). Target HEK293 cells are encapsulated within a non-adjacent layer separated from neurons by a neurite-promoting gradient (Patent Figure 16).



Patent Figure 16 Separation of cell bodies from synapses. Neurons synapse onto HEK cells encapsulate din a non-adjacent layer.

A range of encapsulation cell densities are analyzed to determine which yields the most efficient synaptogenesis. The co-culture system allows for the distinction between self-synapses and synapses onto target cells, which will only express one postsynaptic protein. Synapses are quantified by comparing the number of sites of staining for presynaptic markers (synapsin) to those for postsynaptic markers expressed in neurons and not target cells (PSD95).

A.8.14.1 Outcomes

A set of variables that promotes neurite outgrowth (of length similar to that observed in 2D cultures) while simultaneously inhibiting migration out of the baseline layer in which cells are encapsulated are identified. Adhesion peptides are expected to be effective in directing neurite extension, as gradients of peptides have previously been demonstrated to drive differential outgrowth in hydrogel matrices in 3D (Sundararaghavan, Masand, & Shreiber, 2011).

A.8.14.2 Alternative approaches

A particular degree of difference in biochemical or mechanical variables across layers (i.e., gradient steepness) may selectively promote neurite outgrowth over migration; therefore, varying degrees of difference in HAMA DS or adhesion peptide concentration may be investigated. If no combination of structural and adhesion peptide gradients promotes directional neurite outgrowth, gradients of tethered protein axonal guidance cues are explored.

Further, if mature neurons fail to extend sufficiently long neurites, medium is supplemented with instructional soluble growth factors such as BDNF, which enhances differentiation (Figure 2-27D, (Labelle & Leclerc, 2000)).

If few neurites form synapses, the transfection approach is modified to enhance expression of postsynaptic protein by incorporating more copies of the gene or by using a more active promoter. Alternatively, an alternate target cell type, such as COS7, or a different postsynaptic protein, such as synCAM-1 may be employed.

A.8.15 Comparison of RTT-derived NPCs and neurons to controls

The spatially controlled 3D model of neurodevelopment should be useful to compare NPCs and neurons of distinct genotypes, therefore applicable to answer questions regarding RTT, such as evaluating the effects of either 3D culture microenvironment or scaffold mechanical properties on function and differentiation of human induced pluripotent stem cell derived neuronal progenitor cells into neurons.

A.8.16 NPC migration

The microcephaly often observed in RTT patients and the connection between abnormal neural stem cell migration and autism (Peñagarikano et al., 2011) suggest that NPC migration may be altered in RTT. Migration of RTT and control NPCs is evaluated in the migration-promoting conditions discussed above.

To examine NPC migration, RTT and control NPCs (both expressing eGFP) are encapsulated in the 3D hydrogels in parallel underbFGF2 conditions to promote NPC maintenance. RTT or control NPCs are encapsulated in a hydrogel layer adjacent to a layer containing a gradient promoting unidirectional NPC migration, using the parameters determined earlier. NPC migration is then quantified via live confocal microscopy with time-lapse imaging and at static time points.

A.8.16.1 Alternative strategies

Detection of differences between RTT and controls in the NPC migration assays may not be visible if adhesion peptides presented do not allow for the demonstration of impaired migration, as RTT neurons may not have defective laminin binding. Alternatively, adhesion cues shown to be affected in RTT can be used.

A.8.17 Neurite outgrowth and synaptogenesis

Given our previous results of decreased synapse number and spine density in RTT neurons, we seek to further explore related phenotypes such as neurite extension and dendritic arborization. Dynamic neurite outgrowth in patient-derived RTT neurons has not yet been examined, so these experiments will yield novel results. As 3D

environments enhance connectivity, a more pronounced defect in synaptogenesis is expected.

RTT and control NPCs are induced to differentiate after encapsulation in 3D hydrogel scaffolds constructed using the parameters identified above. To measure neurite outgrowth, cells are immunostained with a neuronal marker (Map2) or transduced with a synapsin::eGFP reporter and imaged via confocal microscopy (with time-lapse imaging as needed). To quantify synapses, target cells (e.g. HEK) expressing a postsynaptic protein are encapsulated in the layer opposite that promoting unidirectional neurite outgrowth. Synapses onto target cells are quantified by confocal microscopy, using antibodies against the presynaptic proteins synapsin and neurexin and two postsynaptic proteins: that expressed by target cells, and one expressed in neurons, e.g. PSD95.

A.8.17.1 Alternative strategies

If no significant differences between RTT and controls in the neurite outgrowth assays are detected, the guidance cues presented may not allow for the demonstration of impaired neurite outgrowth. In that case, guidance cues suggested to be involved in RTT are incorporated instead.

A.9 Claims

All references cited herein, including patents, patent applications, papers, text books, and the like, and the references cited therein, to the extent that they are not already, are hereby incorporated by reference in their entirety. In the event that one or more of the incorporated literature and similar materials differs from or contradicts this

application, including but not limited to defined terms, term usage, described techniques, or the like, this application controls. Although this application has been described in detail above, it will be understood by one of ordinary skill in the art that various modifications can be made without departing from the spirit of the invention. Accordingly, this application is limited only by the following claims.

1. A method for preparing a multicompartment hydrogel comprising:
    a. co-dissolving a polymer precurser with a constituent in multiple solvent fractions to a create prepolymer solutions with different densities;
    b. layering the prepolymer solutions on top of each other from high to low solvent density; and
    c. irradiating the prepolymer solutions to form a polymer.
2. The method of Claim 1, wherein the polymer precurser comprises acrylamide and bisacrylamide.
3. The method of Claim 1, wherein the polymer precurser comprises polyethylene glycol diacrylate (PEGda).
4. The method of Claim 1, wherein the constituent is an acrylated fluorophore or a conjugated adhesion peptide RGDS.
5. The method of Claim 1, wherein one or more of the layers of the prepolymer solutions are irradiated at different times.
6. The method of Claim 1, further comprising the use of an aqueous density modifier.
7. The method of Claim 6, wherein the aqueous density modifier comprises sucrose, iodixanol, or a mixture thereof.
8. The method of Claim 6, wherein the aqueous density modifier is present in an amount of between about 0% to about 15% or between about 10% to about 50%.

9. The method of Claim 6, wherein the method further comprises the step of washing out the density modifier after the polymer is formed.
10. The method of Claim 1, wherein the multicompartment hydrogel is capable of culturing tissue in a three-dimensional arrangement that mimics those in the body.

A.10 Acknowledgements

The contents of Appendix A were adapted for US Patent Application # 13/794,546 and published as “Single step polymerization of covalently bound multilayer matrices.” Karpiak JV**,** Ner Y, Morachis J, Almutairi A. US Patent publication # US20130234372A1, March 11, 2013. The dissertation author was the primary investigator and author of this patent.

Appendix B

Published online DGMP video protocol: JoVE© summary and URL



DGMP: A novel technique for creating multi-compartment, customizable scaffolds for tissue engineering

B.1 Brief introduction and rationale

Complex tissue culture matrices, in which types and concentrations of biological stimuli (e.g. growth factors, inhibitors, or small molecules) or matrix structure (e.g. composition, concentration, or stiffness of the matrix) vary over space, would enable a wide range of investigations concerning how these variables affect cell differentiation, migration, and other phenomena. The major challenge in creating layered matrices is maintaining the structural integrity of layer interfaces without diffusion of individual components from each layer (Place et al., 2009). Current methodologies to achieve this include photopatterning (V. a. Liu, Jastromb, & Bhatia, 2002; Sharma et al., 2007), lithography (Mariah S Hahn et al., 2006), sequential functionalization (Kizilel et al., 2006), freeze drying (Harley et al., 2010), microfluidics (Cuchiara et al., 2010), or centrifugation (Roam et al., 2010), many of which require sophisticated instrumentation and technical skills. Others rely on sequential attachment of individual layers, which may lead to delamination of layers (Gleghorn et al., 2008).

DGMP overcomes these issues by using an inert density modifier such as iodixanol to create layers of varying densities (Karpiak et al., 2012). Since the density modifier can be mixed with any prepolymer or bioactive molecule, DGMP allows each scaffold layer to be customized. Simply varying the concentration of the density modifier prevents mixing of adjacent layers while they remain aqueous. Subsequent single step polymerization gives rise to a structurally continuous multilayered scaffold, in which each layer has distinct chemical and mechanical properties. The density modifier can be easily removed with sufficient rinsing without perturbation of the individual layers or

their components. This technique is therefore well suited for creating hydrogels of various sizes, shapes, and materials.

A protocol for fabricating a 2D-polyethylene glycol (PEG) gel, in which alternating layers incorporate RGDS-350, is outlined below. We use PEG because it is biocompatible and inert. RGDS, a cell adhesion peptide (Pierschbacher & Ruoslahti, 1984), is used to demonstrate spatial restriction of a biological cue, and the conjugation of a fluorophore (Alexa Fluor 350) enables us to visually distinguish various layers. This procedure can be adapted for other materials (e.g. collagen, hyaluronan, etc.) and can be extended to fabricate 3D gels with some modifications (Karpiak et al., 2012).

B.2 Video Link

The video component of this article is published online at the following URL:

http://www.jove.com/video/50018/

B.3 Detailed protocol

B.3.1 Synthesis of fluorescently labeled Acryloyl-PEG-RGDS

1. React the RGDS peptide with acryloyl-PEG- succinimidyl carboxymethyl ester (aPEG-SCM, PEG MW: 3400 g/mol) and N-N diisopropylethylamine (DIPEA) at 1.2:1:2 molar ratios in dimethyl sulfoxide (DMSO) under argon at room temperature overnight.
2. Confirm conjugation by matrix-assisted laser desorption/ionization time of flight (MALDI-TOF) mass spectrometry. Add 1 µl of aPEG-RGDS reaction solution to a sample spot on the MALDI target and dry. Prepare a saturated solution of Universal MALDI Matrix in tetrahydrofuran (THF) and vortex for 1 min. Add ~1 µl of this

solution to the same sample spot. Repeat the procedure for aPEG-SCM for comparison. Load and analyze. The molecular weight of aPEG-RGDS should be greater than aPEG-SCM (Figure 2-2).

3. To conjugate the fluorophore, add an equimolar amount of Alexa Fluor 350 carboxylic acid (succinimidyl ester), dissolved in a minimal volume of DMSO, to the aPEG-RGDS reaction solution from 1.1 and react under argon at room temperature overnight.
4. Purify aPEG-RGDS-350 by dialyzing (MW 3500 Da) against DI-H2O at 4 °C for 48 hr at 1,000:1 volumetric ratio, exchanging dialysate at least twice per day.
5. Freeze dry the purified aPEG-RGDS-350 in a Labconco Freezone Plus or equivalent freeze dry system and store at -20 °C.

B.3.2 Preparation of a 2D mold and fabrication of a 2D PEG gel with alternating RGDS-350 layers

1. Prepare hydrophobic glass slides. Place clean glass slides into a glass dish in a vacuum oven. Heat to 80 °C for 30 min to completely dry the surfaces. Place dish with slides in a fume hood and add 250 µl Sigmacote to each slide, gently rocking for 30 sec to coat entire surface. Thoroughly rinse the coated slides with 100% methanol, followed by washing in distilled water, soaking twice for 5 min in at least 10 ml.
2. Cut silicone spacers (0.8 mm thick) with 10 mm biopsy punches.
3. Autoclave the silicone spacers and Sigmacote-treated glass slides.
4. Formulate solutions for each respective layer in individual microfuge tubes by mixing PEG diacrylate (PEGda) precursor (final concentration 15% w/v) with

different amounts of iodixanol (60% stock solution in water) to yield varying final concentrations (e.g. 40%, 30%, 20% and 10%), supplementing the remaining volume with phosphate buffered saline (PBS) to obtain solutions of graded densities. In a similar manner, for alternating layers, mix aPEG-RGDS-350 (final concentration 8 mM) with iodixanol and PBS to yield various concentrations (e.g. 35%, 25%, and 15%).

5. Add photoinitiator (2-Hydroxy-4'-(2-hydroxyethoxy)-2-methylpropiophenone, 333mg/ml stock in N-vinyl pyrrolidone) to each solution for various layers (10 µl of stock solution per ml of each layer solution). Photoinitiator is added last to prevent polymerization before layering of the gels in the mold, as it is sensitive to light.
6. Subsequent steps of this protocol will be performed in a biosafety cabinet to ensure sterility.
7. Filter-sterilize each solution using a sterile 1 ml syringe and 0.2 µm filter. Assemble the mold setup by sandwiching the spacer between two Sigmacote-treated glass slides and secure with clamps placing as depicted in Figure 2-1B.
8. Cast the layered gels by adding the most dense solution (e.g. PEGda with 40% iodixanol) first, followed by a less dense solution (e.g. aPEGRGDS-350 with 35% iodixanol). Repeat the alternate layering to achieve several layers of desired composition and densities as shown in Figure 2-1B.
9. Irradiate the mold with 365 nm light for 3 min using a portable UVR-9000 lamp. Allow the polymerized gels to cure for 5 min. Remove the clamps, then gently lift the top glass slide and the mold; the stratified DGMP gels will remain on the slides. Using a sterile spatula, carefully place the gels in a 50 ml tube containing sterile PBS or culture medium for washing.

10. Wash the polymerized gels in PBS at 1,000:1 volumetric ratio, exchanging buffer at least twice per day to remove the density modifier, photoinitiator, and unreacted polymer. Alternatively, PBS may be exchanged with cell growth medium. Store the DGMP gels in PBS or growth medium for the cell culture experiment outlined in Step 3.
11. To visualize alternating layers, arrange DGMP gel (these gels will not be usable for cell culture) along a ruler on the sample tray of a VersaDoc gel documentation unit. Expose the gels in 350 nm; the exposure time will vary depending on the concentration of the fluorophore. Alternating dark and blue bands in the DGMP hydrogel demonstrate formation of discrete layers of distinct chemical composition (Figure 2-11).

B.3.3 2D culture on DGMP Gels

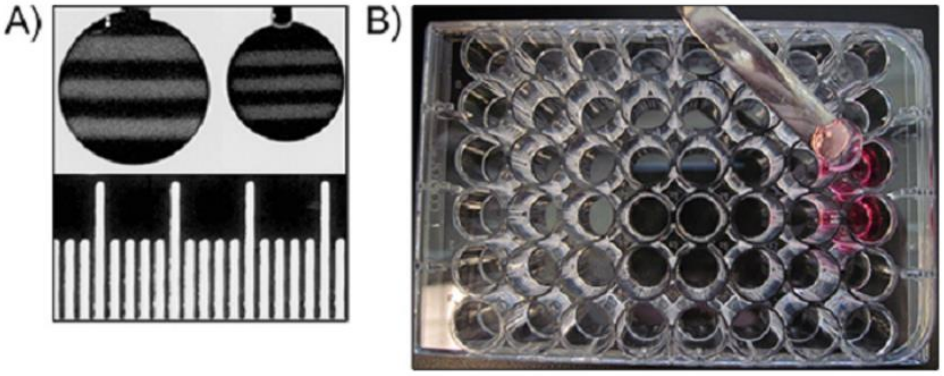
1. For gels incorporating RGDS peptide, use adhesion dependent cells, such as C2C12 myoblasts.
2. Gently insert DGMP gels (stored in PBS) into the wells of 48-well cell culture plates using a sterile cell scraper in a biosafety cabinet.
3. Pre-warm growth medium (Dulbecco's modified Eagle's medium or DMEM supplemented with 10% v/v fetal bovine serum and 1% v/v 100x penicillin-streptomycin solution) and PBS in a water bath set at 37 °C.
4. Wash a 60% confluent plate (10 mm) of C2C1 2 cells three times with PBS. Aspirate off PBS and harvest cells by adding 1 ml of 0.25% Trypsin-EDTA and incubating at 37 °C for 2 min. Re-suspend the cells in growth medium and count cells. Seed the DGMP gel-containing cell culture well with C2C12 myoblasts (20,000 cells/ cm^2).

Incubate the cells at 37 °C in 5%CO2/95% relative humidity. Gently exchange medium after 4 hr, careful not to remove lightly adhered cells.

5. After 24 hr, the attachment of C2C12 myoblasts on the RGDS-containing layers of DGMP gels may be confirmed by epifluorescence and phase contrast microscopy (Zeiss Axiovert 200).

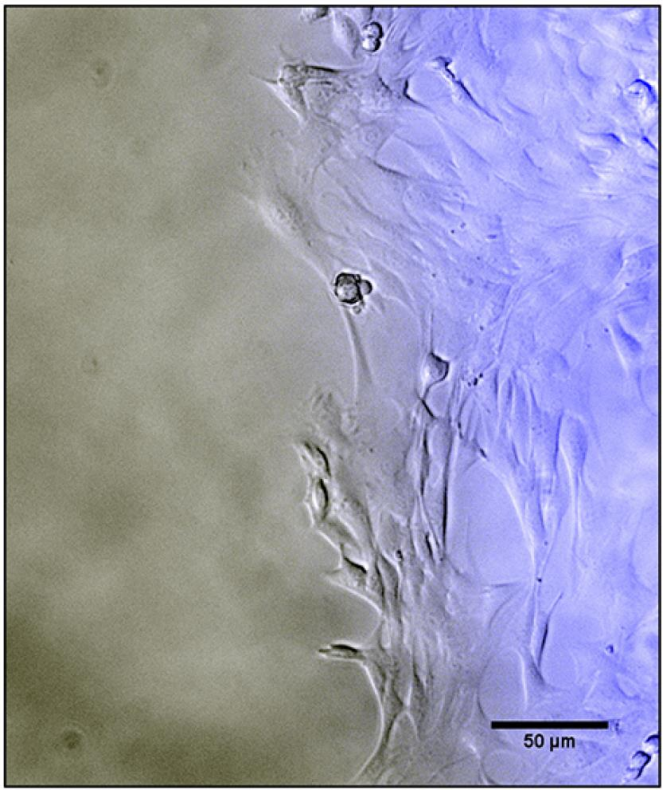
B.4 Representative results

MALDI-TOF analysis confirms the conjugation of RGDS peptide to acryloyl-PEG (Figure 2-2). Gel imaging reveals alternating RGDS- 350 (blue) layers after photopolymerization (JoVE Figure 3A). As shown in JoVE Figure 3A, 2D DGMP gel size can be varied based on the diameter of the silicone molds (10 mm, left ; 8 mm, right), and therefore are easily customizable for use in multiple assays - in this case to fit a 48 well cell culture plate (JoVE Figure 3B).



JoVE Figure 3 A) 2D multilayered gels obtained after photopolymerization imaged using 350 nm and white light channels of VersaDoc gel documentation unit. The grayscale image reveals alternating layers containing RGDS in white. B) Insertion of DGMP gel into 48-well cell culture dishes.

Epifluorescence and phase contrast microscopy of C2C12 myoblasts cultured on a DGMP gel shows selective attachment on RGDS-350-containing PEG layers (JoVE Figure 4), demonstrating compartmentalization of the cell adhesion peptide (RGDS).



JoVE Figure 4 Merged phase contrast and epifluorescence image of C2C12 myoblasts patterned on DGMP gels. Scale bar: 50 µm.

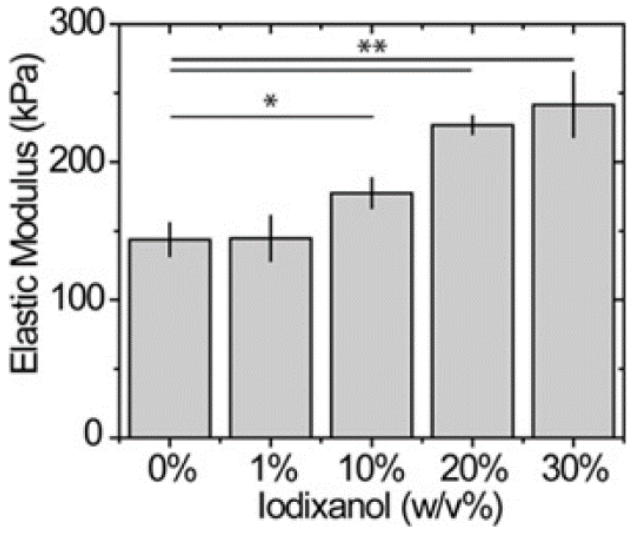
B.5 Summary

DGMP is a simple strategy for preparing multilayered gels that does not rely on expensive instrumentation. This protocol can be adapted for creating scaffolds using other biocompatible materials, such as collagen and hyaluronic acid. Bioactive small molecules, for example cell adhesion-promoting RGDS peptide, can be tethered to the

polymer matrix to prevent mixing of cues between layers. Proteins can be encapsulated in distinct layers without the need for chemical conjugation as they, depending on the matrix mesh size, are less prone to diffuse through hydrogels (Karpiak et al., 2012). Here we used iodixanol (Nycoprep), an inert density modifier, which has previously been used for viable cell applications.

Other density modifiers such as sucrose and dextrose can also be used. By varying the settling time (t_S), one can fine-tune the interfaces between two layers to produce smooth or sharp transitions as needed (longer settling time gives smoother transitions, (Karpiak et al., 2012)). For example, smoother transitions between DGMP gel layers could be used to generate a continuous gradient of a biological cue to study cell processes such as chemotaxis.

The effect of density modifier on gel stiffness is shown in JoVE Figure 5 for a 15% aPEGda gel; a more complete characterization of stiffness and porosity as a function of PEGda and iodixanol concentrations is currently being evaluated. While the PEGda concentration in this example is relatively high, we observed a 60% greater elastic modulus in gels with 30% iodixanol compared to gels without. The change in gel stiffness can be adjusted for by modulating the macromer concentration or crosslinking density.



JoVE Figure 5 Effect of iodixanol on gel surface elasticity. Atomic force microscopy measurements of static samples of crosslinked PEG substrates using previously established methods with a 2 nN force trigger (Kaushik et al., 2011). *p< 0.05 and **p<0.01.

We have also applied the DGMP technique to create 3D multilayered gels using polyacrylamide and PEG precursors (Karpiak et al., 2012). Varying the concentration or the degree of crosslinking of the prepolymer allows structural variation in the scaffolds, which can be used to explore cell behavior such as polarized growth and migration in 3D.

B.6 Conclusions

In conclusion, DGMP is an adaptable technique that can be applied to fabricate 2D and 3D scaffolds from a variety of biocompatible materials for a broad range of biomedical and basic research applications.

B.7 Recognitions

The authors are grateful for support from NIH Director's New Innovator Awards (1 DP2 OD006499-01 to A.A. and 1 DP2 OD006460-01 to A.J.E.), and King Abdulaziz City for Science and Technology (UC San Diego Center of Excellence in

Nanomedicine). We would like to thank Ms. Jessica Moore for her critical comments on the manuscript.

B.8 Acknowledgements

The contents of Appendix B were adapted for the Journal of Visualized Experiments and published as “DGMP: A novel technique for creating multi-compartment, customizable scaffolds for tissue engineering.” Joshi-Barr S, Karpiak JV, Ner Y, Wen JH, Engler AJ, Almutairi A. Journal of Vis Exp, 2013, (72). The dissertation author was the primary investigator and author of this work.

Appendix C

A pilot MEA study: Monolayer iPSC-derived neural cultures reveal electrophysiological phenotypes in *CDKL5*

C.1 Brief introduction and rationale

The human X-linked cyclin-dependent kinase-like 5 gene (*CDKL5*) encodes for a protein with a highly conserved serine-threonine kinase domain in its N-terminal, sharing homology to both members of the mitogen-activated protein (MAP) kinase and cyclin-dependent kinase (CDK) families (Montini et al., 1998). Mutations in *CDKL5* give rise to phenotypes ranging from X-linked infantile spasms to infantile epileptic encephalopathy and often lead to atypical RTT diagnoses (Elia et al., 2008; Evans et al., 2005; Kalscheuer et al., 2003). Sufferers usually show a consistent phenotype of early-onset seizures in the first few weeks to months of life (Bahi-Buisson et al., 2008). While the genetic mutation causing this early onset seizure variant of RTT has been pinpointed, little is known regarding the functional changes in the brain that lead to neurodevelopmental deficiencies. Mouse models of *CDKL5* disorder have not mirrored human symptoms, especially frequent seizures during early stages of development (Amendola et al., 2014; I.-T. J. Wang et al., 2012).

Therefore, using techniques first described by our lab, we have established a human model of neural development using *CDKL5* donor iPSCs. The overarching goal of this study is to bridge the gap of understanding between the genetic origins and resulting symptoms by characterizing dysfunction in diseased neural populations. Thus far, at the time of writing, I have investigated the electrophysiology of *CDKL5* neuronal networks derived from one donor, specifically their firing behavior, network coherence, as a measure of communication proficiency between neurons. Later, this study will include probing response to local-field oscillations in these networks. We expect parallel changes in the macroscopic oscillatory activity of the CDKL5 donors measured with electroencephalogram, previously demonstrated in children with autism (Orekhova

et al., 2007). Consequently, we hope to depict a coherent process across scales - from genetics, to cellular, to behavioral - through which neural communication in *CDKL5* donors, a subset of Rett Syndrome, is disrupted. At the time of writing this dissertation, I had acquired one EEG dataset and measured one passage of donor-derived neural cultures, without an appropriate control EEG dataset.

C.2 Materials and methods

Fibroblasts were obtained via skin biopsy punches from a three year old female *CDKL5* (R59X) donor with the early seizure onset variant of RTT, and her 41 year old maternal parent. Except where stated below, cell culture was carried out as described in section 3.2.2.1; cell reprogramming was carried out as described in 3.2.2.2; neuronal differentiation was carried out as described in 3.2.2.3; and MEA acquisition was carried out similarly as described in 3.2.2.6 except with different plates and custom analyses. EEG data was later recorded from the R59X donor at age 10 and analyzed in MATLAB with custom scripts. A pilot drug screen was then performed with human ES cell-derived neural model (Appendix D).

C.2.1 Electrophysiological analyses

Neuronal activity was recorded using a multi-well MEA system (Maestro, Axion BioSystems, Atlanta, GA, USA). Briefly, 10 x 10^4 NPCs (re-suspended in a 5 µl droplet of NPC medium) were plated on top of 64-electrode arrays inside wells of a 12-well pOrn/Ln pre-coated plate. The day after, neuronal differentiation was initiated. After the third week of differentiation, neuronal medium was switched to Neurobasal medium supplemented with 1 X B-27 and 2 mM Glutamax (Life Technologies) and 0.5% horse

serum. Neuronal activity was continuously recorded for three minutes, 24 hours after media exchange when noted and action potentials were recorded as full waveforms, analyzed using custom MATLAB scripts and visualized sing Axis 2.0 software (Axion Biosystems). A custom script was added to Axion's acquisition line through the software debugger to allow a wider acquisition range 0.1 Hz-5000Hz with no referencing. Median referencing was performed in MATLAB. Binary "spikes" were defined by adaptive threshold crossing at 5.5 x Std Dev, and an inter-spike interval algorithm (interval < 10 ms) was used to identify bursts (3 minimum). Temporal raster plots were generated in the MATLAB-based Neural Metric Tool software (Axion BioSystems). Autocorrelation was compared using custom MATLAB scripts. Power spectra were constructed using custom MATLAB scripts.

C.3 Results

C.3.1 Generation of CDKL5 iPSCs and neural induction for MEA study

Informed consent was obtained, reviewed and approved by the Institutional Review Board at UCSD. Skin biopsies were obtained from one clinically affected three year old with the R59X mutation in the catalytic domain of the CDKL5 protein and her unaffected maternal parent. Fibroblasts were successfully reprogrammed into a pluripotent state (Figure C-1A & B) using a non-integrative method (Okita et al., 2011). The ability of the clones to differentiate into three germ layers *in vitro* was tested by generating embryoid bodies (EBs) in suspension in the absence of growth factors. After 14 days, mature EBs were tested by RT-PCR for markers of the three primary germ layers (Figure C-1C). No karyotypic abnormalities were observed at the iPSC stage in clones used in this pilot study (Figure C1-D & E). Figure C-1F shows immunostaining

for pluripotency markers (Nanog and Lin28) of the CDKL5-mutant-derived iPSC colonies, further indicating successful reprogramming. iPSCs were then induced to differentiate using our in-house protocol, as noted in the methods section, generating neural precursor cells (NPCs) and neurons (Figure C-1G - I). These cells were generated to evaluate the baseline electrophysiology of our CDKL5 neural development model with the intention to later test the therapeutic effect of selected drugs on abnormal neurological activity *in vitro* (Figure C-1J).

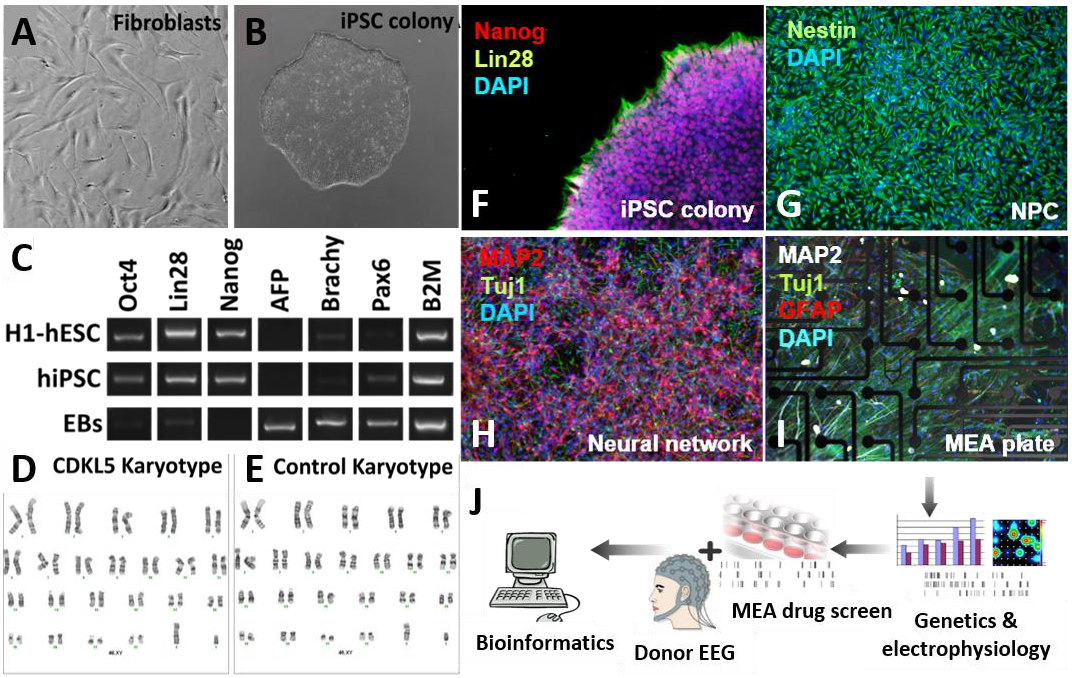


Figure C-1 Human iPSCs, NPCs and neurons derived from CDLK5 patients. A) Human fibroblasts before reprogramming. B) iPSC colonies. (C) RT-PCR for pluripotency markers and three germ cell layers. D) & E) No karyotypic abnormalities were observed in iPSC clones. F) Expression of pluripotency markers in iPSCs. G) Expression of neural precursor maker in NPCs. (H) and I) Expression of neural markers in a 4 weeks-old CDKL5 iPSC-derived differentiation. J) Schematic of the work in progress and future directions.

C.3.2 Basal electrophysiology of CDKL5 model

CDKL5 and control NPCs were differentiated *in situ* on MEA substrates and recorded activity five weeks after bFGF2 removal. Bright field images show mature neural morphology at five weeks (Figure C-2A). Initially six wells were prepared for each condition, however two CDKL5 cultures lifted during differentiation (Figure C-2A, wells “6” and “8”). Cumulative electrode spiking over three minutes of recording, defined with as binary 5.5 standard deviations above or below noise cutoff, reveals localized centers of activity (Figure C-2B). Temporal raster plots for select wells (Figure C-2C & D, see differentially dashed outlines throughout in Figure C-2 for consistency across analyses) represent gross differences in network wide behavior between CDKL5 and control wells. Cumulative well wide spiking emphasizes secondary patterns (Figure C-2E & F) that give rise to autocorrelative periodicity (Figure C-2G & H). The network autocorrelation shows the correlation of summed network spiking activity with itself, at different lag times. For a signal with no periodicity, the correlation would be 1 at lag zero, and decrease monotonically as lag time increases. In contrast, when a peak occurs at a subsequent lag time, it suggests that there exists periodic behavior in the signal. The height of this secondary peak represents the regularity of the periodicity, or, in the context of network spiking, the strength and consistency of network-wide synchrony.

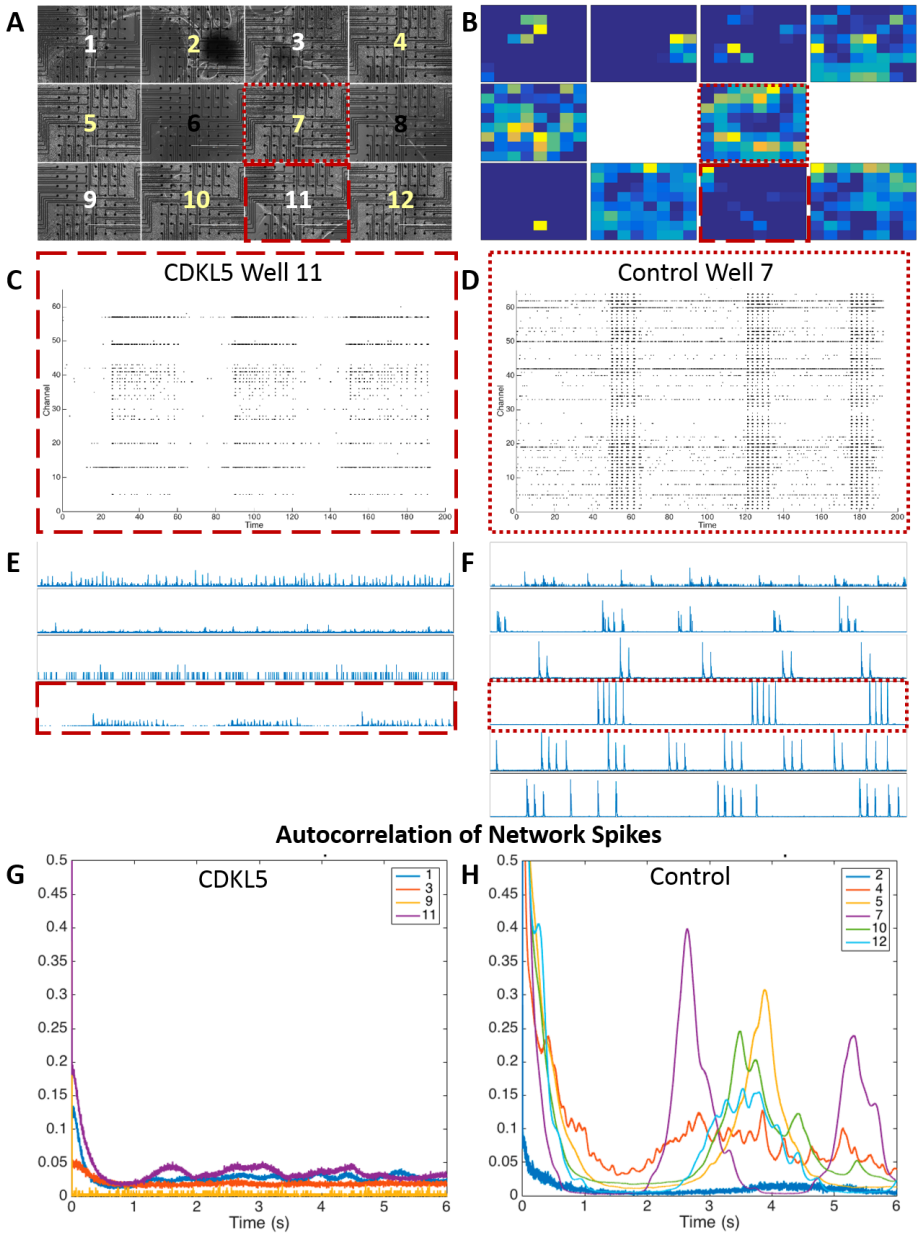


Figure C-2 Baseline CDKL5 neural MEA activity compared to unaffected maternal control. A) Bright field image of CDKL5 (wells 1, 3, 9, 11) and maternal control (wells 2, 4, 5, 7, 10, 12) iPSC-derived neural cultures in a "checker-board" arrangement (wells 6 & 8 detached). B) Heat map depicting number of spikes per electrode relative for each well. C) & D) Representative temporal raster plot for all electrodes in CDKL5-well 11 & Control-well 7, respectively. E) & F) Cumulative plots of well-wide spikes for each of four CDKL5-wells & six Control-wells. Wells depicted in (C) & (D) are outlined in corresponding different dashed red lines in (A), (B), (E) & (F) for clarity. G) & H) Autocorrelation histograms of network spiking for each well plotted over 6 seconds for CDKL5 & Control, respectively.

These results show iPSC-derived neurons spontaneously generated action potentials verifying our neural development model as a robust platform to generate functional CDKL5 neurons. However, comparing the CDKL5 neural networks maternal control networks revealed several differences. The number of spiking channels per well normalized by individual well cell coverage and ratio of bursting channels to spiking channels was substantially lower for CDKL5 networks (Figure C-3D & E). The mean spike rate for active channels followed this trend, although the experiment was not powered well enough to demonstrate significance (Figure C-3A). Interestingly, despite having a similar burst rate for “bursty” channels (Figure C-3B), the mean number of spikes per burst was significantly lower for CDKL5 (Figure C-3C).

And, although the autocorrelative magnitudes were far lower in CDKL5 networks, there was no difference in short term periodicity (Figure C-3F) nor in long-term periodicity (not shown). In the control wells, the network spiking function shows strong self-similarity at a lag time of 2-4 s, which can also be seen in the raster plots. In comparison, the CDKL wells also show periodicity, but at a much lower amplitude, even after adjusting for total spike rate (normalized to 1 at lag zero). This decreased synchronization suggests poorer network connectivity, as activity propagates through the network more slowly and inconsistently. Overall, the consistent appearance of periodicity in global network spiking is an interesting result, which may relate to neural oscillations at much larger spatial scales in the developed brain, such as the alpha oscillation (8-12 Hz). We can conjecture that the absence of a prominent alpha peak in patient EEG is possibly related to the weak network synchronization in the MEA. These results suggest that although CDKL5 iPSCs generate functional neurons, their coordinated activity at the network level is altered and in some aspects reduced

compared to control cells at the five-week stage of *in vitro* development. These findings are significant and very interesting, however, further higher powered studies with more individual donors or controls is necessary to support further conclusions.

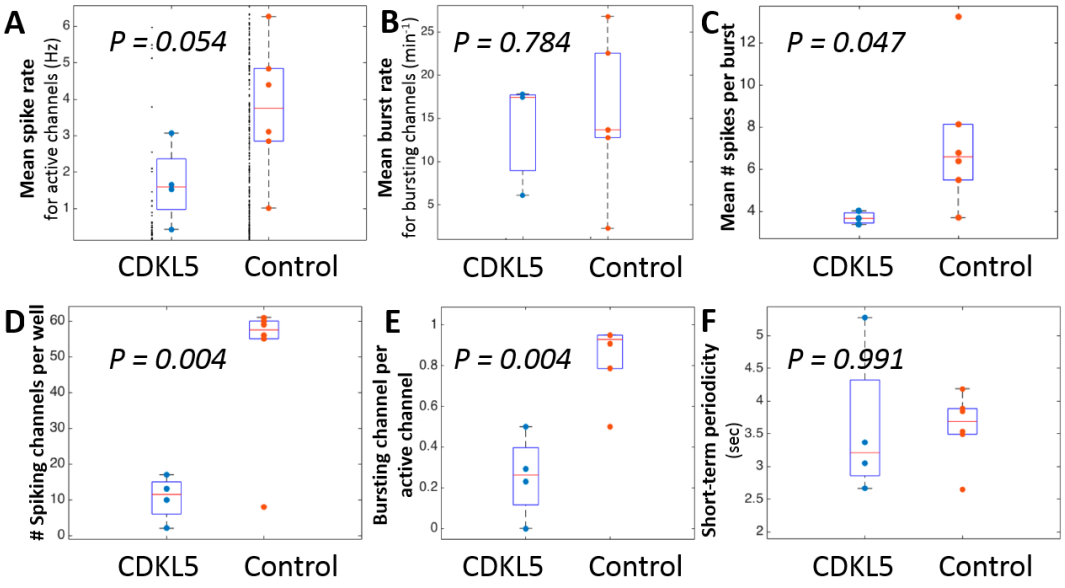


Figure C-3 CDKL5 neural cultures exhibit reduced spiking, altered bursting dynamics, and muted activity autocorrelation. A) Mean spike rate for active (>0.1 Hz) electrodes. B) Mean burst rate for "bursty" electrodes (>0.1 Hz). C) Mean spikes in each burst (ISI <10 mS). D) Number of active channels per well (>0.1 Hz). E) Ratio of bursty channels to active channels. F) Short-term (6 s) periodicity. Means are denoted, box plots represent interquartile, caps are range excluding 3Xσ outliers; p-values are displayed for two-tailed student t-test assuming unequal variance.

C.3.3 CDKL5 (R59X): Donor EEG *vs.* iPSC MEA

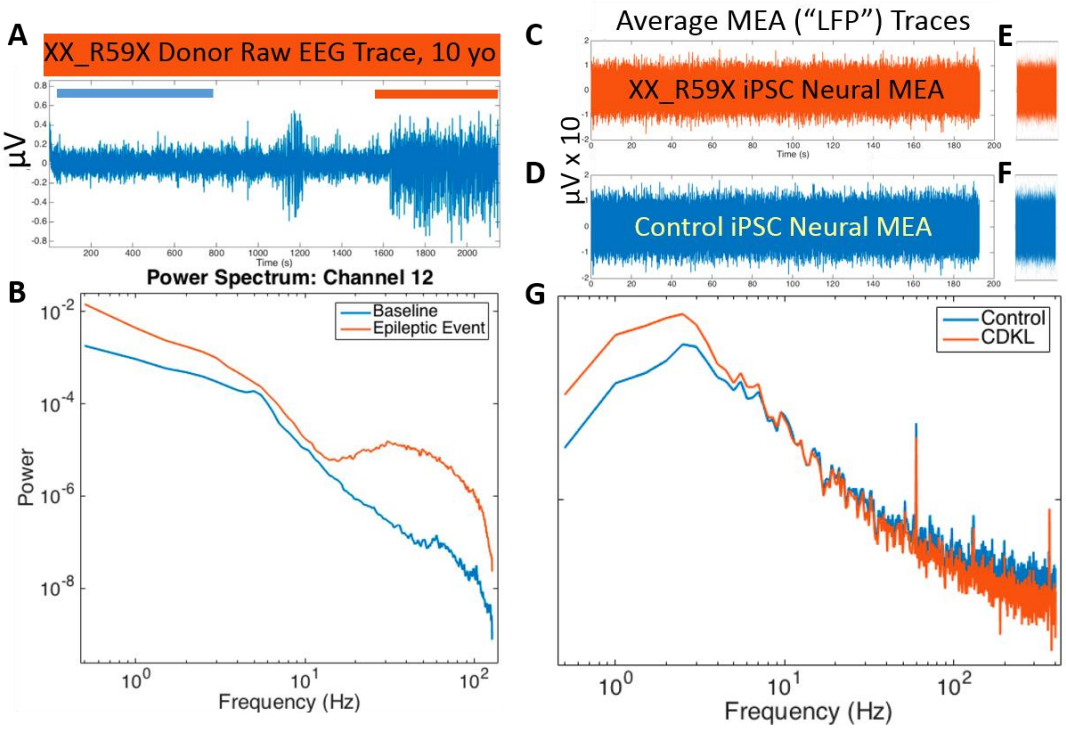


Figure C-4 CDKL5 donor EEG compared to averaged iPSC-derived neural MEA "LFP." A) 35 minute raw EEG trace from 10 year-old female (46XX) donor with R59X nonsense mutation in *CDKL5*. B) Frequency power spectrum demonstrating baseline and an epileptic event. C) 3 minute MEA "LFP" trace (300 Hz low end cut-off) averaged from four wells of same female R59X donor's iPSC-derived neural cultures. D) 3 min MEA LFP trace averaged from six wells of unaffected maternal iPSC-derived neural cultures. E) & F) Duplicate traces time-scaled to match the EEG in (A). G) Frequency power spectrum averaged for CDKL5 and paternal Control, respectively.

C.4 Summary

Baseline electrophysiology of CDKL5-derived neurons was determined by MEA. I established new methods for the Muotri Lab to potentially identify electrophysiological profiles for comparison to donor EEG data. This study is ongoing in collaboration with the Voytek Lab for cognitive and computational neuroscience.

C.5 Recognitions

We are grateful for support from the International Foundation for CDKL5 research (IFCR).

C.6 Acknowledgements

The contents of Appendix C highlights my contributions to an evolving project currently in development through collaboration between the laboratories of Alysson Muotri and Bradley Voytek. Key investigators Priscilla Negraes, PhD and Richard Gao will continue this work towards a peer-reviewed publication as a continuation of our IFCR funded project entitled: “Modeling CDKL5 Syndrome using human Neurons.“ The dissertation author was the primary investigator and author of this work.

Appendix D

A pilot API study: MEA platform to screen epilepsy drugs

D.1 Brief introduction and rationale

Epilepsy is one of the most common neurological disorders, characterized mainly by atypical neural network electrophysiology, leading to a series of recurrent seizures (Fisher et al., 2005). Over 30% of people who suffer seizures present drug-resistance to antiepileptic drugs. These individuals frequently experience psychological dysfunction and increased risk of mortality (Laxer et al., 2014). Current treatments, including medications and surgery, may eliminate or reduce the frequency and intensity of seizures, however, the cause(s) of this condition remains unclear. Therefore, there is an unmet need for better treatments and causal understanding of seizures in order to prevent the disabling physical, cognitive and behavioral consequences of epilepsy. Human-derived stem cell models offer a strategy to link genetic alterations to molecular mechanisms and complex behavioral and cognitive phenotypes (Chailangkarn, Acab, & Muotri, 2012). Additionally, *in vitro* human neural disease models offer a safe platform in which to investigate potential therapeutics such as direct screening of active pharmaceutical ingredients (APIs).

To prepare for our novel *CDKL5* drug screen, I performed a pilot feasibility study for an archetypal chronic drug-response and recovery in a H9 (human ESC)-derived neural model. This study is ongoing based on the preliminary observations described in this section and will encompass different *CDKL5* mutations, gender, familial and X-inactivation derived isogenic controls. Once baseline profiles are established for all experimental groups, the Muotri Lab will continue to screen an in-house library of over fifteen neurotransmitter modulator compounds to test potential therapeutic candidates. In this section I describe *in vitro* neural network response to one model active

pharmaceutical ingredient tetrahydrocannabinol (THC); however, a comprehensive description of this emergent study is beyond the scope of my dissertation.

D.2 Materials and methods

D.2.1 Active pharmaceutical ingredient (API) response study

Small molecule active pharmaceutical ingredients (APIs) are often dissolved in organic solvents such as dimethyl sulfoxide, which can affect assay performance. Therefore, assay sensitivity to these solvents must be examined. The two APIs interrogated in this pilot feasibility study are dissolved in ethanol or methanol. For the purpose of this pilot study, I administered matching doses of corresponding solvent in control wells for each group. Prior to future studies, the assay's sensitivity to additional solvents will be performed. H9-derived NPCs were plated and differentiated on MEA substrates as previously described. Note, it is important to randomize sample placement in the multiwall plates used in this study to rule out occasionally observed signal bleed across rows or columns. After five weeks, baseline activity was recorded. Then THC or CBD were administered at 10 µM twice per week, or corresponding volumes of methanol or ethanol, respectively. In parallel cells were plated on pOrn/Ln-coated coverslips and treated for immunocytochemistry one week after initiation of treatment. All CBD-treated neural cultures lifted within 48 hrs of initial treatment and are not included in the analyses. All treated immunocytochemistry cultures failed within one week. MEA measurements were recorded four days prior to initial drug loading, the day after and once a week for an additional three weeks. API dosing was stopped and replaced with methanol after four weeks of recording. Two post-treatment recordings were performed one day and four days after API was removed to assess

recovery potential. Ten days later THC was re-administered at 0.1 to previously treated wells and CBD was loaded into ethanol treated previous control wells to assess another dosing concentration.

D.3 Results

D.3.1 Cannabinoid API reduces network synchrony and overall neuronal activity in a recoverable manner.

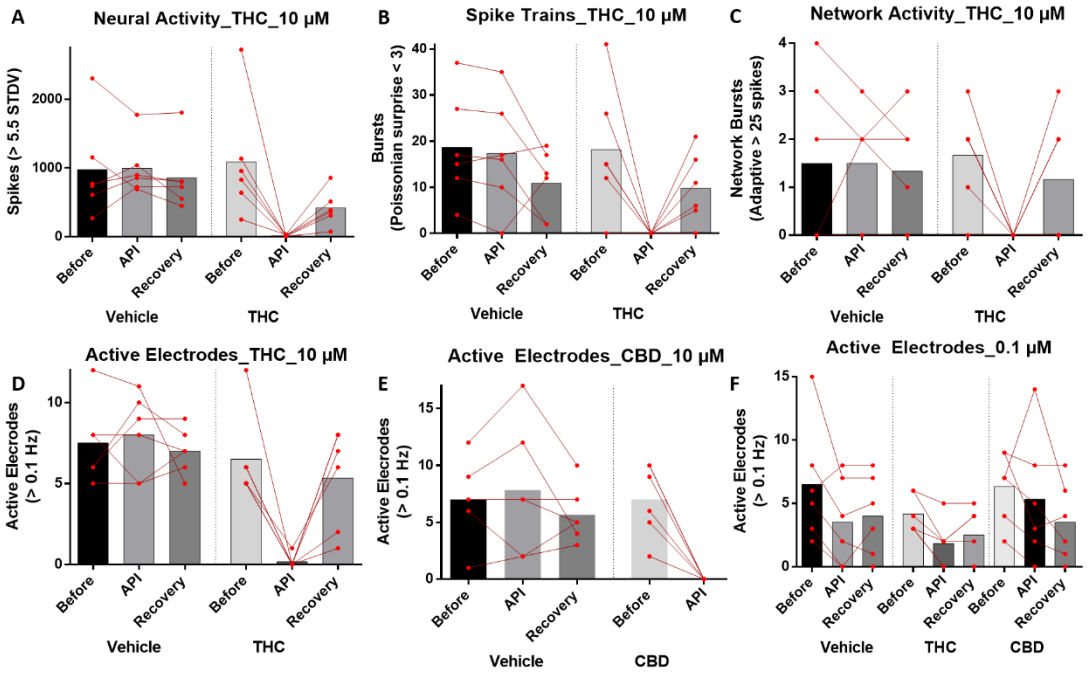


Figure D-1 Cannabinoids alter neural network activity.

D.4 Summary

We successfully performed a pilot study using ESC-derived monolayer neural cultures to screen baseline cannabinoid active pharmaceutical ingredient (API) effects on neuronal network function. My findings that cannabinoid API reduced neural activity

in a recoverable manner in H9-derived monolayer neural cultures provides strong rationale to continue using the MEA screening platform I established to additional screen epilepsy APIs. These results, together with results outlined in Appendix C will drive further development of our MEA platform for functional epilepsy drug screening using *CDKL5* iPSCs.

D.5 Acknowledgements

The contents of Appendix D highlights my contributions to an evolving project currently in development through collaboration between the laboratories of Alysson Muotri and Bradley Voytek. Key investigators Priscilla Negraes, PhD and Richard Gao will continue this work towards a peer-reviewed publication as a continuation of our IFCR funded project entitled: “Modeling CDKL5 Syndrome using human Neurons.“ The dissertation author was the primary investigator and author of this work.

REFERENCES

Affolter, M., & Weijer, C. J. (2005). Signaling to cytoskeletal dynamics during chemotaxis. *Developmental Cell*, *9*, 19–34. http://doi.org/10.1016/j.devcel.2005.06.003

Allen, N. J. (2014). Astrocyte regulation of synaptic behavior. *Annual Review of Cell and Developmental Biology*, *30*, 439–63. http://doi.org/10.1146/annurev-cellbio-100913-013053

Allen, N. J., Bennett, M. L., Foo, L. C., Wang, G. X., Chakraborty, C., Smith, S. J., & Barres, B. A. (2012). Astrocyte glypicans 4 and 6 promote formation of excitatory synapses via GluA1 AMPA receptors. *Nature*, *486*(7403), 410–4. http://doi.org/10.1038/nature11059

Amendola, E., Zhan, Y., Mattucci, C., Castroflorio, E., Calcagno, E., Fuchs, C., Lonetti, G., Silingardi, D., Vyssotski, A. L., Farley, D., Ciani, E., Pizzorusso, T., Giustetto, M., & Gross, C. T. (2014). Mapping pathological phenotypes in a mouse model of CDKL5 disorder. *PLoS ONE*, *9*(5), 5–16. http://doi.org/10.1371/journal.pone.0091613

Amir, R. E., Van den Veyver, I. B., Wan, M., Tran, C. Q., Francke, U., & Zoghbi, H. Y. (1999). Rett syndrome is caused by mutations in X-linked MECP2, encoding methyl-CpG-binding protein 2. *Nat Genet*, *23*(2), 185–188. http://doi.org/10.1038/13810

Ananiev, G., Williams, E. C., Li, H., & Chang, Q. (2011). Isogenic pairs of wild type and mutant induced pluripotent stem cell (iPSC) lines from Rett syndrome patients as in vitro disease model. *PloS One*, *6*(9), e25255. http://doi.org/10.1371/journal.pone.0025255

Anderson, C. M., & Nedergaard, M. (2003). Astrocyte-mediated control of cerebral microcirculation. *Trends in Neurosciences*, *26*(7), 340–344. http://doi.org/10.1016/S0166-2236(03)00141-3

Andrade, L., Nathanson, J., Yeo, G., Menck, C., & Muotri, A. (2012). Evidence for premature aging due to oxidative stress in iPSCs from Cockayne syndrome. *Human Molecular Genetics*, *21*(17), 3825–3834. http://doi.org/10.1093/hmg/dds211

Anlar, B., & Gunel-Ozcan, A. (2012). Tenascin-R: role in the central nervous system. *The International Journal of Biochemistry & Cell Biology*, *44*(9), 1385–9. http://doi.org/10.1016/j.biocel.2012.05.009

Armstrong, D., Dunn, J. K., Antalffy, B., & Trivedi, R. (1995). Selective dendritic alterations in the cortex of Rett syndrome. *J Neuropathol Exp Neurol*, *54*(2), 195–201.

Aznavoorian, S., Stracke, M. L., Krutzsch, H., Schiffmann, E., & Liotta, L. a. (1990). Signal transduction for chemotaxis and haptotaxis by matrix molecules in tumor cells. *Journal of Cell Biology*, *110*(4), 1427–1438. http://doi.org/10.1083/jcb.110.4.1427

Bacci, A., Verderio, C., Pravettoni, E., & Matteoli, M. (1999). The role of glial cells in synaptic function. *Philos Trans R Soc Lond, B, Biol Sci*, *354*, 403–409.

http://doi.org/10.1098/rstb.1999.0393

Bahi-Buisson, N., Nectoux, J., Rosas-Vargas, H., Milh, M., Boddaert, N., Girard, B., Cances, C., Ville, D., Afenjar, A., Rio, M., Héron, D., N'Guyen Morel, M. A., Arzimanoglou, A., Philippe, C., Jonveaux, P., Chelly, J., & Bienvenu, T. (2008). Key clinical features to identify girls with CDKL5 mutations. *Brain*, *131*(10), 2647–2661. http://doi.org/10.1093/brain/awn197

Baik, M., Yu, J., & Hennighausen, L. (2011). Growth hormone-STAT5 regulation of growth, hepatocellular carcinoma, and liver metabolism. *Ann N Y Acad Sci*, *1229*, 29–37. http://doi.org/10.1016/j.biotechadv.2011.08.021.Secreted

Bamji, S. X., Shimazu, K., Kimes, N., Huelsken, J., Birchmeier, W., Lu, B., & Reichardt, L. F. (2003). Role of beta-catenin in synaptic vesicle localization and presynaptic assembly. *Neuron*, *40*(4), 719–731. Retrieved from http://www.ncbi.nlm.nih.gov/pubmed/14622577

Baneyx, G., Baugh, L., & Vogel, V. (2002). Fibronectin extension and unfolding within cell matrix fibrils controlled by cytoskeletal tension. *Proceedings of the National Academy of Sciences of the United States of America*, *99*, 5139–5143. http://doi.org/10.1073/pnas.072650799

Beck, K. D., Powell-Braxton, L., Widmer, H. R., Valverde, J., & Hefti, F. (1995). Igf1 gene disruption results in reduced brain size, CNS hypomyelination, and loss of hippocampal granule and striatal parvalbumin-containing neurons. *Neuron*, *14*(4), 717–730. http://doi.org/10.1016/0896-6273(95)90216-3

Belichenko, P. V, Wright, E. E., Belichenko, N. P., Masliah, E., Li, H. H., Mobley, W. C., & Francke, U. (2009). Widespread changes in dendritic and axonal morphology in Mecp2-mutant mouse models of rett syndrome: Evidence for disruption of neuronal networks. *The Journal of Comparative Neurology*, *514*(3), 240–258. http://doi.org/10.1002/cne.22009

Bellail, A. C., Hunter, S. B., Brat, D. J., Tan, C., & Van Meir, E. G. (2004). Microregional extracellular matrix heterogeneity in brain modulates glioma cell invasion. *The International Journal of Biochemistry & Cell Biology*, *36*(6), 1046–69. http://doi.org/10.1016/j.biocel.2004.01.013

Bellamkonda, R., Ranieri, J. P., Bouche, N., & Aebischer, P. (1995). Hydrogel-based three-dimensional matrix for neural cells. *J Biomed Mater Res*, *29*(5), 663–671.

Benavides-Piccione, R., Ballesteros-Yáñez, I., DeFelipe, J., & Yuste, R. (2002). Cortical area and species differences in dendritic spine morphology. *J. Neurocytol.*, *31*, 337–346.

Benjamini, Y., & Hochberg, Y. (1995). Controlling the False Discovery Rate: A Practical and Powerful Approach to Multiple Testing. *Journal of the Royal Statistical Society. Series B (Methodological)*, *57*(1), 289 – 300. http://doi.org/10.2307/2346101

Berry, M. F., Engler, A. J., Woo, Y. J., Pirolli, T. J., Bish, L. T., Jayasankar, V., Morine, K. J., Gardner, T. J., Discher, D. E., & Sweeney, H. L. (2006). Mesenchymal stem cell injection after myocardial infarction improves myocardial compliance. *American Journal of Physiology. Heart and Circulatory Physiology*, *290*(6), H2196–H2203. http://doi.org/10.1152/ajpheart.01017.2005

Bezakova, G., & Ruegg, M. a. (2003). New insights into the roles of agrin. *Nature Reviews. Molecular Cell Biology*, *4*(4), 295–308. http://doi.org/10.1038/nrm1074

Bignami, A., Hosley, M., & Dahl, D. (1993). Hyaluronic acid and hyaluronic acid-binding proteins in brain extracellular matrix. *Anat Embryol (Berl)*, *188*(5), 419–433. Retrieved from http://www.ncbi.nlm.nih.gov/pubmed/7508695

Blankenship, A. G., & Feller, M. B. (2010). Mechanisms underlying spontaneous patterned activity in developing neural circuits. *Nature Reviews. Neuroscience*, *11*(1), 18–29. http://doi.org/10.1038/nrn2759

Blewitt, M. J., & Willits, R. K. (2007). The effect of soluble peptide sequences on neurite extension on 2D collagen substrates and within 3D collagen gels. *Ann Biomed Eng*, *35*(12), 2159–2167. http://doi.org/10.1007/s10439-007-9389-4

Boland, T., Xu, T., Damon, B., & Cui, X. (2006). Application of inkjet printing to tissue engineering. *Biotechnology Journal*, *1*(9), 910–7. http://doi.org/10.1002/biot.200600081

Bonanni, B., Kamruzzahan, A. S. M., Bizzarri, A. R., Rankl, C., Gruber, H. J., Hinterdorfer, P., & Cannistraro, S. (2005). Single Molecule Recognition between Cytochrome C 551 and Gold-Immobilized Azurin by Force Spectroscopy. *Biophys J*, *89*(4), 2783–2791. http://doi.org/10.1529/biophysj.105.064097

Bourdon, M. A., & Ruoslahti, E. (1989). Tenascin mediates cell attachment through an RGD-dependent receptor. *Journal of Cell Biology*, *108*(3), 1149–1155. http://doi.org/10.1083/jcb.108.3.1149

Brace, L. E., Vose, S. C., Vargas, D. F., Zhao, S., Wang, X. P., & Mitchell, J. R. (2013). Lifespan extension by dietary intervention in a mouse model of Cockayne Syndrome uncouples early postnatal development from segmental progeria. *Aging Cell*, *12*(6), 1144–1147. http://doi.org/10.1111/acel.12142

Bradsher, J., Auriol, J., De Santis, L., Iben, S., Vonesch, J., Grummt, I., & Egly, J. (2002). CSB is a component of RNA pol I transcription. *Molecular Cell*, *10*(4), 819–829. http://doi.org/10.1016/S1097-2765(02)00678-0

Brennand, K. J., Marchetto, M. C., Benvenisty, N., Brustle, O., Ebert, A., Izpisua Belmonte, J. C., Kaykas, A., Lancaster, M. A., Livesey, F. J., McConnell, M. J., McKay, R. D., Morrow, E. M., Muotri, A. R., Panchision, D. M., Rubin, L. L., Sawa, A., Soldner, F., Song, H., Studer, L., Temple, S., Vaccarino, F. M., Wu, J., Vanderhaeghen, P., Gage, F. H., & Jaenisch, R. (2015). Creating Patient-Specific Neural Cells for the In Vitro Study of Brain Disorders. *Stem Cell Reports*, *5*(6), 933–945.

http://doi.org/10.1016/j.stemcr.2015.10.011

Brewer, G. J., & Torricelli, J. R. (2007). Isolation and culture of adult neurons and neurospheres. *Nature Protocols*, *2*(6), 1490–8. http://doi.org/10.1038/nprot.2007.207

Brodmann, K. (1909). *Localisation in the Cerebral Cortex*. http://doi.org/10.1097/00005053-191012000-00013

Brooks, P. (2013). Blinded by the UV light: How the focus on transcription-coupled NER has distracted from understanding the mechanisms of Cockayne syndrome neurologic disease. *DNA Repair*, *12*, 656–671. http://doi.org/10.1016/j.biotechadv.2011.08.021.Secreted

Buescher, A. V, Cidav, Z., Knapp, M., & Mandell, D. S. (2014). Costs of autism spectrum disorders in the United Kingdom and the United States. *JAMA Pediatr*, *168*(8), 721–728. http://doi.org/10.1001/jamapediatrics.2014.210

Burdick, J. a, Khademhosseini, A., & Langer, R. (2004). Fabrication of gradient hydrogels using a microfluidics/photopolymerization process. *Langmuir : The ACS Journal of Surfaces and Colloids*, *20*(13), 5153–6. http://doi.org/10.1021/la049298n

Buttini, M., Masliah, E., Barbour, R., Grajeda, H., Motter, R., Johnson-Wood, K., Khan, K., Seubert, P., Freedman, S., Schenk, D., & Games, D. (2005). Beta-amyloid immunotherapy prevents synaptic degeneration in a mouse model of Alzheimer's disease. *The Journal of Neuroscience*, *25*(40), 9096–9101. http://doi.org/10.1523/JNEUROSCI.1697-05.2005

Calvert, P., Frechette, J., & Souvignier, C. (1998). Mineralization of multilayer hydrogels as a model for mineralization of bone. *Materials Research Society Symposium - Proceedings*, *489*, 153–159. Retrieved from http://www.scopus.com/inward/record.url?eid=2-s2.0-0032311961&partnerID=40&md5=033d7548ff73734482e72d2f297cfbc0

Carouge, D., Host, L., Aunis, D., Zwiller, J., & Anglard, P. (2010). CDKL5 is a brain MeCP2 target gene regulated by DNA methylation. *Neurobiology of Disease*, *38*(3), 414–424. http://doi.org/http://dx.doi.org/10.1016/j.nbd.2010.02.014

Castro, J., Garcia, R. I., Kwok, S., Banerjee, A., Petravicz, J., Woodson, J., Mellios, N., Tropea, D., & Sur, M. (2014). Functional recovery with recombinant human IGF1 treatment in a mouse model of Rett Syndrome. *Proceedings of the National Academy of Sciences of the United States of America*, *111*(27), 9941–6. http://doi.org/10.1073/pnas.1311685111

Cencetti, F., Bruno, G., Blescia, S., Bernacchioni, C., Bruni, P., & Donati, C. (2014). Lysophosphatidic acid stimulates cell migration of satellite cells: a role for sphingosine kinase/sphingosine 1-phosphate axis. *The FEBS Journal*, *281*, 4467–4478. http://doi.org/10.1111/febs.12955

Chailangkarn, T., Acab, A., & Muotri, A. R. (2012). Modeling neurodevelopmental

disorders using human neurons. *Current Opinion in Neurobiology*, *22*(5), 785–90. http://doi.org/10.1016/j.conb.2012.04.004

Chambers, S. M., Fasano, C. A., Papapetrou, E. P., Tomishima, M., Sadelain, M., & Studer, L. (2009). Highly efficient neural conversion of human ES and iPS cells by dual inhibition of SMAD signaling. *Nat. Biotechnol.*, *27*(3), 275–280. http://doi.org/10.1016/j.devcel.2008.08.012.The

Chatre, L., Biard, D. S. F., Sarasin, A., & Ricchetti, M. (2015). Reversal of mitochondrial defects with CSB-dependent serine protease inhibitors in patient cells of the progeroid Cockayne syndrome. *Proceedings of the National Academy of Sciences*, 201422264. http://doi.org/10.1073/pnas.1422264112

Chatterjee, K., Lin-Gibson, S., Wallace, W. E., Parekh, S. H., Lee, Y. J., Cicerone, M. T., Young, M. F., & Simon, C. G. (2010). The effect of 3D hydrogel scaffold modulus on osteoblast differentiation and mineralization revealed by combinatorial screening. *Biomaterials*, *31*(19), 5051–5062. http://doi.org/10.1016/j.biomaterials.2010.03.024

Chen, C., Jiang, P., Xue, H., Peterson, S. E., Tran, H. T., McCann, A. E., Parast, M. M., Li, S., Pleasure, D. E., Laurent, L. C., Loring, J. F., Liu, Y., & Deng, W. (2014). Role of astroglia in Down's syndrome revealed by patient-derived human-induced pluripotent stem cells. *Nature Communications*, *5*, 4430. http://doi.org/10.1038/ncomms5430

Chen, Q., Zhu, Y. C., Yu, J., Miao, S., Zheng, J., Xu, L., Zhou, Y., Li, D., Zhang, C., Tao, J., & Xiong, Z. Q. (2010). CDKL5, a protein associated with rett syndrome, regulates neuronal morphogenesis via Rac1 signaling. *J Neurosci*, *30*(38), 12777–12786. http://doi.org/10.1523/jneurosci.1102-10.2010

Chen, W. G., Chang, Q., Lin, Y., Meissner, A., West, A. E., Griffith, E. C., Jaenisch, R., & Greenberg, M. E. (2003). Derepression of BDNF Transcription Involves Calcium-Dependent Phosphorylation of MeCP2. *Science*, *302*(5646), 885–889. http://doi.org/10.1126/science.1086446

Cheung, A. Y. L., Horvath, L. M., Grafodatskaya, D., Pasceri, P., Weksberg, R., Hotta, A., Carrel, L., & Ellis, J. (2011). Isolation of MECP2-null Rett Syndrome patient hiPS cells and isogenic controls through X-chromosome inactivation. *Human Molecular Genetics*, *20*(11), 2103–2115. http://doi.org/10.1093/hmg/ddr093

Chirasatitsin, S., & Engler, A. J. (2010). Detecting cell-adhesive sites in extracellular matrix using force spectroscopy mapping. *Journal of Physics. Condensed Matter : An Institute of Physics Journal*, *22*(19), 194102. http://doi.org/10.1088/0953-8984/22/19/194102

Choi, H. K., Won, L., & Heller, A. (1993). Dopaminergic neurons grown in three-dimensional reaggregate culture for periods of up to one year. *Journal of Neuroscience Methods*, *46*(3), 233–244. http://doi.org/http://dx.doi.org/10.1016/0165-0270(93)90072-Y

Choi, S. H., Kim, Y. H., Hebisch, M., Sliwinski, C., Lee, S., D'Avanzo, C., Chen, H., Hooli, B., Asselin, C., Muffat, J., Klee, J. B., Zhang, C., Wainger, B. J., Peitz, M., Kovacs, D. M., Woolf, C. J., Wagner, S. L., Tanzi, R. E., & Kim, D. Y. (2014). A three-dimensional human neural cell culture model of Alzheimer's disease. *Nature*, *515*(7526), 274–278. http://doi.org/10.1038/nature13800

Christopherson, K. S., Ullian, E. M., Stokes, C. C. A., Mullowney, C. E., Hell, J. W., Agah, A., Lawler, J., Mosher, D. F., Bornstein, P., & Barres, B. A. (2005). Thrombospondins are astrocyte-secreted proteins that promote CNS synaptogenesis. *Cell*, *120*(3), 421–33. http://doi.org/10.1016/j.cell.2004.12.020

Chwalek, K., Levental, K. R., Tsurkan, M. V., Zieris, A., Freudenberg, U., & Werner, C. (2011). Two-tier hydrogel degradation to boost endothelial cell morphogenesis. *Biomaterials*, *32*, 9649–9657. http://doi.org/10.1016/j.biomaterials.2011.08.078

Ciaffardini, F., Nicolai, S., Caputo, M., Canu, G., Paccosi, E., Costantino, M., Frontini, M., Balajee, a S., & Proietti-De-Santis, L. (2014). The cockayne syndrome B protein is essential for neuronal differentiation and neuritogenesis. *Cell Death & Disease*, *5*(5), e1268. http://doi.org/10.1038/cddis.2014.228

Cleaver, J. E., Bezrookove, V., Revet, I., & Huang, E. J. (2013). Conceptual developments in the causes of Cockayne syndrome. *Mechanisms of Ageing and Development*, *134*(5-6), 284–290. http://doi.org/10.1016/j.mad.2013.02.005

Cockayne, E. (1936). Dwarfism with retinal atrophy and deafness. *Archives of Disease in Childhood*, *21*(105), 52–54. http://doi.org/10.1136/adc.21.105.52

Colella, S., Nardo, T., Botta, E., Lehmann, a R., & Stefanini, M. (2000). Identical mutations in the CSB gene associated with either Cockayne syndrome or the DeSanctis-cacchione variant of xeroderma pigmentosum. *Human Molecular Genetics*, *9*(8), 1171–1175.

Conforti, L., Adalbert, R., & Coleman, M. (2007). Neuronal death: where does the end begin? *Trends in Neurosciences*, *30*(4), 159–166. http://doi.org/10.1016/j.tins.2007.02.004

Cosson, S., Kobel, S. a., & Lutolf, M. P. (2009). Capturing complex protein gradients on biomimetic hydrogels for cell-based assays. *Advanced Functional Materials*, *19*(21), 3411–3419. http://doi.org/10.1002/adfm.200900968

Croci, L., Barili, V., Chia, D., Massimino, L., van Vugt, R., Masserdotti, G., Longhi, R., Rotwein, P., & Consalez, G. G. (2011). Local insulin-like growth factor I expression is essential for Purkinje neuron survival at birth. *Cell Death and Differentiation*, *18*(1), 48–59. http://doi.org/10.1038/cdd.2010.78

Cuchiara, M. P., Allen, A. C. B., Chen, T. M., Miller, J. S., & West, J. L. (2010). Multilayer microfluidic PEGDA hydrogels. *Biomaterials*, *31*(21), 5491–7. http://doi.org/10.1016/j.biomaterials.2010.03.031

Danen, E. H. J., & Sonnenberg, A. (2003). Integrins in regulation of tissue development and function. *The Journal of Pathology*, *201*(4), 632–41. http://doi.org/10.1002/path.1472

De Arcangelis, A., & Georges-Labouesse, E. (2000). Integrin and ECM functions: roles in vertebrate development. *Trends in Genetics : TIG*, *16*(9), 389–95. http://doi.org/S0168-9525(00)02074-6 [pii]

DeForest, C. A., & Tirrell, D. A. (2015). A photoreversible protein-patterning approach for guiding stem cell fate in three-dimensional gels. *Nat Mater*, *14*(5), 523–531. http://doi.org/10.1038/nmat4219

Del Álamo, J. C., Meili, R., Álvarez-González, B., Alonso-Latorre, B., Bastounis, E., Firtel, R., & Lasheras, J. C. (2013). Three-Dimensional Quantification of Cellular Traction Forces and Mechanosensing of Thin Substrata by Fourier Traction Force Microscopy. *PLoS ONE*, *8*(9), 1–39. http://doi.org/10.1371/journal.pone.0069850

DeLong, S. a., Gobin, A. S., & West, J. L. (2005). Covalent immobilization of RGDS on hydrogel surfaces to direct cell alignment and migration. *Journal of Controlled Release*, *109*(1-3), 139–148. http://doi.org/10.1016/j.jconrel.2005.09.020

Deutsch, S. I., Burket, J. A., & Katz, E. (2010). Does subtle disturbance of neuronal migration contribute to schizophrenia and other neurodevelopmental disorders? Potential genetic mechanisms with possible treatment implications. *European Neuropsychopharmacology*, *20*(5), 281–287. http://doi.org/Doi 10.1016/J.Euroneuro.2010.02.005

Dianov, G., Houle, J., Iyer, N., Bohr, V., & Friedberg, E. (1997). Reduced RNA polymerase II transcription in extracts of Cockayne syndrome and xeroderma pigmentosum/Cockayne syndrome cells. *Nucleic Acids*, *25*(9), 3636–3642.

DiMilla, P. A., Stone, J. A., Quinn, J. A., Albelda, S. M., & Lauffenburger, D. A. (1993). Maximal migration of human smooth muscle cells on fibronectin and type IV collagen occurs at an intermediate attachment strength. *The Journal of Cell Biology*, *122*(3), 729–37. http://doi.org/10.1083/jcb.122.3.729

Dityatev, A., & Schachner, M. (2003). Extracellular matrix molecules and synaptic plasticity. *Nat Rev Neurosci*, *4*(6), 456–468. http://doi.org/10.1038/nrn1115

Dobin, A., Davis, C. A., Schlesinger, F., Drenkow, J., Zaleski, C., Jha, S., Batut, P., Chaisson, M., & Gingeras, T. R. (2013). STAR: ultrafast universal RNA-seq aligner. *Bioinformatics (Oxford, England)*, *29*(1), 15–21. http://doi.org/10.1093/bioinformatics/bts635

Dvir, T., Timko, B. P., Kohane, D. S., & Langer, R. (2011). Nanotechnological strategies for engineering complex tissues. *Nat Nanotechnol*, *6*(1), 13–22. http://doi.org/10.1038/nnano.2010.246

Ehrlich, J. S., Hansen, M. D. H., & Nelson, W. J. (2002). Spatio-temporal regulation of

Rac1 localization and lamellipodia dynamics during epithelial cell-cell adhesion. *Developmental Cell*, *3*(2), 259–270. http://doi.org/10.1016/S1534-5807(02)00216-2

Elia, M., Falco, M., Ferri, R., Spalletta, a., Bottitta, M., Calabrese, G., Carotenuto, M., Musumeci, S. a., Lo Giudice, M., & Fichera, M. (2008). CDKL5 mutations in boys with severe encephalopathy and early-onset intractable epilepsy. *Neurology*, *71*(13), 997–999. http://doi.org/10.1212/01.wnl.0000326592.37105.88

Engler, A., Bacakova, L., Newman, C., Hategan, A., Griffin, M., & Discher, D. (2004). Substrate Compliance versus Ligand Density in Cell on Gel Responses. *Biophysical Journal*, *86*(1), 617–628. http://doi.org/10.1016/S0006-3495(04)74140-5

Engler, A. J., Sen, S., Sweeney, H. L., & Discher, D. E. (2006). Matrix Elasticity Directs Stem Cell Lineage Specification. *Cell*, *126*(4), 677–689. http://doi.org/10.1016/j.cell.2006.06.044

Englund, U., Björklund, A., & Wictorin, K. (2002). Migration patterns and phenotypic differentiation of long-term expanded human neural progenitor cells after transplantation into the adult rat brain. *Developmental Brain Research*, *134*(1–2), 123–141. http://doi.org/http://dx.doi.org/10.1016/S0165-3806(01)00330-3

Evans, J. C., Archer, H. L., Colley, J. P., Ravn, K., Nielsen, J. B., Kerr, A., Williams, E., Christodoulou, J., Gécz, J., Jardine, P. E., Wright, M. J., Pilz, D. T., Lazarou, L., Cooper, D. N., Sampson, J. R., Butler, R., Whatley, S. D., & Clarke, A. J. (2005). Early onset seizures and Rett-like features associated with mutations in CDKL5. *European Journal of Human Genetics : EJHG*, *13*(10), 1113–1120. http://doi.org/10.1038/sj.ejhg.5201451

Fairbanks, B. D., Schwartz, M. P., Bowman, C. N., & Anseth, K. S. (2009). Photoinitiated polymerization of PEG-diacrylate with lithium phenyl-2,4,6-trimethylbenzoylphosphinate: polymerization rate and cytocompatibility. *Biomaterials*, *30*(35), 6702–6707. http://doi.org/10.1016/j.biomaterials.2009.08.055

Fisher, R. S., Van Emde Boas, W., Blume, W., Elger, C., Genton, P., Lee, P., & Engel, J. (2005). Epileptic seizures and epilepsy: Definitions proposed by the International League Against Epilepsy (ILAE) and the International Bureau for Epilepsy (IBE). *Epilepsia*, *46*(4), 470–472. http://doi.org/10.1111/j.0013-9580.2005.66104.x

Flanagan, L. A., Ju, Y. E., Marg, B., Osterfield, M., & Janmey, P. A. (2002). Neurite branching on deformable substrates. *NeuroReport*, *13*(18), 2411–2415. http://doi.org/10.1097/01.wnr.0000048003.96487.97

Fletcher, D. A., & Mullins, R. D. (2010). Cell mechanics and the cytoskeleton. *Nature*, *463*(7280), 485–492. http://doi.org/10.1038/nature08908

Freeman, M. R. (2005). Glial control of synaptogenesis. *Cell*. http://doi.org/10.1016/j.cell.2005.01.021

Fuhrmann, A., Anselmetti, D., Ros, R., Getfert, S., & Reimann, P. (2008). Refined

procedure of evaluating experimental single-molecule force spectroscopy data. *Physical Review E - Statistical, Nonlinear, and Soft Matter Physics*, *77*(3), 1–10. http://doi.org/10.1103/PhysRevE.77.031912

Gaudet, C., Marganski, W. a, Kim, S., Brown, C. T., Gunderia, V., Dembo, M., & Wong, J. Y. (2003). Influence of type I collagen surface density on fibroblast spreading, motility, and contractility. *Biophysical Journal*, *85*(5), 3329–3335. http://doi.org/10.1016/S0006-3495(03)74752-3

Gautier, L., Cope, L., Bolstad, B. M., & Irizarry, R. A. (2004). Affy - Analysis of Affymetrix GeneChip data at the probe level. *Bioinformatics*, *20*(3), 307–315. http://doi.org/10.1093/bioinformatics/btg405

Gefen, A., & Margulies, S. S. (2004). Are in vivo and in situ brain tissues mechanically similar? *J Biomech*, *37*(9), 1339–1352. http://doi.org/10.1016/j.jbiomech.2003.12.032

Georges, P. C., Hui, J.-J., Gombos, Z., McCormick, M. E., Wang, A. Y., Uemura, M., Mick, R., Janmey, P. a, Furth, E. E., & Wells, R. G. (2007). Increased stiffness of the rat liver precedes matrix deposition: implications for fibrosis. *American Journal of Physiology. Gastrointestinal and Liver Physiology*, *293*(6), G1147–G1154. http://doi.org/10.1152/ajpgi.00032.2007

Georges, P. C., Miller, W. J., Meaney, D. F., Sawyer, E. S., & Janmey, P. A. (2006). Matrices with compliance comparable to that of brain tissue select neuronal over glial growth in mixed cortical cultures. *Biophys J*, *90*(8), 3012–3018. http://doi.org/10.1529/biophysj.105.073114

Giannone, G., Dubin-Thaler, B. J., Döbereiner, H. G., Kieffer, N., Bresnick, A. R., & Sheetz, M. P. (2004). Periodic lamellipodial contractions correlate with rearward actin waves. *Cell*, *116*(3), 431–443. http://doi.org/10.1016/S0092-8674(04)00058-3

Gil, V., & del Rio, J. A. (2012). Analysis of axonal growth and cell migration in 3D hydrogel cultures of embryonic mouse CNS tissue. *Nat. Protocols*, *7*(2), 268–280. http://doi.org/http://www.nature.com/nprot/journal/v7/n2/abs/nprot.2011.445.html#supplementary-information

Gleghorn, J. P., Lee, C. S. D., Cabodi, M., Stroock, A. D., & Bonassar, L. J. (2008). Adhesive properties of laminated alginate gels for tissue engineering of layered structures. *Journal of Biomedical Materials Research. Part A*, *85*(3), 611–8. http://doi.org/10.1002/jbm.a.31565

Graziani-Bowering, G. M., Graham, J. M., & Filion, L. G. (1997). A quick, easy and inexpensive method for the isolation of human peripheral blood monocytes. *J Immunol Methods*, *207*(2), 157–168. http://doi.org/10.1016/S0022-1759(97)00114-2

Grevesse, T., Versaevel, M., & Gabriele, S. (2014). Preparation of hydroxy-PAAm hydrogels for decoupling the effects of mechanotransduction cues. *Journal of Visualized Experiments : JoVE*, (90). http://doi.org/10.3791/51010

Griesi-Oliveira, K., Acab, A., Gupta, A. R., Sunaga, D. Y., Chailangkarn, T., Nicol, X., Nunez, Y., Walker, M. F., Murdoch, J. D., Sanders, S. J., Fernandez, T. V., Ji, W., Lifton, R. P., Vadasz, E., Dietrich, A., Pradhan, D., Song, H., Ming, G. I., Gu, X., Haddad, G., Marchetto, M. C., Spitzer, N., Passos-Bueno, M. R., State, M. W., & Muotri, A. R. (2015). Modeling non-syndromic autism and the impact of TRPC6 disruption in human neurons. *Mol. Psychiatry*, *20*(November 2014), 1350–1365. http://doi.org/10.1038/mp.2014.141

Hachet, E., Van Den Berghe, H., Bayma, E., Block, M. R., & Auzely-Velty, R. (2012). Design of Biomimetic Cell-Interactive Substrates Using Hyaluronic Acid Hydrogels with Tunable Mechanical Properties. *Biomacromolecules*, *13*(6), 1818–1827. http://doi.org/Doi 10.1021/Bm300324m

Hack, I., Bancila, M., Loulier, K., Carroll, P., & Cremer, H. (2002). Reelin is a detachment signal in tangential chain-migration during postnatal neurogenesis. *Nature Neuroscience*, *5*(10), 939–945. http://doi.org/10.1038/nn923

Hahn, M. S., Miller, J. S., & West, J. L. (2005). Laser Scanning Lithography for Surface Micropatterning on Hydrogels. *Advanced Materials*, *17*(24), 2939–2942. http://doi.org/10.1002/adma.200500184

Hahn, M. S., Taite, L. J., Moon, J. J., Rowland, M. C., Ruffino, K. A., & West, J. L. (2006). Photolithographic patterning of polyethylene glycol hydrogels. *Biomaterials*, *27*(12), 2519–24. http://doi.org/10.1016/j.biomaterials.2005.11.045

Haidet-Phillips, A. M., Gross, S. K., Williams, T., Tuteja, A., Sherman, A., Ko, M., Jeong, Y. H., Wong, P. C., & Maragakis, N. J. (2013). Altered astrocytic expression of TDP-43 does not influence motor neuron survival. *Experimental Neurology*, *250*, 250–259. http://doi.org/10.1016/j.expneurol.2013.10.004

Hanawalt, P., & Spivak, G. (2008). Transcription-coupled DNA repair: two decades of progress and surprises. *Nature Reviews. Molecular Cell Biology*, *9*(12), 958–970. http://doi.org/10.1038/nrm2549

Hardwick, S. a, Reuter, K., Williamson, S. L., Vasudevan, V., Donald, J., Slater, K., Bennetts, B., Bebbington, A., Leonard, H., Williams, S. R., Smith, R. L., Cloosterman, D., & Christodoulou, J. (2007). Delineation of large deletions of the MECP2 gene in Rett syndrome patients, including a familial case with a male proband. *European Journal of Human Genetics : EJHG*, *15*(12), 1218–1229. http://doi.org/10.1038/sj.ejhg.5201911

Harley, B. a., Lynn, A. K., Wissner-Gross, Z., Bonfield, W., Yannas, I. V., & Gibson, L. J. (2010). Design of a multiphase osteochondral scaffold III: Fabrication of layered scaffolds with continuous interfaces. *Journal of Biomedical Materials Research - Part A*, *92*(3), 1078–1093. http://doi.org/10.1002/jbm.a.32387

He, J., Du, Y., Villa-Uribe, J. L., Hwang, C., Li, D., & Khademhosseini, A. (2010). Rapid generation of biologically relevant hydrogels containing long-range chemical gradients. *Advanced Functional Materials*, *20*(1), 131–137.

http://doi.org/10.1002/adfm.200901311

Hersel, U., Dahmen, C., & Kessler, H. (2003). RGD modified polymers: biomaterials for stimulated cell adhesion and beyond. *Biomaterials*, *24*(24), 4385–4415. Retrieved from http://www.ncbi.nlm.nih.gov/pubmed/12922151

Herz, J., & Chen, Y. (2006). Reelin, lipoprotein receptors and synaptic plasticity. *Nature Reviews. Neuroscience*, *7*(11), 850–859. http://doi.org/10.1038/nrn2009

Hoffman, B. D., Grashoff, C., & Schwartz, M. a. (2011). Dynamic molecular processes mediate cellular mechanotransduction. *Nature*, *475*(7356), 316–323. http://doi.org/10.1038/nature10316

Hoffmann, J. C., & West, J. L. (2010). Three-dimensional photolithographic patterning of multiple bioactive ligands in poly(ethylene glycol) hydrogels. *Soft Matter*, *6*, 5056. http://doi.org/10.1039/c0sm00140f

Hopkins, A. M., DeSimone, E., Chwalek, K., & Kaplan, D. L. (2015). 3D in vitro modeling of the central nervous system. *Progress in Neurobiology*, *125*, 1–25. http://doi.org/10.1016/j.pneurobio.2014.11.003

Horie, H., & Akahori, Y. (1994). Three-dimensional cell aggregation enhances growth-promoting activity of NGF in adult DRG. *NeuroReport*, *6*(1), 37–40.

Hwang, Y., Zhang, C., & Varghese, S. (2010). Poly(ethylene glycol) cryogels as potential cell scaffolds: effect of polymerization conditions on cryogel microstructure and properties. *Journal of Materials Chemistry*, *20*(2), 345. http://doi.org/10.1039/b917142h

Hynes, S. R., Rauch, M. F., Bertram, J. P., & Lavik, E. B. (2009). A library of tunable poly(ethylene glycol)/poly(L-lysine) hydrogels to investigate the material cues that influence neural stem cell differentiation. *Journal of Biomedical Materials Research - Part A*, *89*(2), 499–509. http://doi.org/10.1002/jbm.a.31987

J.C., H., & J.L., W. (2010). Three-dimensional photolithographic patterning of multiple bioactive ligands in poly(ethylene glycol) hydrogels. *Soft Matter*, *6*(20), 5056–5063. http://doi.org/10.1039/c0sm00140f

Jian, L., Nagarajan, L., de Klerk, N., Ravine, D., Bower, C., Anderson, A., Williamson, S., Christodoulou, J., & Leonard, H. (2006). Predictors of seizure onset in Rett syndrome. *The Journal of Pediatrics*, *149*(4), 542–7. http://doi.org/10.1016/j.jpeds.2006.06.015

Joshi-Barr, S., Karpiak, J. V, Ner, Y., Wen, J. H., Engler, A. J., & Almutairi, A. (2013). Density gradient multilayered polymerization (DGMP): a novel technique for creating multi-compartment, customizable scaffolds for tissue engineering. *Journal of Visualized Experiments : JoVE*, (72), 1–5. http://doi.org/10.3791/50018

Kalscheuer, V. M., Tao, J., Donnelly, A., Hollway, G., Schwinger, E., Kübart, S.,

Menzel, C., Hoeltzenbein, M., Tommerup, N., Eyre, H., Harbord, M., Haan, E., Sutherland, G. R., Ropers, H.-H., & Gécz, J. (2003). Disruption of the serine/threonine kinase 9 gene causes severe X-linked infantile spasms and mental retardation. *American Journal of Human Genetics*, *72*(6), 1401–1411. http://doi.org/10.1086/375538

Kamenisch, Y., Fousteri, M., Knoch, J., von Thaler, A., Fehrenbacher, B., Kato, H., Becker, T., Dollé, M., Kuiper, R., Majora, M., Schaller, M., van der Horst, G., van Steeg, H., Röcken, M., Rapaport, D., Krutmann, J., Mullenders, L., & Berneburg, M. (2010). Proteins of nucleotide and base excision repair pathways interact in mitochondria to protect from loss of subcutaneous fat, a hallmark of aging. *The Journal of Experimental Medicine*, *207*(2), 379–390. http://doi.org/10.1084/jem.20091834

Karpiak, J. V., Ner, Y., & Almutairi, A. (2012). Density gradient multilayer polymerization for creating complex tissue. *Advanced Materials*, *24*(11), 1466–1470. http://doi.org/10.1002/adma.201103501

Katayama, Y., Battista, M., Kao, W. M., Hidalgo, A., Peired, A. J., Thomas, S. a., & Frenette, P. S. (2006). Signals from the sympathetic nervous system regulate hematopoietic stem cell egress from bone marrow. *Cell*, *124*(2), 407–421. http://doi.org/10.1016/j.cell.2005.10.041

Kaushik, G., Fuhrmann, A., Cammarato, A., & Engler, A. J. (2011). In situ mechanical analysis of myofibrillar perturbation and aging on soft, bilayered Drosophila myocardium. *Biophysical Journal*, *101*(11), 2629–37. http://doi.org/10.1016/j.bpj.2011.10.042

Kenet, T., Bibitchkov, D., Tsodyks, M., Grinvald, A., & Arieli, A. (2003). Spontaneously emerging cortical representations of visual attributes. *Nature*, *425*(6961), 954–956. http://doi.org/10.1038/nature02078

Khademhosseini, A., & Langer, R. (2007). Microengineered hydrogels for tissue engineering. *Biomaterials*, *28*(34), 5087–92. http://doi.org/10.1016/j.biomaterials.2007.07.021

Khetan, S., & Burdick, J. (2009). Cellular encapsulation in 3D hydrogels for tissue engineering. *Journal of Visualized Experiments : JoVE*, (32), 3–7. http://doi.org/10.3791/1590

Khetan, S., Guvendiren, M., Legant, W. R., Cohen, D. M., Chen, C. S., & Burdick, J. A. (2013). Degradation-mediated cellular traction directs stem cell fate in covalently crosslinked three-dimensional hydrogels. *Nat Mater*, *12*(5), 458–465. http://doi.org/10.1038/nmat3586

Khwaja, O. S., Ho, E., Barnes, K. V, O'Leary, H. M., Pereira, L. M., Finkelstein, Y., Nelson, C. a, Vogel-Farley, V., DeGregorio, G., Holm, I. a, Khatwa, U., Kapur, K., Alexander, M. E., Finnegan, D. M., Cantwell, N. G., Walco, A. C., Rappaport, L., Gregas, M., Fichorova, R. N., Shannon, M. W., Sur, M., & Kaufmann, W. E. (2014). Safety, pharmacokinetics, and preliminary assessment of efficacy of mecasermin

(recombinant human IGF-1) for the treatment of Rett syndrome. *Proceedings of the National Academy of Sciences of the United States of America*, *111*(12), 4596–601. http://doi.org/10.1073/pnas.1311141111

Kim, H.-D., & Peyton, S. R. (2012). Bio-inspired materials for parsing matrix physicochemical control of cell migration: A Review. *Integrative Biology*, *4*(1), 37. http://doi.org/10.1039/c1ib00069a

Kim, J.-E., O'Sullivan, M. L., Sanchez, C. A., Hwang, M., Israel, M. A., Brennand, K., Deerinck, T. J., Goldstein, L. S. B., Gage, F. H., Ellisman, M. H., & Ghosh, A. (2011). Investigating synapse formation and function using human pluripotent stem cell-derived neurons. *Proceedings of the National Academy of Sciences*, *108*(7), 3005–3010. http://doi.org/10.1073/pnas.1007753108

Kim, K. Y., Hysolli, E., & Park, I. H. (2011). Neuronal maturation defect in induced pluripotent stem cells from patients with Rett syndrome. *Proc Natl Acad Sci U S A*, *108*(34), 14169–14174. http://doi.org/10.1073/pnas.1018979108

Kim, T. K., Sharma, B., Williams, C. G., Ruffner, M. a., Malik, a., McFarland, E. G., & Elisseeff, J. H. (2003). Experimental model for cartilage tissue engineering to regenerate the zonal organization of articular cartilage. *Osteoarthritis and Cartilage*, *11*, 653–664. http://doi.org/10.1016/S1063-4584(03)00120-1

Kim, Y., & Kumar, S. (2014). CD44-mediated adhesion to hyaluronic acid contributes to mechanosensing and invasive motility. *Mol Cancer Res*, *12*(10), 1416–1429. http://doi.org/10.1158/1541-7786.MCR-13-0629

Kishi, N., & Macklis, J. D. (2004). MECP2 is progressively expressed in post-migratory neurons and is involved in neuronal maturation rather than cell fate decisions. *Molecular and Cellular Neuroscience*, *27*(3), 306–321. http://doi.org/http://dx.doi.org/10.1016/j.mcn.2004.07.006

Kizilel, S., Sawardecker, E., Teymour, F., & Pérez-Luna, V. H. (2006). Sequential formation of covalently bonded hydrogel multilayers through surface initiated photopolymerization. *Biomaterials*, *27*(8), 1209–1215. http://doi.org/10.1016/j.biomaterials.2005.08.025

Kocgozlu, L., Lavalle, P., Koenig, G., Senger, B., Haikel, Y., Schaaf, P., Voegel, J. C., Tenenbaum, H., & Vautier, D. (2010). Selective and uncoupled role of substrate elasticity in the regulation of replication and transcription in epithelial cells. *J Cell Sci*, *123*(Pt 1), 29–39. http://doi.org/10.1242/jcs.053520

Koob, M., Laugel, V., Durand, M., Fothergill, H., Dalloz, C., Sauvanaud, F., Dollfus, H., Namer, I. J., & Dietemann, J. L. (2010). Neuroimaging in Cockayne syndrome. *American Journal of Neuroradiology*, *31*(9), 1623–1630. http://doi.org/10.3174/ajnr.A2135

Kraus, S., Lehner, B., Reichhart, N., Couillard-Despres, S., Wagner, K., Bogdahn, U., Aigner, L., & Strauß, O. (2013). Transforming growth factor-β1 primes proliferating

adult neural progenitor cells to electrophysiological functionality. *Glia*, *61*(11), 1767–1783. http://doi.org/10.1002/glia.22551

Kriegstein, A., & Alvarez-Buylla, A. (2009). The glial nature of embryonic and adult neural stem cells. *Annual Review of Neuroscience*, *32*, 149–184. http://doi.org/10.1146/annurev.neuro.051508.135600

Kuckling, D., & Pareek, P. (2008). Bilayer hydrogel assembly. *Polymer*, *49*(6), 1435–1439. http://doi.org/10.1016/j.polymer.2008.01.069

Kwan, K. Y., Sestan, N., & Anton, E. S. (2012). Transcriptional co-regulation of neuronal migration and laminar identity in the neocortex. *Development*, *139*(9), 1535–1546. http://doi.org/10.1242/dev.069963

Labelle, C., & Leclerc, N. (2000). Exogenous BDNF, NT-3 and NT-4 differentially regulate neurite outgrowth in cultured hippocampal neurons. *Developmental Brain Research*, *123*(1), 1–11. Retrieved from http://www.sciencedirect.com/science/article/pii/S0165380600000699

Lampe, K. J., Antaris, A. L., & Heilshorn, S. C. (2013). Design of three-dimensional engineered protein hydrogels for tailored control of neurite growth. *Acta Biomater*, *9*(3), 5590–5599. http://doi.org/10.1016/j.actbio.2012.10.033

Lauffenburger, D. a., & Linderman, J. J. (1996). *Receptors: models for binding, trafficking, and signaling*. *Journal of Controlled Release* (Vol. 39). http://doi.org/10.1016/S0168-3659(96)90009-7

Laxer, K. D., Trinka, E., Hirsch, L. J., Cendes, F., Langfitt, J., Delanty, N., Resnick, T., & Benbadis, S. R. (2014). The consequences of refractory epilepsy and its treatment. *Epilepsy and Behavior*, *37*, 59–70. http://doi.org/10.1016/j.yebeh.2014.05.031

Lee, K. Y., & Mooney, D. J. (2001). Hydrogels for Tissue Engineering. *Chemical Reviews*, *101*(7), 1869–1880. http://doi.org/10.1021/cr000108x

Lee, V. M., Louis, S. A., & Reynolds, B. A. (2015). Neural Stem Cells Mini-Review, (April). Retrieved from https://www.stemcell.com/~/media/Technical Resources/0/0/29019_Neural.pdf?la=en

Lehmann, A. R. (2003). DNA repair-deficient diseases , xeroderma pigmentosum , Cockayne syndrome and trichothiodystrophy. *Biochimie*, *85*, 1101–1111. http://doi.org/10.1016/j.biochi.2003.09.010

Leipzig, N. D., & Shoichet, M. S. (2009). The effect of substrate stiffness on adult neural stem cell behavior. *Biomaterials*, *30*(36), 6867–6878. http://doi.org/10.1016/j.biomaterials.2009.09.002

Leslie-Barbick, J. E., Saik, J. E., Gould, D. J., Dickinson, M. E., & West, J. L. (2011). The promotion of microvasculature formation in poly(ethylene glycol) diacrylate hydrogels by an immobilized VEGF-mimetic peptide. *Biomaterials*, *32*(25), 5782–5789.

http://doi.org/10.1016/j.biomaterials.2011.04.060

Li, W., Fan, J., Chen, M., Guan, S., Sawcer, D., Bokoch, G. M., & Woodley, D. T. (2004). mechanism of human dermal fibroblast migration driven by type I collagen and platelet derived growth factor-BB. *Molecular Biology of the Cell*, *15*(January), 294–309. http://doi.org/10.1091/mbc.E03

Li, Y., Gautam, A., Yang, J., Qiu, L., Melkoumian, Z., Weber, J., Telukuntla, L., Srivastava, R., Whiteley, E. M., & Brandenberger, R. (2013). Differentiation of oligodendrocyte progenitor cells from human embryonic stem cells on vitronectin-derived synthetic peptide acrylate surface. *Stem Cells Dev*, *22*(10), 1497–1505. http://doi.org/10.1089/scd.2012.0508

Lindwall, C., Olsson, M., Osman, A. M., Kuhn, H. G., & Curtis, M. A. (2013). Selective expression of hyaluronan and receptor for hyaluronan mediated motility (Rhamm) in the adult mouse subventricular zone and rostral migratory stream and in ischemic cortex. *Brain Res*, *1503*, 62–77. http://doi.org/10.1016/j.brainres.2013.01.045

Lioy, D. T., Garg, S. K., Monaghan, C. E., Raber, J., Foust, K. D., Kaspar, B. K., Hirrlinger, P. G., Kirchhoff, F., Bissonnette, J. M., Ballas, N., & Mandel, G. (2011). A role for glia in the progression of Rett's syndrome. *Nature*, *475*(7357), 497–500. http://doi.org/10.1038/nature10214

Liu, V. A., & Bhatia, S. N. (2002). Three-Dimensional Photopatterning of Hydrogels Containing Living Cells. *Biomedical Microdevices*, *4*(4), 257–266. http://doi.org/10.1023/A:1020932105236

Liu, V. a., Jastromb, W. E., & Bhatia, S. N. (2002). Engineering protein and cell adhesivity using PEO-terminated triblock polymers. *Journal of Biomedical Materials Research*, *60*(1), 126–134. http://doi.org/10.1002/jbm.10005

Lo, C. M., Wang, H. B., Dembo, M., & Wang, Y. L. (2000). Cell movement is guided by the rigidity of the substrate. *Biophysical Journal*, *79*(1), 144–152. http://doi.org/10.1016/S0006-3495(00)76279-5

Lobsiger, C. S., & Cleveland, D. W. (2007). Glial cells as intrinsic components of non-cell-autonomous neurodegenerative disease. *Nature Neuroscience*, *10*(11), 1355–60. http://doi.org/10.1038/nn1988

Lu, Y. B., Franze, K., Seifert, G., Steinhauser, C., Kirchhoff, F., Wolburg, H., Guck, J., Janmey, P., Wei, E. Q., Kas, J., & Reichenbach, A. (2006). Viscoelastic properties of individual glial cells and neurons in the CNS. *Proc Natl Acad Sci U S A*, *103*(47), 17759–17764. http://doi.org/10.1073/pnas.0606150103

Luo, Y., & Shoichet, M. S. (2004). A photolabile hydrogel for guided three-dimensional cell growth and migration. *Nat Mater*, *3*(4), 249–253. http://doi.org/http://www.nature.com/nmat/journal/v3/n4/suppinfo/nmat1092_S1.html

Lutolf, M. P., & Hubbell, J. a. (2005). Synthetic biomaterials as instructive extracellular

microenvironments for morphogenesis in tissue engineering. *Nature Biotechnology*, *23*(1), 47–55. http://doi.org/10.1038/nbt1055

Ma, P. X. (2008). Biomimetic materials for tissue engineering. *Advanced Drug Delivery Reviews*, *60*(2), 184–98. http://doi.org/10.1016/j.addr.2007.08.041

Ma, W., Tavakoli, T., Derby, E., Serebryakova, Y., Rao, M. S., & Mattson, M. P. (2008). Cell-extracellular matrix interactions regulate neural differentiation of human embryonic stem cells. *BMC Dev Biol*, *8*, 90. http://doi.org/10.1186/1471-213X-8-90

Mackay, A. R., Gomez, D. E., Nason, A. M., & Thorgeirsson, U. P. (1994). Studies on the Effects of Laminin, E-8 Fragment of Laminin and Synthetic Laminin Peptides Pa22-2 and Yigsr on Matrix Metalloproteinases and Tissue Inhibitor of Metalloproteinase Expression. *LABORATORY INVESTIGATION*.

Maezawa, I., Swanberg, S., Harvey, D., LaSalle, J. M., & Jin, L.-W. (2009). Rett syndrome astrocytes are abnormal and spread MeCP2 deficiency through gap junctions. *The Journal of Neuroscience : The Official Journal of the Society for Neuroscience*, *29*(16), 5051–5061. http://doi.org/10.1523/JNEUROSCI.0324-09.2009

Majima, T., Schnabel, W., & Weber, W. (1991). Phenyl-2,4,6-Trimethylbenzoylphosphinates as Water-Soluble Photoinitiators - Generation and Reactivity of O=P(C6h5)(O-) Radical-Anions. *Makromolekulare Chemie-Macromolecular Chemistry and Physics*, *192*(10), 2307–2315. Retrieved from <Go to ISI>://WOS:A1991GP21100010

Marchetto, M., Carromeu, C., Acab, A., Yu, D., Yeo, G., Mu, Y., Chen, G., Gage, F., & Muotri, A. (2010). A model for neural development and treatment of Rett syndrome using human induced pluripotent stem cells. *Cell*, *143*(4), 527–39. http://doi.org/10.1016/j.cell.2010.10.016.A

Mariani, J., Coppola, G., Zhang, P., Abyzov, A., Provini, L., Tomasini, L., Amenduni, M., Szekely, A., Palejev, D., Wilson, M., Gerstein, M., Grigorenko, E. L., Chawarska, K., Pelphrey, K. A., Howe, J. R., & Vaccarino, F. M. (2015). FOXG1-Dependent Dysregulation of GABA/Glutamate Neuron Differentiation in Autism Spectrum Disorders. *Cell*, *162*(2), 375–390. http://doi.org/10.1016/j.cell.2015.06.034

Mariani, J., Simonini, M. V., Palejev, D., Tomasini, L., Coppola, G., Szekely, A. M., Horvath, T. L., & Vaccarino, F. M. (2012). Modeling human cortical development in vitro using induced pluripotent stem cells. *Proceedings of the National Academy of Sciences*, *109*(31), 12770–12775. http://doi.org/10.1073/pnas.1202944109

Marin, O., Valiente, M., Ge, X., & Tsai, L. H. (2010). Guiding neuronal cell migrations. *Cold Spring Harb Perspect Biol*, *2*(2), a001834. http://doi.org/10.1101/cshperspect.a001834

Markham, K., Schuurmans, C., & Weiss, S. (2007). STAT5A/B activity is required in the developing forebrain and spinal cord. *Molecular and Cellular Neuroscience*, *35*(2), 272–282. http://doi.org/10.1016/j.mcn.2007.03.001

Marklein, R. a., & Burdick, J. a. (2010). Spatially controlled hydrogel mechanics to modulate stem cell interactions. *Soft Matter*, *6*(1), 136. http://doi.org/10.1039/b916933d

Mason, H. A., Ito, S., & Corfas, G. (2001). Extracellular Signals That Regulate the Tangential Migration of Olfactory Bulb Neuronal Precursors: Inducers, Inhibitors, and Repellents. *The Journal of Neuroscience*, *21*(19), 7654–7663. Retrieved from http://www.jneurosci.org/content/21/19/7654.abstract

McKinnon, D. D., Kloxin, A. M., & Anseth, K. S. (2013). Synthetic hydrogel platform for three-dimensional culture of embryonic stem cell-derived motor neurons. *Biomaterials Science*, *1*(5), 460–469. http://doi.org/10.1039/c3bm00166k

Menck, C., & Munford, V. (2014). DNA repair diseases: What do they tell us about cancer and aging? *Genetics and Molecular Biology*, *37*(1), 220–233. http://doi.org/10.1590/S1415-47572014000200008

Messager, L., Portecop, N., Hachet, E., Lapeyre, V., Pignot-Paintrand, I., Catargi, B., Auzely-Velty, R., & Ravaine, V. (2013). Photochemical crosslinking of hyaluronic acid confined in nanoemulsions: towards nanogels with a controlled structure. *Journal of Materials Chemistry B*, *1*(27), 3369–3379. http://doi.org/Doi 10.1039/C3tb20300j

Meunier, D., Lambiotte, R., & Bullmore, E. T. (2010). Modular and Hierarchically Modular Organization of Brain Networks. *Frontiers in Neuroscience*, *4*(December), 1–11. http://doi.org/10.3389/fnins.2010.00200

Misumi, S., Kim, T. S., Jung, C. G., Masuda, T., Urakawa, S., Isobe, Y., Furuyama, F., Nishino, H., & Hida, H. (2008). Enhanced neurogenesis from neural progenitor cells with G1/S-phase cell cycle arrest is mediated by transforming growth factor ??1. *European Journal of Neuroscience*, *28*(6), 1049–1059. http://doi.org/10.1111/j.1460-9568.2008.06420.x

Montini, E., Andolfi, G., Caruso, a, Buchner, G., Walpole, S. M., Mariani, M., Consalez, G., Trump, D., Ballabio, a, & Franco, B. (1998). Identification and characterization of a novel serine-threonine kinase gene from the Xp22 region. *Genomics*, *51*(3), 427–433. http://doi.org/10.1006/geno.1998.5391

Mountcastle, V. B. (1997). The columnar organization of the neocortex. *Brain : A Journal of Neurology*, *120 (Pt 4*, 701–22. http://doi.org/10.1093/brain/120.4.701

Musah, S., Morin, S. A., Wrighton, P. J., Zwick, D. B., Jin, S., & Kiessling, L. L. (2012). Glycosaminoglycan-binding hydrogels enable mechanical control of human pluripotent stem cell self-renewal. *ACS Nano*, *6*(11), 10168–10177. http://doi.org/10.1021/nn3039148

Nagtegaal, A. P., Rainey, R. N., van der Pluijm, I., Brandt, R. M. C., van der Horst, G. T. J., Borst, J. G. G., & Segil, N. (2015). Cockayne Syndrome Group B (Csb) and Group A (Csa) Deficiencies Predispose to Hearing Loss and Cochlear Hair Cell Degeneration in Mice. *Journal of Neuroscience*, *35*(10), 4280–4286. http://doi.org/10.1523/JNEUROSCI.5063-14.2015

Nance, M. A., & Berry, S. A. (1992). Cockayne syndrome: review of 140 cases. *Am J Med Genet*, *42*(1), 68–84. http://doi.org/10.1002/ajmg.1320420115

Natale, V. (2011). A comprehensive description of the severity groups in Cockayne syndrome. *American Journal of Medical Genetics, Part A*, *155*(5), 1081–1095. http://doi.org/10.1002/ajmg.a.33933

Neul, J. L., & Zoghbi, H. Y. (2004). Rett syndrome: a prototypical neurodevelopmental disorder. *Neuroscientist*, *10*(2), 118–128.

Newman, J. C., Bailey, A. D., & Weiner, A. M. (2006). Cockayne syndrome group B protein (CSB) plays a general role in chromatin maintenance and remodeling. *Proceedings of the National Academy of Sciences of the United States of America*, *103*(25), 9613–8. http://doi.org/10.1073/pnas.0510909103

Niedernhofer, L. J., Garinis, G. A., Raams, A., Lalai, A. S., Robinson, A. R., Appeldoorn, E., Odijk, H., Oostendorp, R., Ahmad, A., Leeuwen, W. Van, Theil, A. F., Vermeulen, W., Horst, G. T. J. Van Der, Meinecke, P., Kleijer, W. J., Vijg, J., Jaspers, N. G. J., & Hoeijmakers, J. H. J. (2006). A new progeroid syndrome reveals that genotoxic stress suppresses the somatotroph axis. *Nature*, *444*, 1038–1043. http://doi.org/doi:10.1038/nature05456

Noctor, S. C., Flint, A. C., Weissman, T. A., Dammerman, R. S., & Kriegstein, A. R. (2001). Neurons derived from radial glial cells establish radial units in neocortex. *Nature*, *409*(6821), 714–720. http://doi.org/Doi 10.1038/35055553

Nomizu, M., Weeks, B. S., Weston, C. A., Kim, W. H., Kleinman, H. K., & Yamada, Y. (1995). Structure-activity study of a laminin alpha 1 chain active peptide segment Ile-Lys-Val-Ala-Val (IKVAV). *FEBS Letters*, *365*(2-3), 227–231. http://doi.org/10.1016/0014-5793(95)00475-O

Odawara, A., Gotoh, M., & Suzuki, I. (2013a). A three-dimensional neuronal culture technique that controls the direction of neurite elongation and the position of soma to mimic the layered structure of the brain. *RSC Advances*, *3*(45), 23620. http://doi.org/10.1039/c3ra44757j

Odawara, A., Gotoh, M., & Suzuki, I. (2013b). Control of neural network patterning using collagen gel photothermal etching. *Lab on a Chip*, *13*(11), 2040–2046. http://doi.org/10.1039/c3lc00036b

Odawara, A., Saitoh, Y., Alhebshi, A. H., Gotoh, M., & Suzuki, I. (2014). Long-term electrophysiological activity and pharmacological response of a human induced pluripotent stem cell-derived neuron and astrocyte co-culture. *Biochem Biophys Res Commun*, *443*(4), 1176–1181. http://doi.org/10.1016/j.bbrc.2013.12.142

Okita, K., Matsumura, Y., Sato, Y., Okada, A., Morizane, A., Okamoto, S., Hong, H., Nakagawa, M., Tanabe, K., Tezuka, K., Shibata, T., Kunisada, T., Takahashi, M., Takahashi, J., Saji, H., & Yamanaka, S. (2011). A more efficient method to generate integration-free human iPS cells. *Nature Methods*, *8*(5), 409–412.

http://doi.org/10.1038/nmeth.1591

Orekhova, E. V., Stroganova, T. a., Nygren, G., Tsetlin, M. M., Posikera, I. N., Gillberg, C., & Elam, M. (2007). Excess of High Frequency Electroencephalogram Oscillations in Boys with Autism. *Biological Psychiatry*, *62*, 1022–1029. http://doi.org/10.1016/j.biopsych.2006.12.029

Otsuji, T. G., Bin, J., Yoshimura, A., Tomura, M., Tateyama, D., Minami, I., Yoshikawa, Y., Aiba, K., Heuser, J. E., Nishino, T., Hasegawa, K., & Nakatsuji, N. (2014). A 3D sphere culture system containing functional polymers for large-scale human pluripotent stem cell production. *Stem Cell Reports*, *2*(5), 734–745. http://doi.org/10.1016/j.stemcr.2014.03.012

Park, S., Chang, S., Cho, S., Baek, H., & Lee, D. (1994). Cockayne syndrome: A case with hyperinsulinemia and growth hormone deficiency. *Journal of Korean Medical Science*, *9*(1), 74–77.

Pasca, A. M., Sloan, S. A., Clarke, L. E., Tian, Y., Makinson, C. D., Huber, N., Kim, C. H., Park, J. Y., O'Rourke, N. A., Nguyen, K. D., Smith, S. J., Huguenard, J. R., Geschwind, D. H., Barres, B. A., & Pasca, S. P. (2015). Functional cortical neurons and astrocytes from human pluripotent stem cells in 3D culture. *Nat Methods*, *12*(7), 671–678. http://doi.org/10.1038/nmeth.3415

Pascucci, B., Lemma, T., Iorio, E., Giovannini, S., Vaz, B., Iavarone, I., Calcagnile, A., Narciso, L., Degan, P., Podo, F., Roginskya, V., Janjic, B., Van Houten, B., Stefanini, M., Dogliotti, E., & D'Errico, M. (2012). An altered redox balance mediates the hypersensitivity of Cockayne syndrome primary fibroblasts to oxidative stress. *Aging Cell*, *11*(3), 520–529. http://doi.org/10.1111/j.1474-9726.2012.00815.x

Patel, R. K., & Jain, M. (2012). NGS QC Toolkit: a toolkit for quality control of next generation sequencing data. *PloS One*, *7*(2), e30619. http://doi.org/10.1371/journal.pone.0030619

Pelham Jr., R. J., & Wang, Y. (1997). Cell locomotion and focal adhesions are regulated by substrate flexibility. *Proc Natl Acad Sci U S A*, *94*(25), 13661–13665. Retrieved from http://www.ncbi.nlm.nih.gov/pubmed/9391082

Peñagarikano, O., Abrahams, B. S., Herman, E. I., Winden, K. D., Gdalyahu, A., Dong, H., Sonnenblick, L. I., Gruver, R., Almajano, J., Bragin, A., Golshani, P., Trachtenberg, J. T., Peles, E., & Geschwind, D. H. (2011). Absence of CNTNAP2 leads to epilepsy, neuronal migration abnormalities, and core autism-related deficits. *Cell*, *147*(1), 235–246. http://doi.org/10.1016/j.cell.2011.08.040

Peng, R., Yao, X., & Ding, J. (2011). Effect of cell anisotropy on differentiation of stem cells on micropatterned surfaces through the controlled single cell adhesion. *Biomaterials*, *32*(32), 8048–8057. http://doi.org/10.1016/j.biomaterials.2011.07.035

Peppas, N. a., Keys, K. B., Torres-Lugo, M., & Lowman, A. M. (1999). Poly(ethylene glycol)-containing hydrogels in drug delivery. *Journal of Controlled Release*, *62*(1-2),

81–87. http://doi.org/10.1016/S0168-3659(99)00027-9

Perea, G., Navarrete, M., & Araque, A. (2009). Tripartite synapses: astrocytes process and control synaptic information. *Trends in Neurosciences*, *32*(8), 421–431. http://doi.org/10.1016/j.tins.2009.05.001

Peretz, H., Talpalar, A. E., Vago, R., & Baranes, D. (2007). Superior survival and durability of neurons and astrocytes on 3-dimensional aragonite biomatrices. *Tissue Eng*, *13*(3), 461–472.

Peters, A., & Feldman, M. L. (1976). The projection of the lateral geniculate nucleus to area 17 of the rat cerebral cortex. I. General description. *Journal of Neurocytology*, *5*(1), 63–84. http://doi.org/10.1007/BF01176183

Peyton, S. R., & Putnam, A. J. (2005). Extracellular matrix rigidity governs smooth muscle cell motility in a biphasic fashion. *Journal of Cellular Physiology*, *204*(1), 198–209. http://doi.org/10.1002/jcp.20274

Pierschbacher, M. D., & Ruoslahti, E. (1984). Cell attachment activity of fibronectin can be duplicated by small synthetic fragments of the molecule. *Nature*, *309*(5963), 30–33. http://doi.org/10.1038/309030a0

Pini, G., Scusa, M. F., Congiu, L., Benincasa, A., Morescalchi, P., Bottiglioni, I., Di Marco, P., Borelli, P., Bonuccelli, U., Della-Chiesa, A., Prina-Mello, A., & Tropea, D. (2012). IGF1 as a Potential Treatment for Rett Syndrome: Safety Assessment in Six Rett Patients. *Autism Research and Treatment*, *2012*, 1–14. http://doi.org/10.1155/2012/679801

Place, E. S., Evans, N. D., & Stevens, M. M. (2009). Complexity in biomaterials for tissue engineering. *Nature Materials*, *8*(6), 457–70. http://doi.org/10.1038/nmat2441

Prince, M., Wimo, A., Guerchet, M., Gemma-Claire, A., Wu, Y.-T., & Prina, M. (2015). World Alzheimer Report 2015: The Global Impact of Dementia - An analysis of prevalence, incidence, cost and trends. *Alzheimer's Disease International*, 84. http://doi.org/10.1111/j.0963-7214.2004.00293.x

Pulsipher, A., & Yousaf, M. N. (2010). Surface chemistry and cell biological tools for the analysis of cell adhesion and migration. *Chembiochem : A European Journal of Chemical Biology*, *11*(6), 745–53, 730. http://doi.org/10.1002/cbic.200900787

Raichle, M. E., & Mintun, M. a. (2006). Brain work and brain imaging. *Annual Review of Neuroscience*, *29*, 449–76. http://doi.org/10.1146/annurev.neuro.29.051605.112819

Rakic, P. (1972). Mode of cell migration to the superficial layers of fetal monkey neocortex. *The Journal of Comparative Neurology*, *145*(1), 61–83. http://doi.org/10.1002/cne.901450105

Ramalingam, M. (2012). *Integrated biomaterials for biomedical technology*. Hoboken, N.J.Salem, Mass.: John Wiley & Sons ;Scrivener Pub.

Ranieri, J. P., Bellamkonda, R., Bekos, E. J., Vargo, T. G., Gardella, J. a., & Aebischer, P. (1995). Neuronal cell attachment to fluorinated ethylene propylene films with covalently immobilized laminin oligopeptides YIGSR and IKVAV. II. *J. Biomed. Mater. Res.*, *29*(6), 779–785. http://doi.org/10.1002/jbm.820290614

Rapin, I., Weidenheim, K., Lindebbaum, Y., Rosenbaum, P., Merchant, S., Krishna, S., & Dickson, D. (2006). Cockayne Syndrome in Adults: Review With Clinical and Pathologic Study of a New Case. *Changes*, *21*(11), 991–1006. http://doi.org/10.1016/j.biotechadv.2011.08.021.Secreted

Rauch, U. (2004). Extracellular matrix components associated with remodeling processes in brain. *Cellular and Molecular Life Sciences : CMLS*, *61*(16), 2031–2045. http://doi.org/10.1007/s00018-004-4043-x

Reinhart-King, C. a, Dembo, M., & Hammer, D. a. (2005). The dynamics and mechanics of endothelial cell spreading. *Biophysical Journal*, *89*(1), 676–689. http://doi.org/10.1529/biophysj.104.054320

Ricoult, S. G., Pla-Roca, M., Safavieh, R., Lopez-Ayon, G. M., Grütter, P., Kennedy, T. E., & Juncker, D. (2013). Large dynamic range digital nanodot gradients of biomolecules made by low-cost nanocontact printing for cell haptotaxis. *Small*, *9*(19), 3308–3313. http://doi.org/10.1002/smll.201202915

Roam, J. L., Xu, H., Nguyen, P. K., & Elbert, D. L. (2010). The formation of protein concentration gradients mediated by density differences of poly(ethylene glycol) microspheres. *Biomaterials*, *31*(33), 8642–50. http://doi.org/10.1016/j.biomaterials.2010.07.085

Roberts, M. J., Bentley, M. D., & Harris, J. M. (2012). Chemistry for peptide and protein PEGylation. *Advanced Drug Delivery Reviews*. http://doi.org/10.1016/j.addr.2012.09.025

Ronan, L., Voets, N., Rua, C., Alexander-Bloch, A., Hough, M., Mackay, C., Crow, T. J., James, A., Giedd, J. N., & Fletcher, P. C. (2014). Differential tangential expansion as a mechanism for cortical gyrification. *Cerebral Cortex*, *24*(8), 2219–2228. http://doi.org/10.1093/cercor/bht082

Ronnett, G. V, Leopold, D., Cai, X., Hoffbuhr, K. C., Moses, L., Hoffman, E. P., & Naidu, S. (2003). Olfactory biopsies demonstrate a defect in neuronal development in Rett's syndrome. *Annals of Neurology*, *54*(2), 206–218. http://doi.org/10.1002/ana.10633

Ruoslahti, E. (1996). Brain extracellular matrix. *Glycobiology*, *6*(5), 489–492. http://doi.org/10.1093/glycob/6.5.489

Sarnat, H. B., Nochlin, D., & Born, D. E. (1998). Neuronal nuclear antigen (NeuN): A marker of neuronal maturation in the early human fetal nervous system. *Brain and Development*, *20*(2), 88–94. http://doi.org/10.1016/S0387-7604(97)00111-3

Scala, E., Ariani, F., Mari, F., Caselli, R., Pescucci, C., Longo, I., Meloni, I., Giachino,

D., Bruttini, M., Hayek, G., Zappella, M., & Renieri, A. (2005). CDKL5/STK9 is mutated in Rett syndrome variant with infantile spasms. *J Med Genet*, *42*(2), 103–107. http://doi.org/10.1136/jmg.2004.026237

Schafe, G. E. (2014). *Neuronal Networks in Brain Function, CNS Disorders, and Therapeutics*. *Neuronal Networks in Brain Function, CNS Disorders, and Therapeutics*. http://doi.org/10.1016/B978-0-12-415804-7.00013-7

Scheibye-knudsen, M., Croteau, D. L., & Bohr, V. A. (2013). Mitochondrial deficiency in Cockayne syndrome. *Mechanisms of Ageing and Development*, *134*(5-6), 275–283. http://doi.org/10.1016/j.mad.2013.02.007

Scheibye-Knudsen, M., Ramamoorthy, M., Sykora, P., Maynard, S., Lin, P., Minor, R., Wilson, D., Cooper, M., Spencer, R., de Cabo, R., Croteau, D., & Bohr, V. (2012). Cockayne syndrome group B protein prevents the accumulation of damaged mitochondria by promoting mitochondrial autophagy. *Journal of Experimental Medicine*. http://doi.org/10.1084/jem.20111721

Schmittgen, T. D., & Livak, K. J. (2008). Analyzing real-time PCR data by the comparative C(T) method. *Nature Protocols*, *3*(6), 1101–1108. http://doi.org/10.1038/nprot.2008.73

Schultz, K. M., Kyburz, K. A., & Anseth, K. S. (2015). Measuring dynamic cell-material interactions and remodeling during 3D human mesenchymal stem cell migration in hydrogels. *Proc Natl Acad Sci U S A*, *112*(29), E3757–64. http://doi.org/10.1073/pnas.1511304112

Seidlits, S. K., Khaing, Z. Z., Petersen, R. R., Nickels, J. D., Vanscoy, J. E., Shear, J. B., & Schmidt, C. E. (2010). The effects of hyaluronic acid hydrogels with tunable mechanical properties on neural progenitor cell differentiation. *Biomaterials*, *31*(14), 3930–3940. Retrieved from http://www.sciencedirect.com/science/article/pii/S0142961210001730

Selby, C., & Sancar, A. (1997). Cockayne syndrome group B protein enhances elongation by RNA polymerase II. *Proceedings of the National Academy of Sciences of the United States of America*, *94*(21), 11205–11209.

Sharma, B., Williams, C. G., Kim, T. K., Sun, D., Malik, A., Khan, M., Leong, K., & Elisseeff, J. H. (2007). Designing zonal organization into tissue-engineered cartilage. *Tissue Engineering*, *13*(2), 405–14. http://doi.org/10.1089/ten.2006.0068

Shcheglovitov, A., Shcheglovitova, O., Yazawa, M., Portmann, T., Shu, R., Sebastiano, V., Krawisz, A., Froehlich, W., Bernstein, J. a, Hallmayer, J. F., & Dolmetsch, R. E. (2013). SHANK3 and IGF1 restore synaptic deficits in neurons from 22q13 deletion syndrome patients. *Nature*, *503*(7475), 267–71. http://doi.org/10.1038/nature12618

Silva, G. A., Czeisler, C., Niece, K. L., Beniash, E., Harrington, D. A., Kessler, J. A., & Stupp, S. I. (2004). Selective differentiation of neural progenitor cells by high-epitope density nanofibers. *Science*, *303*(5662), 1352–1355.

http://doi.org/10.1126/science.1093783

Singelyn, J. M., DeQuach, J. a., Seif-Naraghi, S. B., Littlefield, R. B., Schup-Magoffin, P. J., & Christman, K. L. (2009). Naturally derived myocardial matrix as an injectable scaffold for cardiac tissue engineering. *Biomaterials*, *30*(29), 5409–5416. http://doi.org/10.1016/j.biomaterials.2009.06.045

Smeds, K. a., Pfister-Serres, A., Hatchell, D. L., & Grinstaff, M. W. (1999). Synthesis of a Novel Polysaccharide Hydrogel. *Journal of Macromolecular Science, Part A*, *36*(7-8), 981–989. http://doi.org/10.1080/10601329908951194

Smith, M. L., Gourdon, D., Little, W. C., Kubow, K. E., Eguiluz, R. A., Luna-Morris, S., & Vogel, V. (2007). Force-induced unfolding of fibronectin in the extracellular matrix of living cells. *PLoS Biology*, *5*(10), e268. http://doi.org/10.1371/journal.pbio.0050268

Straley, K. S., & Heilshorn, S. C. (2009). Dynamic, 3d-pattern formation within enzyme-responsive hydrogels. *Advanced Materials*, *21*(41), 4148–4152. http://doi.org/10.1002/adma.200901865

Stuss, D. P., Boyd, J. D., Levin, D. B., & Delaney, K. R. (2012). MeCP2 mutation results in compartment-specific reductions in dendritic branching and spine density in layer 5 motor cortical neurons of YFP-H mice. *PLoS ONE*, *7*(3), e31896.

Sullivan, K. E., Quinn, K. P., Tang, K. M., Georgakoudi, I., & Black, L. D. (2014). Extracellular matrix remodeling following myocardial infarction influences the therapeutic potential of mesenchymal stem cells. *Stem Cell Research & Therapy*, *5*(1), 14. http://doi.org/10.1186/scrt403

Sundararaghavan, H. G., Masand, S. N., & Shreiber, D. I. (2011). Microfluidic Generation of Haptotactic Gradients through 3D Collagen Gels for Enhanced Neurite Growth. *Journal of Neurotrauma*, *28*, 2377–2387. http://doi.org/10.1089/neu.2010.1606

Takahashi, K., Tanabe, K., Ohnuki, M., Narita, M., Ichisaka, T., Tomoda, K., & Yamanaka, S. (2007). Induction of pluripotent stem cells from adult human fibroblasts by defined factors. *Cell*, *131*(5), 861–872. http://doi.org/10.1016/j.cell.2007.11.019

Tang, J., Peng, R., & Ding, J. (2010). The regulation of stem cell differentiation by cell-cell contact on micropatterned material surfaces. *Biomaterials*, *31*(9), 2470–6. http://doi.org/10.1016/j.biomaterials.2009.12.006

Tang, N., Zhao, Y., Feng, R., Liu, Y., Wang, S., Wei, W., Ding, Q., An, M. S., Wen, J., & Li, L. (2014). Lysophosphatidic acid accelerates lung fibrosis by inducing differentiation of mesenchymal stem cells into myofibroblasts. *Journal of Cellular and Molecular Medicine*, *18*(1), 156–69. http://doi.org/10.1111/jcmm.12178

Tao, X., Jin, G., Zou, L., Li, H., & Qin, J. (2015). IGF2 Regulates Neuronal Differentiation of Hippocampal Radial Glial Cells In Vitro. *Journal of Cytology & Histology*, *06*(02). http://doi.org/10.4172/2157-7099.1000312

Tate, M. C., García, A. J., Keselowsky, B. G., Schumm, M. A., Archer, D. R., & LaPlaca, M. C. (2004). Specific β1 integrins mediate adhesion, migration, and differentiation of neural progenitors derived from the embryonic striatum. *Molecular and Cellular Neuroscience*, *27*(1), 22–31. Retrieved from http://www.sciencedirect.com/science/article/pii/S1044743104001058

Taylor-Weiner, H., Ravi, N., & Engler, A. J. (2015). Traction forces via integrin signaling are necessary for definitive endoderm specification. *Journal of Cell Science*, *128*(10), 1961–1968. http://doi.org/10.1242/jcs.166157

Temple, S. (2001). The development of neural stem cells. *Nature*, *414*, 112–117. http://doi.org/10.1038/35102174

Thompson, P. M., & Toga, A. W. (2003). Cerebral Cortex Diseases and Cortical Localization. *Encyclopedia of Life Sciences*. http://doi.org/10.1038/npg.els.0002195

Thomson, J. A., Itskovitz-Eldor, J., Shapiro, S. S., Waknitz, M. A., Swiergiel, J. J., Marshall, V. S., & Jones, J. M. (1998). Embryonic stem cell lines derived from human blastocysts. *Science (New York, N.Y.)*, *282*(5391), 1145–1147.

Trappmann, B., Gautrot, J. E., Connelly, J. T., Strange, D. G. T., Li, Y., Oyen, M. L., Cohen Stuart, M. a., Boehm, H., Li, B., Vogel, V., Spatz, J. P., Watt, F. M., & Huck, W. T. S. (2012). Extracellular-matrix tethering regulates stem-cell fate. *Nature Materials*, *11*(8), 742–742. http://doi.org/10.1038/nmat3387

Tse, J. R., & Engler, A. J. (2010). Preparation of Hydrogel Substrates with Tunable Mechanical Properties. In *Current Protocols in Cell Biology*. John Wiley & Sons, Inc. http://doi.org/10.1002/0471143030.cb1016s47

Tse, J. R., & Engler, A. J. (2011). Stiffness gradients mimicking in vivo tissue variation regulate mesenchymal stem cell fate. *PloS One*, *6*(1), e15978. http://doi.org/10.1371/journal.pone.0015978

Ullian, E. M., Christopherson, K. S., & Barres, B. A. (2004). Role for glia in synaptogenesis. *GLIA*. http://doi.org/10.1002/glia.20082

Van der Horst, G. T. J., Van Steeg, H., Berg, R. J. W., Van Gool, A. J., De Wit, J., Weeda, G., Morreau, H., Beems, R. B., Van Kreijl, C. F., De Gruijl, F. R., Bootsma, D., & Hoeijmakers, J. H. J. (1997). Defective transcription-coupled repair in Cockayne syndrome B mice is associated with skin cancer predisposition. *Cell*, *89*(3), 425–435. http://doi.org/10.1016/S0092-8674(00)80223-8

Van Der Pluijm, I., Garinis, G. a., Brandt, R. M. C., Gorgels, T. G. M. F., Wijnhoven, S. W., Diderich, K. E. M., De Wit, J., Mitchell, J. R., Van Oostrom, C., Beems, R., Niedernhofer, L. J., Velasco, S., Friedberg, E. C., Tanaka, K., Van Steeg, H., Hoeijmakers, J. H. J., & Van Der Horst, G. T. J. (2007). Impaired genome maintenance suppresses the growth hormone-insulin-like growth factor 1 axis in mice with cockayne syndrome. *PLoS Biology*, *5*(1), 0023–0038. http://doi.org/10.1371/journal.pbio.0050002

Vélez-Cruz, R., & Egly, J. (2013). Cockayne syndrome group B (CSB) protein : At the crossroads of transcriptional networks. *Mechanisms of Ageing and Development*, *134*, 234–242. http://doi.org/10.1016/j.mad.2013.03.004

Venema, J., Mullenders, L. H., Natarajan, a T., van Zeeland, a a, & Mayne, L. V. (1990). The genetic defect in Cockayne syndrome is associated with a defect in repair of UV-induced DNA damage in transcriptionally active DNA. *Proceedings of the National Academy of Sciences of the United States of America*, *87*(12), 4707–4711. http://doi.org/10.1073/pnas.87.12.4707

Vessoni, A. T., Herai, R. H., Karpiak, J. V., Leal, A. M. S., Trujillo, C. A., Quinet, A., Agnez Lima, L. F., Menck, C. F. M., & Muotri, A. R. (2016). Cockayne Syndrome-derived neurons display reduced synapse density and altered neural network synchrony. *HMG Advance Abstract*. http://doi.org/10.1093/hmg/ddw008

Vincent, L. G., Choi, Y. S., Alonso-Latorre, B., Del Álamo, J. C., & Engler, A. J. (2013). Mesenchymal stem cell durotaxis depends on substrate stiffness gradient strength. *Biotechnology Journal*, *8*(4), 472–484. http://doi.org/10.1002/biot.201200205

Vogel, V., & Sheetz, M. (2006). Local force and geometry sensing regulate cell functions. *Nature Reviews. Molecular Cell Biology*, *7*(4), 265–275. http://doi.org/10.1038/nrm1890

Walshe, T. E., Leach, L. L., & D'Amore, P. a. (2011). TGF-β signaling is required for maintenance of retinal ganglion cell differentiation and survival. *Neuroscience*, *189*, 123–131. http://doi.org/10.1016/j.neuroscience.2011.05.020

Wang, I.-T. J., Allen, M., Goffin, D., Zhu, X., Fairless, A. H., Brodkin, E. S., Siegel, S. J., Marsh, E. D., Blendy, J. a, & Zhou, Z. (2012). Loss of CDKL5 disrupts kinome profile and event-related potentials leading to autistic-like phenotypes in mice. *Proceedings of the National Academy of Sciences of the United States of America*, *109*(52), 21516–21. http://doi.org/10.1073/pnas.1216988110

Wang, Y., Chakravarty, P., Ranes, M., Kelly, G., Brooks, P., Neilan, E., Stewart, A., Schiavo, G., & Svejstrup, J. (2014). Dysregulation of gene expression as a cause of Cockayne syndrome neurological disease. *Proceedings of the National Academy of Sciences*, *111*(40), 14454–14459. http://doi.org/10.1073/pnas.1412569111

Weber, L. M., Cheung, C. Y., & Anseth, K. S. (2007). Multifunctional Pancreatic Islet Encapsulation Barriers Achieved Via Multilayer PEG Hydrogels. *Cell Transplantation*, *16*(10), 1049–1057. http://doi.org/10.3727/000000007783472336

Wegiel, J., Kuchna, I., Nowicki, K., Imaki, H., Wegiel, J., Marchi, E., Ma, S. Y., Chauhan, A., Chauhan, V., Bobrowicz, T. W., de Leon, M., Louis, L. A., Cohen, I. L., London, E., Brown, W. T., & Wisniewski, T. (2010). The neuropathology of autism: defects of neurogenesis and neuronal migration, and dysplastic changes. *Acta Neuropathol*, *119*(6), 755–770. http://doi.org/10.1007/s00401-010-0655-4

Weidenheim, K., Dickson, D., & Rapin, I. (2009). Neuropathology of Cockayne

syndrome: Evidence for impaired development, premature aging, and neurodegeneration. *Mechanisms of Ageing and Development*, *130*(9), 619–636. http://doi.org/10.1016/j.mad.2009.07.006

Wells, R. G. (2008). The role of matrix stiffness in regulating cell behavior. *Hepatology*, *47*(4), 1394–1400. http://doi.org/10.1002/hep.22193

Wen, J. H., Vincent, L. G., Fuhrmann, A., Choi, Y. S., Hribar, K. C., Taylor-Weiner, H., Chen, S., & Engler, A. J. (2014). Interplay of matrix stiffness and protein tethering in stem cell differentiation. *Nature Materials*, *advance on*, 1–21. http://doi.org/10.1038/nmat4051

Williams, E. C., Zhong, X., Mohamed, A., Li, R., Liu, Y., Dong, Q., Ananiev, G. E., Mok, J. C., Lin, B. R., Lu, J., Chiao, C., Cherney, R., Li, H., Zhang, S. C., & Chang, Q. (2014). Mutant astrocytes differentiated from Rett syndrome patients-specific iPSCs have adverse effects on wild-type neurons. *Hum Mol Genet*, *23*(11), 2968–2980. http://doi.org/10.1093/hmg/ddu008

Wong, J., Visanji, N., Dabek, M., Laposa, R., & Hazrati, L. (2013). Dendritic spine density is altered in a mouse model of Cockayne syndrome. *Neuropathology and Applied Neurobiology*, 437–440. http://doi.org/10.1111/j.1365-2990.2012.01305.x

Wong, R. O. L., & Ghosh, A. (2002). Activity-dependent regulation of dendritic growth and patterning. *Nature Reviews Neuroscience*, *3*(10), 803–812. http://doi.org/10.1038/nrn941

Wylie, R. G., Ahsan, S., Aizawa, Y., Maxwell, K. L., Morshead, C. M., & Shoichet, M. S. (2011). Spatially controlled simultaneous patterning of multiple growth factors in three-dimensional hydrogels. *Nat Mater*, *10*(10), 799–806. http://doi.org/http://www.nature.com/nmat/journal/v10/n10/abs/nmat3101.html#supplementary-information

Yamaguchi, Y. (2000). Lecticans: organizers of the brain extracellular matrix. *Cellular and Molecular Life Sciences : CMLS*, *57*(2), 276–289. http://doi.org/10.1007/PL00000690

Yang, C., Tibbitt, M. W., Basta, L., & Anseth, K. S. (2014). Mechanical memory and dosing influence stem cell fate. *Nat Mater*, *13*(6), 645–652. http://doi.org/10.1038/nmat3889

Yu, X., Dillon, G. P., & Bellamkonda, R. B. (1999). A laminin and nerve growth factor-laden three-dimensional scaffold for enhanced neurite extension. *Tissue Eng*, *5*(4), 291–304.

Yuan, S. H., Martin, J., Elia, J., Flippin, J., Paramban, R. I., Hefferan, M. P., Vidal, J. G., Mu, Y., Killian, R. L., Israel, M. A., Emre, N., Marsala, S., Marsala, M., Gage, F. H., Goldstein, L. S., & Carson, C. T. (2011). Cell-surface marker signatures for the isolation of neural stem cells, glia and neurons derived from human pluripotent stem cells. *PLoS ONE*, *6*(3), e17540. http://doi.org/10.1371/journal.pone.0017540

Zaari, N., Rajagopalan, P., Kim, S. K., Engler, A. J., & Wong, J. Y. (2004). Photopolymerization in microfluidic gradient generators: Microscale control of substrate compliance to manipulate cell response. *Advanced Materials*, *16*(23-24), 2133–2137. http://doi.org/10.1002/adma.200400883

Zhang, Z., Lai, Y., Yu, L., & Ding, J. (2010). Effects of immobilizing sites of RGD peptides in amphiphilic block copolymers on efficacy of cell adhesion. *Biomaterials*, *31*(31), 7873–7882. http://doi.org/10.1016/j.biomaterials.2010.07.014

Zimmermann, D. R., & Dours-Zimmermann, M. T. (2008). Extracellular matrix of the central nervous system: From neglect to challenge. *Histochemistry and Cell Biology*, *130*, 635–653. http://doi.org/10.1007/s00418-008-0485-9

Zorlutuna, P., Annabi, N., Camci-Unal, G., Nikkhah, M., Cha, J. M., Nichol, J. W., Manbachi, A., Bae, H., Chen, S., & Khademhosseini, A. (2012). Microfabricated biomaterials for engineering 3D tissues. *Adv Mater*, *24*(14), 1782–1804. http://doi.org/10.1002/adma.201104631